



# Naval Research Laboratory

Washington, DC 20375-5320

NRL/MR/6720--02-8605

## Advanced Radiation Theory Support Annual Report 2001, Final Report

JACK DAVIS

*Radiation Hydrodynamics Branch  
Plasma Physics Division*

September 30, 2002

Approved for public release; distribution is unlimited.

20021011 065

# REPORT DOCUMENTATION PAGE

Form Approved  
OMB No. 0704-0188

Public reporting burden for this collection of information is estimated to average 1 hour per response, including the time for reviewing instructions, searching existing data sources, gathering and maintaining the data needed, and completing and reviewing this collection of information. Send comments regarding this burden estimate or any other aspect of this collection of information, including suggestions for reducing this burden to Department of Defense, Washington Headquarters Services, Directorate for Information Operations and Reports (0704-0188), 1215 Jefferson Davis Highway, Suite 1204, Arlington, VA 22202-4302. Respondents should be aware that notwithstanding any other provision of law, no person shall be subject to any penalty for failing to comply with a collection of information if it does not display a currently valid OMB control number. PLEASE DO NOT RETURN YOUR FORM TO THE ABOVE ADDRESS.

1. REPORT DATE (DD-MM-YYYY) September 30, 2002		2. REPORT TYPE Memorandum Report		3. DATES COVERED (From - To) October 1, 2000-September 30, 2001
4. TITLE AND SUBTITLE  Advanced Radiation Theory Support Annual Report 2001, Final Report				5a. CONTRACT NUMBER
				5b. GRANT NUMBER
				5c. PROGRAM ELEMENT NUMBER
6. AUTHOR(S)  Jack Davis, Radiation Hydrodynamics Branch				5d. PROJECT NUMBER
				5e. TASK NUMBER
				5f. WORK UNIT NUMBER
7. PERFORMING ORGANIZATION NAME(S) AND ADDRESS(ES)  Naval Research Laboratory, Code 6720 4555 Overlook Avenue, SW Washington, DC 20375-5320				8. PERFORMING ORGANIZATION REPORT NUMBER  NRL/MR/6720--02-8605
9. SPONSORING / MONITORING AGENCY NAME(S) AND ADDRESS(ES)  Defense Threat Reduction Agency 6801 Telegraph Road Alexandria, VA 22310				10. SPONSOR / MONITOR'S ACRONYM(S)
				11. SPONSOR / MONITOR'S REPORT NUMBER(S)
12. DISTRIBUTION / AVAILABILITY STATEMENT  Approved for public release; distribution is unlimited.				
13. SUPPLEMENTARY NOTES  This research was sponsored by the Defense Threat Reduction Agency under Job Order Title "Advanced Radiation Theory Support," MIPR No. 012383				
14. ABSTRACT  This report describes the work of the Radiation Hydrodynamics Branch during FY 2001 in support of the DTRA PRS program. Critical issues covered are: (1) the production of high energy photons, (2) multigroup radiative diffusion, (3) comparison of time-resolved and time-integrated X-ray data, (4) modeling enhanced energy coupling in Z-pinch plasmas, (5) fusion driven K-shell yield production, (6) magnetic flux compression, and (7) assessment of Decade Quad argon double puff nozzle experiments.				
15. SUBJECT TERMS Decade; Enhanced energy dissipation; Long time implosions; Large radius implosions; Transport coefficients; Diagnostic line ratios; Rayleigh-Taylor instability; Plasma radiation source; Radiation MHD; Z-pinch physics				
16. SECURITY CLASSIFICATION OF:  a. REPORT Unclassified		17. LIMITATION OF ABSTRACT UL	18. NUMBER OF PAGES 177	19a. NAME OF RESPONSIBLE PERSON J. Ward Thornhill
b. ABSTRACT Unclassified		19b. TELEPHONE NUMBER (include area code) (202) 404-4383		
c. THIS PAGE Unclassified				

## CONTENTS

Executive Summary .....	v
I. High Energy Photon Radiation from a Z-Pinch Plasma .....	1
II. Comparative Analysis of Time-Resolved and Time-Integrated X-Ray Data from Long Pulse Z-Pinch Implosions on Saturn .....	38
III. Au/CH/DT Implosions on 20, 40, and 60 MA Z Pinches .....	82
IV. Free Surface Boundary Conditions for Diffusive Radiation Transport in PRS Simulations .....	101
V. Modeling Enhanced Energy Absorption in Long Current-Risetime Saturn Experiments .....	107
VI. K-shell Yield Scaling Review for Argon Loads on Decade Quad .....	136
VII. Magnetic Flux Compression by Plasma Shells .....	151



## EXECUTIVE SUMMARY

This report describes the theory support of DTRA's Plasma Radiation Source (PRS) program carried out by NRL's Radiation Hydrodynamics Branch (Code 6720) in FY 2001. Included is work called for in DTRA MIPR 01-2383 - "Plasma Radiation Theory Support" and in Sandia National Laboratories' document number 19079 - "Diagnostic and Spectroscopic Calculations and Analysis."

The record 275 kilojoules of argon K-shell radiation that was achieved last year on Sandia National Laboratories' Z generator demonstrated that it is possible to efficiently produce K-shell emission from large radius argon loads. This year, the same load configuration was used effectively on Decade Quad (DQ) to produce 28 kJ of argon K-shell emission. This yield was substantially in excess of an  $I^2$  scaling projection from previous yields attained on Double Eagle, and therefore puts the Decade program firmly on the way to achieving its goal of efficiently producing argon K-shell yield from long implosion time, inductive store, generators. While the Z machine and Decade Quad experiments were successful (given the currents achieved), it presently is not understood why DQ and Z failed to attain their anticipated current levels. Power flow is suspected to be responsible for this behavior, but there is also strong evidence that extra impedance due to magnetic bubbles and/or other anomalous heating mechanisms is playing a role. These issues are discussed in this report.

In addition to the success with gas puff loads, substantial progress was made in understanding the dynamics of wire array loads. For example, the aluminum experiments performed on the long pulse Saturn generator have further quantified the wire number and gap spacing conditions that maximize power. For the first time, a decrease in x-ray power was observed with very high wire number loads in these experiments. The results of the titanium/aluminum experiments performed on the Z generator also showed interesting effects of wire number on penetration of the outer wire array through the inner array. Detailed data from these Saturn and Z experiments are being prepared by our co-workers at Sandia, for analysis at NRL.

Improving power flow and employing larger radius loads to make available more useful machine energy for K-shell emission are two traditional paths that have been followed in plasma radiation source (PRS) development. There were several theoretical efforts made this year in

support of these paths, including: improving our analysis of diagnostic measurements to provide a better picture of the state of the plasma, improving two-dimensional modeling capabilities to better assess multi-dimensional effects inherent to large radius loads, and assessing load performance by comparing measured currents, implosion times, and K-shell yields with values calculated using our radiation magnetohydrodynamic (RMHD) models. In addition to supporting these traditional paths, for which progress is often achieved by fine tuning PRS knowledge, substantial effort was expended to find new and innovative paths to aid and improve PRS development. These efforts include: establishing the importance of designing loads that promote recombination radiation as a source of high energy photons, investigating fusion assisted load designs for achieving temperatures and densities required to produce copious high energy photons, and investigating load designs that harness, and radiate in the K shell, the additional energy (factors of 2 or more greater than JXB) that is coupled to long implosion time loads..

In this report the progress made in load design, model development and assessment, and in diagnostic development for the purposes of improving PRS understanding and performance is discussed section by section:

(1) Given that it may be some time before the Z machine is upgraded, it will be awhile before high energy K-shell ( $> 7$  keV) yields are substantially increased by using higher drive currents to produce K-shell emission via the conventional approach, i.e. by ionizing a high Z plasma to the K-shell that emits in the required high energy range. We therefore have developed a parallel strategy. In this innovative approach it is determined that it may be advantageous to produce the required high energy x rays by recombination radiation emitted from a lower atomic number plasma than would otherwise be required if the photons were generated by K-shell line emission. The optimal load conditions for maximizing the high energy free-bound continuum radiation that can be produced in a given spectral range are analyzed. The largest yield is expected from a highest-atomic-number element that could efficiently produce K-shell yield on a given pulse power machine. Two options available for the choice of a wire array material to generate x rays with photon energies above 7-8 keV are identified and discussed, aluminum and titanium. Our analytical estimates and simulation results for Z machine implosions show that continuum radiation from an aluminum plasma in this spectral range could exceed the K-shell output from nickel. If a titanium plasma could be ionized to a H-like state on "Z", then its yield above 7 keV

should be higher compared to that of aluminum by a factor of 3 to 4. This section also stresses the importance of making measurements of the high energy continuum component of the x-ray spectrum (which has not been done on past experiments) to test the ideas of this approach as well as to provide important diagnostic information about the state of the plasma region from which this radiation is emitted.

(2) It is essential to have reliable feedback between experiment, model development and load design in order to obtain new understanding and sustain improvements in PRS. This feedback is in large part provided by plasma diagnostics and analysis. The work presented in this section demonstrates how our knowledge of the state of the plasma progressively improves with increased spatial and temporal resolution of the measured and theoretical spectral information (e.g., total powers, K-shell powers, size of K-shell emission region, line ratios, spatially resolved spectra, time integrated and resolved spectra). By comparing measured spectral information to calculated information based on theoretical density and temperature profiles which are modified until agreement is reached (calculated with our ionization and radiation transport models), one can infer a state-of-the-art view of the plasma. This year an investigation was undertaken to answer the question: How do the deductions regarding the properties of Z pinches depend on the spatial and temporal resolution present in the data or temperature and density profiles assumed in the model? The results of this investigation clearly and dramatically demonstrate the importance and benefits of improved experimental and theoretical resolution in both space and time. Extending our present 1D diagnostic/analysis capabilities to multidimensions is a possible next step in this direction.

(3) The recent successes with large Z-pinch devices such as the Saturn and Z facilities at Sandia National Laboratories have increased interest in Z-pinch fusion. Our estimates show that currents in excess of 20-30 MA may produce magnetic fields sufficient to confine  $\alpha$ - particles. In this investigation we performed a series of calculations with Au/CH/DT loads with peak currents ranging from 20 to 60 MA. The D-T yield and the yield of the  $\alpha$ -particles deposited in the plasma are calculated for each configuration. While this initial investigation focused on calculating fusion yields, the next step is to calculate the plasma heating generated by these fusion products. The advantage of these fusion assisted loads is that they may be able to reach the high temperature and density conditions that are required to produce copious high energy ( $> 10$  keV) photons at substantially reduced current levels.

(4) We are in the process of adapting Code 6720 radiation transport capabilities to the Mach2 MHD code. A two-dimensional MHD model that incorporates a realistic treatment of ionization dynamics and radiation transport is essential for understanding the roles that plasma instabilities and initial asymmetries are playing in affecting the radiation characteristics of PRS loads. In this regard, this section discusses a free surface boundary condition for diffusive radiation transport that is to be implemented in Mach2's radiation diffusion model. This is a substantial improvement to Mach2 because this condition frees the model of any requirement to know in advance the radiation temperature at the boundary. Presently, the temperature is set in an *ad hoc* manner in Mach2. In addition, this boundary condition technique is readily adapted to multigroup radiative diffusion, which is important because we are currently extending Mach2's capabilities to include multigroup diffusion.

(5) The reconfiguration of Saturn from a short pulse to a long pulse machine has produced significant increases in total x-ray output by factors of 2 to 4. This output energy, which primarily showed up as subkilovolt x rays, cannot be accounted for by the input  $J \times B$  work. A recently hypothesized magnetic flux tube mechanism (1999 Annual Report) for extracting this energy from the circuit is phenomenologically modeled and extended to match the data taken from a series of long pulse Saturn aluminum experiments. One of the main purposes of the analysis described in this section is to investigate prospects for diverting more of the flux tube energy into the K-shell. A new shot plan for Saturn is devised that is predicted to accomplish this goal.

(6) The K-shell yield performance of Titan double-shell argon gas puff loads imploded on the Z machine and DQ is examined relative to the performance of similar Double Eagle loads employing the same nozzle configuration. Specifically, the K-shell yields obtained on the Z and DQ generators are compared with  $I^4$ ,  $I^2$ , and  $I^0$  scaling projections made from Double Eagle yields, where  $I$  is the peak load current. This analysis automatically takes into account initialization and multidimensional effects as long as the performance of a load is viewed in terms of its scaling projections from the same nozzle's performance on Double Eagle (same ratio of inner to outer shell masses, same amount of recession into the cathode, preionization, pinch length, etc). This projection analysis serves as a valuable tool for evaluating Z-pinch load performance because it can be related to the same  $I^4$ ,  $I^2$ , and  $I^0$  K-shell yield scaling transitions that a load, of a given specific energy, is predicted to undergo as the total load mass increases. Our analysis shows that

the maximum K-shell yields were near optimum for the nozzle configuration used and the energy coupled to the load in these experiments. At present it is not well understood why an additional 22 nH of inductance for DQ, 6 nH for the Z machine, and 8 nH for Double Eagle is required in their respective circuits to reasonably match measured peak currents and implosion times. It is plausible that there are multidimensional, mass distribution or other anomalous load effects that can account for this additional impedance. The extra 22 nH required for DQ also suggest that for this generator there may be a more fundamental power flow issue. These issues and effects are addressed in this work.

(7) Magnetic Flux compression represents a new opportunity for using low-cost energy sources to generate the tens of MA that are required to produce copious amounts of  $> 10$  keV photons from a Z pinch. In this section we discuss approximate analytical models that describe the dynamics of imploding Z-pinch shells. The results of 1D and 2D numerical simulations are presented. In particular it is determined that the diffusive loss of magnetic flux does not constitute a major limitation of the magnetic flux compression approach to producing large currents that can be used to drive high-energy photon producing Z-pinch loads.

# High energy photon radiation from a Z-pinch plasma

## I. INTRODUCTION

The Z-pinch plasma radiation source (PRS) development program focuses on achieving substantial amounts of x rays in keV photon energies<sup>1</sup> by stripping moderate atomic number elements to their K-shells and utilizing the very strong lines which radiate from the hydrogen- and helium-like ions to produce the bulk of the keV yield. Since the energy required to strip an element of atomic number  $Z$  to its K-shell while heating it to an efficient radiating temperature varies as  $Z^{11/3}$ , see Ref. 2, the emphasis has been on using ever higher currents to impart more energy to the load. This approach has been very successful, recently culminating in the achievement of nearly 300 kJ of Ar K-shell x-rays at 3-4 keV and 125 kJ of Ti K-shell x-rays at ~4.8 keV from Sandia's "Z" generator.<sup>3,4</sup>

However, production of harder x rays is increasingly difficult,<sup>5</sup> i. e. the most recent results for Ni and Cu K-shell x rays at 7-8 keV are only 10-20 kJ, as seen in Fig. 1. This is true not only because of increasingly high energy that must be coupled to each ion, but, in addition, because heating of high-atomic-number plasmas is also a serious problem. The energy supplied to a plasma of a high-atomic-number element, i. e., via conversion of the imploding plasma's kinetic energy to thermal energy at stagnation, is partially lost through subkilovolt line radiation of outer atomic orbitals at the rate that rapidly increases with  $Z$ , see Refs. 6, 7. As a result, the plasma temperature can remain too low for producing a substantial fraction of H- and He-like ions, and therefore, a large amount of K-shell radiation. The problem of sub-keV radiation losses becomes more severe with increased  $Z$ , as the simulation results of Refs. 6, 7 and the experimental trend of Fig. 1 demonstrate.

Are there any alternatives to the conventional method of hard x-ray radiation production outlined above? In this paper, we discuss one that uses radiation of lower-atomic number elements than otherwise would be required if the radiation came from K-shell lines. These lower atomic number elements have no spectral lines in the range of high photon energies of interest. However, they do emit free-bound (recombination) radiation, as well as free-free (bremsstrahlung) at energies well in excess of their K-shell excitation potentials. An obvious advantage of a lower atomic number plasma is that one need not pay the large energetic price of stripping many electrons to reach a K-shell radiating hard x-ray lines, as is the case with Cu and Ni, for example. The disadvantage is that continuum emission processes are inherently less efficient than line radiation. For example, for an argon plasma at an electron temperature of 3 keV, the electron collisional rate for exciting the very strong H-like line at 3321 eV is a factor of 7 greater than the rate for radiative recombination which produces free-bound continuum emission at energies above 4426 eV. The free-free radiation emission coefficient is another factor of 6 below that of this free-bound process. However, it has already been demonstrated that heating argon to temperatures of 2-3 keV and producing efficient argon K-shell emission are possible,<sup>3</sup> so that we do not need any alternative methods for producing 3.1 keV quanta with a lower-than-argon atomic number material. The real question is whether on a “Z”-class machine, a Z pinch could produce more radiation at 7-8 keV in the continuum from argon (or aluminum, or titanium) plasma than nickel would emit in its K-shell. This essential question is one of tradeoffs and efficiencies, and our results indicate that the answer to this question may well be affirmative.

We emphasize that the present work considers thermal recombination only. Analysis of some early “Z” experiments (see Fig. 5 of Ref. 9) indicates that a fast electron population can account for a significant portion of the yield at photon energies above 5 keV.

The paper is structured as follows. In Sec. II, we present analytical estimates of the hard x-ray yield that could be produced by continuum radiation mechanisms, and formulate the optimization criteria. Section III presents the results of numerical simulation for hard x-ray continuum production in aluminum and titanium implosions on “Z”. In Sec. IV we conclude with a discussion.

## II. ANALYTICAL ESTIMATES

### A. Direct recombination continuum

Here we present some simple analytical estimates referring to the continuum radiation mechanisms, which have not been emphasized in recent years. Our goal is to use continuum radiation mechanisms for generating large amounts of hard x-rays, with photon energies exceeding a certain pre-defined value,  $h\nu > E_0$  (for our estimates, we take  $E_0$  equal to either 7 or 10 keV.) The issues of interest are: What load material is best for generating continuum radiation in a given spectral range? What are the optimum temperature and density of stagnated plasma, and the corresponding load dimensions and mass?

Let us estimate the free-bound (direct or radiative recombination) radiation yield in the energy range  $h\nu > E_0$ . The total radiation power per unit volume of an (almost)

fully ionized plasma is given by Eq. (9.6) of Ref. 10 for the particular case of radiative recombination onto bare nuclei:

$$P_{rr}^{(total)} = \frac{128\sqrt{2}\pi^{7/2}e^{10}}{3\sqrt{3}m_e^{1/2}h^3c^3} \frac{Z^5n^2}{T^{1/2}}, \quad (1)$$

(here and below, we use Gaussian units), where  $T$  is the electron temperature; the difference between the Gaunt factors and unity is neglected, as well as the contribution of recombination to the excited levels. In deriving (1), we assume that the plasma is overheated, almost fully ionized, so that the quasi-neutrality condition can be used in the form:

$$n_e = Zn_Z + (Z-1)n_{Z-1} \approx Zn, \quad (2)$$

where we denote by  $n \equiv n_Z$  the number density of fully stripped ions (similarly,  $n_{Z-1}$  is the number density of hydrogen-like ions), and

$$n = n_Z \gg n_{Z-1}. \quad (3)$$

This implies that the plasma temperature is high enough to strip the atoms beyond the H-like state. A condition of “almost full ionization” is derived from the state of collisional-radiative equilibrium (CRE), and can be written as

$$T > T_{\min} = \alpha E_H \times s Z^\sigma = \frac{4\pi^3 e^6 m_e}{h^3 c} \times s Z^\sigma = (0.0993 \text{ eV}) \times s Z^\sigma, \quad (4)$$

where  $\alpha = 2\pi e^2 / hc = 1/137.04$  is the fine structure constant. The power  $\sigma$  and the dimensionless coefficient of order unity  $s$  are obtained from the CRE calculations and are slowly varying functions of plasma density: for  $n_i$  increased from  $10^{18}$  to  $10^{21} \text{ cm}^{-3}$ ,  $\sigma$  and  $s$  vary from 3.47 to 3.86 and from 1.67 to 0.429, respectively. For our estimates we will use the values found at  $n_i = 10^{20} \text{ cm}^{-3}$ :  $s = 0.655$ ,  $\sigma = 3.75$ .

### The thermal recombination radiation spectrum above the ionization energy

threshold  $h\nu > E_z = E_H Z^2$  (where  $E_z$  is the ionization energy of hydrogen-like ions with charge  $Z$ ,  $E_H = 2\pi^2 e^4 m_e / h^2 = 13.6$  eV being the ionization energy of a hydrogen atom, the Rydberg energy unit), is exponential:  $P_{rr}(v)dv \propto \exp(-h\nu/T)dv$ . We are interested in producing radiation in a “hard” energy range, where our low-atomic-number element emits no lines; therefore, we have to assume that  $E_z < E_0$ . The power of free-bound radiation in the “hard” energy range  $h\nu > E_0$  is then given by

$$\begin{aligned} P_{rr}^{(hard)} &= \frac{128\sqrt{2}\pi^{7/2}e^{10}}{3\sqrt{3}m_e^{1/2}h^3c^3} \frac{Z^5n^2}{T^{1/2}} \exp\left(-\frac{E_0 - Z^2E_H}{T}\right) \\ &= 4.18 \times 10^{-31} \frac{Z^5n^2}{T^{1/2}} \exp\left(-\frac{E_0 - Z^2E_H}{T}\right) \text{ W/cm}^3 \end{aligned} \quad (5)$$

where the number density is expressed in  $\text{cm}^{-3}$ , the temperature and energy in eV. In the limit  $E_z \rightarrow E_0$ , (5) reduces to (1).

From (5), we can estimate the yield  $Y$  in the “hard” energy range  $h\nu > E_0$ . To do this, in a way similar to that used in Ref. 11 for estimating K-shell yield, we assume the stagnated radiating plasma column to be quasi-uniform, well-characterized by its average values of temperature and density. Then the yield is estimated as

$$Y = \pi R_f^2 \tau_r P_{rr}^{(hard)}, \quad (6)$$

where  $R_f$  is the final radius of the pinch,  $\tau_r$  is the hydrodynamic confinement time:

$$\tau_r = \frac{R_f}{\left[3\frac{(1+Z)T}{m_i}\right]^{1/2}} \cong \frac{R_f}{\left[3\frac{(1+Z)T}{2Zm_u}\right]^{1/2}} \cong R_f \left(\frac{2m_u}{3T}\right)^{1/2} = 830 \frac{R_f}{T^{1/2}} \text{ ns}, \quad (7)$$

where  $m_u = 1.6605 \times 10^{-24}$  g is the atomic mass unit, and we approximated the atomic weight for a moderate number element as  $A \approx 2Z$ . Note that hard x-ray radiation often comes from a small fraction of the plasma mass. It is by no means certain that duration of the radiation pulse, particularly in the high-energy spectral range, is actually determined by the hydrodynamic confinement time (7) estimated from the average parameters of the radiating plasma column. However, analysis of numerous experimental results demonstrates that (7) is a conservative estimate of the radiation pulse FWHM from below. Making such an estimate for titanium implosions on “Z”,<sup>4</sup> we take  $R_f = 1.25$  to 1.5 mm,  $T = 2.7$  to 3.2 keV (Ref. 4, Table II), to obtain  $\tau_r$  from 1.8 to 2.4 ns, whereas the observed K-shell radiation pulse FWHM was 6 ns or more. Similarly, for argon implosions on “Z”,<sup>3</sup> taking  $R_f = 2.5$  mm and  $T = 2.4$  keV, we find  $\tau_r = 4.2$  ns, the observed K-shell radiation pulse FWHM being about 12 ns. In the high-energy continuum spectral range, opacity effects are negligible, and we can assume all radiated photons to escape the pinch plasma. Finally, we express the average ion number density  $n$  via the line ion density  $N$  and final radius of the plasma column  $R_f$  as

$$n = \frac{N}{\pi R_f^2}. \quad (8)$$

Substituting (5), (7) and (8) into (6), we obtain:

$$\begin{aligned} Y &= \frac{256\pi^{5/2} e^{10} m_u^{1/2}}{9m_e^{1/2} h^3 c^3} \frac{N^2 Z^5}{R_f T} \exp\left(-\frac{E_0 - Z^2 E_H}{T}\right) \\ &= 1.1 \times 10^{-37} \frac{N^2 Z^5}{R_f T} \exp\left(-\frac{E_0 - Z^2 E_H}{T}\right) \text{ J/cm} \end{aligned} \quad (9)$$

For a given pinch current, there is a tradeoff between the plasma temperature and density: magnetic pressure of the current can confine the pinch plasma only up to a

certain value of  $NT$ . In a steady state, this fact is expressed by the Bennett relation. Here, we choose a slightly different approximation to relate the density and temperature at stagnation to the implosion parameters. We assume that the thermal energy available for conversion into hard radiation is proportional to kinetic energy of the imploded plasma:

$$E = \frac{3}{2} ZNT = \varepsilon K, \quad (10)$$

where the kinetic energy  $K$  is given by the conventional

$$K = a \frac{I_m^2}{c^2} \ln \frac{R_0}{R_f}, \quad (11)$$

$I_m$  is the peak current and  $a$  is the dimensionless parameter describing the current pulse shape ( $a = 1$  for implosion by a constant current; for most implosions,  $a = 0.6$  is a good approximation, and we will use this value for our estimates below),  $R_0$  and  $R_f$  are initial and final radii of the pinch, respectively. As usual,<sup>11</sup> introduction of the parameter  $\varepsilon$  involves a certain ambiguity. A Z-pinch could convert into thermal energy and radiate much more (sometimes by a factor from 3 to 4) than the kinetic energy  $K$ , see Ref. 12. But most of this radiation is emitted as low-energy photons, so it would be unrealistic to expect  $\varepsilon > 1$ . This parameter should account for energy spent on ionization, energy losses due to low-energy radiation while the plasma is heated to its peak temperature, and for the difference between the peak values of density and temperature and those averaged over the duration of the radiation pulse. One can expect  $\varepsilon$  to be about  $1/2$ , maybe somewhat lower for higher  $Z$ , as confirmed by our simulations results, see Section III.

Then

$$N = \frac{2a\varepsilon}{3ZT} \frac{I_m^2}{c^2} \ln \frac{R_0}{R_f}. \quad (12)$$

Substituting this value into (9), we obtain:

$$Y = \frac{1024\pi^{5/2}e^{10}m_u^{1/2}}{81m_e^{1/2}h^3c^7} \frac{a^2\epsilon^2Z^3I_m^4}{R_f T^3} \left( \ln \frac{R_0}{R_f} \right)^2 \exp \left( -\frac{E_0 - Z^2 E_H}{T} \right), \quad (13)$$

$$= 1.91 \times 10^6 \frac{a^2\epsilon^2Z^3I_m^4}{R_f T^3} \left( \ln \frac{R_0}{R_f} \right)^2 \exp \left( -\frac{E_0 - Z^2 E_H}{T} \right) \text{ J/cm}$$

where the peak current  $I_m$  is expressed in MA, the radii  $R_0$  and  $R_f$  - in cm, the temperature and energy in eV, as above. The dependence  $Y \propto I_m^4$  indicates an “inefficient” regime of radiation generation,<sup>13</sup> i. e., when only a small fraction of the total plasma energy is converted into radiation in the desired spectral range. This is indeed the case for the present generation of the pulsed power facilities and in the “hard” spectral range, say, above 7 keV.

The expression (13) clearly peaks at a certain optimum value of temperature, see Fig. 2. Differentiating the right-hand side of (13), we find this peak value:

$$T_{\text{peak}} = \frac{E_0 - Z^2 E_H}{3}. \quad (14)$$

It should be noted that the peak temperature is fully determined by our choice of the “hard” x-ray threshold,  $E_0$ , above which we want a maximum yield in the recombination continuum, and by the material,  $Z$ , selected to radiate. It is independent of the parameters  $\epsilon$ ,  $a$ , and the compression ratio. For instance, if we generate continuum radiation with an aluminum pinch, and want to optimize radiation yield above  $E_0 = 7$  keV, then the optimum temperature equals 1.57 keV. This is a somewhat higher temperature than that achieved in the aluminum implosions on “Z”<sup>9</sup>, about 1 keV.

Equation (14) does not imply that  $T_{\text{peak}}$  can be made small or even zero for a given  $E_0$  and sufficiently high  $Z$ . Indeed, the plasma must be (almost) fully ionized, which requires the condition (4) to be satisfied. From observation of Fig. 2, it is clear that in case  $T_{\text{peak}} > T_{\text{min}}$  the highest yield in the temperature range (4) is achieved at  $T = T_{\text{peak}}$ . On the other hand, if  $T_{\text{peak}} < T_{\text{min}}$ , then the yield decreases as the temperature increases above  $T_{\text{min}}$ . Therefore, the highest yield would be expected at the lower boundary of this interval,  $T = T_{\text{min}}$ , that is, at the lowest temperature required to achieve almost full ionization. Combining the above statements, we can write the following expression for the optimum plasma temperature

$$T_{\text{opt}} = \max(T_{\text{peak}}, T_{\text{min}}). \quad (15)$$

For a given value of  $E_0$ , the temperature  $T_{\text{peak}}$  decreases with  $Z$ , whereas  $T_{\text{min}}$  increases. The value of  $Z = Z_m(E_0)$  where these two lines intersect,  $T_{\text{peak}} = T_{\text{min}}$  corresponds therefore to the lowest optimum temperature for a given  $E_0$ , and is found numerically from the equation

$$\frac{E_0 - Z^2 E_H}{3} = \alpha E_H s Z^\sigma. \quad (16)$$

For  $E_0 = 7$  and 10 keV we find:  $Z_m = 14.3$  and 16.07, respectively. As shown in Fig. 3, for any  $Z$ , the corresponding optimum temperature (15) exceeds the value corresponding to (16),  $T_{\text{opt}} \geq T_m$ , where

$$\frac{T_m}{E_0} = \frac{1}{3} - \frac{Z_m^2(E_0) E_H}{3 E_0}, \quad (17)$$

and for  $E_0$  between 7 and 10 keV the ratio (17) varies between 0.2 and 0.22. We see that optimal recombination radiation could be produced at temperatures noticeably lower than the threshold of the desired spectral range,  $E_0$ .

The values  $Z = Z_m$ ,  $T = T_m$  separate the “low- $Z$ ” ( $T_{\text{opt}} = T_{\text{peak}}$ ) and “high- $Z$ ” ( $T_{\text{opt}} = T_{\text{min}}$ ) ranges for our problem of continuum radiation generation, see Fig. 3. In the low- $Z$  range, the optimum temperature decreases with increased  $Z$  according to (14). For a given current, this means that the optimum mass of the load increases, see below. In the high- $Z$  range, on the contrary, the optimum temperature increases with  $Z$  according to (4), so that the optimum mass of the load decreases. Note that the “high- $Z$ ” branch of the curve  $T_{\text{opt}}(Z)$  on  $Z$  does not depend on  $E_0$ . Expressing  $E_0$  from (16), we can determine the upper limit on  $E_0$ , for which an element with a given  $Z$  belongs to the high- $Z$  branch optimizing the recombination continuum yield in the spectral range  $h\nu > E_0$ . The result is

$$E_0 < (1 + 3\alpha\sigma Z^{\sigma-2}) \times Z^2 E_H. \quad (18)$$

For aluminum, argon and titanium, this translates into  $E_0 < 5.2$ ,  $14.4$ , and  $27.7$  keV, respectively. For a given  $Z$ , the temperature, at which the plasma would produce the highest yield in any spectral range  $h\nu > E_0$  (provided that  $E_0$  is below the upper limit given above), is the lowest temperature consistent with (almost) full ionization of the plasma with a given  $Z$ .

It should also be noted that  $Z = Z_m$ ,  $T = T_m$  correspond to the highest load mass optimized for a given value of  $E_0$ . Since for matched loads the plasma temperature scales as  $(R_0 / \tau)^2$ , we find that for a given current rise time  $\tau$  the load with  $Z = Z_m$  could be

imploded from the smallest radius, which reduces the instability problems. This is why  $Z$  found from (16) seems to be close to the optimum choice of  $Z$  for a given value of  $E_0$ , albeit it is not one corresponding to the highest yield, see below.

Now let us estimate the optimized yield, starting from the low- $Z$  range.

Substituting  $T = T_{\text{peak}}$  into (13), we find the corresponding value of the yield:

$$\begin{aligned} Y_{\text{opt}} &= \frac{1024 \exp(-3) \pi^{5/2} e^{10} m_u^{1/2}}{3m_e^{1/2} h^3 c^7} \frac{a^2 \epsilon^2}{R_f} \left( \ln \frac{R_0}{R_f} \right)^2 \frac{I_m^4 Z^3}{(E_0 - Z^2 E_H)^3} \\ &= 2.6 \times 10^6 \frac{a^2 \epsilon^2}{R_f} \left( \ln \frac{R_0}{R_f} \right)^2 \frac{I_m^4 Z^3}{(E_0 - Z^2 E_H)^3} \text{ J/cm} \end{aligned} \quad (19)$$

[the denominator here cannot be too small, see (17) and Fig. 3.] For aluminum, assuming a 15-fold radial compression ratio, taking  $I_m = 15$  MA,  $a = 0.6$ ,  $R_f = 1$  mm,  $E_0 = 7$  keV, we obtain from (19):

$$Y_{\text{opt}} = 73 \epsilon^2 \text{ kJ/cm}. \quad (20)$$

Then, varying  $\epsilon$  in the range between 0.25 and 0.5, for a “Z” aluminum implosion with the pinch length  $l = 2$  cm, we find the continuum yield above 7 keV predicted between 7 and 36 kJ, which is not far from the highest Ni K-shell yield obtained on “Z”<sup>5</sup>. To obtain this yield, aluminum should be heated at stagnation above 1.6 keV.

For the high- $Z$  range, substituting  $T = T_{\text{min}}$  from (4) into (13), we find the yield:

$$\begin{aligned} Y_{\text{opt}} &= \frac{16m_u^{1/2} h^6}{81\pi^{13/2} m_e^{7/2} e^8 c^4} \frac{a^2 \epsilon^2 I_m^4}{s^3 Z^{3\sigma-3} R_f} \left( \ln \frac{R_0}{R_f} \right)^2 \exp \left[ -\frac{1}{\alpha s Z^{\sigma-2}} \left( \frac{E_0}{Z^2 E_H} - 1 \right) \right] \\ &= 1.96 \times 10^9 \frac{a^2 \epsilon^2 I_m^4}{s^3 Z^{3\sigma-3} R_f} \left( \ln \frac{R_0}{R_f} \right)^2 \exp \left[ -\frac{1}{\alpha s Z^{\sigma-2}} \left( \frac{E_0}{Z^2 E_H} - 1 \right) \right] \text{ J/cm}. \end{aligned} \quad (21)$$

For the same value of  $E_0 = 7$  keV, let us consider titanium ( $Z = 22$ ), which obviously corresponds to this limit, see Fig. 2:  $T_{\text{opt}} = T_{\text{min}} = 7$  keV. Assuming, as above, a 15-fold radial compression ratio, taking  $I_m = 15$  MA,  $a = 0.6$ ,  $R_f = 1$  mm, we find the same value as for aluminum:

$$Y_{\text{opt}} = 73\epsilon^2 \text{ kJ/cm.} \quad (22)$$

Let us now estimate the masses of the optimized loads. One can use Eq. (12) for such an estimate. Multiplying it by  $m_i = m_u A \approx 2m_u Z$ , we obtain an expression for the line mass:

$$\mu = \frac{4m_u}{3c^2} \frac{a\epsilon I_m^2}{T} \ln \frac{R_0}{R_f}. \quad (23)$$

Substituting into (23)  $T = T_{\text{peak}}$ , we obtain the expression for the optimum mass in the low- $Z$  range:

$$\begin{aligned} \mu_{\text{opt}} &= \frac{4m_u}{c^2} \frac{a\epsilon I_m^2}{E_0 - Z^2 E_H} \ln \frac{R_0}{R_f} \\ &= 4.15 \times 10^4 \frac{a\epsilon I_m^2}{E_0 - Z^2 E_H} \ln \frac{R_0}{R_f} \text{ } \mu\text{g/cm.} \end{aligned} \quad (24)$$

For the parameters of the above example of Al, we find from (24):

$$\mu_{\text{opt}} = 3230\epsilon \text{ } \mu\text{g/cm.} \quad (25)$$

With  $\epsilon$  varied between 1/2 and 1/4, we find  $\mu_{\text{opt}}$  varying between 1613 and 807  $\mu\text{g/cm.}$

Substituting into (23)  $T = T_{\text{min}}$ , we obtain the expression for the optimum mass in the high- $Z$  range:

$$\begin{aligned}
\mu_{\text{opt}} &= \frac{m_u h^3 c}{3\pi^3 e^6 m_e} \frac{a\epsilon l_m^2}{sZ^\sigma} \ln \frac{R_0}{R_f} \\
&= 1.39 \times 10^5 \frac{a\epsilon l_m^2}{sZ^\sigma} \ln \frac{R_0}{R_f} \text{ } \mu\text{g/cm,}
\end{aligned} \tag{26}$$

For the parameters of the above example of Ti, we find from (26):

$$\mu_{\text{opt}} = 720\epsilon \text{ } \mu\text{g/cm.} \tag{27}$$

With  $\epsilon$  varied between 1/2 and 1/4, we find  $\mu_{\text{opt}}$  varying between 360 and 180  $\mu\text{g/cm}$ , which is well below the lower limit of masses that can be imploded in "Z" experiments without serious concern about the effects of instabilities on large initial radius loads.

However, (22) and (27) are very conservative estimates for the optimized hard x-ray yield and the load mass from above and from below, respectively. To produce appreciable hard x-ray yield in a continuum radiation of a high-Z plasma, we do not necessarily need it to be fully ionized. The recombination rate onto hydrogen-like states is not much different from the recombination rate onto bare nuclei. At the temperatures near the peak population of the H-like ions, when  $n_i \approx n_{Z-1}$ , and recombination onto bare nuclei is no longer dominant, the power generated in the hard x-ray continuum via radiative and dielectronic recombination (see below) is not far from that predicted by (1) for the same values of  $T$  and  $n_i$ . For titanium, this means temperature in the range between 4.5 and 5 keV instead of 7 keV. This allows for higher masses than predicted by (25) and better matching of the load to the machine, higher densities at stagnation, and, due to the  $T^3$  dependence of the yield given by (13), an increase in the total yield by a factor of 3-4 compared to the estimate (22). Indeed, our numerical simulations presented in Section III confirm this prediction.

## B. Bremsstrahlung and dielectronic recombination continuum

Let us briefly discuss other continuum radiation mechanisms that could also contribute to production of hard x-rays. First, let us demonstrate that the contribution of free-free, bremsstrahlung radiation of a fully ionized plasma for the conditions of interest, is relatively small, albeit not negligible. The bremsstrahlung radiation power is given by Eq. (5.16) of Ref. 10, or, which is the same, by Eq. (9.4) of Ref. 14:

$$P_{brems} = \frac{32\sqrt{2}\pi^{3/2}}{3\sqrt{3}} \frac{e^6}{m_e^{3/2}hc^3} Z^3 T^{1/2} n^2. \quad (28)$$

Comparing (28) with (1), we find that

$$\frac{P_{brems}}{P_{rr}^{(total)}} = \frac{T}{2Z^2 E_H}. \quad (29)$$

Substituting into (29) the appropriate temperatures (15) for low- $Z$  and high- $Z$  ranges, we find:

$$\frac{P_{brems}}{P_{rr}^{(total)}} = \begin{cases} \frac{1}{6} \left( \frac{E_0}{Z^2 E_H} - 1 \right) & \text{for low } Z; \\ \frac{\alpha s Z^{\sigma-2}}{2} & \text{for high } Z. \end{cases} \quad (30)$$

The bremsstrahlung spectrum is also exponential,<sup>10, 14</sup> but, in contrast with the free-bound radiation, has no energy threshold, so the total power given by (27) is distributed over a wider energy spectrum, and hence, contribution of bremsstrahlung to radiation in the desired spectral range,  $h\nu > E_0$ , is somewhat less than estimated by (30). We see that in the most efficient high- $Z$  range, the total contribution of bremsstrahlung is always less than unity. Even for the temperature of 7 keV predicted by (4) for titanium (which is too high for applications, see below), the ratio (30) only 0.5. In the low- $Z$  range, it is

somewhat larger, although not by much: e. g., for the above example of aluminum ( $E_0 = 7$  keV), the corresponding ratio is 34%. This ratio only becomes unity at  $E_0 = 7Z^2 E_H$ , which, say, for aluminum, would mean  $E_0 = 16$  keV, the x-ray energy too high for generating it via continuum transitions in a  $Z = 13$  plasma. Therefore in the parameter range of practical interest, the contribution of bremsstrahlung is at best of order of 30%, a welcome addition but not the main term.

Radiative recombination and bremsstrahlung are the dominant mechanisms of continuum radiation for almost completely ionized plasmas. If the plasma is not fully ionized, and a substantial fraction of its ions are at least hydrogen-like, then the dominant electron-ion recombination process is dielectronic recombination.<sup>10, 15</sup> This is a two-step process involving a radiationless capture of an electron into a doubly excited state of the recombined ion, followed by a stabilizing radiative transition of the ion into a state below its ionization threshold, most likely into its ground state.<sup>10, 15-17</sup> There is no simple analytical formula to estimate the radiative power due to dielectronic recombination. A rough estimate of the relative contributions of dielectronic and radiative recombination is derived from the results of Refs. 10, 15:

$$\frac{P_{dr}}{P_{rr}^{(total)}} \approx \frac{\sqrt{3\pi} n \hbar c E_H}{32 e^2 T} = \frac{2 \text{ keV}}{T}. \quad (31)$$

The stabilizing transitions emit radiation mainly below the ionization energy,  $h\nu < E_Z$ , thus contributing little to the radiative output in the hard energy range. Equation (31) demonstrates that for efficient production of hard x-rays we need temperatures exceeding 2 keV. The results of Refs. 16, 17 based on a detailed description of transitions between ion energy levels associated with the dielectronic recombination indicate that a decrease

in the predicted hard x-ray output due to incomplete ionization of a low atomic number plasma at the temperatures about 2 keV should be largely compensated by the radiation generated in direct recombination onto H-like ions (as is the case in our simulations reported below, where dielectronic recombination is taken into account.) For high atomic number elements, the temperature range where the radiative recombination dominates over both dielectronic recombination and bremsstrahlung is relatively narrow. This is illustrated by Fig. 4 showing the energy loss rates of various radiation cooling processes vs. temperature in calcium plasma ( $Z = 20$ ), calculated in the same way as described in Ref. 15. Note that the temperature (4)  $T_{\min} = 4.9 \text{ keV} = 5.7 \times 10^8 \text{ K}$  is high enough to make dielectronic recombination rate less than both that the radiative recombination and bremsstrahlung rates.

### III. NUMERICAL SIMULATION

The numerical simulations were done using the Lagrangian 1D radiative-MHD code developed at the High Current Electronics Institute (Tomsk, Russia). This code is described in detail in Refs. 18. It was applied for modeling argon implosions reported in Ref. 19, and additionally benchmarked vs. the results of Ref. 3. In this code, a collisional-radiative model is used to calculate the radiation losses and the distribution of plasma ionization states. It takes into account the following elementary processes: electron collisional excitation; spontaneous and stimulated emission; collisional and photoionization; three-body, direct radiative and dielectronic recombination. For the calculation of plasma ionization states, the quasi-steady approach is used in the model, that is, the plasma ionization states are determined by solving time-dependent equations

of ionization dynamics, while the population density is found by solving the stationary rate equation, since the relaxation time of the excited ion levels is considerably less than the ionization state relaxation time. In the simulations reported here, seven spectral lines were retained per each ionization state.

Calculations were made for aluminum and titanium driven by a "Z" circuit, with the actual voltage multiplied by a factor of 0.87, which makes the peak current decrease to 16-17 MA, as in the experiments of Ref. 3. The load length was taken to be 2 cm. The initial conditions corresponded to a "shell-on-fill" load structure: 7/8 of the total load mass uniformly distributed within an annulus whose median radius and thickness were 3 cm and 5 mm, respectively, whereas the remaining 1/8 was uniformly distributed inside the annulus. To avoid the radiative collapse, the current through the load was shut down when a 10-fold radial compression was achieved. After that, the plasma cylinder, which continued to implode inertially, started to expand from its periphery.

Figure 5 shows the hard x-ray yield vs. line mass of an aluminum load. The peak yield in both spectral ranges, above 7 keV and above 10 keV, is achieved with the load mass  $\mu = 1200 \mu\text{g/cm}$ , which, according to (24), would correspond to  $\varepsilon = 0.37$ . The total optimized yield  $> 7 \text{ keV}$ , according to (19) (where the coefficient should be replaced with 103 kJ/cm, as appropriate for the peak current  $I_m = 17.8 \text{ MA}$  obtained in this run, all other parameters being equal), would be 28 kJ, and with addition of bremsstrahlung it should correspond to something like 37 kJ. The energy coupled to the plasma with  $\mu = 1200 \mu\text{g/cm}$  is about 550 kJ/cm (total 1100 kJ), quite close to the estimate (11) predicting 514 kJ/cm for the peak current 17.8 MA shown in Fig. 5, compression ratio 15 and  $a = 0.6$ . The coefficient  $\varepsilon$ , defined as the ratio of the peak thermal energy to the energy

coupled to the liner is about 0.67; being averaged over the duration of the radiation pulse, this estimate would be closer to 0.5. With this value of  $\epsilon$ , the yield in continuum above 7 keV predicted by Eq. (19) would be about 50 kJ, same as in the simulation. The yield above 10 kJ is also quite high, over 20 kJ.

Figure 6 shows the temperature and density profiles for the optimum aluminum load mass  $\mu = 1200 \mu\text{g/cm}$ , at the instant of peak radiation power in the range  $> 10 \text{ keV}$ . The peak plasma temperature shown in Fig. 6 is between 3 and 4 keV; after averaging, we would obtain something about 3 keV, quite close to the optimum predicted by Eq. (14) for the spectral range over 10 keV, 2.6 keV. Since the yield in the range above 7 keV also peaks at this temperature, we can conclude that the hard x-ray yield as a function of temperature, and hence, of the load mass, is not as sharply peaked as Fig. 2 would suggest (cf. Figs. 2 and 5). Not surprisingly, the radial compression predicted by the 1D code is too high, to a final radius about 0.5 mm instead of more realistic values of 1-2 mm. Similarly, the plasma temperature is seen to overshoot the optimum value, 1.6 keV, reaching almost 4 keV at the axis. These overestimates inherent in 1D modeling, however, have more effect on the peak value of radiation power than on the hard x-ray or total radiation yield. For example, when the same code was used to model the argon gas-puff implosion on “Z”<sup>3</sup> (shot Z663), the simulated peak K-shell power exceeded the observed power by a factor of 2, whereas the simulated yield, 260 kJ, was very close to the observed value, 270 kJ.

Figures 7-9 present similar results obtained in a simulation for titanium. The optimum mass, 0.8 mg/cm is less than for aluminum, but not as small as predicted by (27), for the reasons explained in Section II.A. Figures 8, 9 show the results obtained for

this optimum mass. The peak current is 16.1 MA, less than for aluminum, because of the lower mass of the load. The average temperature is about 4 keV, lower than the optimum temperature (15) for Ti, 7 keV. From the energy balance, the parameter  $\varepsilon$  is estimated as 0.5. The peak yield above 7 keV shown in Fig. 7, over 200 kJ, exceeds the conservative prediction (22) (with coefficient corrected for higher peak current, 720 kJ/cm), by almost an order of magnitude. As discussed in Section II.A, the titanium plasma in this example is not completely ionized. Rather, its temperature is between the helium- and hydrogen-like abundance peaks (~2 and ~5 keV, respectively), somewhat closer to the latter, which is consistent with a hard x-ray yield 4 times greater than that predicted for aluminum. The hard x-ray continuum therefore comes mostly from the radiative recombination onto the H-like ion states. This is confirmed by the emission spectrum shown in Fig. 9, which features intense line radiation of He- and H-like ions.

#### IV. CONCLUSIONS

Our analytical estimates and simulations have shown that emission of continuum radiation from an overheated plasma, could be a useful mechanism for producing hard x-rays. In the parameter range of interest, the main contribution to radiation yield is from recombination continuum rather than from bremsstrahlung. The pinch plasma has been demonstrated to be a good recombination radiator in the desired spectral range  $h\nu > E_0$  when its temperature is noticeably less than  $E_0$  (in our examples, by a factor from 2 to 3).

For each energy range  $h\nu > E_0$  we have found the “optimum material”, whose value of  $Z = Z_m$  corresponds to the lowest temperature at stagnation, and the highest line

mass of the load. The optimized yield is found to be an increasing function of  $Z$  – the higher the  $Z$ , the better. However, higher values of  $Z$  require higher temperatures, which are hard to achieve, both due to radiative losses via subkilovolt quanta and to the mass and energy matching requirements of the given machine. There seems to be no point in attempting to generate continuum radiation from the materials whose atomic number is appreciably less than  $Z_m$  evaluated for a given  $E_0$ : we would still have to overcome the same problems as for a higher  $Z$  (higher temperature, lower mass, harder to match), but the expected best-case yield would be much less. The best trade-off is probably achieved at  $Z$  slightly higher than  $Z_m$ , and it remains to be seen, how high above  $Z_m$  we can realistically get. Once we operate in the high- $Z$  range, the largest yield for a given  $Z$  is produced at the lowest possible temperature that is still consistent with a sufficiently high level of ionization. Our simulation done for titanium demonstrated that the higher-atomic-number atoms do not have to be stripped completely. Rather, we need somewhat higher temperatures than required for producing K-shell radiation of this element, to shift the distribution of ions between the He- and H-like states closer to the latter. The higher the  $Z$ , the greater the optimized yield would be, in any spectral range  $h\nu > E_0$ , provided that  $E_0$  is not too large, so that the high- $Z$  condition is satisfied (for aluminum, argon, and titanium this translates into  $E_0 < 5.7$ , 11, and 16.4 keV, respectively).

Simulations done for aluminum and titanium show that titanium emits more continuum radiation than aluminum by about a factor of 4, even though the peak current through the titanium load is less due to a lower optimum mass (harder to match to “ $Z$ ”). This result confirmed that our analytical estimates of yields are conservative in the sense that the plasma does not have to be completely ionized to produce copious continuum

emission. In particular, simulations confirmed our ad hoc estimate of the  $\epsilon$  parameter, about 0.5, as well as the shift to lower optimum mass at higher atomic number in the high-Z range. The plasma temperature and density profiles in these simulations were reasonably uniform, as assumed in the analytical model.

Of course, predictions based on 1D simulations often overestimate the yield. For this reason, qualitative trends and scalings are more reliable than quantitative predictions. For instance, for conditions of titanium implosions on “Z”<sup>4</sup> (load mass in the range between 1.325 and 2.06 mg/cm, initial radius 2 cm), Fig. 7 implies substantially higher yields than actually observed. However, two things should be noted. First, implosion of low masses from higher initial radius, 3 cm in Fig. 6 vs. 2 cm in Ref. 4, couples more machine energy to the load. Second, the trend in the mass scan shown in Fig. 7 agrees with that observed in Ref. 4 – the highest K-shell yield was observed in shot Z119, where the mass was lowest, and the kinetic energy per ion and the electron temperature – the highest.

Appropriate wire array materials for experimental testing of the above concept on “Z” are aluminum and titanium. While there is no point in working with Z below 13 because of low radiation efficiency, ions with  $Z > 22$  are progressively harder to overheat and almost fully ionize. It is even possible that  $Z = 22$  is already too high, and the best element to generate hard x-ray continuum radiation is argon,  $Z = 18$ , implying a gas-puff rather than a wire array load.<sup>3</sup> Table I compares the above predictions for Al and Ti with similar numerical results obtained for argon. For an optimized Ar load, the hard x-ray yield is found to be close to, but slightly higher than, our prediction for Al. Incidentally, a similar relationship holds between the Al and Ar K-shell yields so far obtained on “Z”:

250 kJ and 270 kJ, respectively.<sup>9,3</sup> As the conditions of the Ar gas-puff experiments on “Z” were already close to the optimum shown in Table I, it would be interesting to repeat this experiment with a better diagnostics of the yield in the hard x-ray spectral range.

The optimization conditions outlined above require heating Al and Ti to temperatures ~2 to 2.5 keV and ~4 to 4.5 keV, higher than those achieved previously, in Refs. 12 and 4, by a factor of ~2 and ~1.5, respectively. Overheating aluminum might be easier, whereas titanium promises a more substantial reward.

In both cases, overheating could only be achieved by decreasing the load mass compared to Refs. 12 and 4. To maintain matching the load mass to the “Z” circuit, the initial radius ought to be increased, to at least 3 cm. For the case of titanium, the benefit of overheating is even more important than the peak current loss up to ~15% due to imperfect matching. Finally, to improve the uniformity of the stagnated plasma, nested wire array loads probably should be used.

It should be noted that the radiating mass of the high-Z material does not have to be large. This implies that some additional opportunities could be presented by structuring the load (nesting, etc.) in such a way that its high-Z component is overheated with respect to the average mass temperature. It must also be taken into account, however, that our analytical estimates are based on assumed quasi-uniform temperature and density conditions [e. g., see Eqs. (5), (7) and (8)]. These conditions are not necessarily met in Z-pinch experiments, particularly with wire array loads, where the K-shell radiating mass is a few percent of the total mass.<sup>20</sup> The most successful gas-puff experiments seem to produce more uniform profiles.<sup>3</sup> One of the issues to be studied experimentally is whether the conditions favorable for producing hard x-rays in

continuum could be realized in a Z-pinch implosion. The results of Ref. 3 are very optimistic in this respect. They appear to indicate that a stagnated plasma column that emits a high K-shell yield from a large part of its volume, and hence, is reasonably well described by the parameter values averaged over the pinch length, could indeed be produced in a Z-pinch.

In summary, we have shown that experiments aimed at producing hard continuum x rays from low atomic number elements are likely to be productive both scientifically and in terms of photon yield. At issue is whether the use of lower mass loads at greater initial radii will result in electron temperature sufficiently high to make thermal recombination competitive with the K-shell lines of a higher atomic number element. The detailed measurements of the spectral distributions of the high energy continuum will also provide valuable insight into the presence and importance of a suprathermal electron population in contributing to the x-ray emission.

#### ACKNOWLEDGEMENTS

The authors thank D. Bell (DTRA), V. Harper-Slaboszewicz and C. Deeney (SNL), and I. Vitkovitsky (Logicon) for many helpful discussions.

This work was supported by Defense Threat Reduction Agency.

## References

<sup>1</sup> N. R. Pereira and J. Davis, *J. Appl. Phys.* **64**, R1 (1988).

<sup>2</sup> K. G. Whitney, J. W. Thornhill, J. L. Giuliani, Jr., J. Davis, L. A. Miles, E. E. Nolting, V. L. Kenyon, W. A. Speicer, J. A. Draper, C. R. Parsons, P. Dang, R. B. Spielman, T. J. Nash, J. S. McGurn, L. E. Ruggles, C. Deeney, R. R. Prasad, and L. Warren, *Phys. Rev. E* **50**, 2166 (1994).

<sup>3</sup> H. Sze, J. Banister, P. L. Coleman, B. H. Failor, A. Fisher, J. S. Levine, Y. Song, E. M. Waisman, J. P. Apruzese, R. W. Clark, J. Davis, D. Mosher, J. W. Thornhill, A. L. Velikovich, B. V. Weber, C. A. Coverdale, C. Deeney, T. Gilliland, J. McGurn, R. Spielman, K. Struve, W. Stygar, and D. Bell, *Phys. Plasmas* **8**(7), (2001).

<sup>4</sup> C. Deeney, C. A. Coverdale, M. R. Douglas, T. J. Nash, R. B. Spielman, K. W. Struve, K. G. Whitney, J. W. Thornhill, J. P. Apruzese, R. W. Clark, J. Davis, F. N. Beg and J. Ruiz-Camacho, *Phys. Plasmas* **6**1, 2081 (1999).

<sup>5</sup> P. L. Coleman, J. Banister, B. H. Failor, A. Fisher, J. S. Levine, Y. Song, H. Sze, E. M. Waisman, J. P. Apruzese, J. Davis, D. Mosher, J. W. Thornhill, A. L. Velikovich, B. V. Weber, C. A. Coverdale, C. Deeney, T. Gilliland, J. McGurn, R. Spielman, K. Struve, W. Stygar, and D. Bell, submitted to the 28<sup>th</sup> International Conference on Plasma Science and 13<sup>th</sup> International Pulsed Power Conference (2001).

<sup>6</sup> J. Davis, J. L. Giuliani, and M. Mulbrandon, *Phys. Plasmas* **2**, 1766 (1995).

<sup>7</sup> J. W. Thornhill, K. G. Whitney, J. Davis, and J. P. Apruzese, *J. Appl. Phys.* **80**, 710 (1996).

<sup>8</sup> H. Sze, P. L. Coleman, B. H. Failor, A. Fisher, J. S. Levine, Y. Song, E. M. Waisman, J. P. Apruzese, Y. K. Chong, J. Davis, F. L. Cochran, J. W. Thornhill, A. L. Velikovich, B.

V. Weber, C. Deeney, C. A. Coverdale, and R. Schneider, *Phys. Plasmas* **7**(10), 4223-4226 (2000).

<sup>9</sup> J. P. Apruzese, P. E. Pulsifer, J. Davis, R. W. Clark, K. G. Whitney, J. W. Thornhill, T. W. L. Sanford, G. A. Chandler, C. Deeney, D. L. Fehl, T. J. Nash, R. B. Spielman, W. A. Stygar, K. W. Struve, R. C. Mock, T. L. Gilliland, D. O. Jobe, J. S. McGurn, J. F. Seamen, J. A. Torres, and M. Vargas, *Phys. Plasmas* **5**, 4476 (1998).

<sup>10</sup> H. R. Griem, *Principles of Plasma Spectroscopy* (Cambridge University Press, 1997).

<sup>11</sup> D. Mosher, N. S. Qi, M. Krishnan, *IEEE Trans. Plasma Sci.* **26**, 1052 (1998).

<sup>12</sup> A. L. Velikovich, J. Davis, J. W. Thornhill, J. L. Giuliani, L. I. Rudakov, and C. Deeney, *Phys. Plasmas* **7**, 3265 (2000).

<sup>13</sup> K.G. Whitney, J. W. Thornhill, J. P. Apruzese, and J. Davis, *J. Appl. Phys.* **67**, 1725 (1990).

<sup>14</sup> Ya. B. Zel'dovich and Yu. P. Raizer, *Physics of Shock Waves and High-Temperature Hydrodynamic Phenomena* (Academic Press, New York, 1966), Vol. 1.

<sup>15</sup> A. Burgess, *Astrophys. J.* **139**, 776 (1964); **141**, 1588 (1965).

<sup>16</sup> J. Davis, V. L. Jacobs, P. C. Kepple, and M. Blaha, *J. Quant. Specrosc. Radiat. Transfer* **17**, 139 (1977); V. L. Jacobs, J. Davis, J. E. Rogerson, M. Blaha, *J. Quant. Specrosc. Radiat. Transfer* **19**, 591 (1978).

<sup>17</sup> V. L. Jacobs, J. Davis, J. E. Rogerson, M. Blaha, J. Cain, and M. Davis, *Astrophys. J.* **239**, 1119 (1980).

<sup>18</sup> V. I. Oreshkin, in *Dense Z-Pinches*, edited by N. R. Pereira, J. Davis and P. E. Pulsifer, AIP Conference Proceedings, v. 409 (Woodbury, New York, 1997), p. 215; "Radiative

MHD Modeling of Implosions of Plasma Liners," Preprint #4 (in Russian), High Current Electronics Institute, Tomsk, Russia (1994); Russian Physics Journal **38**, 1203 (1995).

<sup>19</sup> A. V. Shishlov, R. B. Baksht, A. V. Fedyunin, F. I. Fursov, B. M. Kovalchuk, V. A. Kokshenev, N. E. Kurmaev, A. Yu. Labetsky, V. I. Oreshkin, and A. G. Russkikh, Phys. Plasmas **7**, 1252 (2000).

<sup>20</sup> J. P. Apruzese, J. W. Thornhill, K. G. Whitney, J. Davis, C. Deeney, and C. A. Coverdale, "Comparative analysis of time-resolved and time-integrated x-ray data from long pulse Z-pinch implosions on Saturn," to be published in Phys. Plasmas (2001).

## Figure captions

Fig. 1. K-shell yields produced in recent experiments on “Z” (Refs. 3-5) and the corresponding characteristic K-shell energies vs. atomic number Z.

Fig. 2. Yield function (13) calculated for aluminum ( $Z = 13$ ) and  $E_0 = 7$  keV, and shown in arbitrary units. The function peaks at  $T = T_{\text{peak}} = 1.57$  keV.

Fig. 3. The optimum temperature plotted vs. Z for  $E_0 = 7$  and 10 keV;  $\theta = 0.5$ .

Fig. 4. The radiative energy loss efficiencies ( $= P/n_e n_i$  for various mechanisms of emission) for Ca.

Fig. 5. Hard x-ray yield calculated for aluminum on “Z” – mass scan.

Fig. 6. Density and temperature profiles at the instant of peak radiation power above 10 keV in aluminum.

Fig. 7. Hard x-ray yield calculated for titanium on “Z” – mass scan.

Fig. 8. Density and temperature profiles at the instant of peak radiation power above 10 keV in titanium.

Fig. 9. Emission spectrum of titanium at the same instant as in Fig. 8.

Table I. Optimal conditions and predicted hard x-rays yields for a 2 cm long pinch driven by a “Z” circuit.

Load material	Optimum line mass, mg/cm	Yield at $h\nu > 7$ keV, kJ	Yield at $h\nu > 10$ keV, kJ
Al	1.2	52	23
Ar	1.0	68	25
Ti	0.8	210	90

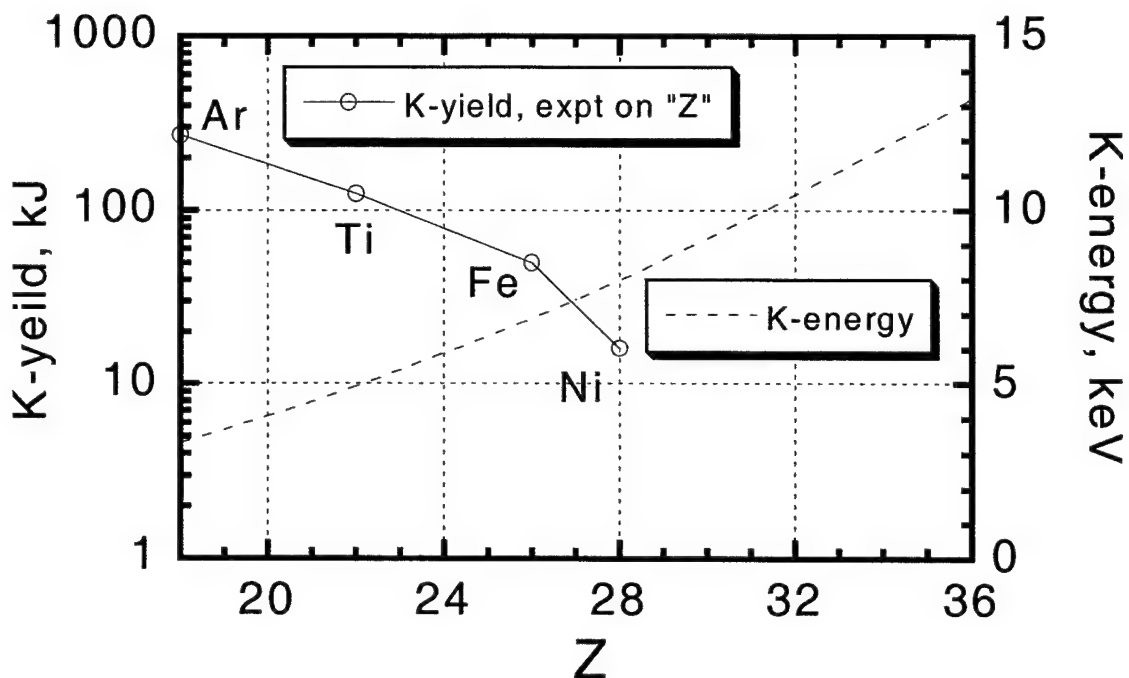


Figure 1. K-shell yields produced in recent experiments on "Z" (Refs. 3-5) and the corresponding characteristic K-shell energies vs. atomic number  $Z$ .

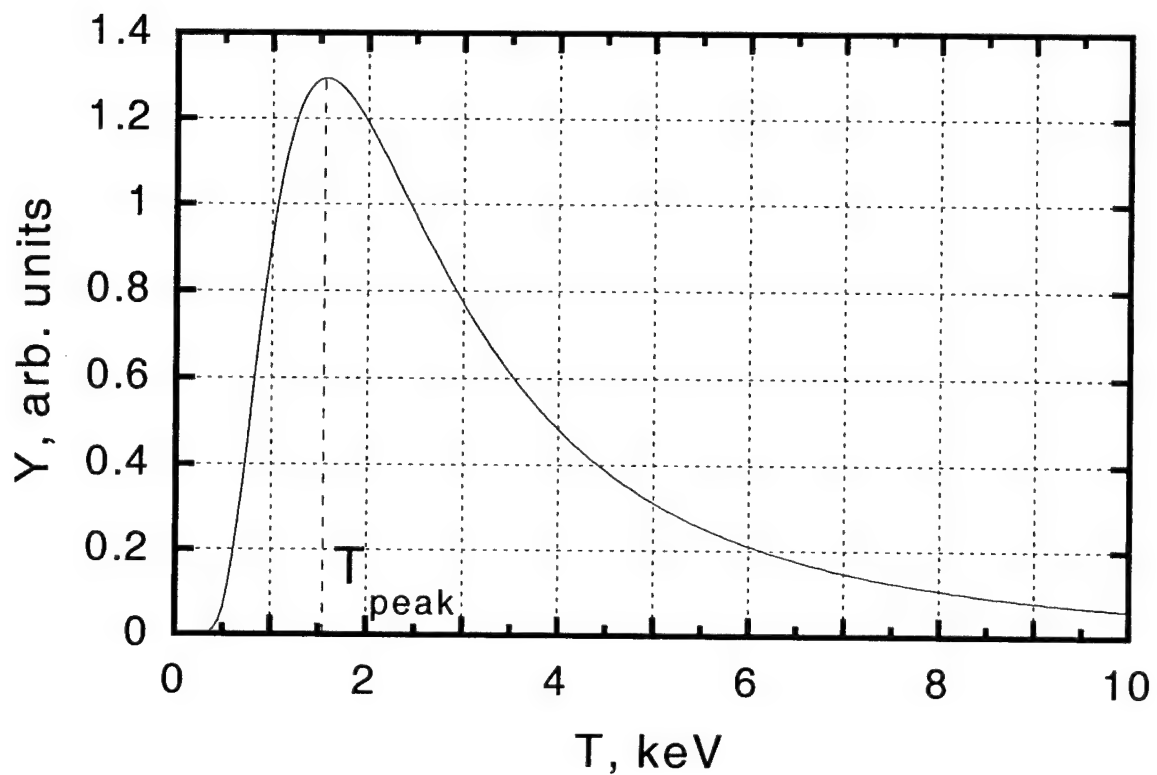


Figure 2. Yield function (13) calculated for aluminum ( $Z = 13$ ) and  $E_0 = 7$  keV, and shown in arbitrary units. The function peaks at  $T = T_{\text{peak}} = 1.57$  keV.

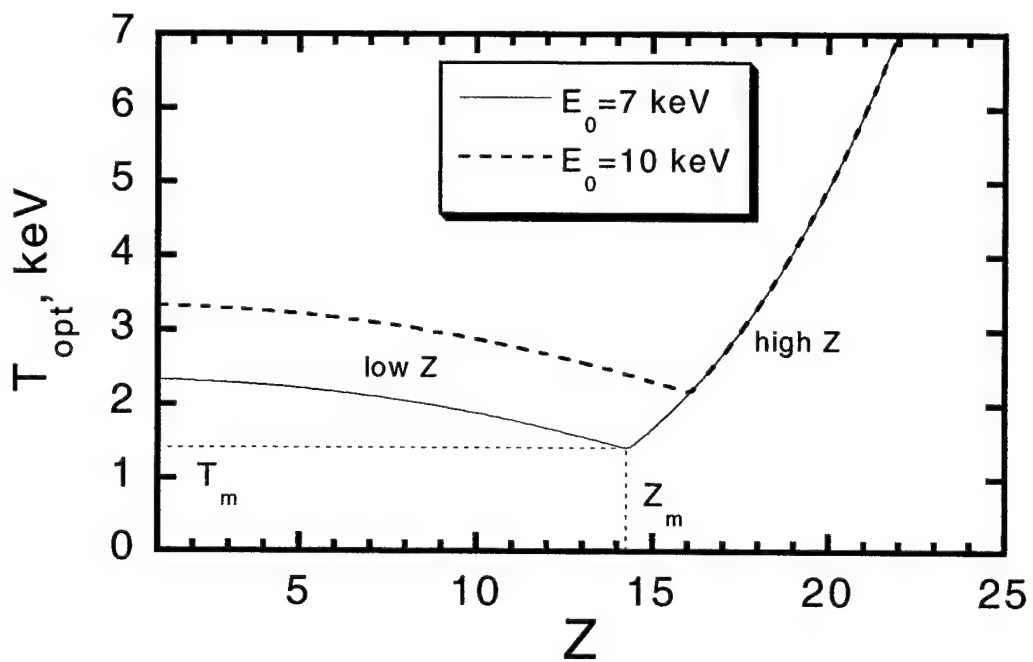


Figure 3. The optimum temperature plotted vs.  $Z$  for  $E_0 = 7$  and 10 keV.

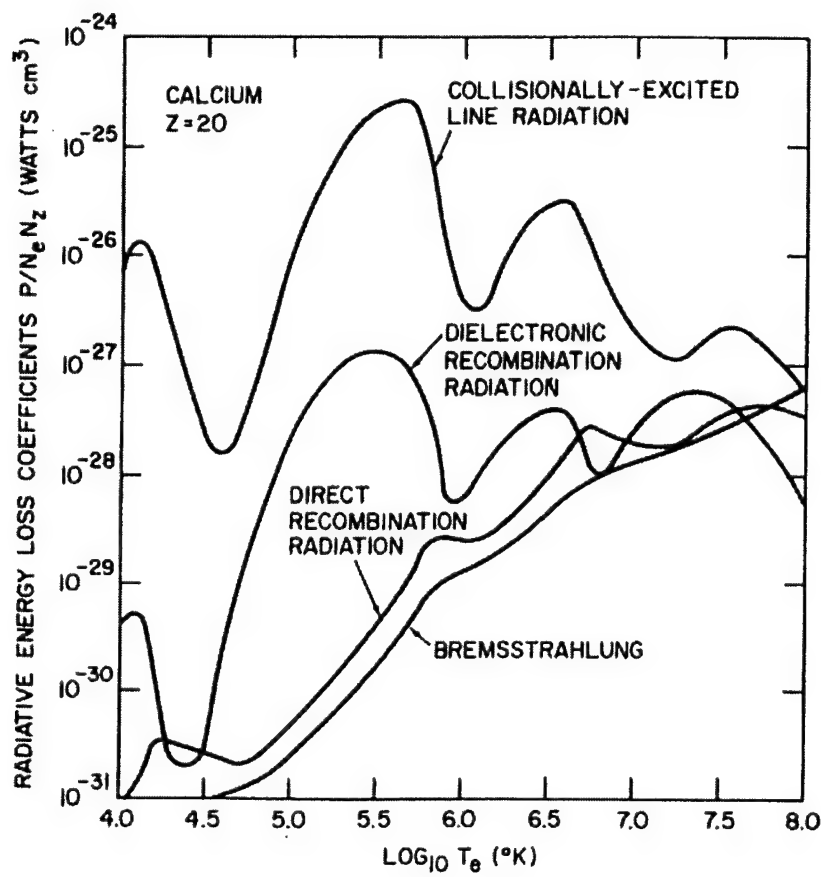


Figure 4. The radiative energy loss efficiencies ( $= P/n_e n_i$  for various mechanisms of emission) for Ca ions.

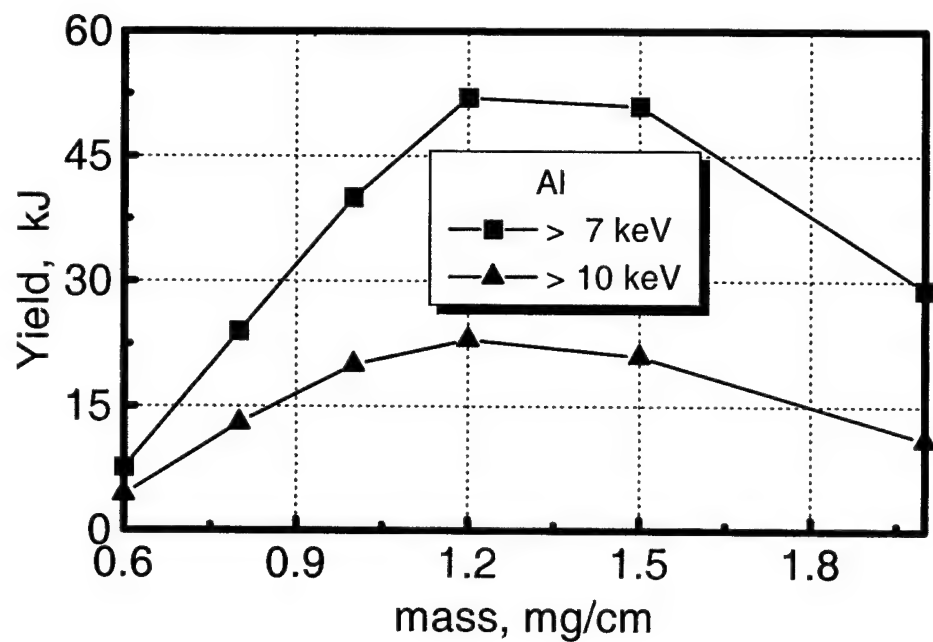


Figure 5. Hard x-ray yield calculated for aluminum on "Z" – mass scan.

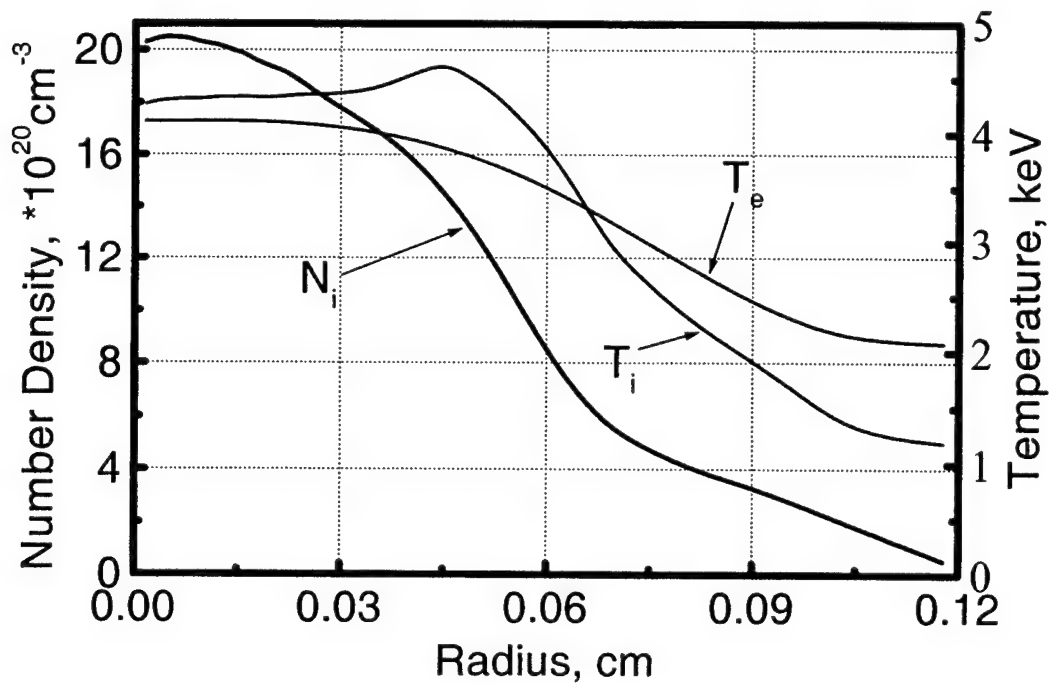


Figure 6. Density and temperature profiles at the instant of peak radiation power above 10 keV in aluminum.

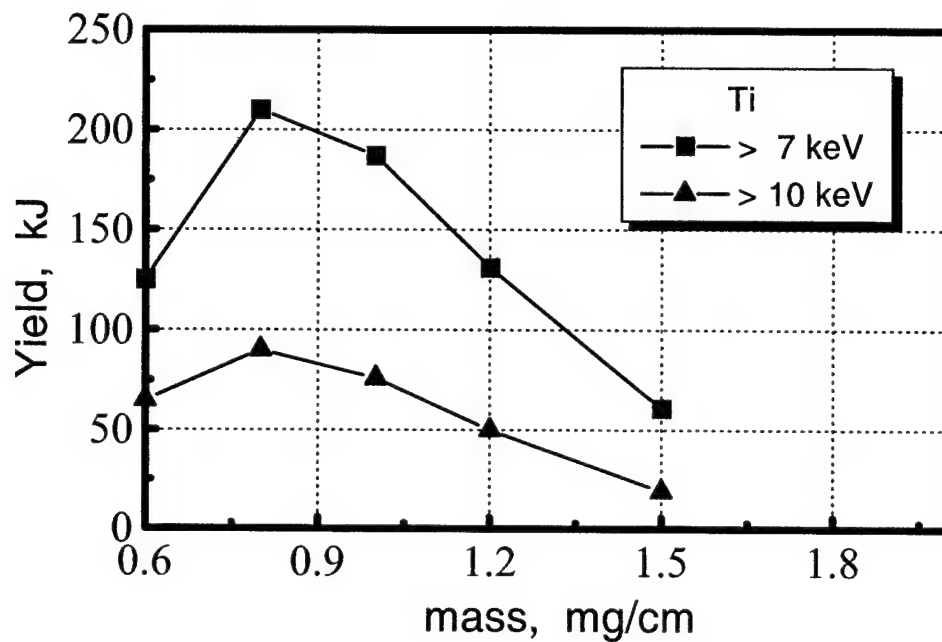


Figure 7. Hard x-ray yield calculated for titanium on “Z” – mass scan.

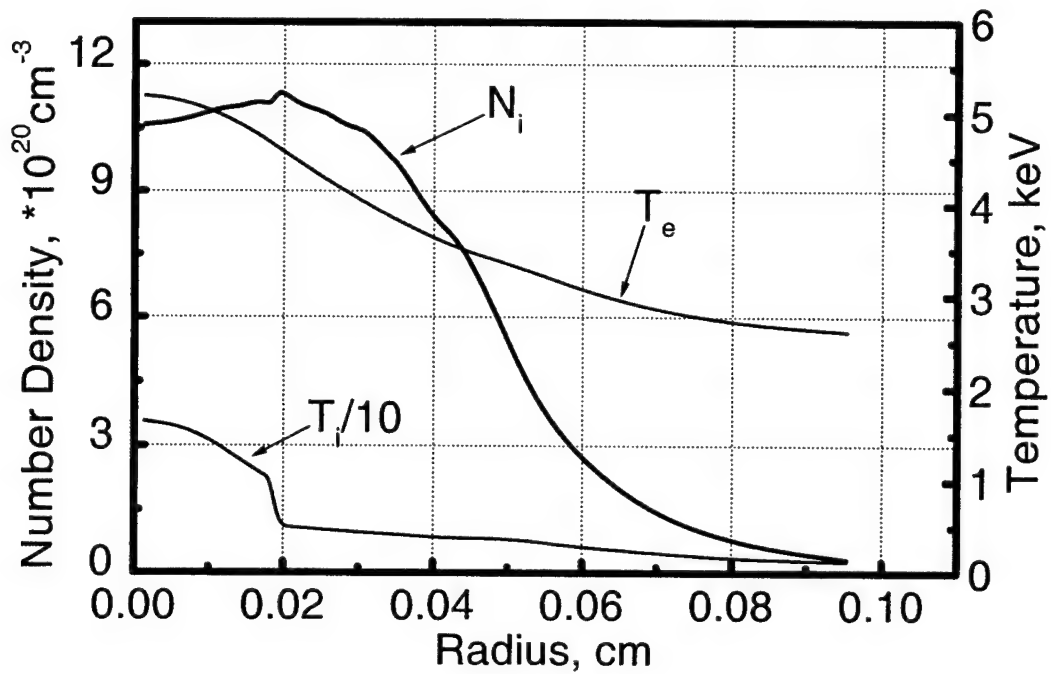


Figure 8. Density and temperature profiles at the instant of peak radiation power above 10 keV in titanium.

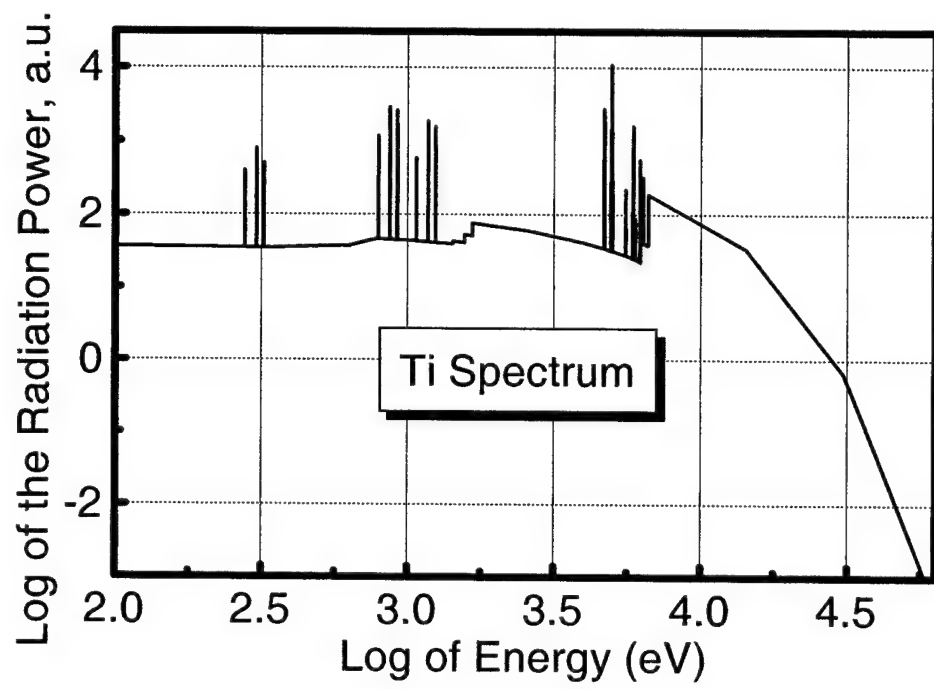


Figure 9. Emission spectrum of titanium at the same instant as in Fig. 8.

## II. COMPARATIVE ANALYSIS OF TIME-RESOLVED AND TIME-INTEGRATED X-RAY DATA FROM LONG PULSE Z-PINCH IMPLOSIONS ON SATURN

### I. INTRODUCTION

Z pinches, a key element in DTRA's simulator program, are presently the most efficient and energetically prolific laboratory sources of x-rays<sup>1-13</sup>. However, the mechanisms by which electrical energy from the driving generator gets converted to radiation are still incompletely understood. Surely, one important mechanism is the generation of kinetic energy through the inward acceleration of the wire or gas puff load by the  $J \times B$  Lorentz force. But it has long been evident that this energy input channel is not the only one, and may not always be the largest. For instance, in the experiments discussed below, total radiative yields several times that of the implosion kinetic energy were measured. Indeed, even a decade ago<sup>3</sup>, evidence existed for some type of anomalous heating mechanism. In tungsten wire array experiments on the Z accelerator, total radiated energy is typically  $\sim 1.5$  times greater than the kinetic energy delivered to the imploding array. Peterson *et al.*<sup>14</sup> offered an explanation of this discrepancy in calculations of where additional work was done by the Lorentz force (initially placed in kinetic energy, then converted to  $pdV$  internal energy) during the radiation pulse. Another candidate for such additional energy coupling is "magnetic bubbles" produced by the development of Rayleigh-Taylor or MHD instabilities<sup>15,16</sup>.

Systematic acquisition and analysis of suites of x-ray data from Z pinches can provide an important path to resolving some of the mysteries of these plasmas. Other probing diagnostics which have been applied include laser interferometry<sup>17-19</sup>, and backlighting of the pinch with either lasers<sup>20</sup> or other x-ray sources<sup>21</sup>. However, the most commonly used experimental diagnostic tool is that of x-ray spectroscopy. Its proper interpretation, however, requires the use of appropriate methods coupled

with detailed models. Depending on the volume and diversity of data acquired in a shot or series of shots, varying levels of detail and complexity can be both inferred and assumed in applying modeling tools to interpret spectroscopic data. For instance, a time-integrated, temperature-dependent line ratio coupled with the measured pinch diameter and power can be used in conjunction with detailed collisional-radiative equilibrium calculations to obtain average pinch conditions<sup>22,23</sup>. This relatively straightforward method has yielded significant insights into the dominant trends governing temperature and radiating mass fraction as a function of driver and load properties<sup>3,4,7,9,11,12</sup>. Recent work relaxing the assumption of radial spatial uniformity and replicating a more comprehensive set of spectroscopic data on each shot indicates that radial temperature gradients are more severe for pinches with short radiation pulsewidths<sup>24,25</sup>.

The present experiments were designed to study the effects of wire number and mass on imploding Z-pinch loads at currents exceeding 7 MA, with relatively long implosion times of  $\sim 150$  ns. The advantages of longer current risetimes are well known and include lower machine cost and reduced pulsed power transmission risk due to the lower voltages required. The longer pulse is likely to affect the degree to which the wire array transitions from individual plasmas to an annulus of plasma prior to its rapid acceleration and on-axis assembly. The objectives of this work are to determine how plasma conditions change with load mass and wire number, and, to assess the effects of spatially and temporally averaging the x-ray data (and thus the inferred temperature and density profiles) on the deduced pinch conditions.

Data averaging could in principle blur the general trends that can be observed, and also, the inferred temperatures and densities change in accordance with the degree of approximation employed in the analysis. In Sec. II, the experiments and principal diagnostic instruments deployed are described. Section III concentrates on the model, analysis procedures, and the results of the analysis using time-integrated data from the wire number and mass scans. Section IV analyzes time-resolved data

from one shot in detail, and compares the deduced profiles to those inferred from x-ray data collected by a time-integrating spectrometer and pinhole camera on the same shot. The work is discussed and summarized in Sec. V.

## II. DESCRIPTION OF EXPERIMENTS

The present experiments were all conducted on the Saturn pulsed power generator at Sandia National Laboratories. Saturn, the world's second most powerful and energetic Z-pinch driver, is described in Ref. 26. For many years this machine has been operated in a short pulse mode in which typical peak load currents of  $\sim 7\text{-}9$  MA are achieved in a risetime of  $\sim 50$  ns. However, recent waterline modifications have made available a long pulse mode in which the same peak load currents are reached in  $\sim 150\text{-}230$  ns. All of the experiments discussed here were performed using the long pulse mode at a  $\sim 160$  ns implosion time.

The loads consisted of arrays of wires composed of the alloy known as Al 5056, which is 95% Al and 5% Mg. In each case, the array diameter was 40 mm. For all of the shots except one, the length of the wires was 20 mm. For the wire number scan, the shots employed 32, 56, 70, 126, 180, and 282 wires, all at a fixed array mass of 0.62 mg/cm. The mass scan shots employed masses of 0.33, 0.62, 1.05, and 1.58 mg/cm, keeping the number of wires between 120 and 180.

On some or all of the shots, the following radiation diagnostics were deployed to measure x-ray yields and powers and provide detailed spectroscopy: Au and Ni bolometers, photoconductive x-ray detectors (PCD's), x-ray diodes (XRD's), time-integrating and time-resolving x-ray spectrometers, and time-resolving and time-integrating x-ray pinhole cameras. A full complement of electrical diagnostics was also present. Peak load currents ranged from 7 MA up to 8.5 MA for the highest mass shots. For the variable wire number shots, the implosion times were clustered around 160 ns. However, for the variable mass shots, the implosion times increased with the load mass, from 130 to 200 ns, in good accord with a zero-dimensional slug model.

### III. ANALYSIS OF TIME-INTEGRATED DATA

#### A. Model and fitting procedures

We infer the properties of the Z-pinch plasma by employing an ionization dynamics and radiation transport model of a cylindrical plasma containing detailed configuration atomic structure for the Li-, He-, and H-like ionic stages of Al and Mg. This model is described in more detail in Ref. 23. It includes the atomic collisional and radiative processes coupling the levels. To get accurate photoexcitation rates and to correctly calculate the self-absorption and power outputs, all optically thick lines are transported, as well as the two free-bound continua arising from radiative recombination to the K-shell ground states. The model solves for the steady-state populations of the individual levels assuming collisional-radiative equilibrium (CRE).

We adopt the following notation for the x-ray spectral lines whose intensities are calculated in the fitting procedures. The He- $\alpha$  line refers to the sum of the intensities of the  $1s^2-1s2p^1P$  and  $1s^2-1s2p^3P$  lines of the He-like stages of either Al or Mg. The He- $\beta$  line refers to the  $1s^2-1s3p^1P$  line of He-like Al, and Ly- $\alpha$  refers to the  $n=1-2$  lines of the corresponding H-like stages of these elements. The higher-level (therefore higher energy) H-like lines are not used in the analyses because in these experiments they are subject to an unknown but likely significant amount of inner shell absorption from cooler Al plasma in the outer regions of the pinch. Fits are found for the following 5 quantities: the measured K-shell power, the ratio of the Al Ly- $\alpha$  to He- $\alpha$  lines, the same ratio for Mg, the ratio of the Al He- $\beta$  to He- $\alpha$  lines, and the ratio of the sum of the Mg  $\alpha$  lines to that of the Al  $\alpha$  lines.

When the profiles of the pinch are assumed to vary one-dimensionally, the fitting is carried out by varying assumed temperature and density profiles, typically requiring dozens to hundreds of separate calculations to find the best fit. Relatively simple but versatile analytic forms for the profiles are adopted, such as sums of power laws and generalized Gaussians. For the 10 shots considered in this work,

the RMS error in matching the data for the five x-ray measurements enumerated above varied from 4% to 16%. This degree of tolerated error is reasonable given the 10% experimental uncertainty in the x-ray line ratios, 15% in K-shell x-ray power, and a similar degree of uncertainty in the collisional excitation rates used in the model<sup>24</sup>.

When the simplest assumption of a uniform plasma is adopted, a unique fit to two of the five data is obtainable by contour plotting, for example, the calculated Al Ly- $\alpha$ /He- $\alpha$  ratio along with the calculated K-shell power, as functions of electron temperature and ion density. The intersection of the contours representing the observed values of the line ratio and power gives the diagnosed electron temperature and ion density in this approximation. Further details regarding this method are given in Refs. 22 and 23.

### B. Wire number scan

The critical x-ray data that were obtained when varying the wire number at a fixed mass of 0.62 mg/cm are presented in Figs. 1a and 1b. The K-shell yields (not shown) were nearly constant as a function of wire number and averaged near 60 kJ. These yields are comparable to those achieved by Saturn in its short pulse mode<sup>9</sup>. It is possible that the longer current risetime allowed for more complete and uniform merger of the exploding wires prior to implosion. This potentially beneficial separation of the explosion and implosion phases is discussed in Refs. 27-29. For 3 of the 6 variable wire number shots, the total radiative yield was measured, and averaged nearly 1 MJ, which is nearly 4 times the estimated 280 kJ kinetic energy imparted to the load. This kinetic energy (60 keV per ion) is equivalent to an  $\eta$  of 4.5, where  $\eta$  of unity means<sup>2</sup> that the kinetic energy is just sufficient to strip each ion to the K-shell and heat the electrons to temperatures supporting efficient K-shell radiation. Note also from Fig. 1a that the K-shell power generally increases with wire number up to 180 wires, as in previous experiments done with a 50 ns current risetime<sup>5,9,11</sup>, but drops at 282 wires (interwire gap of 0.45 mm). For the

previous short pulse shots, x-ray power at all photon energies between 1 and 6 keV continued to increase with decreasing interwire gap down to a gap of at least 0.4 mm. The contrasting decline in power at very high wire number (small interwire gap) for the long pulse shots is not understood at this time<sup>29</sup>.

Prior to discussing the inferred time-averaged profiles shown in Figs. 2-5, it is useful to lay the groundwork for understanding their behavior by considering the diagnostic sensitivities of the 5 x-ray measurements used to derive them.

The Ly- $\alpha$ /He- $\alpha$  ratio for both Al and Mg is predominantly temperature sensitive. However, due to the fact that only 5% of the pinch ions are Mg, the opacity of the Mg lines is more than an order of magnitude smaller than that of the corresponding lines of Al. Therefore, the lines of the two elements provide windows into different depths of the pinch plasma, providing information about temperature profiles as well as the average temperatures. The temperatures derived from the free-bound continuum slope (when it is assumed optically thin) are consistently higher than those obtained from these line ratios (0.6-1.1 keV vs. 0.4-0.7 keV for the line ratios). However, since the continuum absorption cross section varies approximately as  $(h\nu)^{-3}$ , any absorption will occur preferentially near the threshold, flattening the slope and making the plasma appear hotter than its true electron temperature if the continuum opacity is sufficiently large. For the conditions of these experiments, this effect is of order  $\sim 0.3$  keV, which essentially reconciles these two methods.

The calculated K-shell power increases rapidly with temperature up to about 0.4 keV, above which the dependence is slow as the He-like stage ionizes into the H-like and then the bare nucleus appears. Therefore, for the conditions of these experiments, the power is primarily an increasing function of both the density and the size of the K-shell emitting region. Note that the K-shell emitting mass is determined by both the density and the pinch size. We refer to the K-shell emitting mass fraction as the fraction of the total load mass which has been sufficiently heated to emit K-shell radiation. This quantity is determined by interpreting x-ray

data and is a useful parameter for analyzing and comparing experiments. Given the density, the K-shell power is therefore dependent on the K-shell emitting mass fraction, which depends in part on the pinch size.

The  $\text{He-}\beta/\text{He-}\alpha$  ratio is primarily a density indicator, because increasing the electron density more closely collisionally couples the  $n=2$  and  $n=3$  levels of the He-like ions, bringing their population fractions closer to their local thermodynamic equilibrium (LTE) values. This line ratio therefore increases as the electron density increases. Our calculations of the density dependence of this line ratio for Al give results equivalent to those of Weisheit *et al.*<sup>30</sup> for Si (see Fig. 3 of Ref. 30).

We have described the diagnostic sensitivities of 4 of the 5 x-ray measurements which are used to infer pinch conditions. The fifth of these quantities, the ratio of the sum of the Mg  $\alpha$  lines to the sum of the Al  $\alpha$  lines, is primarily sensitive to the K-shell opacity of the plasma. As this opacity increases, the Al lines are subject to greater self-absorption, whereas their Mg counterparts generally suffer little attenuation since Mg is only 5% of the plasma. Therefore, the higher the Mg-to-Al line ratio, the greater the opacity. Invariably, this ratio well exceeds Mg's 5% share of the pinch ions, and is typically measured at  $\sim 0.12$  in the experiments analyzed in the present work. The line opacities are inversely proportional to the line widths, which are indicative of ion temperatures of  $\sim 20$  keV. However, if the optical depths obtained by assuming an ion temperature of 20 keV are used in the calculations, the Mg/Al  $\alpha$  ratio is typically calculated to be  $\sim 0.2$  rather than the observed  $\sim 0.12$ . This discrepancy lies well outside the bounds of the experimental and atomic data uncertainties mentioned in the previous section. If all the optical depths are halved, however, good fits can and have been obtained for all the data we have considered. No explanation of this need to adjust the opacity is demonstrable at present. However, the model used to interpret the data is of a 1D cylinder, and it is thus not entirely surprising that opacities obtained from this simplified geometry need some modification in order to agree with those measured from an

inhomogeneous pinch which is at best a distorted version of a cylinder. In an actual pinch the density does not vary only with radius as is necessarily assumed in a 1D model. We now turn to a discussion of the inferred profiles, their dependences, and the underlying physics.

The electron temperature and ion density profiles derived for the experiments in which wire number was varied are shown in Figs. 2 and 3. Note that the ion density peaks sharply at the core, at values exceeding  $10^{20} \text{ cm}^{-3}$ . However, the electron temperature falls off more slowly. It is the temperature scale length which corresponds to the measured pinch diameter. The necessity for a high density core can be understood as follows. Calculations performed with a broad, several-mm region of lower ion density of a few times  $10^{19} \text{ cm}^{-3}$  do agree with the measured K-shell power, but fail to account for the measured He- $\beta$ /He- $\alpha$  ratios of about 0.17, instead yielding a ratio  $\sim 0.12$ . The core ion densities shown in Fig. 2, exceeding  $10^{20} \text{ cm}^{-3}$ , account for both the line ratio and the power, but only if the radius of this core, i.e., the density scale length, is restricted to  $\sim 0.2\text{-}0.3$  mm. The observed x-ray images of the pinches (displayed and discussed further below) do show both small cores and less dense, few-mm halos which scatter the K-shell lines from the cores as well as produce some self-emission. There is little or no systematic variation in the core temperature with wire number. The K-shell power trend of Fig. 1a is primarily a result of the density coupled with density scale length, i.e., the K-shell radiating mass.

Fig. 4 displays the fraction of the load mass which is calculated to be radiating in the K shell, as a function of wire number, for both the 0D (uniform plasma assumption) and 1D analyses. Both analyses show the radiating mass fraction maximizing at the same wire number, 180, at which the K-shell power maximizes (see Fig. 1a). Also obvious in Fig. 4 is that the 0D analysis gives radiating mass fractions of 13-20% that are well above the values of 4-9% obtained from the 1D fitting procedure. Recall that the 0D analysis assumes that the pinch is

homogeneous within the measured diameter, and uses only the K-shell power and Al Ly- $\alpha$ /He- $\alpha$  ratio to obtain an average electron temperature and ion density. Since the specifically density-dependent He- $\beta$ /He- $\alpha$  line ratio is not considered, and only the measured K-shell power is replicated, the 0D analysis gives densities an order of magnitude lower than the 1D case because the measured pinch volume is assumed uniformly filled. Since less dense plasma radiates less efficiently, more plasma, i.e., a greater radiating mass fraction (resulting from the uniform density volume) must be invoked to account for the measured power when this 0D analysis is performed.

The mass-averaged electron temperatures as a function of wire number, deduced from both the 0D and 1D analysis procedures, are shown in Fig. 5. The temperatures obtained from the 0D analysis range from 0.6 to 1.2 keV, and are uniformly higher than those obtained from the 1D fits, which cluster near 0.6 keV. This difference derives from the uniformly lower densities deduced in 0D. It is well known that the average charge state of moderately dense plasma, though primarily dependent on electron temperature, is also an increasing function of density. In the process of ladder ionization<sup>23</sup>, electron collisional excitation to excited states is followed by ionization from those states, whose rate coefficients generally greatly exceed those from the ground state. This process can be enhanced by photoexcitation of the excited states<sup>24</sup>. As the density increases, so do the excited state populations and ionization from those states. Therefore, the lower densities deduced from the 0D analysis require correspondingly higher electron temperatures to account for a given, ionization-dependent H-like to He-like line ratio.

### C. Load mass scan

As mentioned above in Sec. II, a series of 4 shots was taken with the initial array diameter fixed at 40 mm, but by increasing the wire thicknesses, the load masses were progressively increased (0.33, 0.62, 1.05, and 1.58 mg/cm). The  $\eta$ 's for these shots were, respectively, 6.4, 4.5, 3.2, and 2.3. The basic x-ray data obtained from these 4 shots are shown in Figs. 6a and 6b. It is seen that the density-dependent

Al He- $\beta$ /He- $\alpha$  and the opacity-dependent Mg/Al  $\alpha$  ratios show little or no trend as a function of load mass. The temperature-dependent Al and Mg Ly- $\alpha$ /He- $\alpha$  ratios both show a slight maximum at the lowest load mass. The K-shell power, however, exhibits a strong maximum of 1.7 TW/cm at a mass of 0.62 mg/cm, and the K-shell pinch diameters are largest, exceeding 3 mm, at the highest load masses. The K-shell yields were 50, 59, 38, and 51 kJ, respectively, as a function of increasing load mass. Given the fixed initial array diameter, the heavier loads take longer to implode as is clearly seen in Fig. 6c which displays the measured currents and K-shell x-ray pulses for these four shots. Due to the longer implosion time as the mass load increases, the peak load current systematically increases with mass, from 6.8 MA for the lowest mass to 9.0 MA for the heaviest. Since the strong K-shell power maximum occurs at the second lowest current, its existence is not due to higher load current.

An interesting feature of the analysis results concerns the behavior of the radiating plasma mass as the load mass increases (see Figs. 7 and 8). Neither the variations in on-axis densities nor the density scale lengths seem to correlate with the variations in load masses. Note, however, in all cases the presence of dense cores of a few tenths of a mm in extent, as was found in the wire number scan analysis. Also, the fraction of the original load mass that radiates in the K-shell correlates with and trends downward with increasing load mass regardless of whether a 0D or 1D approach is used in the analysis (Fig. 8). A similar trend was seen previously with high mass loads for pinches with shorter implosion times and lower wire numbers (see, e.g., Fig. 13 of Ref. 9). The reasons that the 0D K-shell emitting masses always exceed those obtained from the 1D fits are the same as those discussed above in Sec. III B. The 1D radiating mass itself, as opposed to the radiating fraction, peaks sharply at a load mass of 0.62 mg/cm (whose radiating mass is 57  $\mu$ g/cm, but only 25-29  $\mu$ g/cm for the other 3 shots).

As in the wire number scan, it is the electron temperature scale lengths which

define the pinch sizes rather than the density scale lengths, as shown in Fig. 9. The core electron temperatures are between 0.55 and 0.60 keV for all 4 shots. Also, as was the case for the wire number scan, the average electron temperatures obtained from the 0D analysis always exceed those inferred from the 1D data fitting procedure (Fig. 10), for the same reasons cited in the previous section. Temperatures inferred from the 0D analysis are 0.6-1.1 keV, as opposed to the 0.55-0.60 keV cited above from the 1D profiles.

#### **IV. COMPARISON OF TIME-RESOLVED AND TIME-INTEGRATED ANALYSES**

In the previous sections, we have considered two series of Al:Mg wire implosions on the Saturn pulsed-power generator. In one series, the number of wires was varied, while fixing the load mass. In the other, the load mass was varied while keeping the number of wires approximately constant. X-ray data collected during these implosions was analyzed with a CRE plasma model alternately assuming either a uniform plasma pinch (0D) or one-dimensional variation in the average pinch parameters (1D). This fixed perspective on the plasma was required since all the data considered (except for the K-shell power) was time-integrated. In this section we broaden that perspective to examine and analyze time-resolved data. By comparing this analysis to one performed with time-integrated data taken on the same shot, we quantify how and why time resolution refines the derived properties of a Z pinch.

For one shot (Saturn 2706), which was not part of either the wire number or mass variation series, a full set of both time-integrated and time-resolved spectra and K-shell x-ray images was obtained. This shot was identical to the 180-wire, 0.62 mg/cm shot analyzed in Sec. III except that the array length was 25 mm instead of 20 mm. The K-shell yield of shot 2706 was 55 kJ, very close to the 59 kJ obtained from the similar 2.0 cm array length shot. The critical spectroscopic data was collected in 6 frames, separated by intervals of 3 ns, and is plotted as a

function of time in Fig. 11. The Mg He- $\alpha$  line was outside the range of the crystal used in the time-resolving spectrometer, but the Mg Ly- $\alpha$  / Al Ly- $\alpha$  ratio can serve as an opacity indicator rather than the ratio of the sum of the  $\alpha$  lines as was the case for the time-integrated data. The same time-integrating spectrometer that was employed in the wire number and mass scan series was also deployed on shot 2706. The time integrated values of the Al Ly- $\alpha$ /He- $\alpha$  and He- $\beta$ /He- $\alpha$  line ratios are, respectively, 1.3, and 0.16. Note, however, from Fig. 11, that the Al He- $\beta$ /He- $\alpha$  ratio as recorded by the time-resolving spectrometer never drops below a value of 0.19 and attains a peak value of 0.4 during an interval near peak power. At first these sharply contrasting data for the Al He- $\beta$ /He- $\alpha$  ratio would appear to be inconsistent. However, no indication of malfunction appeared in either spectrometer, nor was the He- $\alpha$  line saturated. More recent streaked spectrometer Al data obtained on Saturn by P. Coleman<sup>31</sup> show that the He- $\alpha$  line radiates for some tens of ns following peak K-shell emission without any detectable intensity in the  $\beta$  line. A similar scenario for shot 2706 would account for the much lower  $\beta$ -to- $\alpha$  ratio when time-integrated over the entire shot as compared to the interval near peak K-shell power. Therefore, we believe that the data from both spectrometers are accurate and mutually consistent.

The He- $\beta$ /He- $\alpha$  ratio is principally a density indicator, and is an increasing function of density, as discussed above in Sec. III B. Since the time-resolving spectrometer shows that this ratio has a maximum more than twice its time-integrated value, it is evident that the plasma's maximum density well exceeds the average value obtained from fitting the time-integrated data. As also discussed above in III B, this means that the density scale length needed to fit an instantaneous K-shell power must be smaller when inferred from time-resolved data than the typical values of  $\sim 0.2$ - $0.3$  mm derived from the time-integrated data of the wire number and mass scan shots.

Fig. 12 shows the ion density profiles inferred from 4 key frames of the time-resolved spectroscopy and power measurements. The central ion densities now

exceed  $10^{21} \text{ cm}^{-3}$ , and the density scale lengths during the peak K-shell radiation (from 160-166 ns) are  $\sim 0.02\text{-}0.03 \text{ mm}$ . This suggests that the effective diameters of the dense K-shell radiating regions during this time span are less than  $100 \mu\text{m}$ . By  $t=169 \text{ ns}$ , however, both the K-shell power and the  $\text{He-}\beta/\text{He-}\alpha$  line ratio are significantly lower than their peak values (see Fig. 11). This results in an inferred density profile that is broader in its spatial extent (scale length of  $\sim 0.07 \text{ mm}$ ) and lower in central density by about a factor of 5 from its maximum at  $t=163 \text{ ns}$ .

The picture of the pinch developed by time-resolved spectroscopic analysis is qualitatively consistent with the K-shell pinhole framing images shown in Fig. 13. These images show, during the time of maximum K-shell emission, intense radiating spots whose characteristic sizes are of the order of a pixel ( $\sim 300 \mu\text{m}$ ). Such features have, of course, been noticed before in Z pinches and plasma focus discharges<sup>3,32,33</sup>. For instance, Fig. 5 of Ref. 32 shows areas of intense K-shell radiation, whose diameters are less than  $\sim 100 \mu\text{m}$ , which developed during the implosion of an Al wire array by a peak current of 3 MA. Often called “hot spots” or “bright spots”, the present analysis indicates that these features are probably localized density enhancements. As the K-shell power declines, these intense radiating spots become less numerous and the pinch acquires a broader, more diffuse character when imaged in K-shell x-rays. Also shown in Fig. 13 is a calculated K-shell pinhole image for  $t=168 \text{ ns}$  based on the profiles obtained from the analysis of the time-resolved spectroscopy. The image was simulated using the method described in Ref. 25. This image simulation demonstrates both the advantages and limitations of a model which assumes one-dimensional geometry but contains a much more detailed treatment of radiation physics than is presently available in 2D models. Note that the high-intensity barlike structure at the axis of the simulated image is qualitatively similar to the small, intense radiating structures seen in the time-resolved experimental images. The existence of such a high-density, copiously radiating core can be inferred without reference

to the experimental pinhole images by applying the detailed 1D radiation model to fit the spectroscopic data. Experimental Z-pinch images contain far more detail reflecting a proliferation of structures than can be inferred from an analysis of x-ray data similar to that used in the present work. The detailed radiation treatment and parameter fitting algorithms which are feasible with 1D models are not yet practical when applied to two or three dimensions. Moreover, the axially averaged, radially varying profiles inferred in the present analysis already provide significant challenges to both 1D and 2D hydrodynamics models to replicate.

An alternative approach for the near future might well be the use of a hybrid model in which the pinch consists of sequential axial sections, each characterized by 1D radial variations which can differ from section to section. Such a model may well provide a better description of the assembled pinch without sacrificing the valuable asset of detailed configuration, spectroscopic quality radiation.

As discussed in Sec. III B, a uniform lower density can necessitate that more plasma participate in the radiation in order to produce a given power, since less dense plasma radiates less intensely. Accordingly, as shown in Fig. 14, the interplay of these density and size effects results in the K-shell radiating mass actually maximizing slightly after peak power. Note also that at 163 ns, the time of peak K-shell power, the radiating mass of  $6 \mu\text{g}/\text{cm}^2$  represents just 1% of the load. The much higher density inferred from the time-resolved analysis results in much less mass being needed to radiate a given power.

How does the picture of dense, K-shell radiating spots, so consistent with both time-resolved spectroscopy and time-resolved imaging, change when the same shot is viewed with less time resolution? We consider two types of time-integrated data, that obtained from a time-integrating spectrometer and pinhole camera, and also data resulting from the numerical time-integration of the frames shown in Fig. 11 over the main K-shell pulse. This latter quantity is, in effect, the integral of the radiation emitted in a 15 ns interval surrounding the time of peak K-shell

emission. The density profiles inferred from these two versions of time-integrated data are plotted in Fig. 15. Note that the density profile deduced from the time-integrating spectrometer's data is much broader, with a central density an order of magnitude lower than that inferred from the data integrated only for the 15 ns surrounding peak K-shell power. This broader profile is similar to those obtained from the time-integrated data of the wire number and load mass scans. The time-integrated pinhole image of the pinch (upper left corner of Fig. 13) also shows a smoother, broader, more diffuse area of K-shell emission than is characteristic of the individual frames recorded near the peak of the K-shell emission. Therefore, the time integration of both the spectrum and the image yields data which reflects time-averaged smoothing of the density inhomogeneities, and consequentially a lower peak density. By contrast, the profile obtained from the numerical time-integral of the 154-169 ns data doesn't differ very much from the individual frame profiles (except for 169 ns, Fig. 12) and in an approximate sense may be said to represent an "average" of those density profiles.

The results of the time-resolved analysis for the core electron temperature are shown in Fig. 16. There is only modest variation in the central electron temperature as a function of time within the 15 ns surrounding the peak of the K-shell emission, with the maximum temperature occurring slightly prior to the power maximum. Given enough energy to strip well into the K-shell, it appears that the key to the radiative properties of these pinches involves the density attained and its distribution and variations, rather than the electron temperature, which is generally determined by the balance of power inputs with radiated power output (see Refs. 1 and 34).

## V. CONCLUDING DISCUSSION

X-ray spectroscopy is a well established diagnostic tool for unraveling the properties of Z-pinch plasmas and their trends as a function of both the load and the driving pulsed-power generator. However, spectroscopic data can be obtained

in many forms and with different degrees of resolution in both time and space. The models used to interpret the spectra need sufficient detail and realism with respect to such critical features as atomic structure data and radiation transport. Given an adequately detailed model, the fundamental question arises: how do the deductions regarding the properties of Z pinches depend upon the spatial and temporal resolution present in the data or the temperature and density profiles assumed in the model?

In the present work, we have used various types of x-ray data with contrasting model assumptions to analyze two series of shots taken on the Saturn pulsed-power generator at Sandia National Laboratories. These shots demonstrated that Saturn can be employed in a long pulse (160 ns) mode without reducing either the total or the K shell yields as compared to results obtained previously with a 50 ns current risetime. These aspects of the experimental campaign and their significance are highlighted and discussed elsewhere<sup>29</sup>. We have determined how pinch conditions vary with load mass and wire number and how our picture of the pinch changes as the data used and model assumptions change. Time-integrated and time-resolved x-ray spectroscopy and imaging have been analyzed, assuming alternately that the plasma is uniform (0D) or varies one-dimensionally along its radius (1D).

As either the load mass or wire number is varied, the 0D and 1D analyses generally show the same trends with respect to the important plasma parameters such as electron temperature and density. However, the values of these quantities yielded by the contrasting analysis techniques differ significantly. For instance, the 0D analysis, in every instance studied thus far, infers a higher average electron temperature, a higher K-shell radiating mass fraction, but lower ion density than deduced from a 1D analysis of the same shot. The reasons for these differences are understood and are explained in Sec. III.

Perhaps the most interesting contrast was revealed when the same shot (Saturn 2706) was analyzed using both time-integrated and time-resolved data. High quality

data was obtained on this shot from both time-resolving and time-integrating spectrometers and x-ray pinhole cameras. The most pronounced difference in the two types of spectroscopic data occurred in a density-dependent line ratio, and it indicated that the peak density was nearly an order of magnitude higher, and concentrated in a smaller spatial region, than would be inferred by looking only at the corresponding fully time-integrated data. Comparing the time-integrated pinhole image to the time-resolved framing images near peak K-shell power (see Fig. 13), it is seen that intense K-shell radiating spots are present in the time-resolved images but not in the time-integrated one. The 1D pinhole image simulation (also in Fig. 13), based on the spectroscopic analysis, also exhibits a high intensity, small emitting core. The fact that these features could neither be observed nor determined with 0D, time-integrated data or models demonstrates the benefits of improved experimental and theoretical resolution in both space and time. Our analysis shows that the high x-ray intensity within these spots is the result of localized density enhancements. The sizes of some of these spots are of order one pixel, and in previous work<sup>32</sup> similar spots have been seen whose sizes are less than 100  $\mu\text{m}$ .

The temperature and density profiles that were inferred in the time-resolved analysis replicate the K-shell power, K-shell emission region size, and the line ratio data to within 4 to 16%; however, they contain only a fraction of the mass that was imploded, and they may or may not be consistent with the total x-ray power output generated in the experiment. These are matters that will be the subject of future investigations that attempt to determine whether the average density and temperature profiles inferred from the data analysis can be approximately reproduced in 1D or 2D MHD calculations along with the total power data. If these average profiles can be reproduced, then some of the detailed sub-structures of the Z-pinch plasma might be investigated with greater confidence. Neither a lower limit nor a distribution function of the sizes of these substructures is well-

known at present. They appear to be a significant factor contributing to the high radiating efficiency of Z pinches; thus, understanding their nature and origin might contribute to further advances in enhancing and/or tailoring the emitted radiation. Such gains in understanding would be facilitated by better experimental resolution of the features in both space and time. These intense but small emitting zones may result from various types of instabilities, perhaps kink and sausage MHD instabilities, or Rayleigh-Taylor alone or in interaction with MHD behavior. They may be seeded by asymmetries or imperfections in the wire array. They could also represent regions where partial radiative collapse or condensation has occurred<sup>33,35</sup>. If so, progressively adding a high atomic number component to Al:Mg loads in future experiments might reveal changes in their morphology, number, or persistence as the intrinsic radiating efficiency of the load is enhanced. Future improvements in the realism of coupled radiation-hydrodynamic calculations are also likely to contribute to resolving these issues.

## REFERENCES

1. M. Gersten, W. Clark, J. E. Rauch *et al.*, Phys. Rev. A **33**, 477 (1986).
2. K. G. Whitney, J. W. Thornhill, J. P. Apruzese, and J. Davis, J. Appl. Phys. **67**, 1725 (1990).
3. C. Deeney, T. Nash, R. R. Prasad, L. Warren, K. G. Whitney, J. W. Thornhill, and M. C. Coulter, Phys. Rev. A **44**, 6762 (1991).
4. C. Deeney, P. D. LePell, B. H. Failor *et al.*, Phys. Rev. E **51**, 4823 (1995).
5. T. W. L. Sanford, G. O. Allshouse, B. M. Marder *et al.*, Phys. Rev. Lett. **77**, 5063 (1996).
6. M. K. Matzen, Phys. Plasmas **4**, 1519 (1997).
7. K. G. Whitney, J. W. Thornhill, P. E. Pulsifer, J. P. Apruzese, T. W. L. Sanford, T. J. Nash, R. C. Mock, and R. B. Spielman, Phys. Rev. E **56**, 3540 (1997).
8. K. L. Wong, P. T. Springer, J. H. Hammer *et al.*, Phys. Rev. Lett. **80**, 2334 (1998).
9. C. Deeney, T. J. Nash, R. B. Spielman *et al.*, Phys. Plasmas **5**, 2431 (1998).
10. R. B. Spielman, C. Deeney, G. A. Chandler *et al.*, Phys. Plasmas **5**, 2105 (1998).
11. T. W. L. Sanford, R. C. Mock, T. J. Nash, K. G. Whitney, P. E. Pulsifer, J. P. Apruzese, D. Mosher, D. L. Peterson, and M. G. Haines, Phys. Plasmas **6**, 1270 (1999).
12. C. Deeney, C. A. Coverdale, M. R. Douglas *et al.*, Phys. Plasmas **6**, 2081 (1999).
13. D. D. Ryutov, M. S. Derzon, and M. K. Matzen, Rev. Mod. Phys. **72**, 167 (2000).

14. D. L. Peterson, R. L. Bowers, K. D. McLenithan, C. Deeney, G. A. Chandler, R. B. Spielman, M. K. Matzen, and N. F. Roderick, *Phys. Plasmas* **5**, 3302 (1998).
15. L. I. Rudakov, A. L. Velikovich, J. Davis, J. W. Thornhill, J. L. Giuliani, Jr., and C. Deeney, *Phys. Rev. Lett.* **84**, 3326 (2000).
16. A. L. Velikovich, J. Davis, J. W. Thornhill, J. L. Giuliani, Jr., L. I. Rudakov, and C. Deeney, *Phys. Plasmas* **7**, 3265 (2000).
17. N. Qi, S. F. Fulghum, R. R. Prasad, and M. Krishnan, *IEEE Trans. Plasma Sci.* **26**, 1127 (1998).
18. S. V. Lebedev, I. H. Mitchell, R. Aliaga-Rossel, S. N. Bland, J. P. Chittenden, A. E. Dangor, and M. G. Haines, *Phys. Rev. Lett.* **81**, 4152 (1998).
19. C. H. Moreno, M. C. Marconi, K. Kanizay, J. J. Rocca, Yu. A. Uspenskii, A. V. Vinogradov, and Yu. A. Pershin, *Phys. Rev. E* **60**, 911 (1999).
20. E. J. Yadlowsky, T. B. Settersten, R. C. Hazelton, J. J. Moschella, G. G. Spanjers, J. P. Apruzese, and J. Davis, *Rev. Sci. Instrum.* **66**, 652 (1995).
21. D. H. Kalantar and D. A. Hammer, *Phys. Rev. Lett.* **71**, 3806 (1993).
22. M. C. Coulter, K. G. Whitney, and J. W. Thornhill, *J. Quant. Spectrosc. Radiat. Transfer* **44**, 443 (1990).
23. J. P. Apruzese, K. G. Whitney, J. Davis, and P. C. Kepple, *J. Quant. Spectrosc. Radiat. Transfer* **57**, 41 (1997).
24. J. P. Apruzese, P. E. Pulsifer, J. Davis *et al.*, *Phys. Plasmas* **5**, 4476 (1998).
25. J. P. Apruzese, J. Davis, K. G. Whitney *et al.*, *Phys. Plasmas* **7**, 3399 (2000).
26. R. B. Spielman *et al.*, in *Proceedings of the 2nd International Conference on Dense Z Pinches*, Laguna Beach, CA, 1989, edited by N. R. Pereira, J. Davis, and N. Rostoker (American Institute of Physics, New York, 1989), p. 3
27. M. G. Haines, *IEEE Trans. Plasma Sci.* **26**, 1275 (1998).

28. M. R. Douglas, C. Deeney, R. B. Spielman, C. A. Coverdale, N. F. Roderick, and M. G. Haines, *Phys. Plasmas* **7**, 2945 (2000).
29. C. A. Coverdale *et al.*, submitted to *Phys. Rev. Lett.* (2000).
30. J. C. Weisheit, C. B. Tarter, J. H. Scofield, and L. M. Richards, *J. Quant. Spectrosc. Radiat. Transfer* **16**, 659 (1976).
31. P. Coleman, private communication (2000).
32. P. Burkhalter, J. Davis, J. Rauch, W. Clark, G. Dahlbacka, and R. Schneider, *J. Appl. Phys.* **50**, 705 (1979).
33. K. N. Koshelev, Yu. A. Sidel'nikov, G. Decker *et al.*, *Opt. Spectrosc.* **76**, 198 (1994).
34. J. W. Thornhill, K. G. Whitney, and J. Davis, *J. Quant. Spectrosc. Radiat. Transfer* **44**, 251 (1990).
35. T. A. Shelkovenko, D. B. Sinars, S. A. Pikuz, and D. A. Hammer, *Phys. Plasmas* **8**, 1305 (2001).

## FIGURE CAPTIONS

FIG. 1. (a) The time-integrated  $\text{Ly}\alpha/\text{He}\alpha$  ratios measured for both Al and Mg are plotted as a function of wire number along with the K-shell power. (b) The measured pinch diameter, ratio of the Al  $\text{He}\beta/\text{He}\alpha$  lines and ratio of the sum of the Mg  $\alpha$  lines to the same sum for Al are plotted as a function of wire number. The data are time-integrated.

FIG. 2. (a) The ion density profiles inferred from the 1D analysis are shown for 32, 56, and 70 wire loads. (b) As in (a), except that the wire numbers are 126, 180, and 282.

FIG. 3. (a) The electron temperature profiles inferred from the 1D analysis are shown for 32, 56, and 70 wire loads. (b) As in (a), except that the wire numbers are 126, 180, and 282.

FIG. 4. The inferred K-shell radiating mass fractions are plotted for both the 0D and 1D analyses, as a function of load wire number.

FIG. 5. The mass-averaged electron temperatures derived from the 0D and 1D analyses are plotted as a function of wire number.

FIG. 6. (a) The time-integrated  $\text{Ly}\alpha/\text{He}\alpha$  ratios measured for both Al and Mg are plotted as a function of load mass along with the peak K-shell power. (b) The measured pinch diameter, ratio of the Al  $\text{He}\beta/\text{He}\alpha$  lines and ratio of the sum of the Mg  $\alpha$  lines to the same sum for Al are plotted as a function of load mass. The data are time-integrated. (c) The measured load currents and K-shell x-ray powers are shown as a function of time, for the four different load masses of 0.33, 0.62, 1.05, and 1.58 mg/cm. The higher the load mass, the later the K-shell pulse appears.

FIG. 7. The ion density profiles inferred from the 1D analysis are shown for the 4 different experimental load masses.

FIG. 8. The fraction of the original load mass which radiates in the K-shell is plotted for both the 0D and 1D analyses, as a function of load mass.

FIG. 9. The electron temperature profiles inferred from the 1D analysis are plotted for the 4 different experimental load masses.

FIG. 10. The mass-averaged electron temperatures obtained with the 1D and 0D analyses are shown as a function of experimental array mass.

FIG. 11. The indicated line ratios and K-shell power for Saturn shot 2706 as measured by the time-resolving x-ray spectrometer are plotted as a function of time.

FIG. 12. The ion density profiles, inferred from a 1D CRE analysis, are plotted for 4 times during the K-shell pulse, based on fitting the data of Fig. 11.

FIG. 13. (a) K-shell images from the time-resolving x-ray pinhole camera are shown for 10 frames during the implosion. Also displayed is the image from the time-integrating pinhole camera. (b) An expanded version of the image at 168 ns. (c) calculated K-shell pinhole image for  $t=168$  ns, based on the spectroscopic analysis of the time-resolved data employing a 1D model.

FIG. 14. The K-shell radiating mass for Saturn shot 2706, derived from the time-resolved data, is shown as a function of time.

FIG. 15. Ion density profiles inferred from two sets of time-integrated data are compared. In one instance, the data is integrated over 15 ns surrounding the peak of the K-shell power, in the other, over the entire shot.

FIG. 16. The inferred on-axis electron temperature is plotted as a function of time for Saturn shot 2706.

# Saturn wire number scan

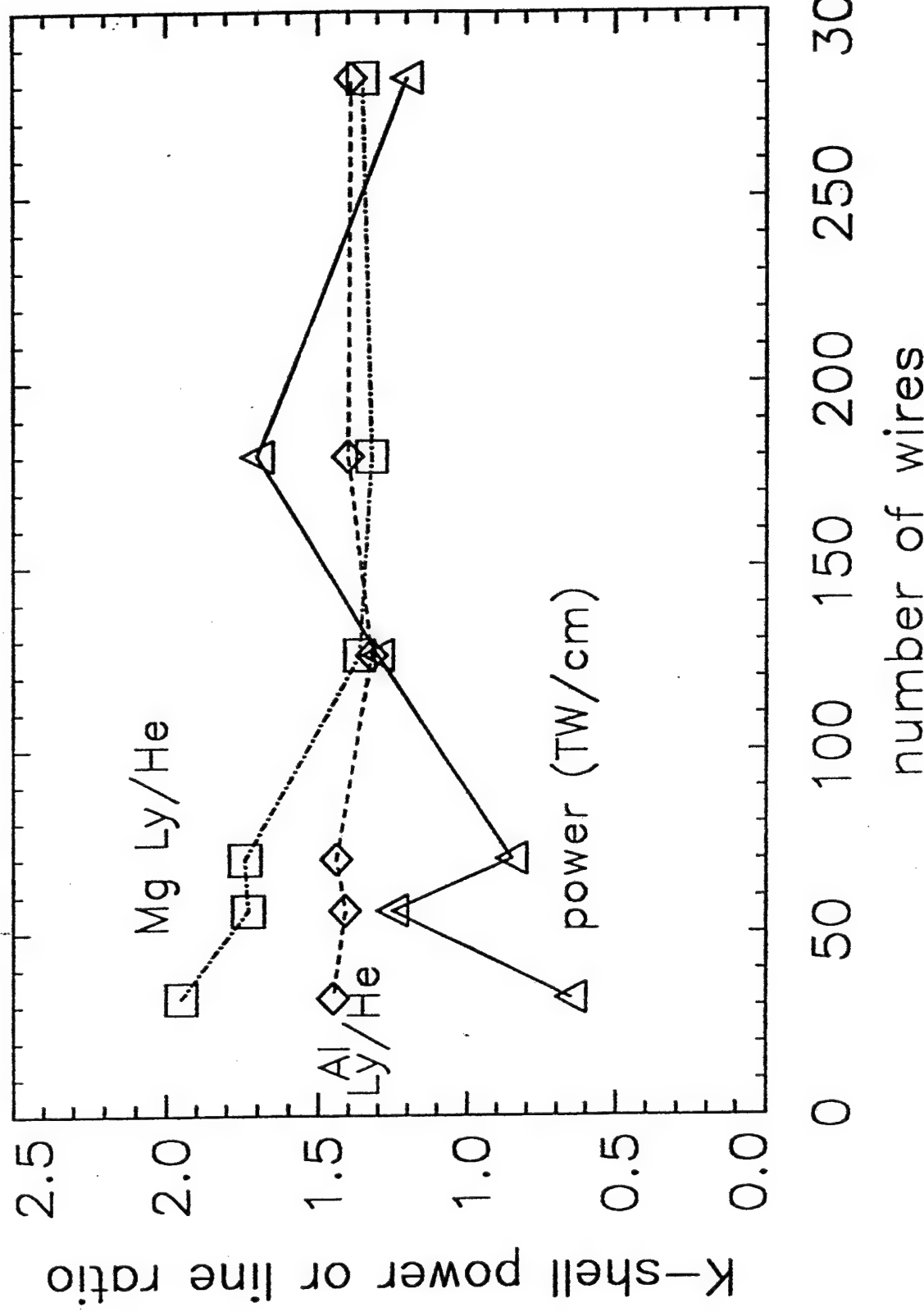


FIG. 1a

Saturn wire number scan

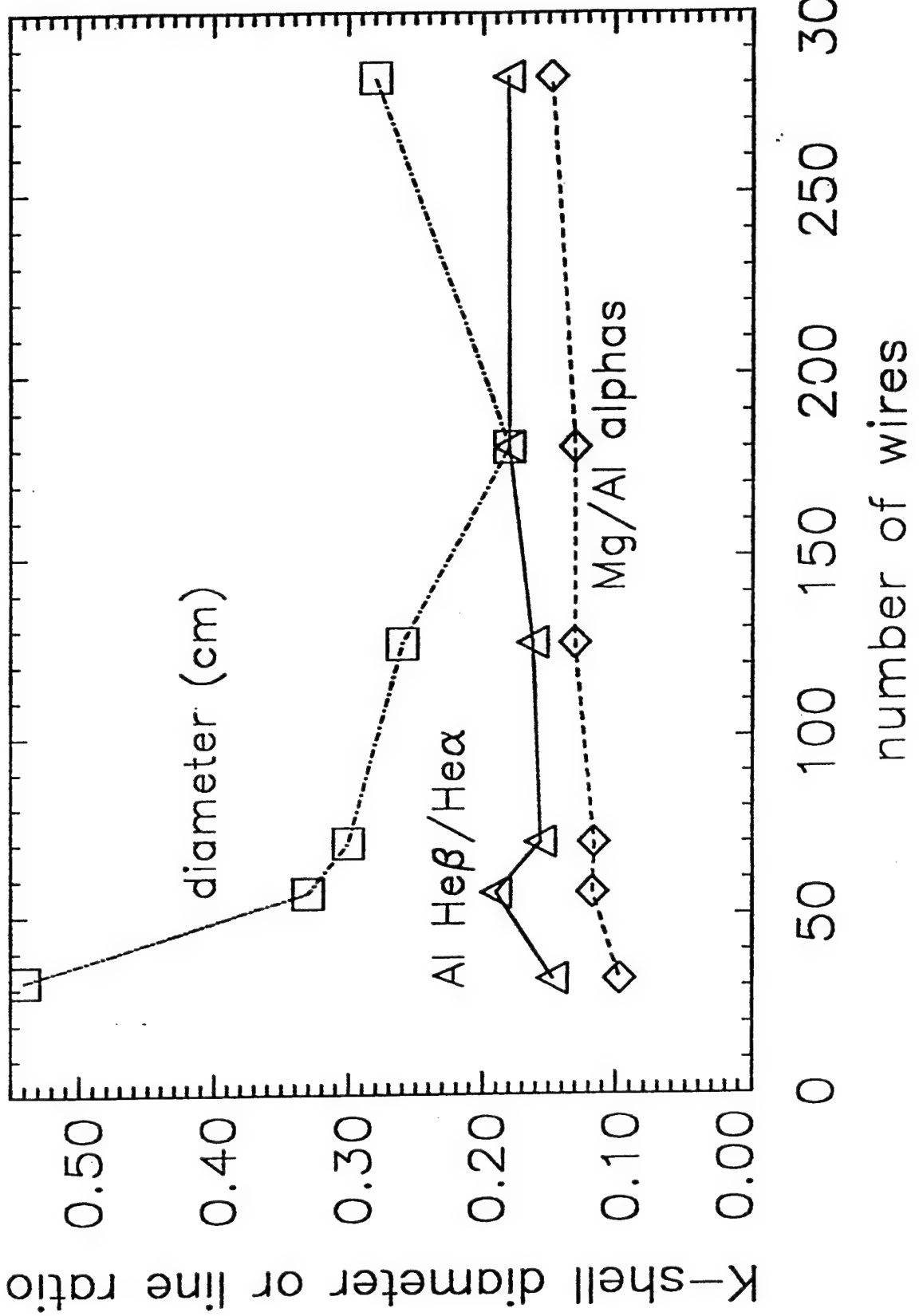


FIG. 1b

Saturn wire number scan

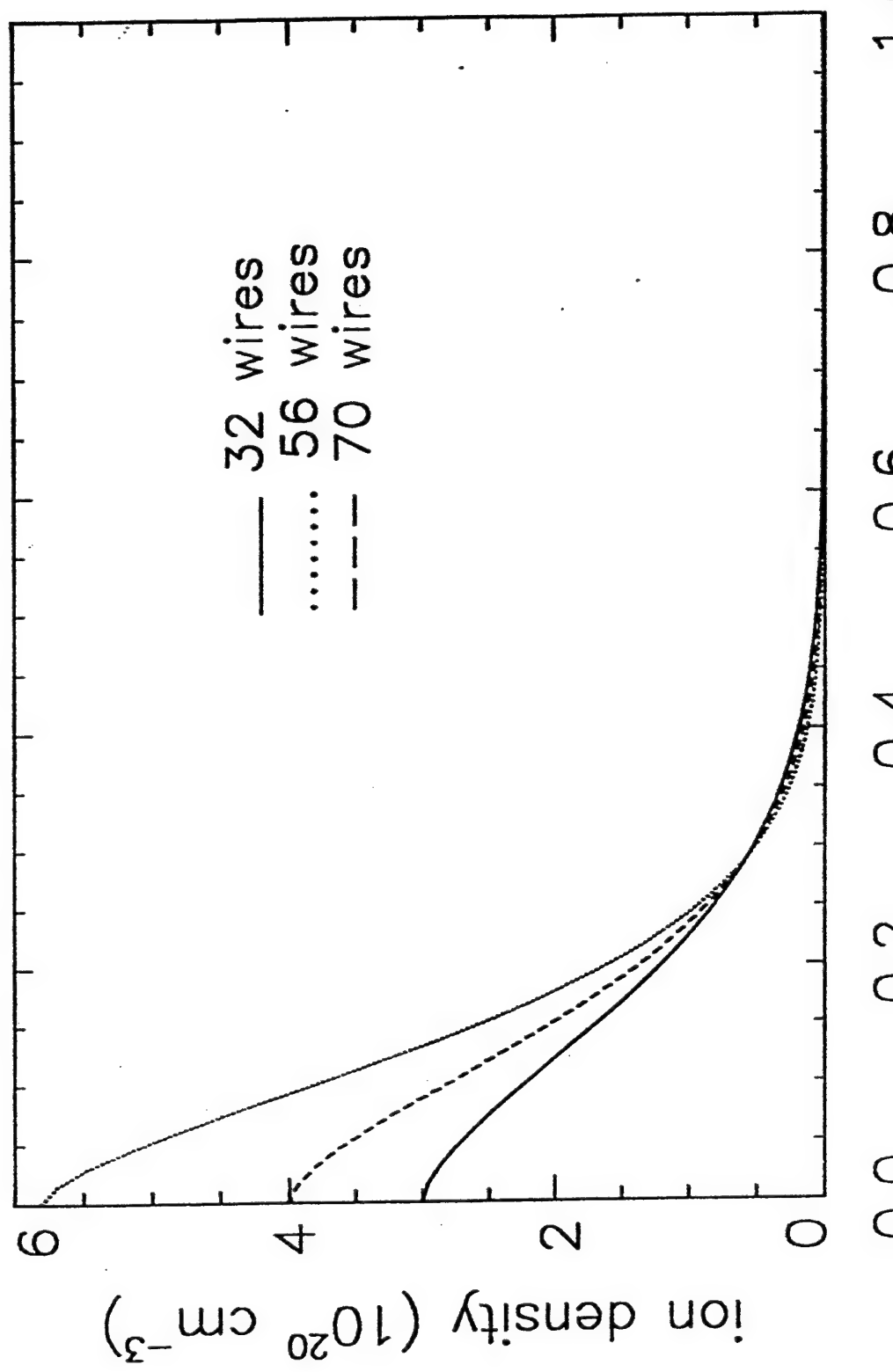


FIG. 2a

Saturn wire number scan

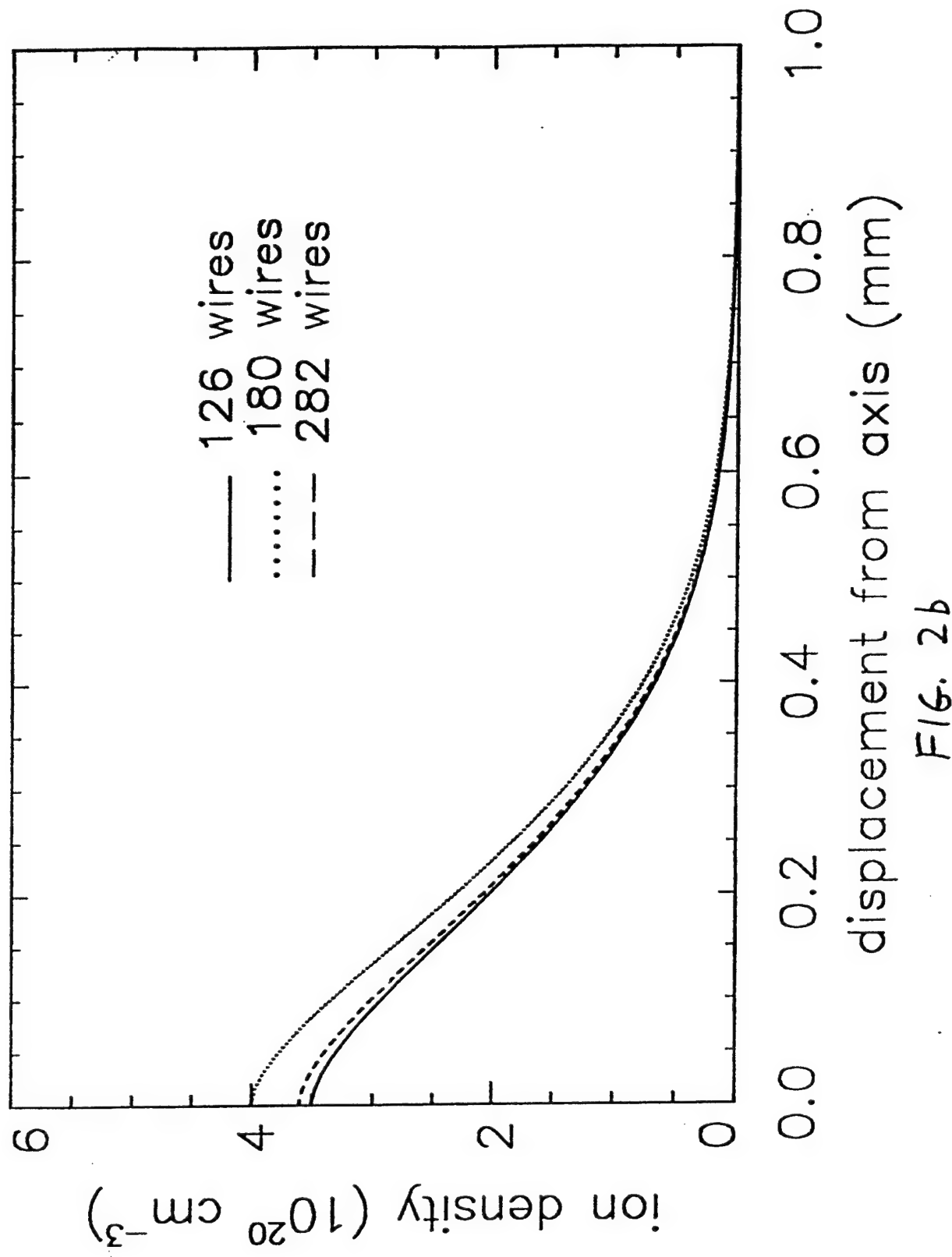


FIG. 2b

# Saturn wire number scan

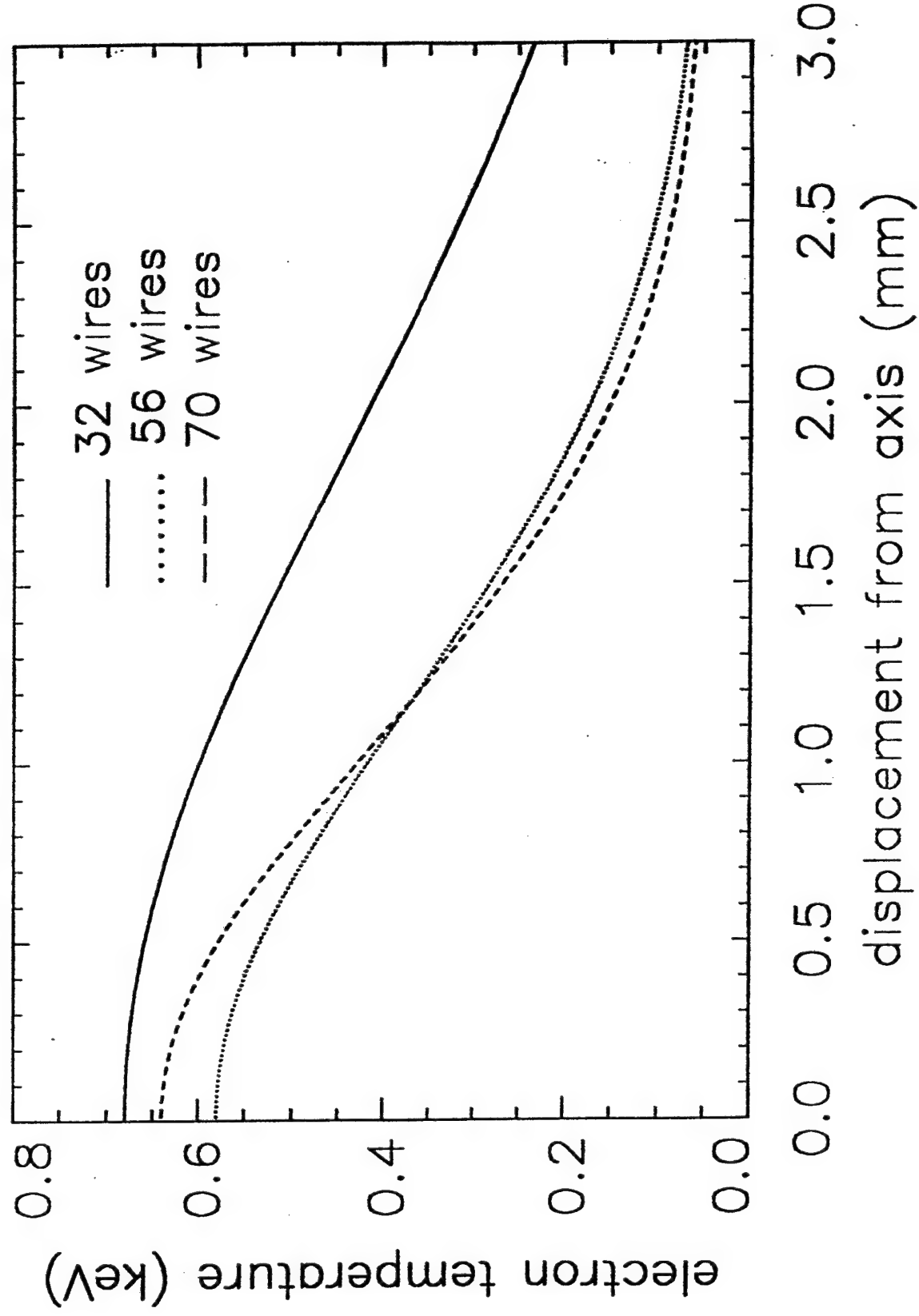


FIG. 3a

Saturn wire number scan

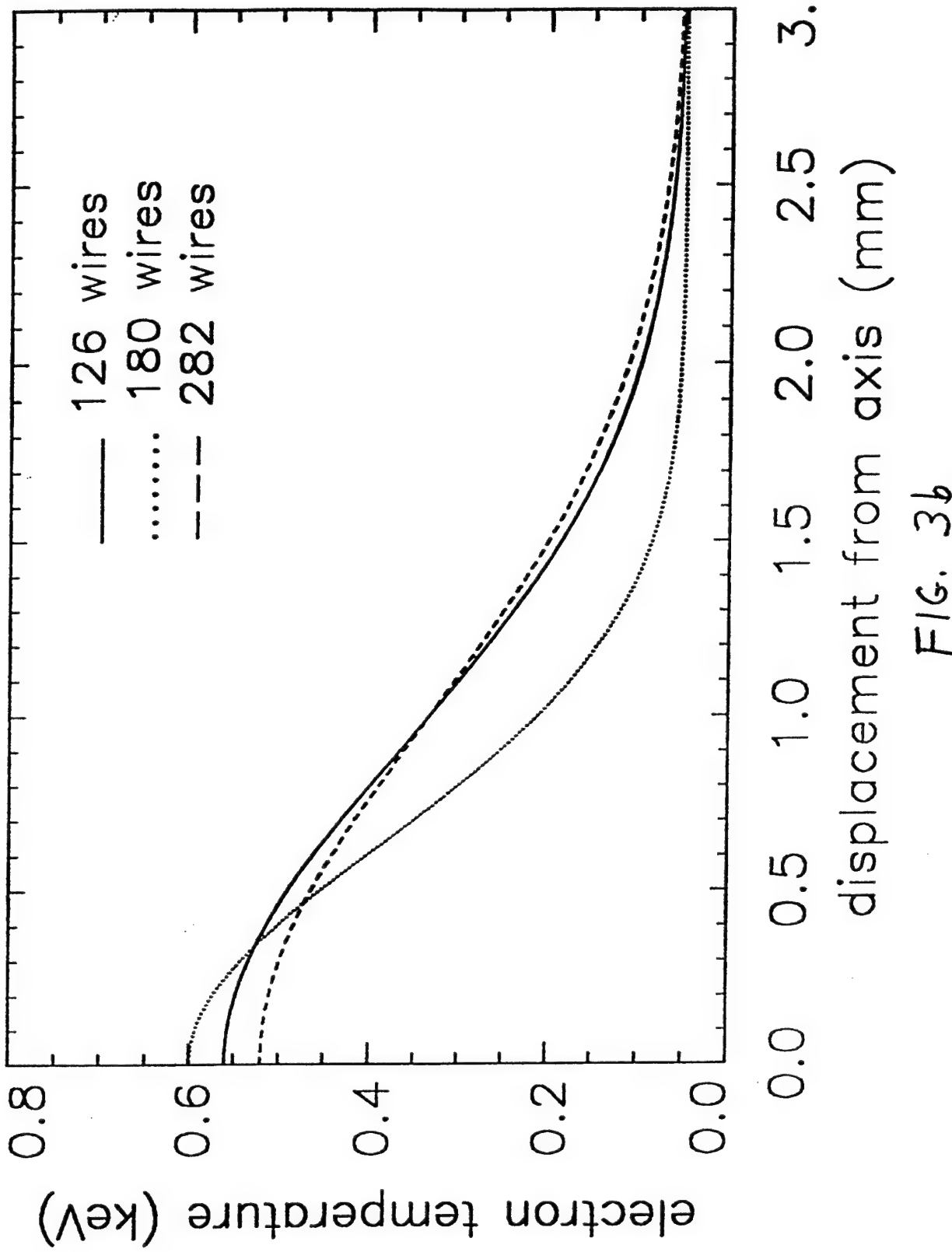


FIG. 3b

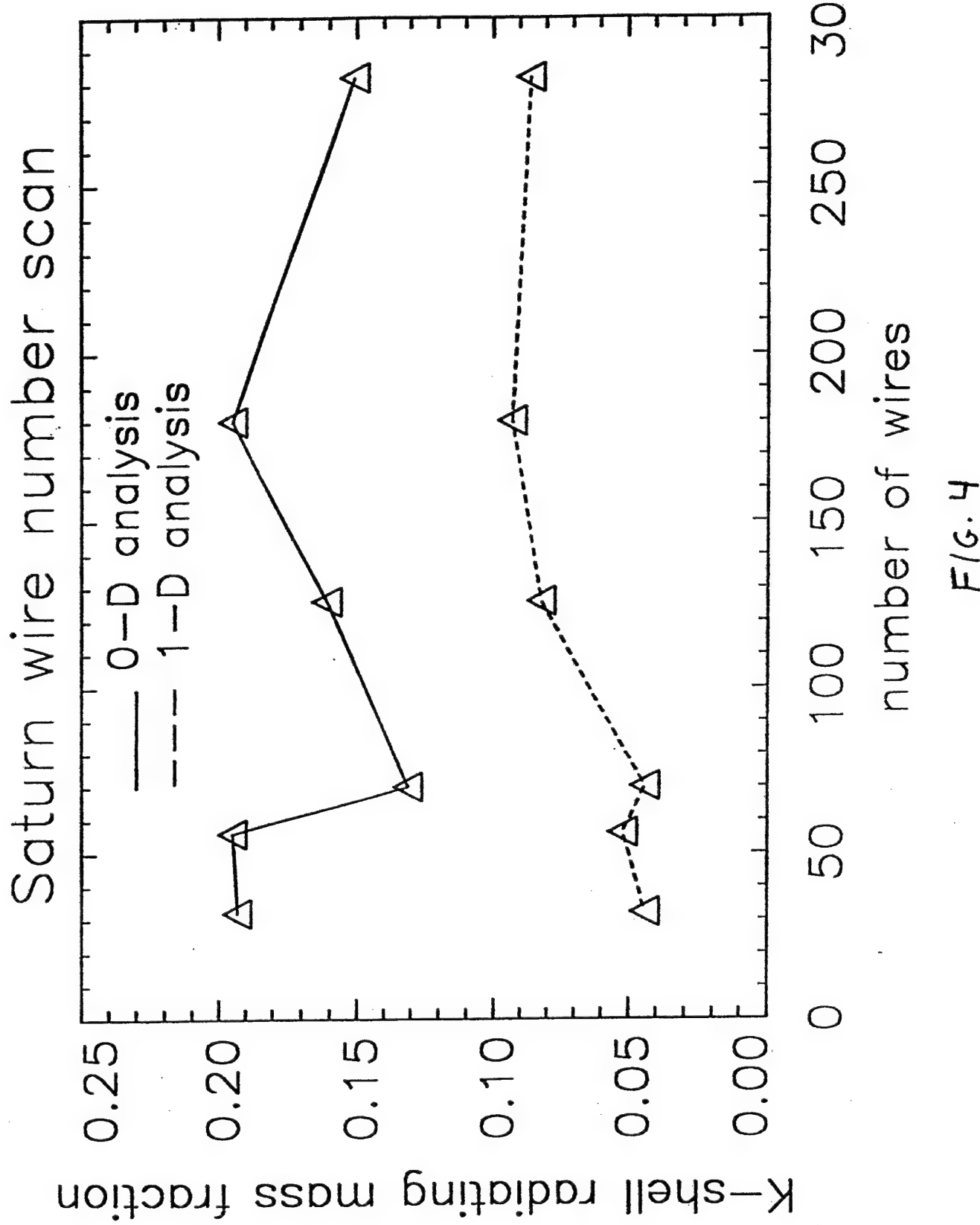


FIG. 4

Saturn wire number scan

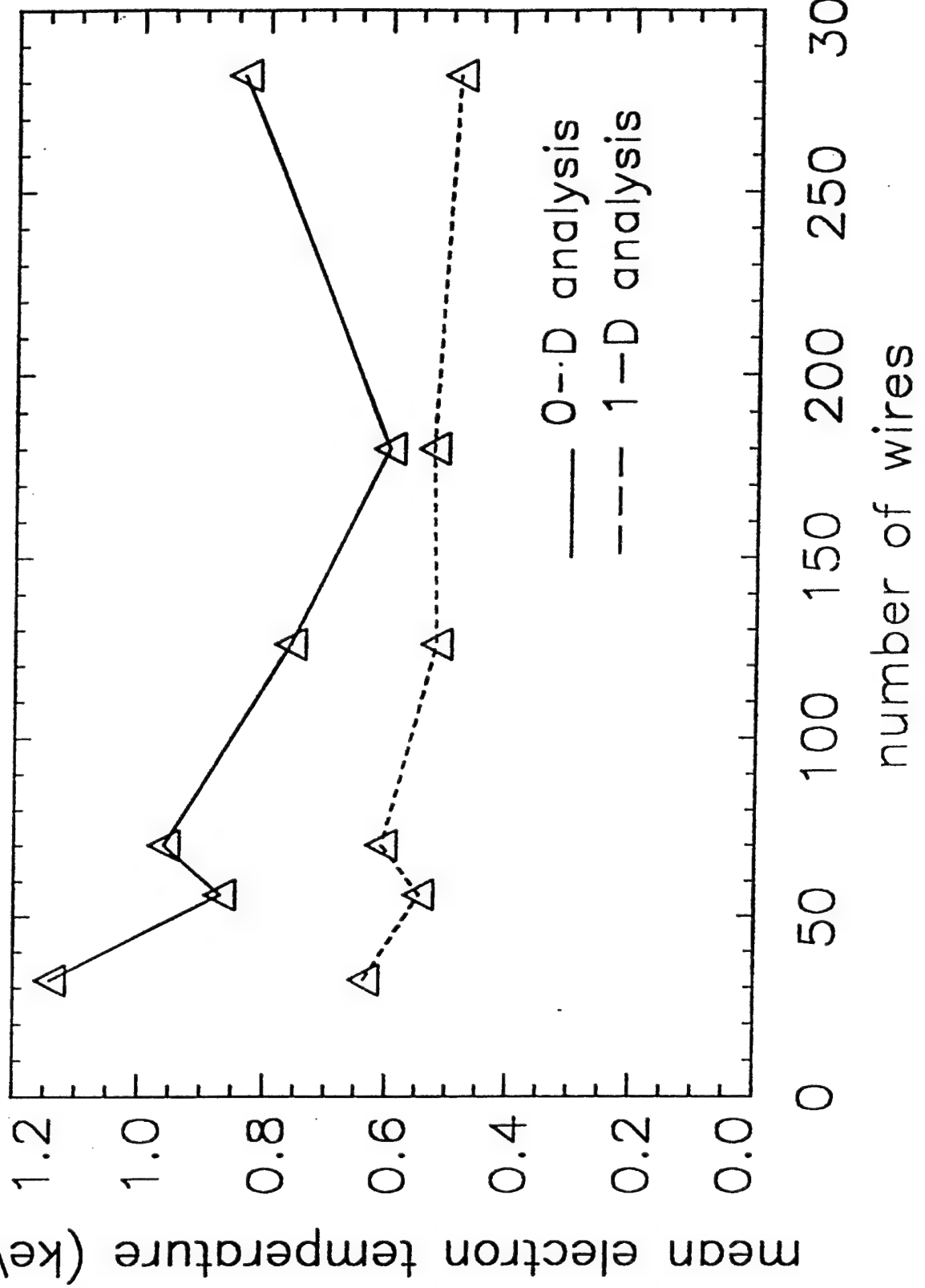
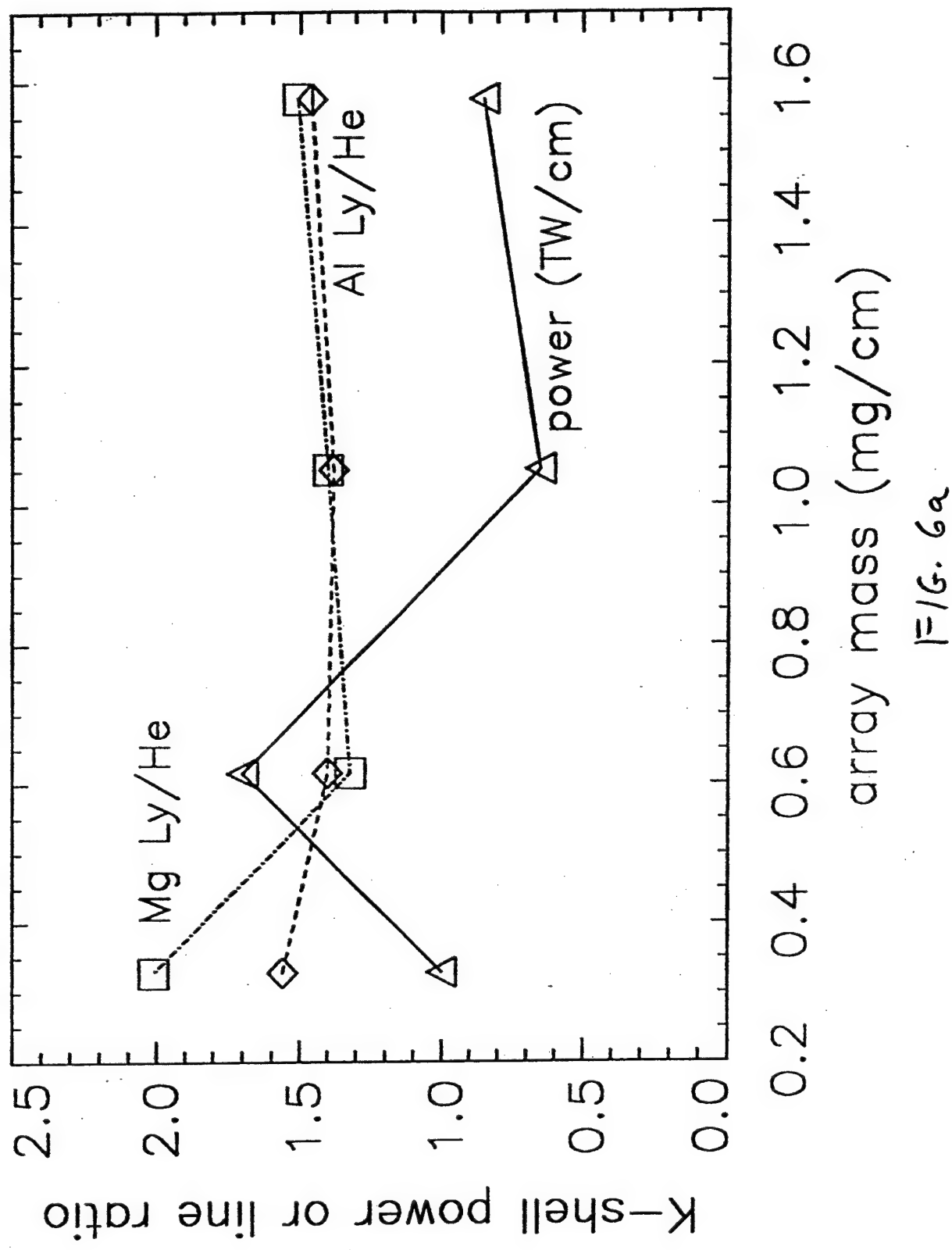


FIG. 5

# Saturn mass scan



Saturn mass scan

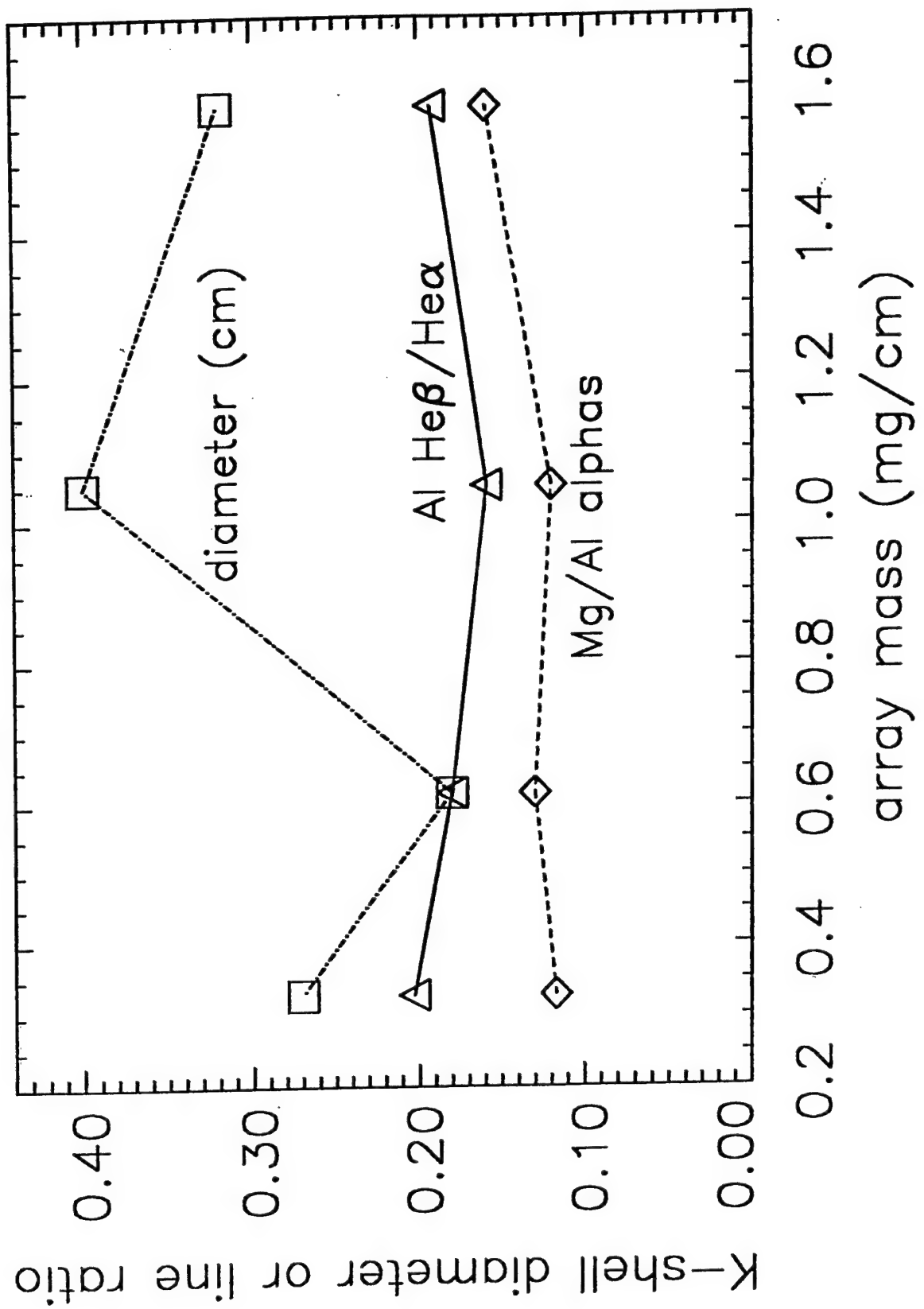


Fig. 6b

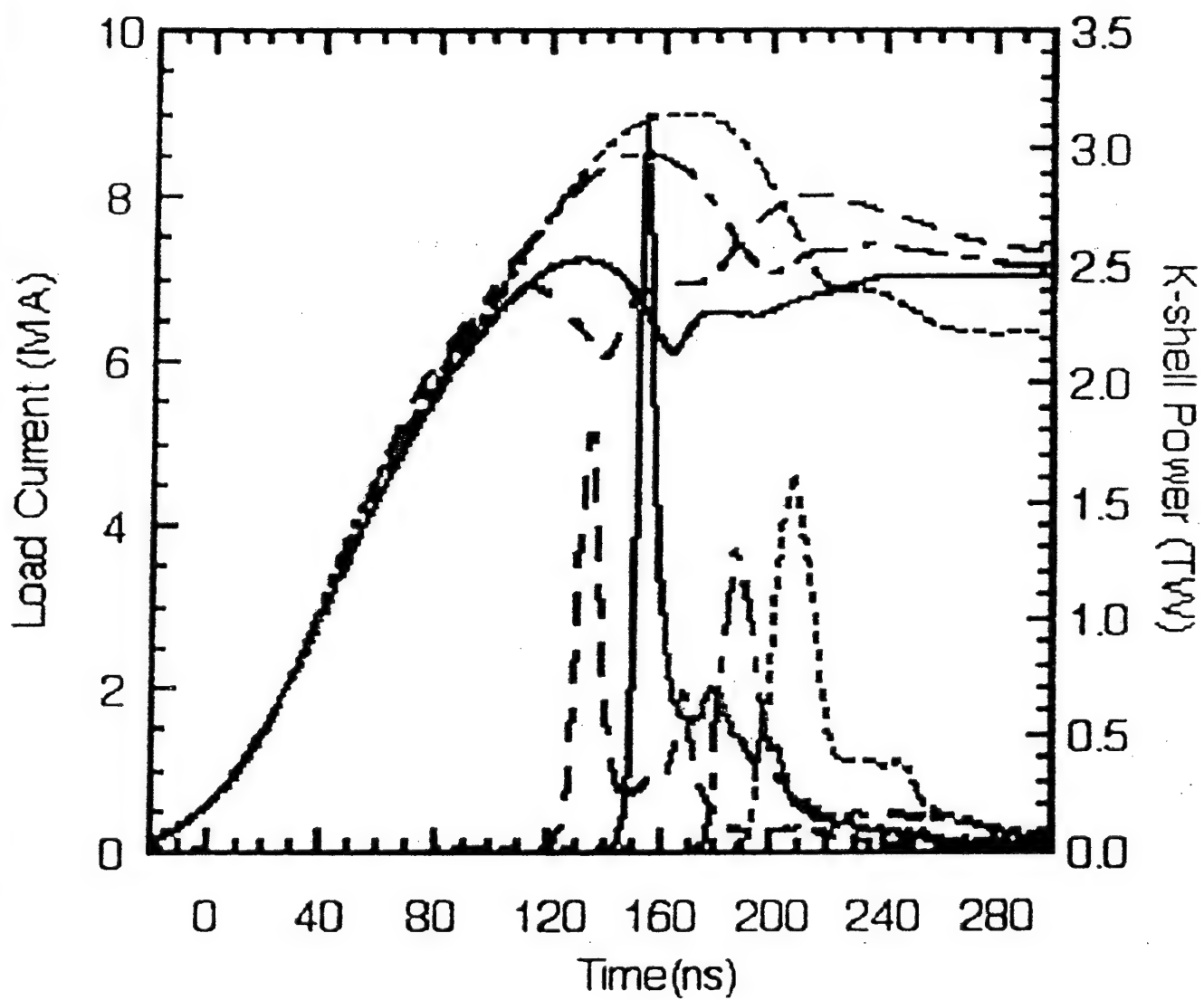


FIG. 6c

Saturn mass scan

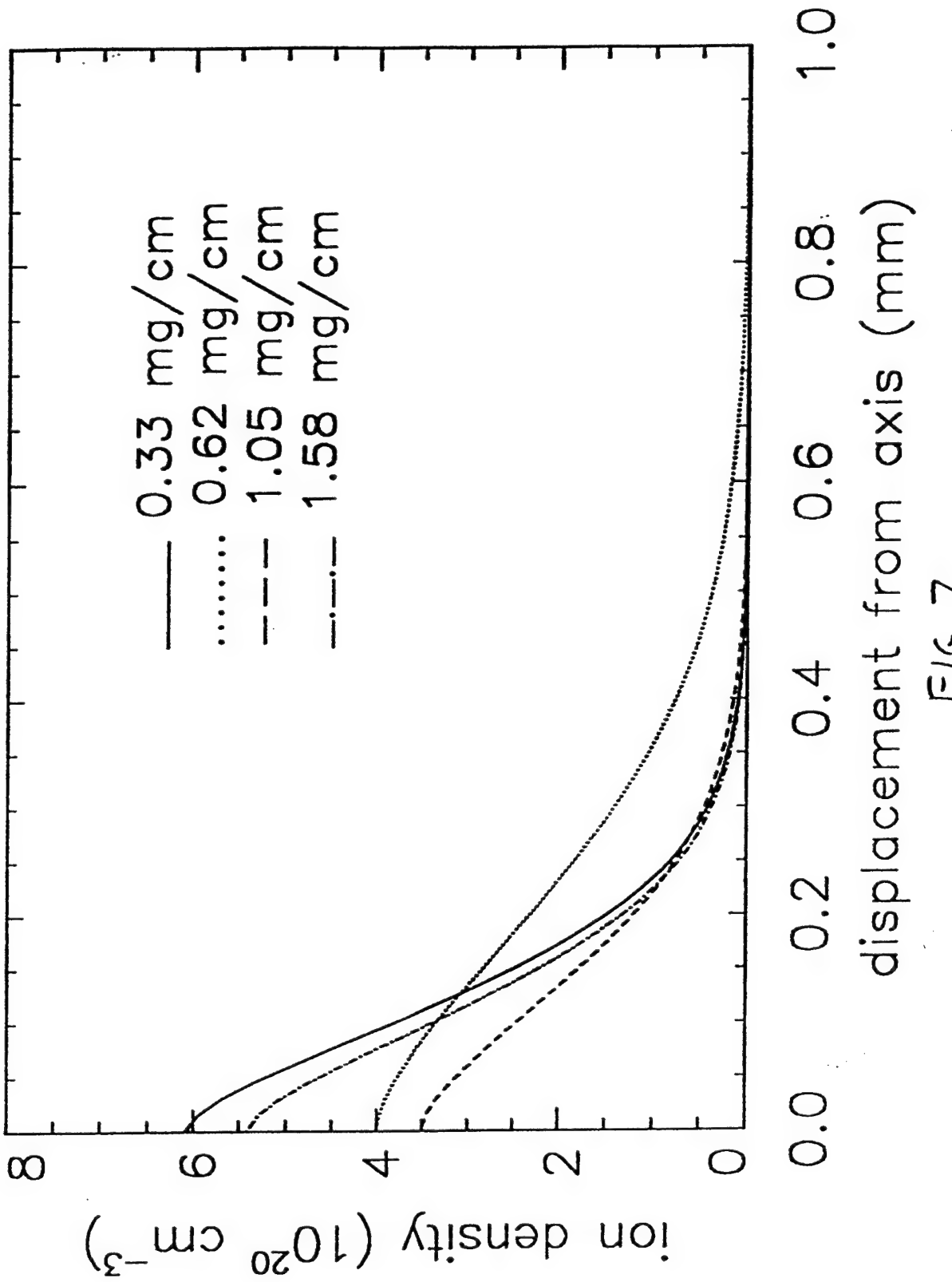


FIG. 7

### Saturn mass scan

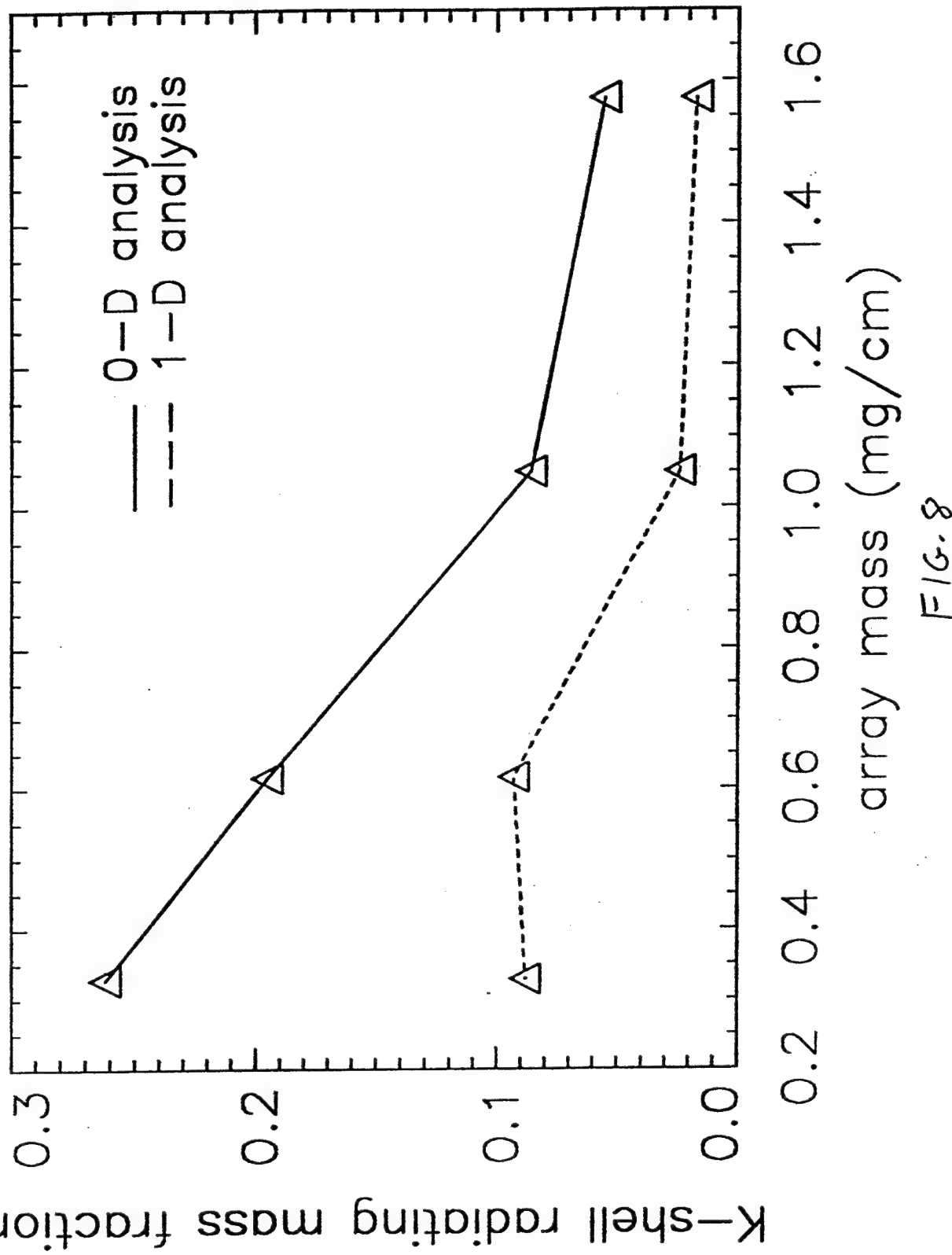
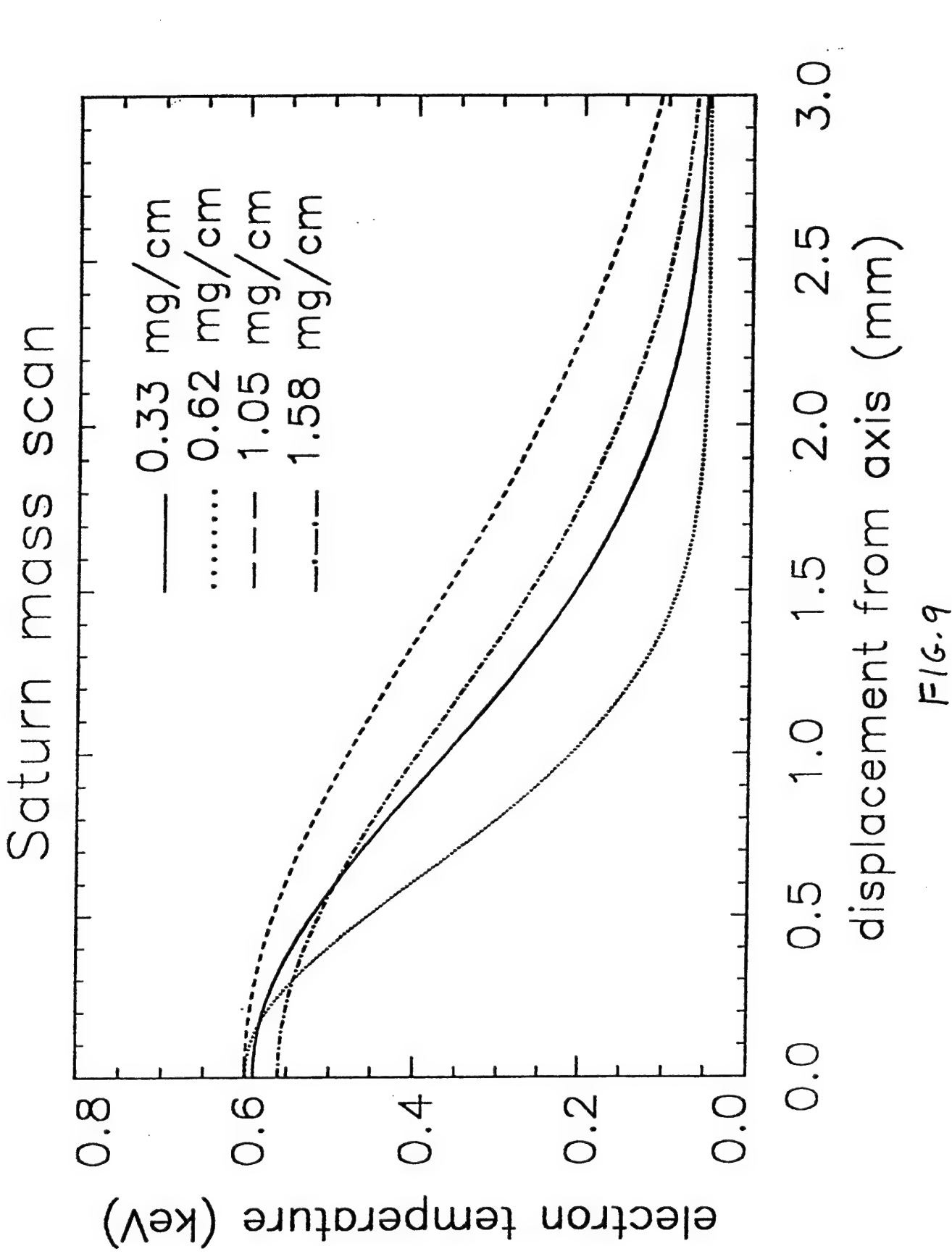


FIG. 8



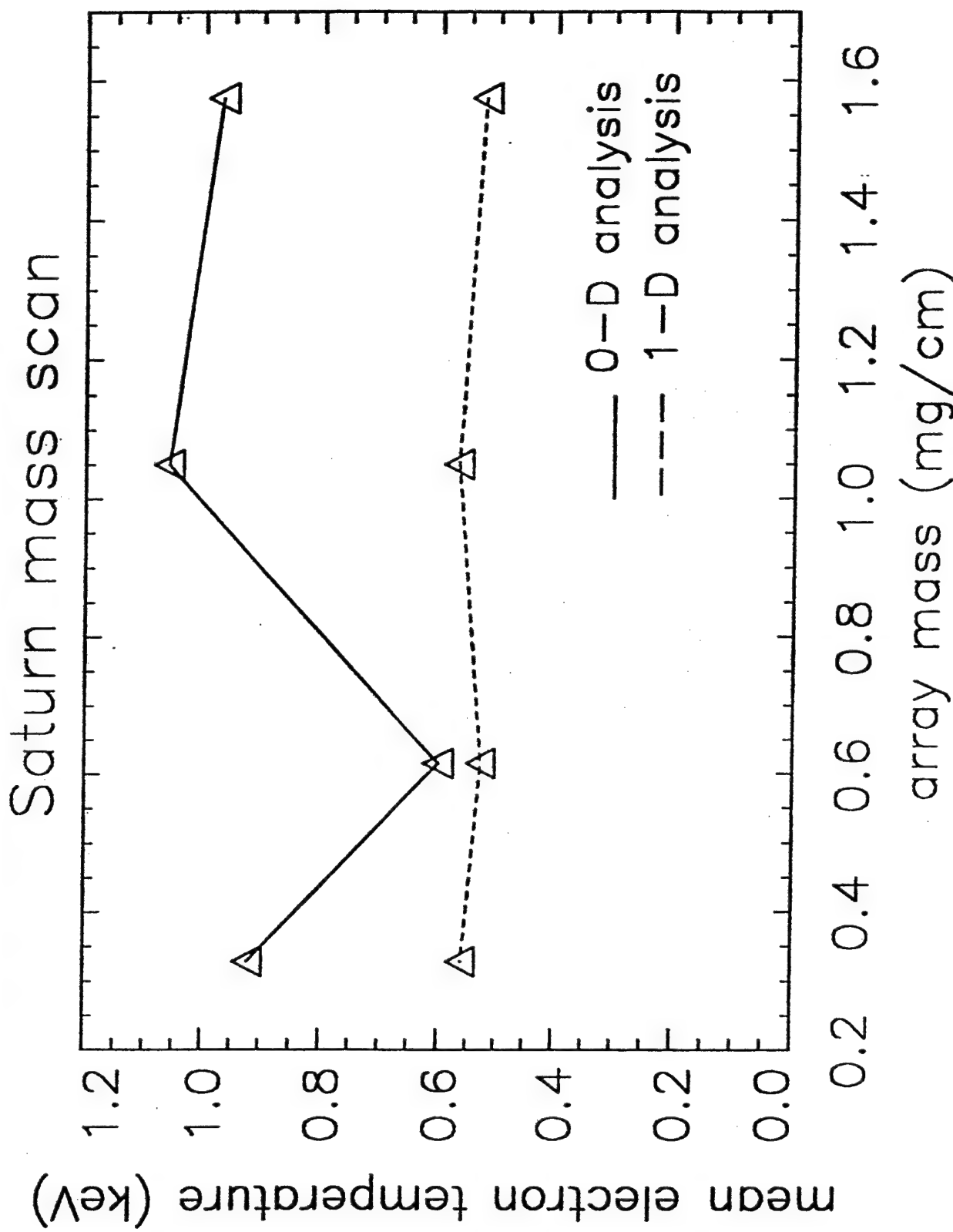


FIG. 10

Saturn shot 2706

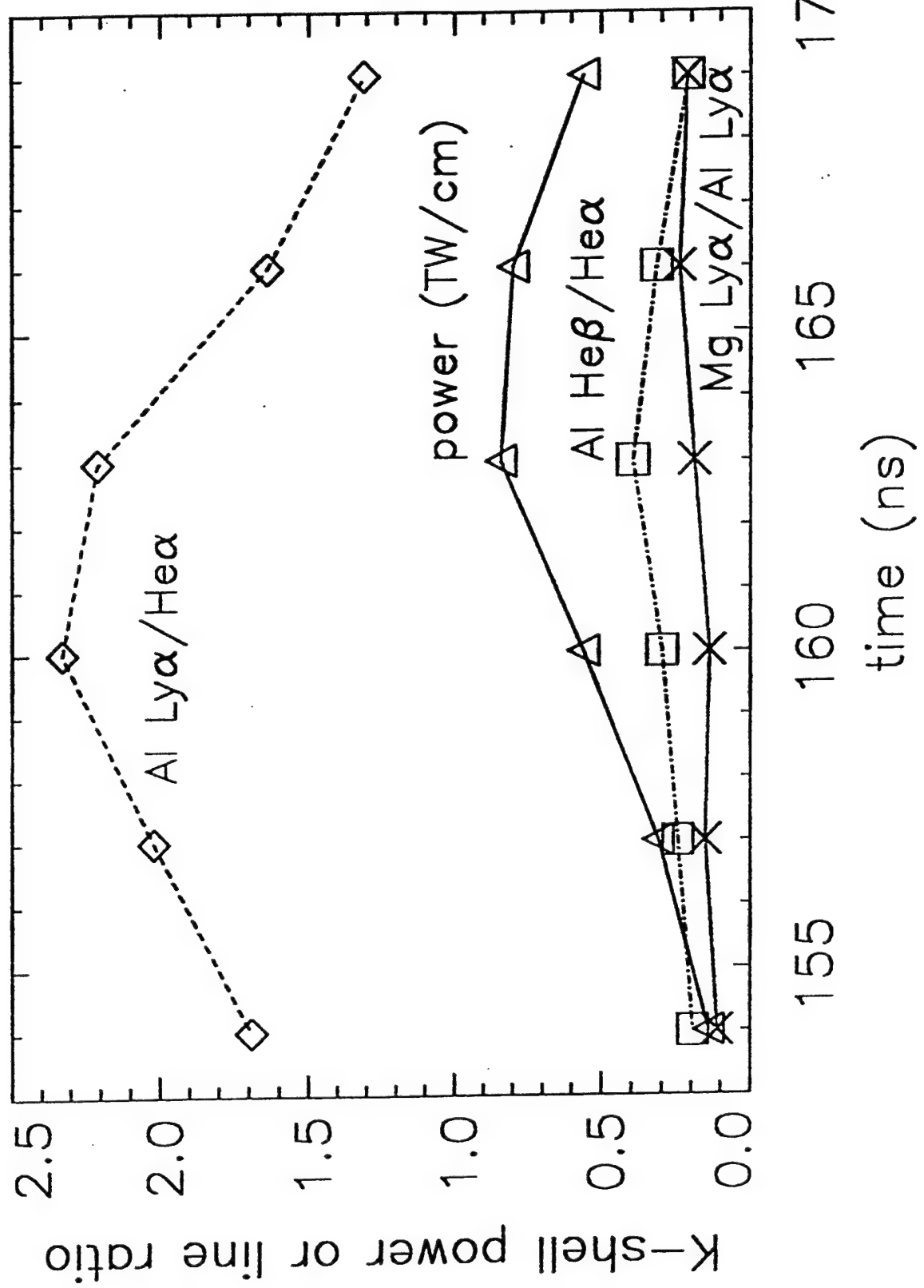


FIG. 11

Saturn shot 2706

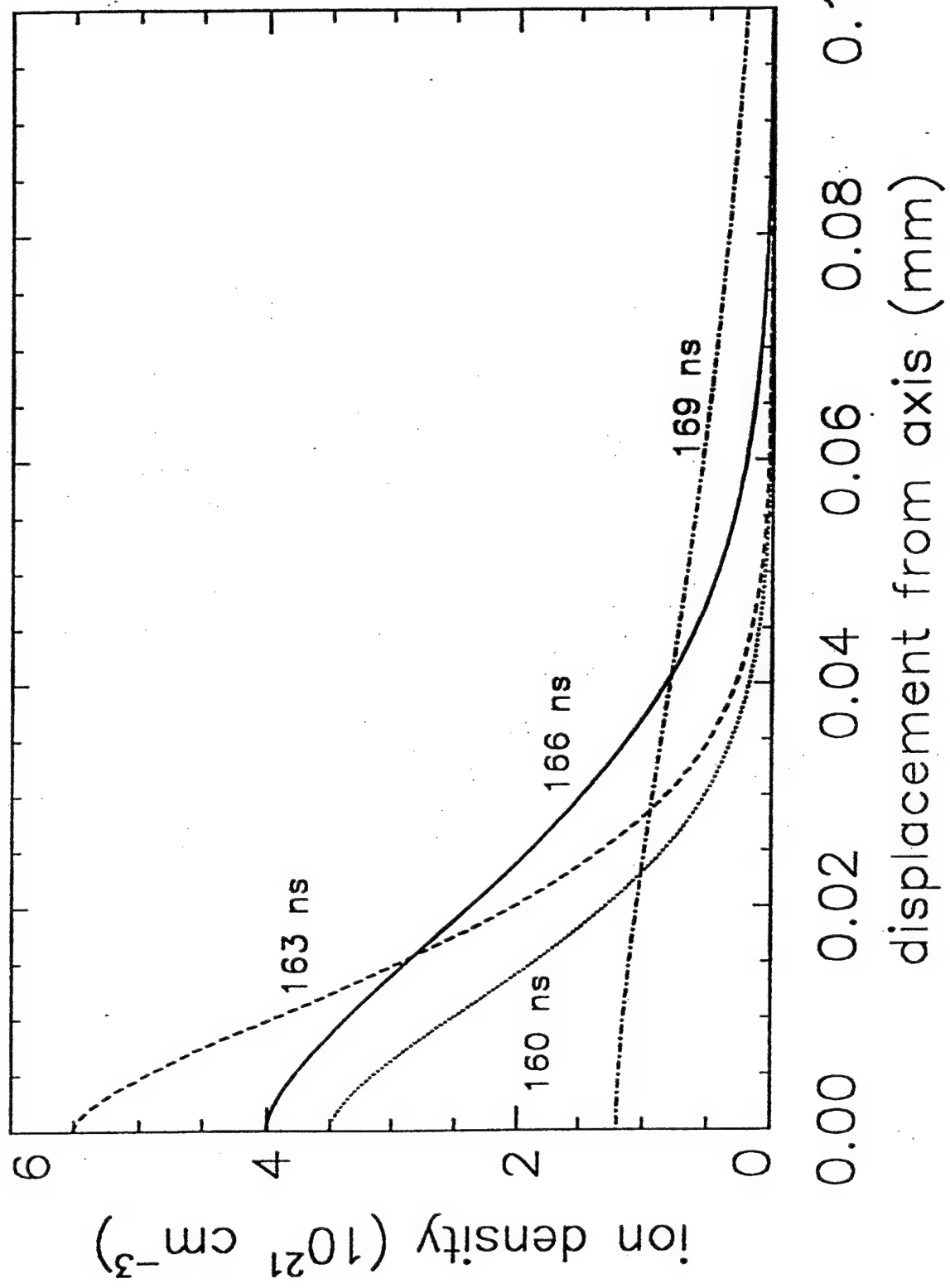


FIG. 12

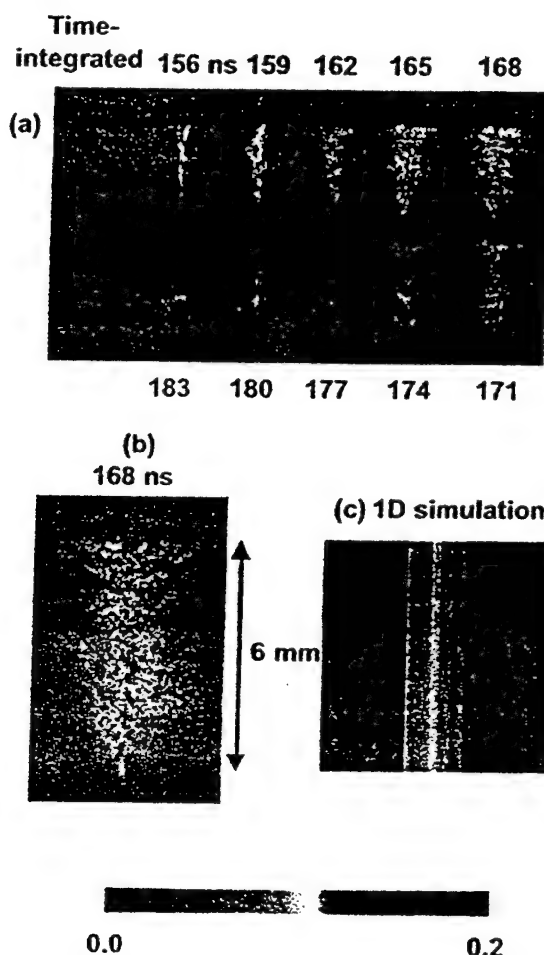
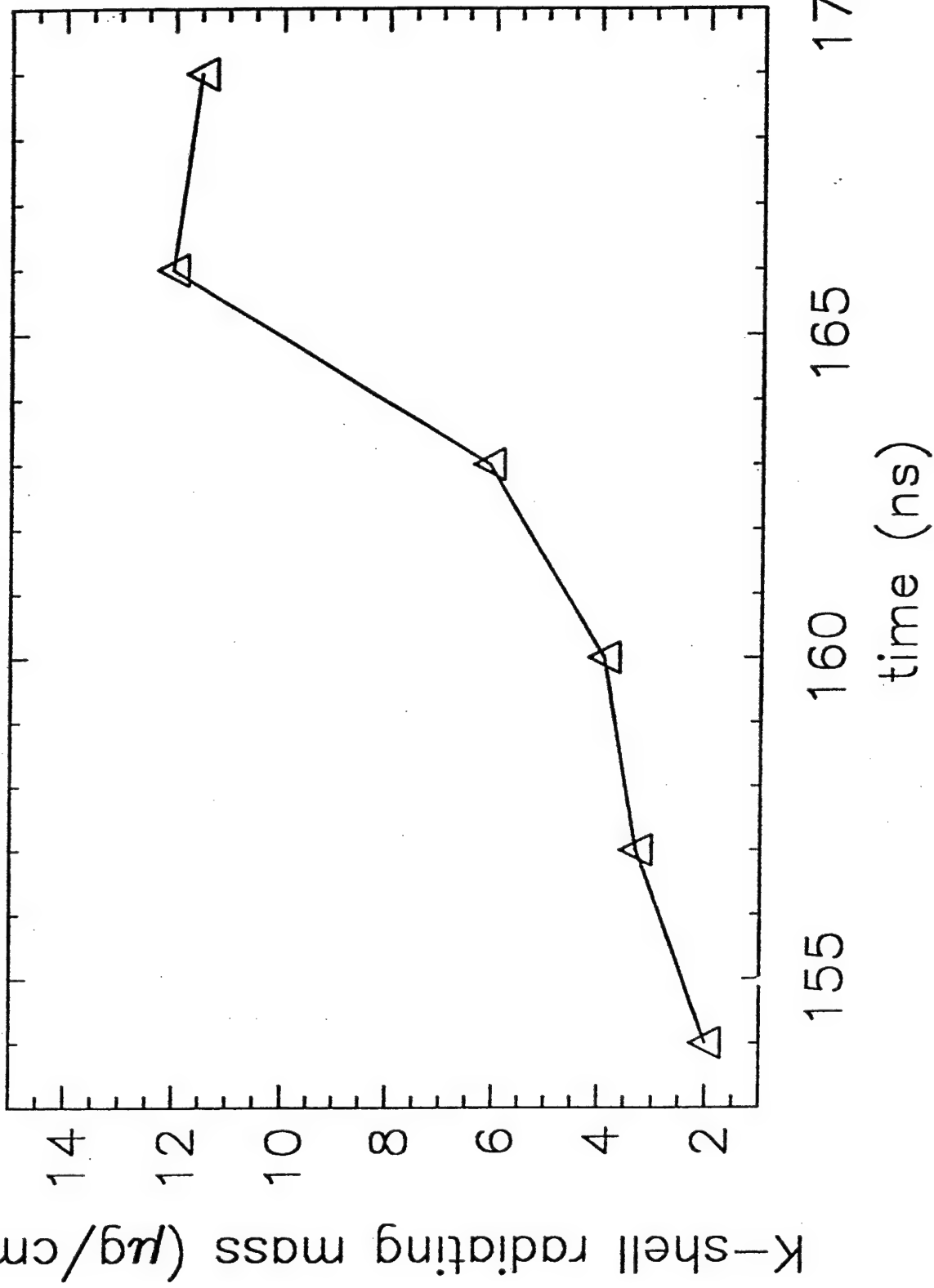


FIG. 13

Saturn shot 2706



F16.14

Saturn shot 2706

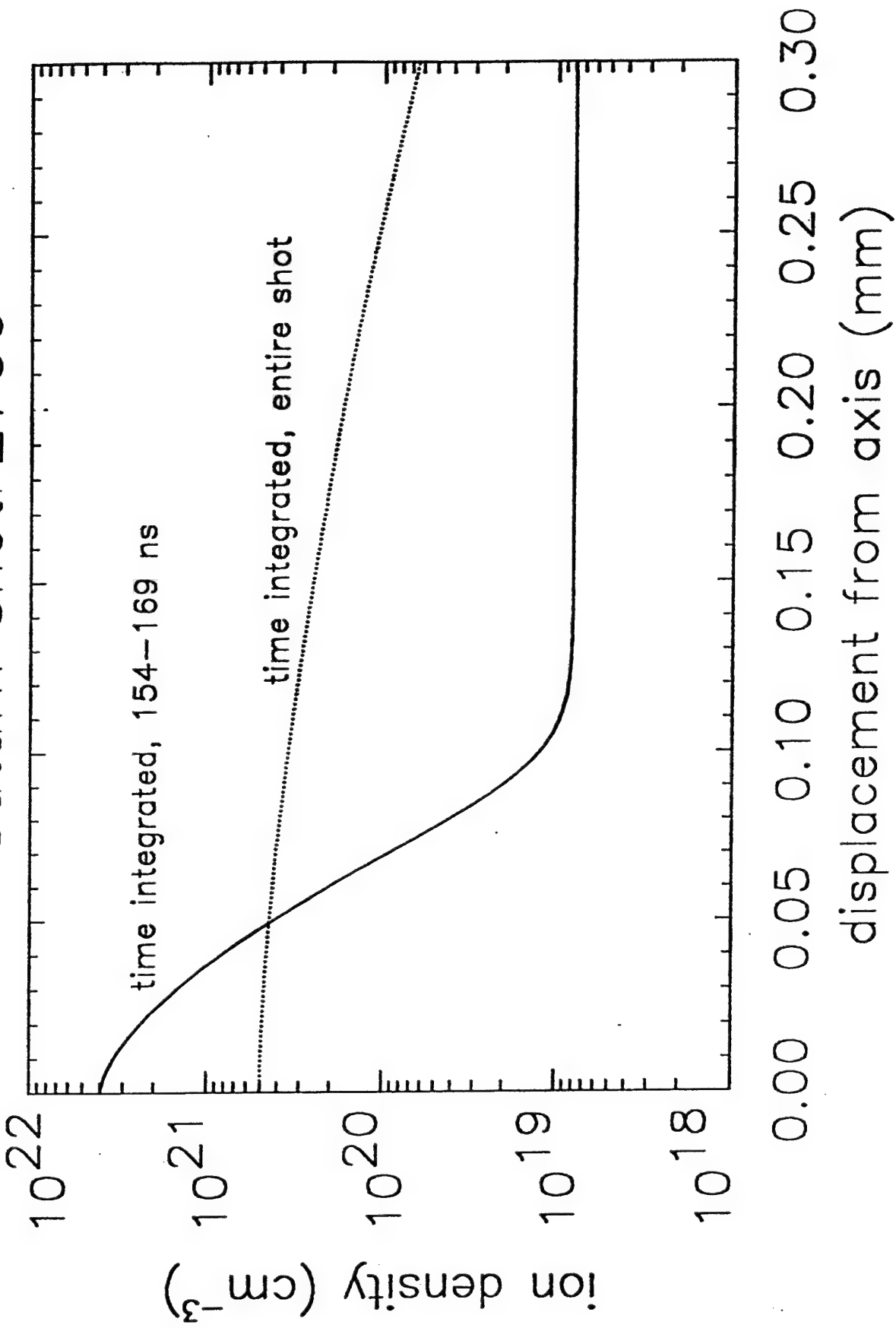
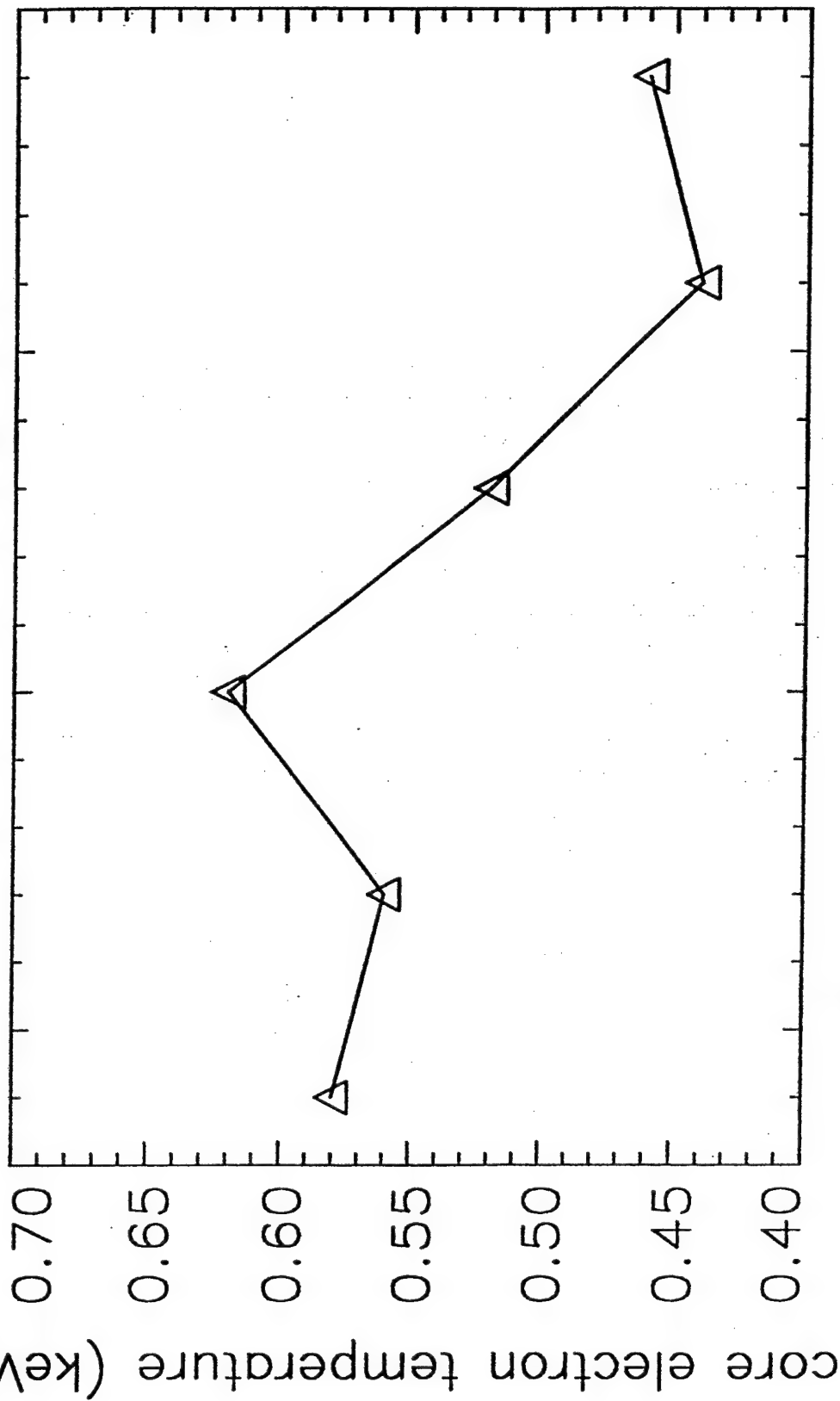


FIG. 15

Saturn shot 2706



170  
165  
160  
155

time (ns)

FIG. 16

### III. Au/ CH/ DT Implosions on 20, 40 and 60 MA Z-Pinches

#### 1. INTRODUCTION

The "Z" facility at Sandia National Laboratory is capable of putting 18-20 MA into a load, and in a few years, the "ZR" machine will be able to produce load currents in excess of 25 MA. The recent successes with large Z-pinch devices have renewed interest in Z-pinch fusion as a process for creating a hot dense plasma. However, the prospects for designing an operating fusion device depend on the results from some very basic research. Can substantial thermonuclear burn be produced in a Z-pinch? How efficiently will the  $\alpha$ -particles, which carry much of the fusion energy, be confined in the plasma? At what values of the magnetic field will magnetic confinement of the  $\alpha$ -particles occur? If breakeven cannot be achieved, will such devices be useful for enhanced high-energy photon PRS output? In a previous study we explored at the prospects for ignition in a high-current Z-pinch and reached a number of conclusions, including: (1) The magnetic fields produced in a 30 MA pinch may be sufficient to confine  $\alpha$ -particles<sup>2</sup>, (2) Low-Z Bremsstrahlung (characteristic of fusion plasmas) may be an attractive alternative for filling in the "bucket" in the photon spectra for PRS applications, and (3) Stabilization in the early phase and high-compression (exceeding Bennett equilibrium) in the final stage is a promising path to Z-pinch fusion. Several different DT/CH configurations were considered to quantify these hypotheses, including a D-T shell with a CH pusher and a  $B_z$  interlayer.

A series of Z-pinch simulations using structured Au/CH/DT loads was investigated. A summary of the various Au/CH/DT configurations is given in Table 1.

Table 1: Initial configurations for Au/CH/DT Z-pinch implosions

## DT/CH/Au Implosions: Initial Conditions



Configuration	Mass [mg]			Current	DT Yield [kJ]		2Ro = 5 cm	
	DT	CH	Au		B <sub>z</sub> (t = 0)	E <sub>burn</sub> E <sub>dep</sub>		
CH/DT/CH/Au (Single shell)	7.812	2.277	0.990	60 MA	0.00 MG	554.40 413.40		
	3.472	1.012	0.440	40 MA		177.40 82.20		
	0.868	0.253	0.110	20 MA		25.78 7.42		
DT uniform fill CH/Au coating (Balloon)	ZAuYSU	6.122	0.879	0.701	20 MA	0.00 MG	7.40 ---	
DT shell + CH shell + Au coating (Nested Shells)	ZAuYSI	0.561	0.523	0.148	20 MA	0.00 MG	6.60 1.02	
	ZAuYSV	5.045	4.703	1.332	60 MA	0.10 MG	803.00 531.00	
	ZAuYSV	2.242	2.090	0.592	40 MA		156.00 112.50	
DT shell + CH shell + Au coating (Nested Shells) B <sub>z</sub> interlayer	ZAuYSI	0.561	0.523	0.148	20 MA		5.20 3.60	

## 2. MODEL

The ionic populations in the plasmas are characterized by sets of atomic rate equations, linking each of the atomic levels included in the models. The rate coefficients that are used to calculate the populating and depopulating processes are calculated using various scattering techniques and the methods used in calculating the corresponding rate coefficients are summarized elsewhere<sup>3</sup>.

Radiation emission from the plasma and its opacity are dependent on the local atomic-level population densities. Except for optically thin plasmas, however, the level populations depend on the radiation field, since optical pumping via photoionization and photoexcitation can produce significant population redistribution. Thus, the ionization and radiation transport processes are strongly coupled and must be solved self-consistently. In this model, an iterative

procedure<sup>4</sup> was used, where level populations are calculated using the radiation field from the previous iteration, then using these populations to calculate a new radiation field until convergence is reached.

The atomic models used in the numerical simulations contain a sufficient number of ground and excited states to accurately account for the radiative energetics and provide useful diagnostics to compare with experiment. Ionization lowering was accounted for by means of an ion sphere model; the bound-free radiation was limited from states which merge with the continuum. Radiation transport was carried out using a probability-of-escape formalism which is described elsewhere<sup>5</sup>.

The dynamics of the radially imploding Z-pinch plasma was simulated using a one-dimensional multi-zone non-LTE radiation-magnetohydrodynamics code, DZAPP<sup>6</sup>, which uses a transmission line circuit model to represent the driving generator. The thermonuclear burn was calculated using rates from Glasstone and Lovberg<sup>7</sup>, and a diffusion model was used for the transport of the  $\alpha$ -particles. The diffusion equation for the  $\alpha$ -particle energy density  $E_\alpha$  takes the form

$$dE_\alpha/dt = (1 - \gamma)E_\alpha(\nabla \cdot \vec{v}) + \nabla \cdot (D \nabla E_\alpha) + S - 2\nu_e E_\alpha$$

where  $\gamma = c_p/c_v$  is the gas constant and  $\vec{v}$  is the velocity. The  $\alpha$ -particle diffusion coefficient and the electron-ion collision frequency are given by

$$D = \frac{Q/(\nu_e m_i)}{(9 + \Omega_i^2/\nu_e^2)}$$

$$\nu_e = \frac{n_e \Lambda Z^2 (m_e/m_i)}{(3.44 \times 10^5 T_e^{3/2})}$$

where  $T_e$  is the electron temperature,  $n_e$  is the electron density,  $\Lambda$  is the Coulomb logarithm, and  $Q$  is the initial  $\alpha$ -particle energy (3.52 MeV). The  $\alpha$ -particle source term is given by  $S = -Qd[T]/dt$ , where  $[T]$  is the local tritium concentration (we assume that  $[D] = [T]$ ). This treatment takes the local transverse magnetic field into account via the term involving the ion cyclotron frequency  $\Omega_i = ZeB_\perp/m_i c$  in the diffusion coefficient  $D$ . Axial electron energy losses were not included in this study; however, we have verified that these can be neglected for sufficiently long pinches.

The circuit model used in the simulations is based on an equivalent circuit for the Z generator. The circuit and voltage waveform is shown in Figure 1. This design puts a nominal peak current of 20 MA through a typical load. For the 40 and 60 MA cases, the circuit elements remain the same, but the voltage is multiplied by 2.0 and 3.0, respectively.

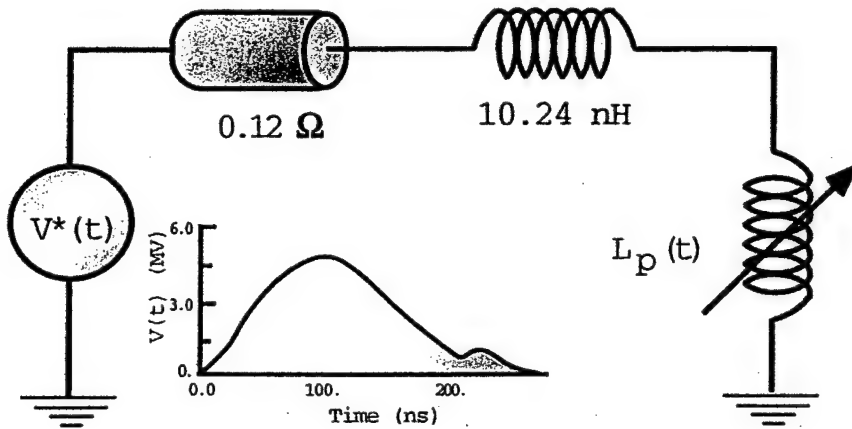


Figure 1: Equivalent circuit for 20 MA simulations.

### 3. RESULTS

A number of different load designs were investigated. The various load parameters (initial radii, masses, etc.) were chosen to give good energy coupling to the load, but were not optimized. It is likely that improved fusion yields could be obtained after some adjustment of these parameters. It is also possible that optimal radiative and fusion yields may be achieved with somewhat different initial conditions.

- **Single Au/CH/DT/CH Shell with different drivers:** The first set of simulations involved a layered Au/CH/DT/CH shell with different drivers (20-60 MA) and with the total mass tailored to the driver, according to the following scaling:

$$M_o = \frac{\mu I_{max}^2 \tau^2}{4\pi \Pi R_o^2},$$

where  $\Pi$  is a dimensionless scaling parameter,  $\mu$  is the vacuum permeability,  $I_{max}$  is the maximum pinch current (which occurs at time  $\tau$ ), and  $R_o$  is the initial radius of the load. The parameters for the simulations in this series are summarized in Table 2.

**Table 2: Parameters for the Single Shell Simulations**

$I_{max}$	$M_o$ [DT]	$M_o$ [CH]	$M_o$ [Au]	$R_o$	$E_{D-T}$	$E_{\alpha-dep}$
20 MA	0.868 mg	0.252 mg	0.110 mg	2.5 cm	25.8 kJ	7.4 kJ
40 MA	3.472 mg	1.012 mg	0.440 mg	2.5 cm	177.4 kJ	82.2 kJ
60 MA	7.812 mg	2.277 mg	0.990 mg	2.5 cm	554.4 kJ	413.4 kJ

The shells were layered, with the DT sandwiched between layers of CH, and with a coating of Au on the outside. The masses were chosen such that, in each case, the DT was 71% of the load, CH was 20%, and Au 9%. D-T yields and the yields of the  $\alpha$ -particles deposited in the plasma are given in Table 2. It can be seen that the D-T and  $\alpha$ -particle yields are very strong functions of current  $I_{max}$ , and scale approximately as

$$E_{D-T} = I_{max}^{2.8}$$

$$E_{\alpha-dep} = I_{max}^{3.6}$$

No attempt was made to optimize the yields by varying the parameters in Table 2. The implosion histories of the three simulations are given in Figures 2-4. Each plot shows contours in  $[r,t]$  for the ion temperature, mass density,  $dE_{D-T}/dt$ , and  $dE_{\alpha-dep}/dt$ . The peak ion temperatures range from about 47 keV for the 20 MA case to 107 keV for the 60 MA case. These are the *peak* values, which usually occur in low-density regions. Efficient thermonuclear burn requires both high temperature and high density. This is borne out by the contours of  $E_{D-T}$ . Also, the minimum radius of the implosion decreases as the peak current rises; the corresponding density increase results in higher burn rates  $dE_{D-T}/dt$ . Finally, it can be seen from the contours that the  $\alpha$ -particle deposition does not coincide with  $\alpha$ -particle production. The  $\alpha$  deposition takes place preferentially in the high-Z plasma, i.e. in the Au layer.

At the ion temperatures reached in these implosions, the D-D reaction rate is still small compared with the D-T rate, as shown in Figure 5. At very high currents, however, D-D burn may become important. Even at lower currents, if pure deuterium is substituted for a D-T mixture (e.g. to minimize the destructive effects of fusion products on an existing platform), the D-D cross section cannot be ignored.

Z20-CH.DT.CH.Au

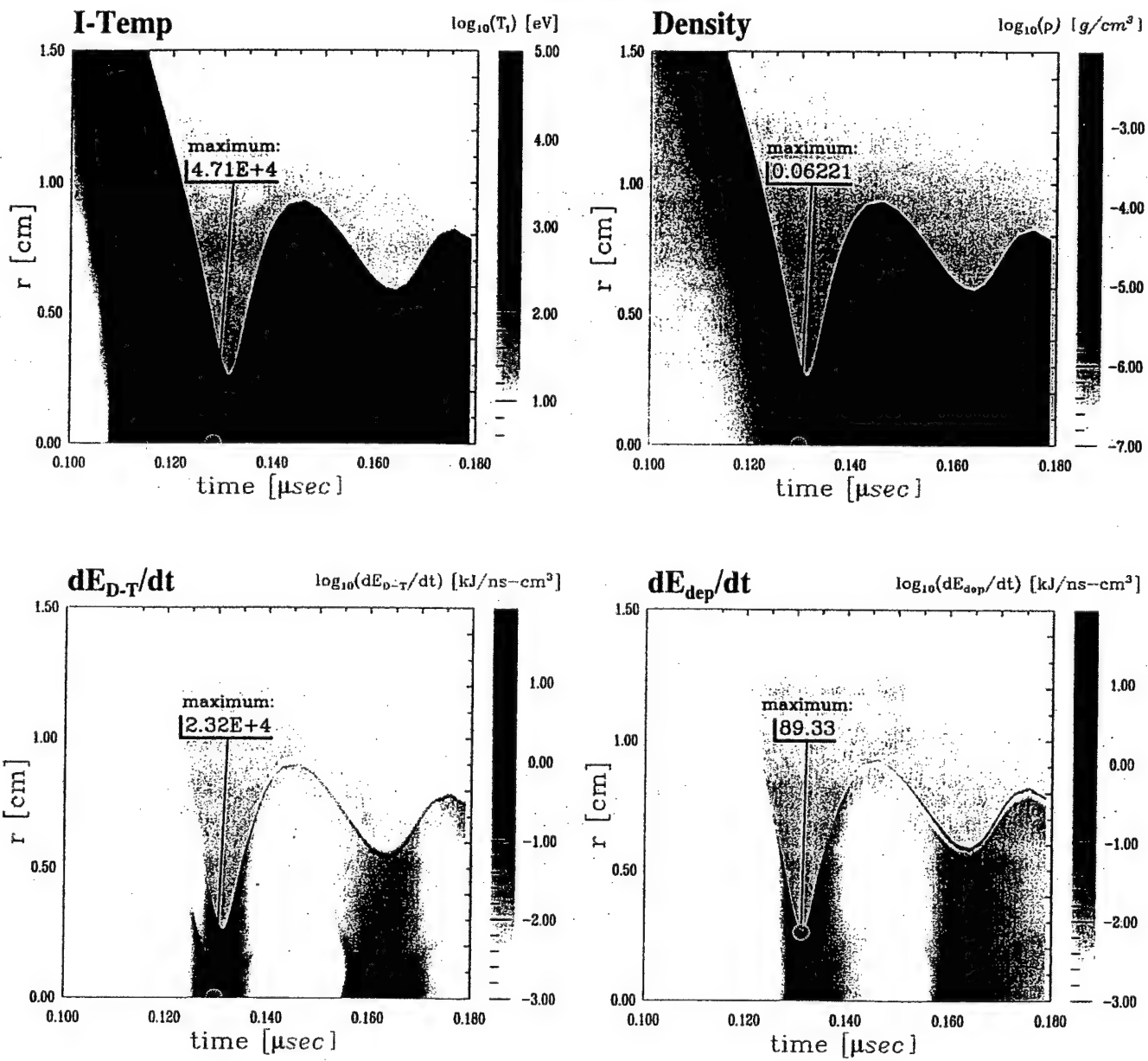


Fig. 2: Implosion history of 20 MA Au/CH/DT/CH Shell.

100

Z40-CH.DT.CH.Au

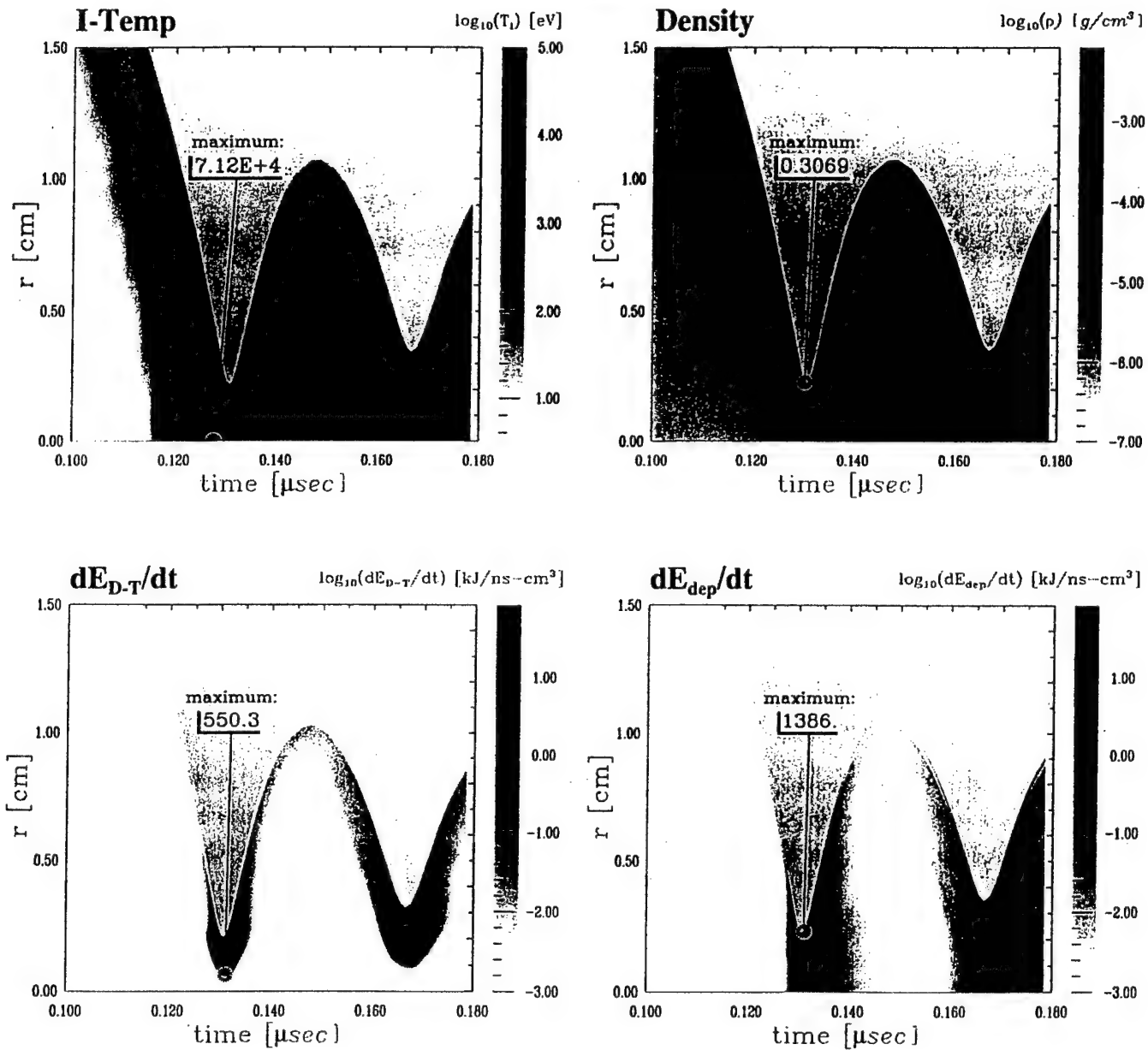


Fig. 3: Implosion history of 40 MA Au/CH/DT/CH Shell.

Z60-CH.DT.CH.Au

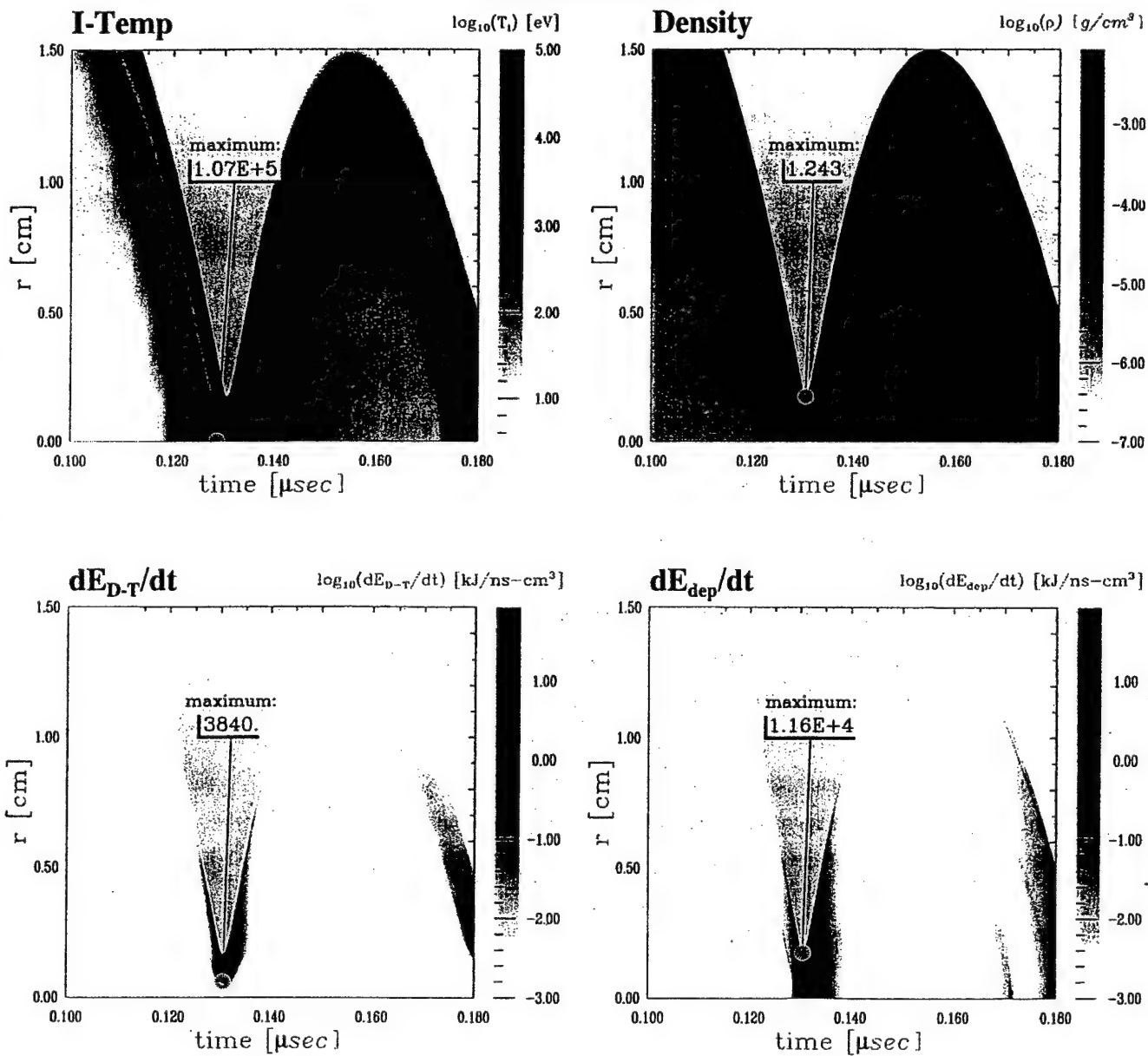


Fig. 4: Implosion history of 60 MA Au/CH/DT/CH Shell.

102

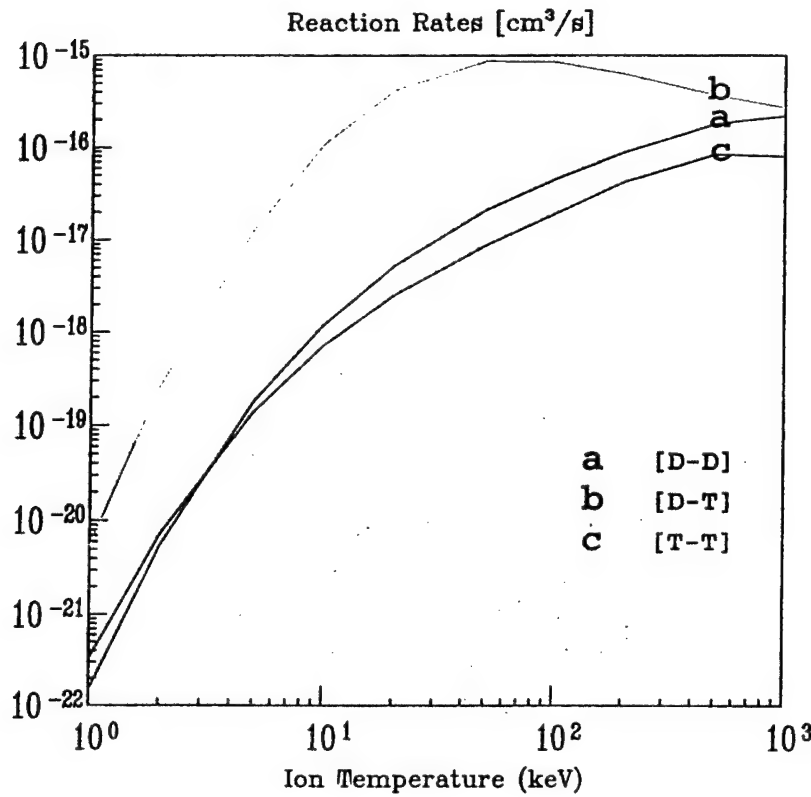


Figure 5: Nuclear fusion reaction rates for deuterium and tritium

- **Au coated CH shell with uniform DT fill:** An Au coated CH shell with a uniform DT fill (balloon) was simulated for the case of a 20 MA driver. The parameters for this case are shown in Table 3. The D-T yield is smaller than for the 20 MA layered shell (above), but the DT balloon may be a promising configuration after some optimization is performed. The total energy deposited by the  $\alpha$  particles was not calculated. However, the implosion history is shown in Figure 6. The peak ion temperature occurs long before the bounce phase. At minimum radius, it does not reach 10 keV. Thus, the D-T burn is relatively inefficient.

Table 3: Parameters for the DT-Filled Balloon Simulation

$I_{max}$	$M_o[DT]$	$M_o[CH]$	$M_o[Au]$	$R_o$	$E_{D-T}$	$E_{\alpha-dep}$
20 MA	6.122 mg	0.879 mg	0.701 mg	0.5 cm	7.4 kJ	— kJ

- **D-T Shell with Au-coated CH Pusher:** In the simple D-T implosions, the thermonuclear burn is inefficient, even at the highest currents. The ion temperature, which approaches 100 keV for the 60 MA case, is certainly sufficient to provide nearly optimum D-T reaction cross-sections. Unfortunately, the plasma density is not very high in the hottest regions. Also, the

Z20-DTfill.CH.Au

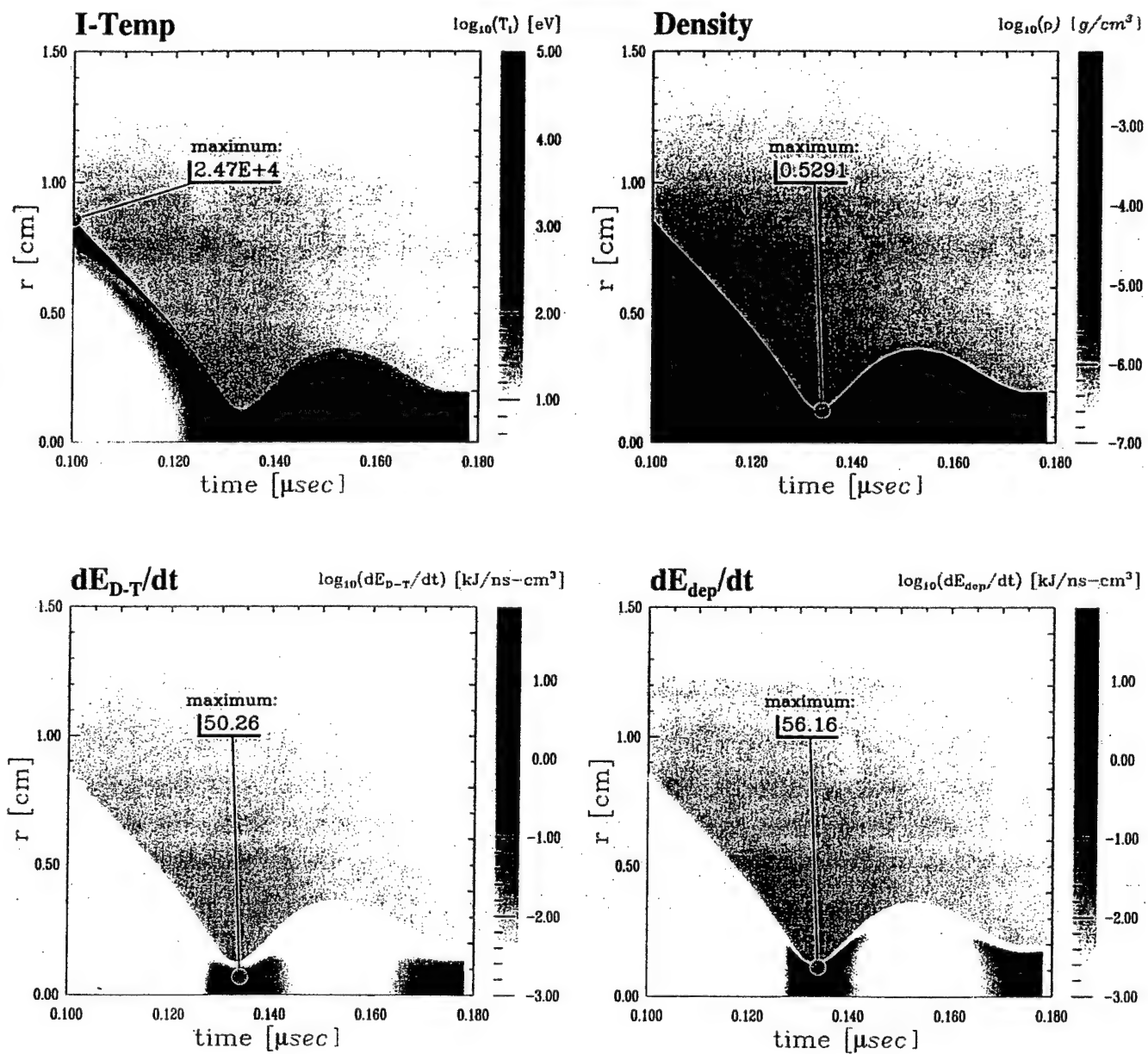


Fig. 6: Implosion history of 20 MA Au coated CH shell with uniform DT fill.

103

Z20-DT-CH.Au-Nested

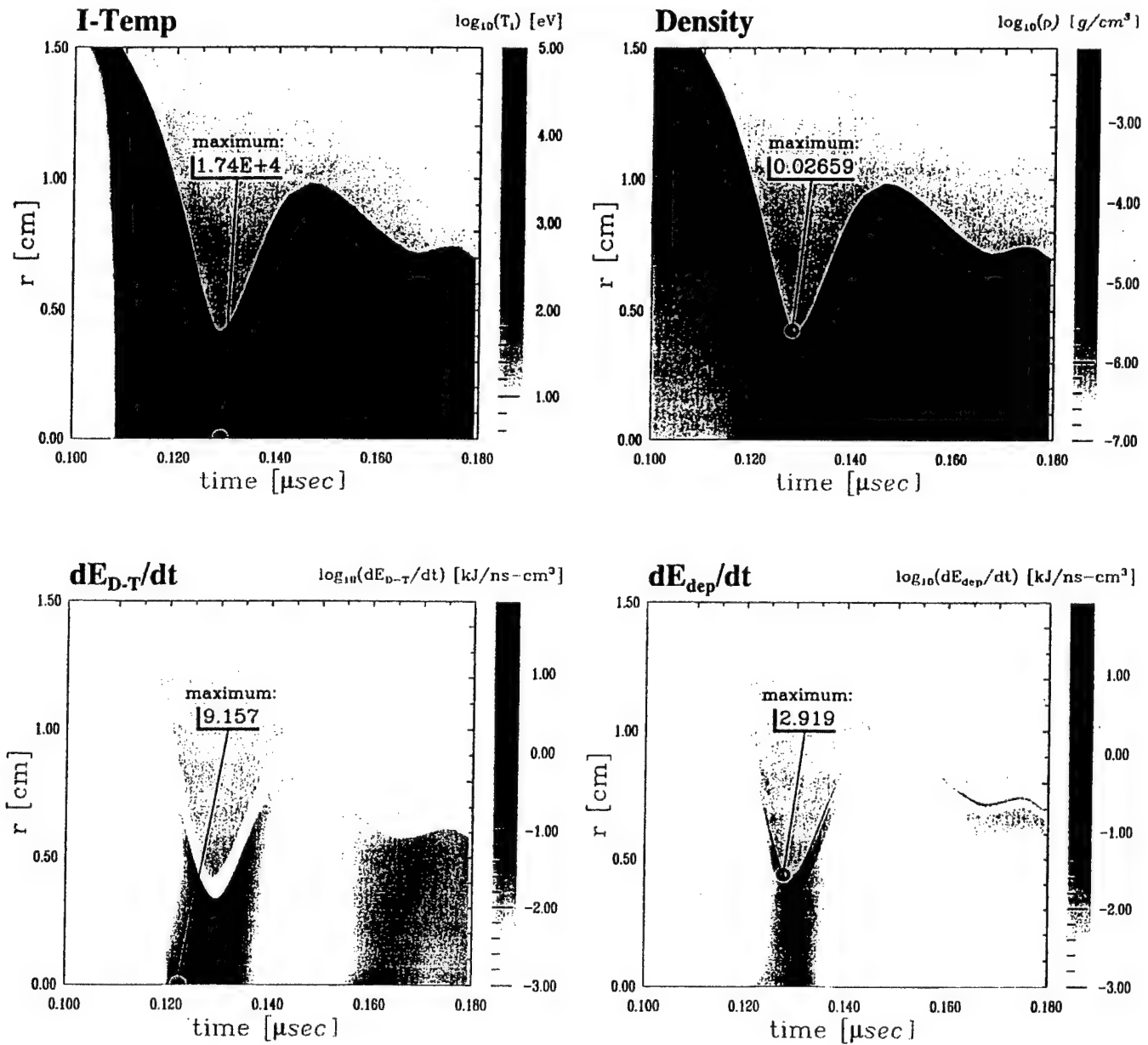


Fig. 7: Implosion history of 20 MA DT shell with Au-coated CH pusher.

plasma bounces, quickly reducing the temperature and density; the D-T becomes too cool for fusion after only a few nanoseconds. A mechanism which could delay the bounce, even by a few nanoseconds, would likely improve the burn efficiency.

An outer shell of Au-coated CH was added to a D-T load, as shown in Table 1. It was hoped that the inertia of this surrounding plasma could help to contain the D-T. Only the 20 MA case was simulated. The parameters (and yields) for this shot is given in Table 4. The masses were chosen such that the shells would be approximately equal mass. Thus, DT was 46% of the load, CH was 42%, and Au 12%. This case was included so that comparison could be made with the implosions in the next section, where a magnetic interlayer is included. The implosion history is shown in Figure 7. The minimum radius is a bit less than 0.5 cm at 129 ns. The modest compression and low ion temperature (17 keV at the bounce) translates into relatively small fusion yields.

**Table 4: Parameters for the D-T Shell with Au-coated CH Pusher**

$I_{max}$	$M_o[DT]$	$M_o[CH]$	$M_o[Au]$	$R_o$	$E_{D-T}$	$E_{\alpha-dep}$
20 MA	0.561 mg	0.523 mg	0.148 mg	3.0 cm	6.6 kJ	1.0 kJ

Although the fusion yield was not impressive at 20 MA, in the next section, we will see that yields go up very quickly with current for nested arrays of this type.

- **D-T Shell with Au-coated CH Pusher and  $B_z$  Interlayer:** The most complex (and promising) series of simulations involved concentric D-T and Au/CH shells (as in the previous section), but separated by a  $B_z$  interlayer. The axial magnetic field is embedded in the plasma at time  $t=0$ , such that it is uniform between the D-T and Au/CH shells and zero elsewhere. It may be difficult to produce this exact situation experimentally, but it has been shown, for example, that such a field configuration can be established between two wire arrays if they are twisted slightly in opposite directions<sup>1</sup>. The initial magnitude of the  $B_z$  interlayer was varied over a fairly large range, and it was found that (a) large values (i.e.  $B_z$  approaching a megagauss) resulted in a larger minimum radius and reduced neutron yields, (b) small values (i.e.  $B_z$  substantially smaller than 50 kilogauss) gave results similar to the zero- $B_z$  limit, (c) values of  $B_z$  near about 100 kilogauss gave the best yields. We will present results for  $B_z(t=0) \sim 100kG$ , for peak currents of 20, 40 and 60 MA. In all cases, as the implosion progresses, the axial field diffuses into (and eventually through) the D-T and Au/CH shells. In addition, when the Au/CH shell impinges on the underlying D-T plasma, the  $B_z$  interlayer is compressed until

it is comparable in magnitude to the azimuthal field  $B_\theta$  driving the implosion. Thus, the  $B_z$  interlayer ultimately becomes quite thin.

The pinch histories near peak implosion for the 20, 40 and 60 MA cases are shown in Figures 8-10. Compare the 20 MA case in Figure 8 with the 20 MA case in the previous section. The only difference in the initial conditions is the magnetic interlayer. Although the gross features of the pinch are similar in both cases (implosion time, minimum radius), the behavior of the ion temperature is completely different. In the present case, MeV ions are generated near the (low density) axis. The burn occurs away from the axis, where temperature and density are both favorable. The magnetic interlayer also has the property of confining the  $\alpha$  particles in the D-T region. The overall yield for the 20 MA case is reduced with the interlayer, but this is not surprising; the same value of  $B_z$  was used for all cases. 100 kG is nearly optimal for the 60 MA case, but should be scaled with current. Too large a field can interfere with the implosion. The yields vary strongly with current,

$$E_{D-T} = I_{max}^{4.5}$$

$$E_{\alpha-dep} = I_{max}^{4.5}$$

It is likely that the use of a constant  $B_z$  for all cases contributed to the strong increase in yield with current.

**Table 5: Parameters for D-T Shell with Au-coated CH Pusher and  $B_z$  Interlayer**

$I_{max}$	$M_o[DT]$	$M_o[CH]$	$M_o[Au]$	$R_o$	$E_{D-T}$	$E_{\alpha-dep}$
20 MA	0.561 mg	0.523 mg	0.148 mg	3.0 cm	5.2 kJ	3.6 kJ
40 MA	2.242 mg	2.090 mg	0.592 mg	3.0 cm	156.0 kJ	112.5 kJ
60 MA	5.045 mg	4.703 mg	1.332 mg	3.0 cm	803.0 kJ	531.0 kJ

In the three simulations, although the *peak ion temperature* does not vary by very much, the temperature in the vicinity of maximum burn increases with current. In addition, the ion density increases with current. The masses were scaled so that the bounce occurs at about 125 ns in each case. At 20 MA, a second bounce occurs, but it is very weak, and little D-T burn occurs. At 40 MA, the subsequent bounce is stronger, and the burn is more robust (but the second pulse of  $\alpha$ -particles is much less than the first). For the 60 MA case, the burn in the second pulse of  $\alpha$ -partivles is nearly as large as the first.

The histories of several important quantities from the 60 MA case are shown in Figure 11: electron temperature  $T_e$ , radiative cooling  $dE_{rad}/dt$ , azimuthal magnetic field  $B_\phi$  and axial

Z20-DT-CH.Au-Bz

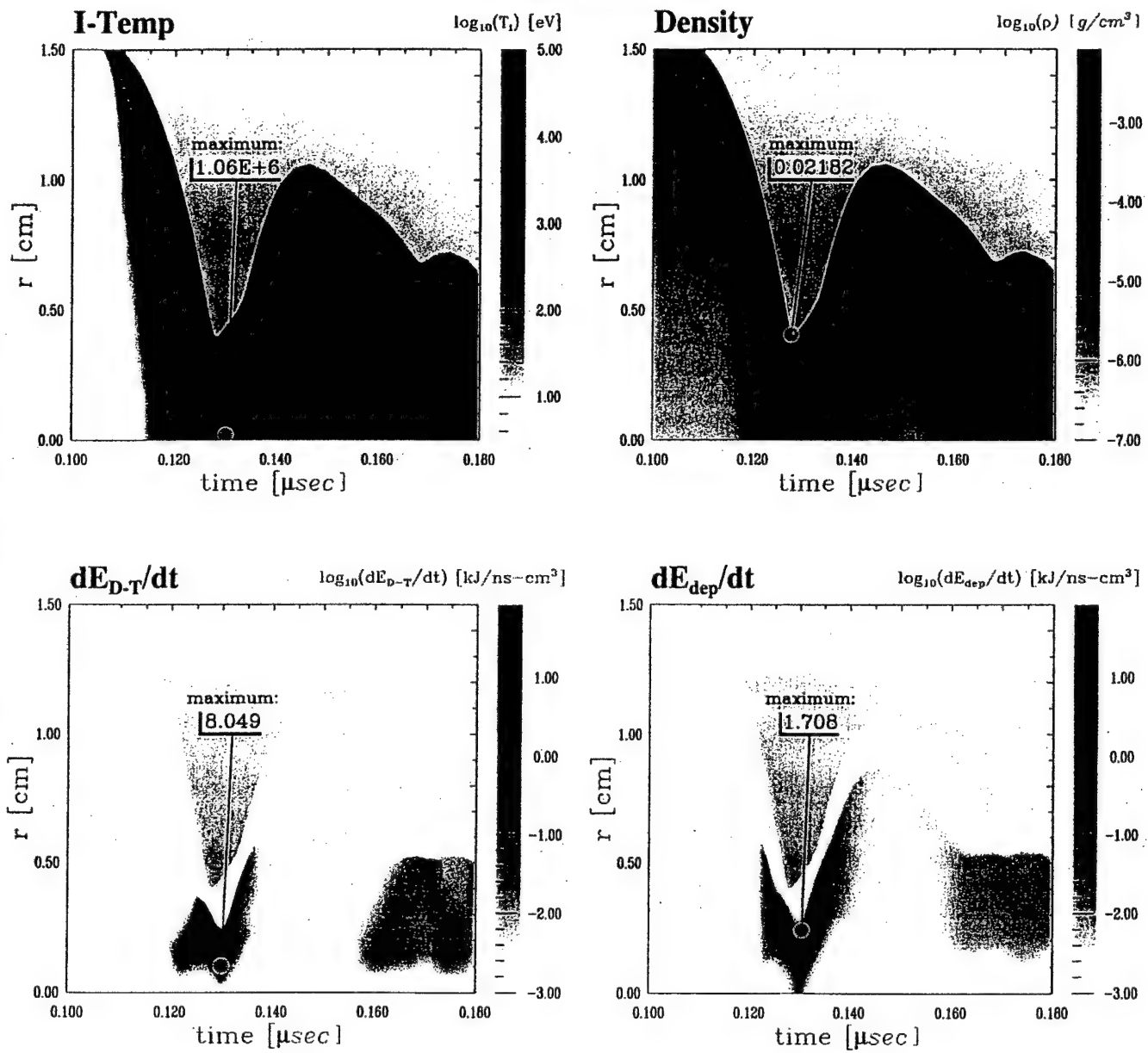


Fig. 8: Implosion history of 20 MA DT shell with Au-coated CH pusher and Bz interlayer.  $^{106}$

Z40-DT-CH.Au-Bz

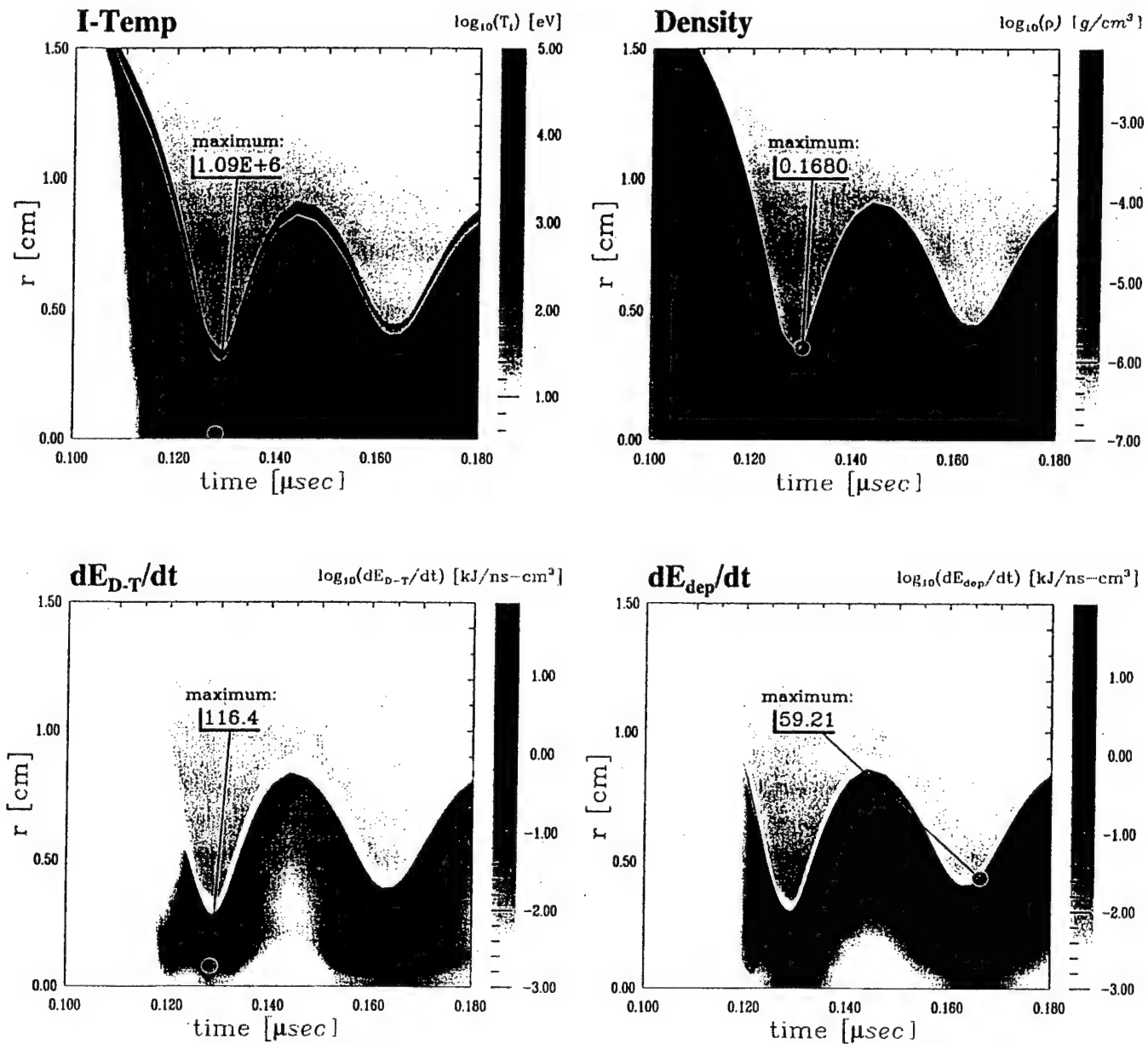


Fig. 9: Implosion history of 40 MA DT shell with Au-coated CH pusher and Bz interlayer.  $^{108}$

Z60-DT-CH.Au-Bz

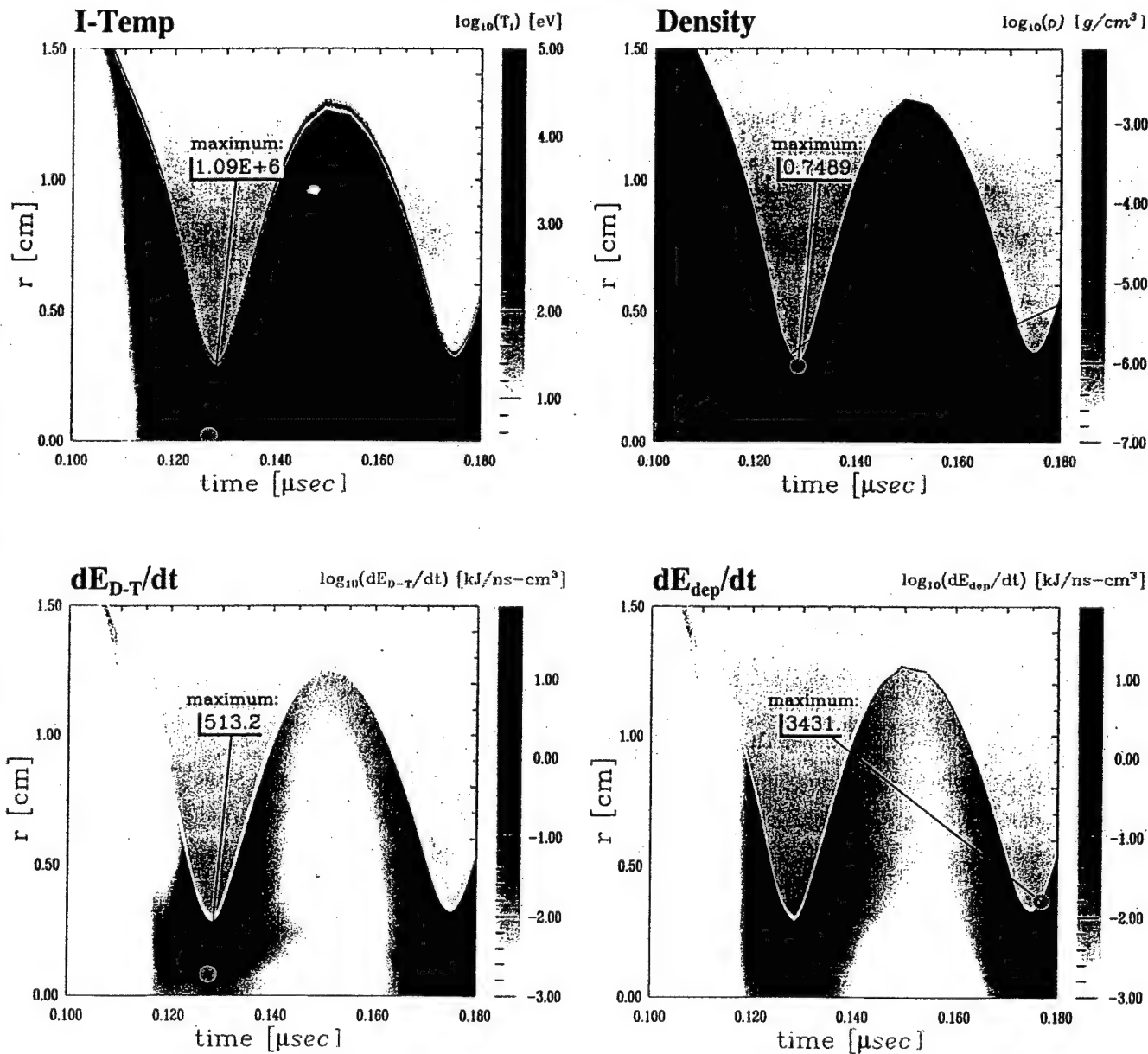


Fig. 10: Implosion history of 60 MA DT shell with Au-coated CH pusher and Bz interlayer. <sup>107</sup>

Z60-DT-CH.Au-Bz

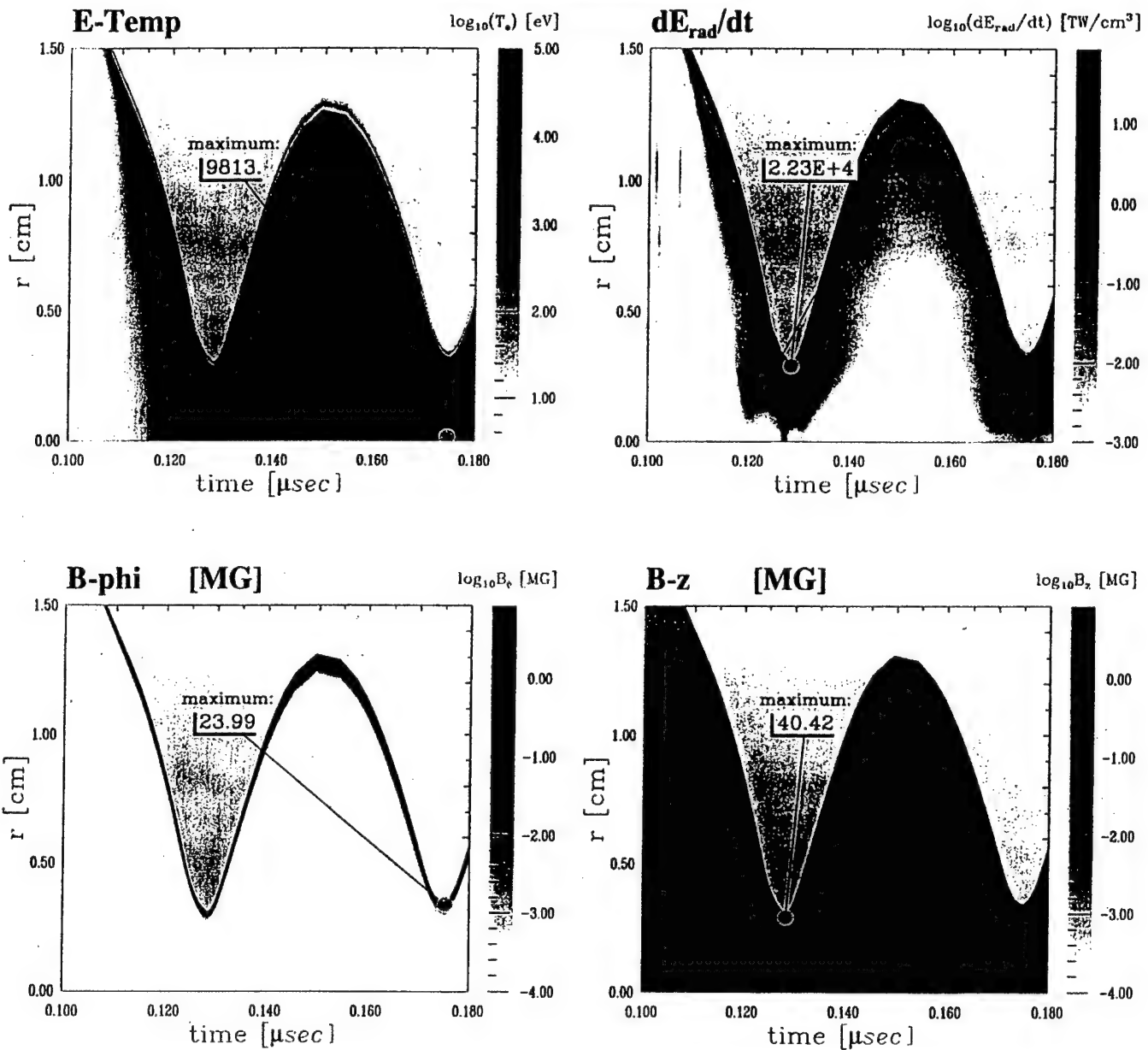


Fig. 11: Implosion history of 60 MA DT shell with Au-coated CH pusher and Bz interlayer. <sub>108</sub>

magnetic field  $B_z$ . As is characteristic of z-pinch implosions, the electrons remain substantially cooler than the ions. Since the electrons get hot only near the bounce phase, the radiation cooling maximizes at this time. There is also substantial cooling near the outside edge of the plasma; this is mostly sub-keV radiation from cool, dense plasma. It can be seen that the azimuthal field diffuses only through the outer portions of the plasma. However, a portion of the axial field diffuses into the D-T plasma and compresses during the bounce phase.

#### 4. CONCLUSIONS

We have investigated several load designs that might be employed to produce D-T fusion in proposed Z-pinch devices. Even the simplest design was capable of yielding in excess of 500 kJ at 60 MA. We have demonstrated that high currents ( $I \simeq 40$  MA) reduce  $\alpha$ -particle losses, but that they are not necessarily deposited where they will do the most good (in terms of increasing the burn fraction). The  $\alpha$ -particle deposition occurs mostly in cool, dense plasma near the outer edge of the pinch. D-T burn in these devices seems to be limited more by density (and the rapidity of the bounce) than by the ion temperature. At the highest currents, it was easy to obtain 100 keV ions near the axis. The yield was improved with a massive Au/CH pusher. It was improved still further when an axial magnetic interlayer was introduced. The magnitude of the initial  $B_z$  was critical, however; yields were degraded when the field was too large or too small relative to the 100 kG initial value employed in the simulations.

The load parameters (initial radii, array masses, etc.) were selected to give good energy coupling to the load, but were not optimized. It is likely that substantially improved fusion-like plasma conditions capable of radiating high-energy photons could be obtained after some adjustment of these parameters. In particular, the nested array simulations assign approximately equal masses to the inner (fuel) and outer (pusher) plasmas. However, the fusion yields do not reach breakeven (even at 60 MA). Substantially higher ion temperatures in the fuel and increased yields could be obtained by decreasing the fuel mass  $M_{D-T}$  and increasing the pusher mass  $M_{pusher}$  such that the total mass  $M_o = M_{D-T} + M_{pusher}$  is unchanged, but with  $M_{pusher}/M_{D-T} \sim 10$ . Simulations with optimized load configurations will be undertaken in the near future.

## REFERENCES

1. "Advanced Radiation Theory Support Annual Report 1998, Final Report", Radiation Hydrodynamics Branch, Naval Research Laboratory.
2. S. M. Gol'berg et al., "Compression, heating and fusion in Megagauss Z-Q pinch systems", in Dense Z-Pinches, ed. N.R. Periera, J. Davis and N. Rostoker (AIP, NY, 1989). *Phys. Rev. Lett.* **81**, 4883 (1998).
3. D. Duston, R. W. Clark, J. Davis and J. P. Apruzese, *Phys. Rev. A* **27**, 1441 (1983).
4. J. P. Apruzese, J. Davis, D. Duston and R. W. Clark, *Phys. Rev. A* **29**, 246 (1984).
5. J. P. Apruzese, *J. Quant. Spectr. Rad. Transf.* **34**, 447 (1985).
6. J. Davis, J. Giuliani, Jr., M. Mulbrandon, *Phys. Plasmas* **2**, 1766 (1995).
7. S. Glasstone and R. H. Lovberg, in "Controlled Thermonuclear Reactions", (Van Nostrand, NY, 1960), Chapt. 2.
8. R. E. Terry, (private communication).

# IV. Free Surface Boundary Conditions for Diffusive Radiation Transport in PRS Simulations

## I. INTRODUCTION

THE computation of radiative losses in a Z-pinch plasma radiation source (PRS) is often attempted through a radiation diffusion model, viz. the introduction of a radiation temperature in addition to electron and ion temperatures. Since the diffusion operator is parabolic one must establish either value or gradient boundary conditions on the radiation temperature at all exterior surfaces of the problem in order to obtain a unique and stable solution. The situation is more complex if a multi-group radiation diffusion picture is sought, for then each component radiation temperature must be assigned a boundary condition. Moreover if an experimental anchor is sought for these boundary values, then the task of measurement and the verification that each surface indeed meets the criteria for a component radiation temperature to make sense are not trivial pursuits.

The use of a free surface boundary condition is motivated by these sources of ambiguity in posing a clean radiation diffusion problem within the context of any given experiment. It is also motivated by the observation that Z-pinch implosions are rather good vacuum pumps, viz. the radiation source is generally surrounded by optically thin material for which radiation diffusion is very poor representation of the propagation. Assuming that radiation diffusion is at all accurate somewhere in the PRS interior, then in all cases a PRS will establish a surface where the natural drop in particle density will force a transition from radiation diffusion to radiation transport.

Stars present a similar density transition and indeed the classic Milne [1] problem forms the starting point for the methods developed here. However, unlike the star, a Z-pinch is often receiving energy from its driving circuit in that same domain where the boundary condition must be established. The result is a decoupling of the electron and radiation temperatures and as shown below the introduction of an additional parameter to the boundary condition statement. The specialization to a true cylindrical geometry also requires some modifications to the standard picture.

The following discussion will first pose the steady state radiation diffusion problem for the systems of interest. The formulation of the solution in cylindrical geometry will be presented and then the implementation of that solution within the Mach2 code will be developed and summarized. Our present implementation within Mach2 [2] rests upon two additional algorithms within the code's non equilibrium, single group radiation diffusion model. First is a calculation of the optical depth along a radial path from the Rosseland opacity. While the second is an isolation of the best steady state radiative energy density profiles

near the free surface that contains the transition from the diffusive to the transport limit, the "Milne" surface. The apparent radiation lost to the problem's exterior is then computed through the Milne condition as modified here. Finally a comparison among: the new model, diffusive radiation calculations done for standard boundary conditions, and more general radiation calculations done with a tabular collisional radiative equilibrium model, will be presented.

## II. THEORETICAL MODEL

The radiation diffusion approximation for transport in a material characterized by a Rosseland mean opacity  $\kappa_R$  and a Planck mean opacity  $\kappa_P$  can be written in plane, cylindrical, or spherical geometry ( $p=0,1,2$ ) as:

$$\frac{1}{c} \left( \frac{Du_R}{Dt} + u_R \nabla \cdot \mathbf{V} \right) - \frac{1}{r^p} \partial_r \left( \frac{r^p}{3\kappa_R} \partial_r u_R \right) = \kappa_P (u_e - u_R) \quad (1)$$

where  $u_R = aT_R^4$  represents the radiation field energy density,  $u_e = aT_e^4$  is the equivalent energy density at the ambient electron temperature,  $a = 4\sigma/c = 137.2$ , and  $r$  is the linear or radial coordinate as determined by the dimension index  $p$ .

When a multi-group formulation is used each radiation temperature, Rosseland, and Planck opacity extends over the domain of frequency groups. The equivalent *steady state* relationship for each group  $[u_k, \kappa_{R,k}, \kappa_{P,k}]$  is therefore written

$$-\frac{1}{r^p} \partial_r \left( \frac{r^p}{3\kappa_{R,k}} \partial_r u_k \right) = \kappa_{P,k} (u_{e,k} - u_k) , \quad (2)$$

with the source term  $u_{e,k} \equiv \mathcal{F}_k a T_e^4$  such that the fractions  $\mathcal{F}_k$  sum to one. These fractions are readily computed from Debye functions once the electron temperature and the frequency groups are specified. The following developments are specialized to only one frequency group, but the extension to many is straightforward.

### A. Dimensionless Representation

At the interface, denoted by  $\tau = 0$  in the figure below, marking a step in the material density down to zero and hence a step to zero for the opacities as well, we seek a "steady state" solution for the energy density profile, viz. a  $u_R : \frac{Du_R}{Dt} + u_R \nabla \cdot \mathbf{V} \equiv 0$ . Note that this doesn't require a state of null fluid motion, but only a situation where the ambient radiation density tracks with the advection and expansion or contraction of the fluid.

As indicated in the figure several dimensionless variables and parameters are useful here. First, using the Rosseland mean opacity to define the optical depth one has:

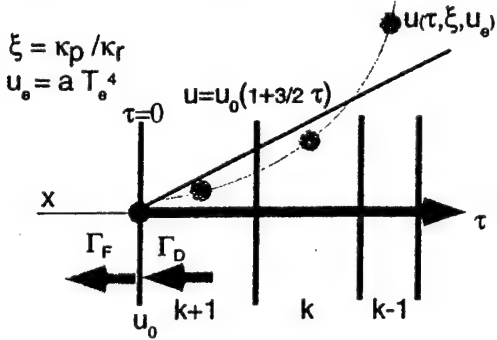
$\tau \equiv - \int_{r_b}^{r_e} \kappa_R dr$ . As a consequence the division of the diffusion equation by  $\kappa_R$  scales the spatial derivatives to be derivatives with respect to the optical depth. In the case that  $p > 0$  the factors  $r^p$  appearing in the diffusion operator can be written  $r^p \mapsto (\tau_m - \tau)^p$  with  $\tau_m = - \int_{r_b}^0 \kappa_R dr$  and  $r_b$  the boundary radius. When the source term on the RHS is scaled by  $\kappa_R$ , the ratio of Planck and Rosseland opacities appears,  $\xi \equiv \frac{\kappa_P}{\kappa_R}$ . Finally, let  $\Psi(\tau) \equiv \frac{u(\tau)}{u(\tau=0)}$  so that  $u_e \mapsto \Psi_e$  and the steady state radiation transport equation becomes

$$\partial_\tau ((\tau_m - \tau)^p \partial_\tau \Psi_p) = 3 \xi (\tau_m - \tau)^p (\Psi_p - \Psi_e) . \quad (3)$$

Here the opacities and ambient electron or fluid temperature are assumed to be constant in space, but either  $\xi(\tau)$  or  $\Psi_e(\tau)$  could be introduced through a series expansion in the neighborhood of  $\tau = 0$ .

### Simple Milne Condition:

$$2 \sigma T_{rad}^{-4} = (a c / 2) T_{k+1}^{-4} / (1 + 3/2 \tau_{k+1})$$



**Surface Conditions for the Milne Problem** — the transported flux must match on either side of the abrupt transition from diffusion to free propagation, viz.  $\Gamma_F = \Gamma_D$

As the problem stands the spatially constant electron temperature is fixed in the parameter  $\Psi_e$  and the relaxation rate for the radiation to meet this source temperature at the boundary is fixed in the parameter  $\xi$ .

### III. CYLINDER SOLUTIONS FOR $\Psi(\tau)$

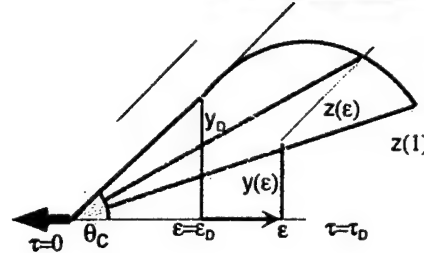
For  $p=1$  the steady state diffusion equation can be recast so that the radius is expressed in terms of an axial optical depth,  $\tau_m$ . The boundary is set at  $\tau=0$ , the parameters  $\Psi_e$  and  $\xi$  are defined above. As indicated in the figure a solution profile must be sought for a given set of interior energy densities, opacities, and grid points.

### A. Surface Boundary Conditions

The classic Milne problem is that of solving the diffusion equation above subject to the boundary conditions (i)  $\Psi_p(0) = 1$  because we require  $u(\tau) \mapsto u_0$  by construction, and (ii)  $\partial_\tau \Psi_p(0) = \frac{3}{2} \zeta_p$  because we require the free streaming flux  $\Gamma_F$  leaving the surface to be in detailed balance with the diffusive flux  $\Gamma_D$  percolating up to the surface. The factor  $\zeta_p$  is exactly one for planar geometry and varies slightly from that value in cylindrical or spherical geometry because the angular integral for the total flux leaving

to free space will depend on the local curvature ( $\tau_m$ ) and opacity. Whatever the radius  $r_b$ , a larger opacity will drive  $\zeta_p$  back toward unity. It is easy to see that for an optically thick planar case with  $\Psi_e = 1$  the linear form  $\Psi_0 = 1 + 3/2\tau$  is obtained [3].

## Geometry of exit rays for a cone at angle $\theta_C$ .



## A.1 Moment Integrals for a Long Cylinder

In contrast to the infinite half space planar problem, the cylinder problem requires integration over two independent angles back from the exit point of a ray that is confined to the surface of a cone with an apex angle  $\theta_c$  and an azimuth  $\phi$ . In reference to the preceding figure, the distance measure of a ray across the cylinder is denoted  $\epsilon$ , a fraction of the diameter,  $d$ . Two distances,  $z(\epsilon)$  and  $y(\epsilon)$  are necessary and sufficient to define the locus where the cone cuts the cylinder wall.

These quantities can also be written as fractions of the diameter and functions of  $\epsilon$

$$\frac{z}{d} = \sqrt{\left(\frac{\epsilon}{\epsilon_d} - 1\right)\epsilon}, \quad \frac{y}{d} = \sqrt{(1 - \epsilon)\epsilon}, \quad (4)$$

with  $\epsilon_d = \cos^2(\theta_c)$  the diameter fraction corresponding to the nearest intercept distance from the cone to the cylinder, viz. the rays from the apex of the cone to the cylinder wall which lay in the plane that cuts the cylinder at a right angle, the *normal plane*.

In order to calculate the location of the intercept point of the cone and the cylinder at any azimuth  $\phi$ , simply move a distance "y" in the normal plane and a distance "z" axially along the cylinder wall. The limits on such distances are  $z(1) = d \tan(\theta_c)$  and  $y(\epsilon_d) = d \cos(\theta_c) \sin(\theta_c)$  with the other limits zero. Expressing the distance along the cone to the cylinder wall as  $\epsilon_w(\theta, \phi)$ , this quantity is seen to be,

$$\epsilon_w(\theta, \phi) = \frac{\cos^2(\theta)}{1 - \sin^2(\theta) \sin^2(\phi)}, \quad (5)$$

and the attenuation factor needed for the radiation moments is then

$$\exp -\tau_d \epsilon_w(\theta, \phi) / \cos(\theta). \quad (6)$$

The required moments are just the radiation flux  $C_1$  and the intensity  $C_0$ . In the planar case the ratio of these quantities is just 1/2, but it will deviate slightly from that for a cylinder of optical depth  $\tau_d$  at its diameter. The required integrals are given by

$$C_1 = 4 \int_0^{1/2\pi} \int_0^{1/2\pi} \sin(\theta) \cos(\theta) (1 - e^{-\frac{\cos(\theta) \tau_d}{1 - \sin^2(\theta) \sin^2(\phi)}}) d\phi d\theta$$

$$C_0 = 4 \int_0^{1/2\pi} \int_0^{1/2\pi} \sin(\theta) (1 - e^{-\frac{\cos(\theta) \tau_d}{1 - \sin^2(\theta) \sin^2(\phi)}}) d\phi d\theta \quad (7)$$

and it is easy to see that at large  $\tau_d$  the ratio  $C_1/C_0 = 1/2$ . The general integration has been evaluated numerically to form the gradient condition  $\Psi'_0(\tau_d)$ . The range of variation with optical depth is considerably greater for the two moments individually than for their ratio. Over three orders of magnitude in optical depth, the ratio varies by about ten percent.

#### A.2 Representations for the gradient

Unlike the planar case the gradient condition at the outer boundary ( $\tau = 0$ ) is itself dependent on the optical depth,  $\tau_d$ . To evaluate the boundary gradient, one uses the optical depth of a diameter  $\tau_d$ , viz. twice that to the axis, let

$$x = \log_{10}(\frac{1}{2\tau_m}).$$

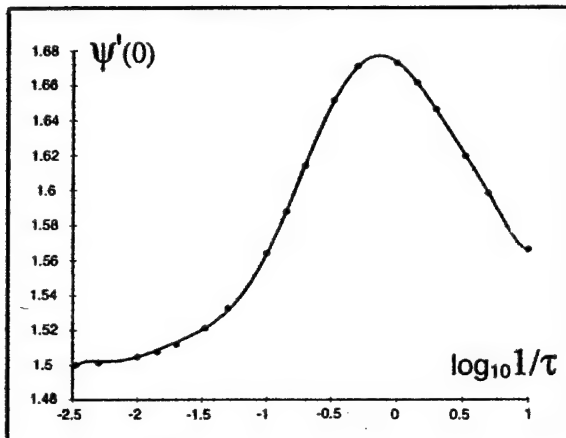
The net effect is to compute a variable Eddington factor only for the surface where the Milne condition is to be applied [4]. The moments are not known analytically but a numerical integration is very well represented by the following Horner polynomial

$$\begin{aligned} \Psi'_0(x) = & 1.673264473 + (-.0529613586 + \\ & (-.176519537 + (.14436233 + (.12020928 + \\ & (-.145075824 + (-.1065219668 + (.0373728221 + \\ & (.05231848514 + (.01753109065 + (.002301232639 + \\ & (.0000536308265 - .00001037472569x) \\ & x)x)x)x)x)x)x)x)x)x)x)x)x)x) \\ (8) \end{aligned}$$

as shown in the following figure. Here the discrete points represent the numerical moment calculation for an isotropic source, while the smooth curve is the polynomial representation. The dynamic range of over a factor of a thousand

in optical depth will cover the domain typical of pinch calculations. The expected planar limit is recovered for large optical depth, while a peak in the gradient occurs for optical depths of order one.

#### Boundary Gradient for a Cylinder



#### B. Solution Profiles

For the cylinder a steady state solution  $\Psi_1$  involves Bessel functions of complex argument. Each term is a separately real linear combination of  $Y_0, J_0, J_1, Y_1$ .

$$\begin{aligned} \Psi_1(\tau, \xi, \tau_m) = & (1 - \frac{Y_1(-i\mathcal{R}) J_0(-i\mathcal{R}(1 - \tau/\tau_m))}{\mathcal{E}} - \\ & \frac{J_1(i\mathcal{R}) Y_0(-i\mathcal{R}(1 - \tau/\tau_m))}{\mathcal{E}}) \Psi_e \\ & + \frac{Y_1(-i\mathcal{R}) J_0(-i\mathcal{R}(1 - \tau/\tau_m))}{\mathcal{E}} + \\ & \frac{J_1(i\mathcal{R}) Y_0(-i\mathcal{R}(1 - \tau/\tau_m))}{\mathcal{E}} \\ & - \frac{Y_0(-i\mathcal{R}) J_0(-i\mathcal{R}(1 - \tau/\tau_m))}{\mathcal{E}\mathcal{R}} + \\ & J_0(i\mathcal{R}) Y_0(-i\mathcal{R}(1 - \tau/\tau_m)) i\tau_m \Psi'_0(\tau_d) \\ & \mathcal{R} = \tau_m \sqrt{3\xi} \\ & \Psi'_0(\tau_d) = \frac{3}{2}\sigma \\ (9) \end{aligned}$$

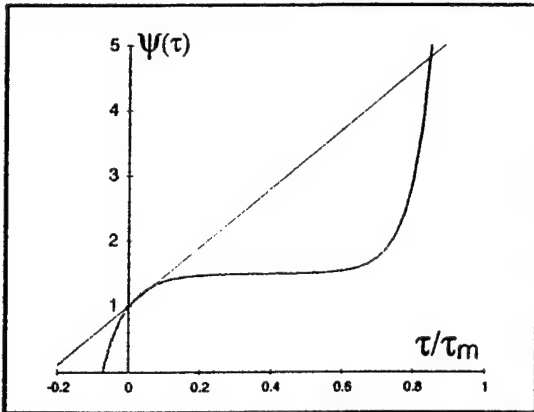
The same terms appear as for the planar case  $\Psi_0$  but are combinations of the hyperbolic functions  $\sinh(\tau\sqrt{3\xi})$  and  $\cosh(\tau\sqrt{3\xi})$ .

The next figure illustrates a typical cylinder solution for a modest axial optical depth and typical order of magnitude

opacity ratio. The cylinder solutions are a bit less sensitive to the  $\Psi_e$  but still show the same critical value behavior in  $\xi$

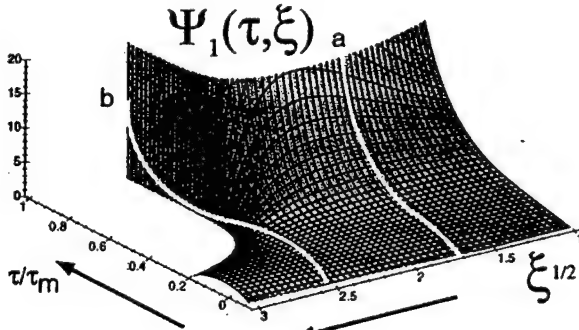
### Cylinder Solutions:

$$\xi=9, \tau_m=3, \Psi_e=1.486, \Psi'(0)=1.63$$



or  $\Psi_e$ . For the cylinder functions values of  $\Psi_e$  lower than about 1.2 will retain a monotone profile for all reasonable values of  $\xi$ . Once  $\Psi_e$  increases a domain of  $\xi$  values will exist for which no steady state solution is possible. In this case for example, if  $\Psi_e$  were increased by even one part in a thousand the solution would be forced negative near the axis. Such unphysical behavior could be changed only by a sink on the axis to drain the energy forced out of the electron fluid by the coupling term.

This critical  $\xi^*$  behavior at fixed  $\Psi_e$  is illustrated as a sort of moving "sink hole" in plots of  $\Psi_1(\tau, \xi)$  as a surface, as shown in the figure above. There  $\Psi_e=1.5$ , slightly larger than in the figure above. In response, the very stiff sloped region has moved in to about  $\xi = 6.25$ . Further increases in  $\Psi_e$  drive this feature, essentially unchanged, to lower  $\xi$  domains. On the other hand lower  $\Psi_e$  values (near one) will move the feature to higher  $\xi$  values and tend to admit the fairly stiff gradient solution over a larger  $\xi$  domain.



Cylinder Solutions at  
 $\tau_m=3.0, \Psi'(0)=1.63$  and  $\Psi_e=1.5$   
 ("a,b" are fitting cases, see text.)

In applying these solutions to the establishment of a boundary value for  $u_e$  it is useful to resolve the location of critical  $\Psi_e^*$  for the expected ranges of  $\tau_m$  and  $\xi$ , but not absolutely necessary. If the solution on the interior of the grid evolves to a shape like case "b" in the figure be-

low, then the fit of  $\Psi_e$  may be more delicate compared to a solution profile like that in case "a" but practically the strong exchange term for large  $\xi$  will be balanced by time dependent contributions and change the profiles.

In either case a sample of at least two interior pairs  $(u_i, \tau_i)$  is required to determine a single  $\Psi_e$  value for a profile because of the very flat character of the solution surface in  $\xi$  near the boundary for a wide range of  $\Psi_e > 1.3$ .

### IV. A SOLUTION ALGORITHM FOR $\Psi_e$

Using the general Bessel function profile, we need "matrix elements" constructed from the two real, linearly independent components of the solution, viz.

$$Q_k \equiv \frac{Y_1(-i\mathcal{R}) J_0(-i\mathcal{R}(1 - \tau_k/\tau_m))}{\mathcal{E}} +$$

$$\frac{J_1(i\mathcal{R}) Y_0(-i\mathcal{R}(1 - \tau_k/\tau_m))}{\mathcal{E}},$$

$$Q'_k \equiv \left( -\frac{Y_0(-i\mathcal{R}) J_0(-i\mathcal{R}(1 - \tau_k/\tau_m))}{\mathcal{E}\mathcal{R}} + \right.$$

$$\left. \frac{J_0(i\mathcal{R}) Y_0(-i\mathcal{R}(1 - \tau_k/\tau_m))}{\mathcal{E}\mathcal{R}} \right) i\tau_m \Psi'_0(2\tau_m),$$

and,

$$\mathcal{E}(\tau_m) = Y_1(-i\mathcal{R}) J_0(i\mathcal{R}) + Y_0(-i\mathcal{R}) J_1(i\mathcal{R}), \quad (10)$$

evaluated at the known arguments  $\tau_k$  where solution grid points lay and the local values of  $\tau_m$  and  $\xi$ . For points near the axis, these functions are very large, so that most profile data in a simulation will be easily covered by small  $\tau$ . Recalling that  $\Psi_e = u_e/u_0$ , we may obtain a best fit to the diffusion profile at the set  $\{\tau_k\}$  by solving the linear relations:

$$1 + Q_k(1 - \Psi_e) + Q'_k = \frac{u_k}{u_0} \equiv \Psi_e \frac{u_k}{u_e}, \quad (11)$$

at several points to obtain:

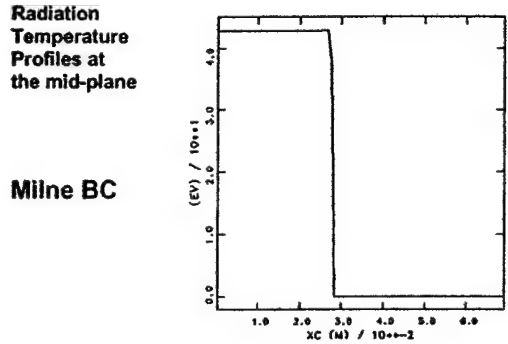
$$\Psi_{ek} = \frac{1 + Q_k + Q'_k}{\frac{u_k}{u_e} + Q_k}. \quad (12)$$

From the figures above, a set  $\{u_k, \tau_k\}$  which are very flat in space will force the solution toward the critical value  $\Psi_e^*$  at any given  $\xi$ . On the other hand, very stiff slopes in the  $\{u_k, \tau_k\}$  will imply a  $\Psi_{ek}$  value nearer to one. If the  $\Psi_{ek}$  are distinct the average of the two nearest the edge is taken. Two interior  $\{u_k, \tau_k\}$  are required to sense the local slope of the function in any case.

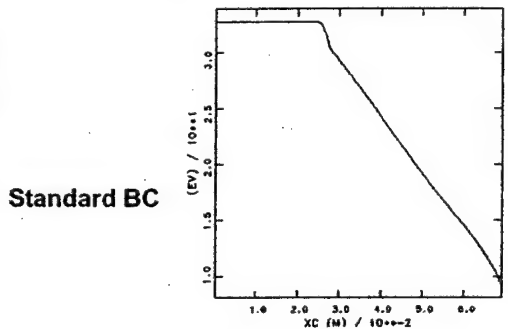
#### A. Domain Splitting

As implemented in Mach2 the solution domain for the radiation temperature or energy density is split into two subdomains. As illustrated below for a case of standard boundary conditions (viz.  $T_R$  fixed at the outer radius) and a similar case with free surface Milne boundary conditions, the natural break point for a global solution is seen to be

correctly "sensed" by the calculation of a critical or trigger optical depth. Once the radiation moves from the diffusive to the free streaming domain, the concept of a radiation temperature is invalid, so the code variable is just set to zero there for the Milne case. The free surface condition now ties the radiation temperature to the local electron temperature at the surface.

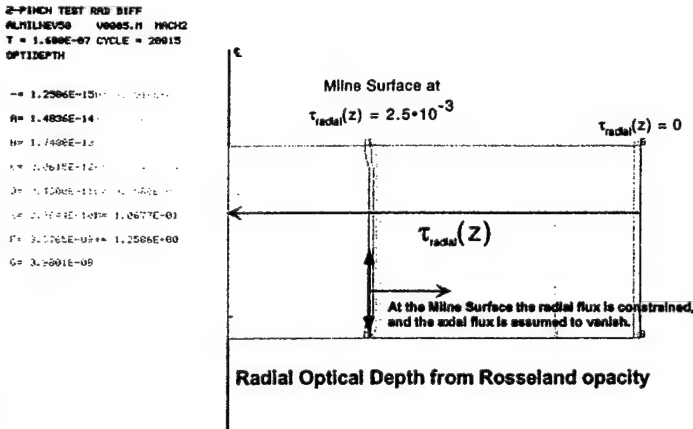


Milne BC profile is "hotter", but breaks at the point where the standard profile abruptly changes the slope.



Test case for a 3 cm radius, 3 cm long, 50 mg Al load driven by 45 MA peak current.

As developed in Mach2 the search for the free surface boundary will typically show the behavior in the figures below. A trigger optical depth of 0.0025 here defines a surface emission between contours "K" and "L" and all radiation diffusion is turned off outside this boundary. As indicated



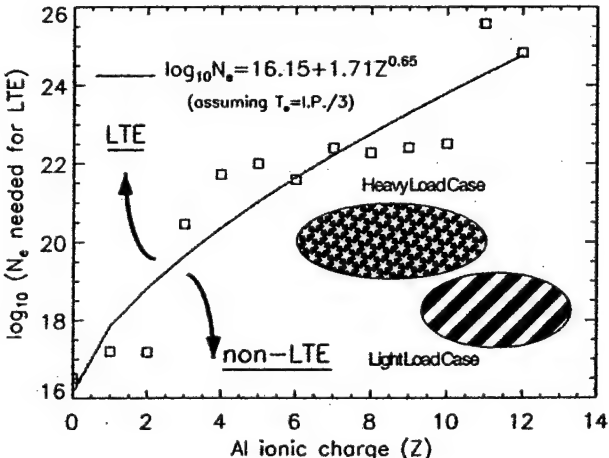
the radial profile is examined for the proper value of  $\Psi_e$  at

each axial location and an assessment of axial transport is not done.

The approximation is not wholly satisfactory but insofar as (i) the axial variations are partially incorporated in the surface integral shown above and (ii) the axial transport tends to wash out the radiation field variations, it can be used here. Additional accuracy could be obtained by using an axial moving average in the model parameters:  $T_e$ ,  $\xi$ , and  $\tau_m$ .

### B. Comparative Energy Loss

The comparisons of energy loss or radiative yield examined here are done with an aluminum material model equipped with the recently advanced Lee-More-Desjarlais [5] resistivity. Using Al as a test material has the advantage of commonality with the radiation databases of other methods like the tabular CRE and the ready availability of modern "Sesame" transport tables for Mach2. The yield results are calculated at a 3 cm length and 3 cm initial radius for two load masses: 3 mg driven by a peak current of 15 MA, and 50 mg driven by 45 MA.



Transition Boundary to LTE Populations for Al  
(a necessary condition for radiation diffusion)

On the other hand Z-pinch implosions in light materials such as Al do not remain optically thick during the later stages of the run down phase. In fact the case just cited has experienced an erosion of optical depth from over 100 at the axis early on to only 1.26 at the time of the profiles examined above. As shown in the figure above, the general criteria for validity of radiation diffusion are not well met in Al Z-pinch implosions. Necessary and sufficient conditions arise for the diffusion method when optical depths are large and electron populations are in LTE.

For the tests made here the light load tends to get so thin that radiation diffusion is nowhere valid and even the surface boundary condition will move its trigger level all the way to the origin. Under such conditions only the yield up to that point is meaningful. The problem can be avoided by lowering the trigger optical depth to match the density change as the load mass drops, but the small optical depths are an important clue that the domain of mathematical application for the diffusion method has far exceeded the domain of physical viability. An even more robust tech-

nique is to evaluate both the optical depth and the radially integrated line density, using the later as a trigger value for the surface boundary condition. When the opacity weakens at higher pinch temperatures upon implosion, the line density remains a relatively constant value. The Milne condition can then be applied at a fixed fraction of the axial line density, using the local values of opacities to set the parameters in the algorithm of Eq. 12. Such a method is potentially misleading however if attention is not paid to the optical depth and LTE criteria shown above in order to justify the radiative diffusion approximation.

In principle, it is also possible to then hold the radiation field to that from an appropriate thin emission model in the exterior regions, but that is beyond the scope of the work here.

Table I. Comparative Yields

Mass	$Y_{TCRE}$	$Y_{MILNE}$	$Y_{STND}$
mg	MJ	MJ	MJ
3	5.7	2.0	0.48
50	8.4	3.2	0.23

As is apparent in the table of yields from a 3 cm long PRS placed at a 3 cm radius, the present free surface condition comes much closer to getting the tabular CRE yield [6] than does the standard boundary condition with a radiation temperature set at the outer boundary. The light and heavy test pinches were driven with 15 MA and 45 MA, respectively, to obtain a 200 ns time to peak compression. The calculations were resolved on dense and sparse meshes and run in an Eulerian mode within Mach2. Mild perturbations in density were introduced to give a small amount of Rayleigh Taylor structure as a test of the surface condition algorithm.

Density perturbations and the pulsating delivery of energy to the Milne surface through ohmic heating generally make the gradient in radiation temperature at the Milne surface periodically show a positive slope with radius — on 10-20 ns timescales. The deposited energy will then relax away and a monotone negative gradient will be reestablished and prevails most of the time.

## V. CONCLUSIONS

The present method has several advantages over the conventional formulation for a radiation diffusion problem in a PRS model. First, it frees the method of any requirement to know the radiation temperature at the boundaries of the problem, viz. a radiation temperature need not even exist there for the problem to remain well defined. Second, it brings the radiation diffusion technique into reasonable congruence with the definitive tabular collisional radiative equilibrium method. Third, the extension to multigroup representations is completely straight forward and offers therefore a sequential path of improvement with respect to describing experimental yields. Fourth, the use of an explicit optical depth provides a means of assessing the general viability of the radiation diffusion method as a *physics*

statement. The domain of accurate physics represented by the radiation diffusion approximation is generally smaller than the domain of mathematical convergence.

## REFERENCES

- [1] E. A. Milne, *Phil. Trans. R.S.L. Series A* **223**(1923),p.201, *Monthly Not. R.A.S.* **81**(1921),p.361
- [2] R. E. Peterkin, M. H. Frese, C.R. Sovinec, *JCP* **140** 148 (1998).
- [3] Ya. B. Zel'dovich, Yu. P. Raizer, *Physics of Shock Waves and High Temperature Phenomena*, Academic Press, 1966 **V1**, p. 160.
- [4] G. C. Pomraning, *JQSRT* **27**(5),p.517,1982,
- [5] M. P. Desjarlais, *private communication*, *Contrib. Plasma Phys.* **41** 2-3,p.267,2001
- [6] J. W. Thornhill, *POP* **8**(7),p.3480,2001

## V. MODELING ENHANCED ENERGY ABSORPTION IN LONG CURRENT-RISETIME SATURN EXPERIMENTS

### I. Introduction

Two phenomena that significantly impact the x-ray performance of z-pinch loads are separately being investigated at Sandia, Imperial College, and NRL. One, at Sandia and Imperial College, concerns the dynamics by which wire loads are vaporized and ionized by generator currents. This dynamics establishes the initial plasma conditions for the pinch run-in dynamics. Recent studies have shown that a precursor plasma is created on axis along with a prefill plasma that occupies the space between the wire cores and the precursor plasma prior to the onset of the pinch implosion. Because of this prefill, deviations from 0-D shell-like implosions have been both predicted and observed. The second factor affecting the implosion dynamics, which is being studied at NRL, concerns the generation of magnetic flux tube energy within the plasma during run-in [L. I. Rudakov, et. al., *Phys. Rev. Lett.*, **84**, 3326 (2000); A. L. Velikovich, et. al., *Phys. of Plasmas*, **7**, 1 (2000)]. This energy buildup, which occurs in addition to  $j \times B$  energy inputs, is postulated to occur as a result of Rayleigh-Taylor instability growth at the surface of the pinch. Its introduction into the implosion dynamics is needed to account for both an observed added load impedance during run-in and the large total x-ray outputs that have been observed during stagnation in recent z-pinch experiments. This output energy cannot be accounted for by the input  $j \times B$  work. In Saturn experiments with aluminum arrays, this enhanced output showed up as subkilovolt x rays from copious L-shell emissions. One of the main purposes of the analysis described here was to investigate prospects for diverting more of the flux tube energy into the K shell. A new shot plan for Saturn was devised that is predicted to accomplish this goal.

In the first part of this section, a model of flux tube energy generation is developed and applied in a 1-D hydrodynamics analysis of x-ray and current data taken in four series of Saturn aluminum array shots. The data was obtained when the Saturn generator was operated in a long current risetime mode. Originally, the x-ray spectral data from these shots had been analyzed for the purpose of inferring the average 1-dimensional temperature and density gradient structures of the assembled pinches. These gradients were required to replicate (to within a reasonable approximation) a number of prominent features of the K-shell spectra. Because only K-shell data was analyzed, an accounting could only be made of the plasma mass that was radiating in the K shell. Also, the analysis had to be based on certain assumptions about the general shape of the gradients. The degree to which these assumptions could be validated by 1-dimensional hydrodynamics modeling needed to be investigated. Before this investigation could be made, however, the problem of replicating the observed energetics of these Saturn shots had to be addressed. The reconfiguration of Saturn from a short to a long current risetime machine had produced significant increases in total x-ray output by factors of 2 to 4.

Because  $j \times B$  forces cannot account for this added energy input, another mechanism for supplying it to the pinch had to be sought. A recently hypothesized magnetic flux tube mechanism for inputting this energy had to be employed within the 1-D hydrodynamics calculations. However, to model the experiments, a phenomenological extension of the flux-tube model was needed. This model extension significantly reduced the energy deficit but did not entirely remove it. The model

was developed and applied in two steps. In the first step, several free parameters in the model were determined by seeking the best agreement between the calculations and data, using data from the most 1-D-like of a series of Saturn aluminum wire array shots in which only the wire number had been varied. In the second step, these parameters were then held fixed and the model was evaluated by comparing its predictions to data from the other three series of Saturn shots in which the aluminum load mass, length, and radius had been separately varied. The agreement between model calculations and experiment was generally found to be quite good. The calculations also suggested a reason for the low K-shell yields and high L-shell yields and led, in the third part of this section, to a proposal for a new series of shots. When hydrodynamics calculations based on the benchmarked flux tube model were carried out for these new series of shots, they predicted significant increases in K-shell emissions with corresponding decreases in L-shell emissions.

## II. Flux Tube Model Development

Z-pinch implosions conducted on the long current-risetime version of Saturn give the wires longer times to vaporize and to ionize prior to their implosion than on the short risetime version of Saturn. Consequently, it is easier for the wire plasmas to merge and to implode as a shell rather than as a random collection of individual plasmas. One of the potential drawbacks of such implosions, however, is that they are carried out from larger initial radii than implosions with shorter current risetimes. Nevertheless, in the Saturn experiments, imploding from radii that were  $\geq 2$  cm turned out to have benefits and no serious drawbacks; namely, the x-ray pulse risetimes and pulsedwidths and the K-shell yields were found to be comparable to those seen in shorter risetime implosions, but much greater amounts of generator energy were also found to be coupled to the loads. Consequently, larger mass loads could be effectively imploded from the larger radii for the same peak current drive.

Because Saturn has an ample supply of current, a sufficient number of wires could be utilized at the 2 cm and larger radii to keep interwire gap spacings small. The small gap spacings allowed plasma shells to form prior to implosion. How gap spacing specifically influenced the shapes of the power pulses was investigated in a series of shots in which only wire number was varied. These experiments were carried out using aluminum wire arrays that were 2 cm long, 4 cm in diameter, and contained  $616 \mu\text{g}/\text{cm}^2$ . These arrays had nearly twice the mass as the arrays that were used in a series of variable wire-number (variable gap-spacing) experiments that had been performed on Saturn when it was operated in a short current risetime mode ( $\sim 70$  ns). Thus, the same current could now be used to vaporize and implode twice the mass as in the earlier experiments, and the implosions produced approximately the same K-shell yields as were obtained in the earlier experiments. These factors may have been instrumental in wire number behavior that was seen for the first time; namely, that peak power slightly declined rather than increased in going from 180 to 282 wires.

Because the 180 wire shot (#2693) produced the highest peak K-shell power with the narrowest pulsedwidth, i.e., because it showed the closest 1-D-like behavior, it was nominally chosen to benchmark the flux tube model. Shot 2693 produced 53 kJ of K-shell radiation, 24 kJ in the main pulse. It also was measured to produce an astonishing 1320 kJ of total x-ray output, of which 580 kJ was in the main pulse. The K-shell pulsedwidth was 7 ns, and the total x-ray pulsedwidth was 9.6 ns (see Figure 1). Zero-D calculations showed that only  $\sim 240$  kJ of kinetic energy was generated in the implosion, far from the amount of energy that had to be supplied

to the pinch for it to radiate in excess of 1 MJ. This shot choice for benchmarking was nominal since, when the shot was repeated, (shot #2636), it produced only 629 kJ of x rays, with 68.6 kJ coming from the K-shell in a pulse that now had only a main pulse and no late-time foot. Note, however, that another shot (#2706) was carried out that was identical with shot 2636 except that the length of the array was increased to 2.5 cm. Its peak x-ray powers were comparable to those of shot 2636, but, unlike shot 2636, the total and K-shell x-ray pulses of shot 2706 had prominent feet following their main pulses (see Figure 2). Such extreme shot-to-shot variability may be the result of variability in the initial conditions that are set up and in the amount of flux-tube energy that is generated in the experiments. Since no guidance on initial conditions was available from the ongoing wire break-down investigations, a 100 zone, shell-like initial condition with only a small amount of pre-fill was chosen for all of the 1-D calculations described in this report.

The magnetic flux tube model describes the buildup of magnetic field energy within the imploding pinch as the consequence of the growth of surface bubbles (and spikes) caused by the Rayleigh-Taylor instability. In the context of a 0-D model, a plasma shell of mass,  $m[\mu\text{g}/\text{cm}]$ , and radius,  $r(t)[\text{cm}]$ , is accelerated inward by the current,  $I[\text{A}]$ , flowing between the cathode and anode:

$$m \frac{d^2r(t)}{dt^2} = \frac{1}{2} \frac{\partial L}{\partial r} I^2 = -\frac{\mu_0}{4\pi} \frac{I^2}{r}.$$

The inductance,  $L(r(t))$ , appearing in this equation, is the sum of the constant diode inductance,  $L_{\text{diode}}$ , and the changing load inductance:

$$L(t) \cong L_{\text{diode}} + \frac{\mu_0 \ell}{2\pi} \ln \left( \frac{r_{rc}}{r(t)} \right),$$

where  $r_{rc}$  is the radius of the return current path and  $\ell$  is the length of the wire array. The growth in flux tube energy impacts the acceleration of the load indirectly through its influence on the external current,  $I$ , since it acts as if it were an added impedance in the generator circuit. This impedance does not enter the circuit equation as an added inductance so it must be put in as an extra resistance,  $R_{\text{flux-tubes}}$ , in the circuit equation:

$$V(t) = (R_{\text{diode}} + R_{z\text{-pinch}} + R_{\text{flux-tubes}})I + \frac{d(LI)}{dt},$$

where  $R_{\text{diode}}$  is the resistance of the diode and  $R_{z\text{-pinch}}$  is the resistance in the z-pinch load. The resistance to current flow posed by the growth in flux tube energy was determined in Physical Review Letters, 84, 3326 (2000) to depend on the load parameters as follows:

$$R_{\text{flux-tubes}} \sim \frac{I[\text{MA}]\ell[\text{cm}]}{\sqrt{m[\mu\text{g}/\text{cm}]r[\text{mm}]}}. \quad [\text{Ohms}]$$

The proportionality numerical factor is of order one.

The flux tube model employed in the 1-D hydrodynamics calculations contains  $R_{\text{flux-tubes}}$  in its circuit equation with an undetermined proportionality factor. There are two other undetermined constants in the model. The  $I^2 R_{\text{flux-tubes}}$  energy that is generated during the run-in is stored and not dissipated as plasma thermal energy until the pinch begins to stagnate on axis. The time

at assembly at which this dissipation begins is the second of the undetermined constants. Finally, the time over which the stored energy is dissipated, which controls the rate of energy dissipation, is the third constant whose value had to be determined phenomenologically. The values for these constants were determined by trial and error, by adjusting their values until the best matchup with the x ray data from shots 2693 and 2636 was obtained. A fourth constant that multiplied the rate of L-shell radiation losses was also introduced into the hydrodynamics code, and its value was adjusted to best match the power output of shot 2636. It was introduced to compensate for the missing atomic level structure in the aluminum L-shell model that was used in the calculations.

The need to delay thermalization of the flux tube energy but not to delay its generation was seen when three cases were run. When both the generation and dissipation of the energy were undelayed, the K-shell power pulse risetime was much longer and the pulse more spreadout than was seen experimentally (see Figure 3). On the other hand, when both generation and dissipation were delayed, the implosion time was too short, the K-shell peak power was much too high, and the calculated power pulse had no foot (see Figure 4). All of these deficits were corrected when the flux tube energy generation was undelayed, while its dissipation was (Figure 5).

One other important benchmark was made. The voltage drive was determined so that the circuit model for the 1-D calculations reproduced the measured short-circuit current.

### III. Flux Tube Model Application

Shot 2636 was one in a series of five shots carried out on Saturn in which array radius and length were both fixed at 2 cm while array mass was varied by changing either the wire number or the wire size. The shot matrix for these experiments is shown in Table I. Note, as the array mass was increased from 328 to 1576  $\mu\text{g}/\text{cm}$  and the implosion times increased from 134 to 208 ns, that the change from 887 to 1050  $\mu\text{g}/\text{cm}$  did not produce a proportionate change in implosion times. This behavior may be associated with the hidden dependence of z-pinch experimental results on wire number and wire size, which cannot be modeled. However, aside from these hidden effects, there are well-defined trends in the data. The question that was investigated in this work was how well can the benchmarked flux-tube model replicate these trends?

As mentioned above, one of the critical features of the benchmarking of flux-tube energy modeling was the need to generate the energy during run-in but to delay its thermalization until assembly on-axis. The undelayed generation added to the load impedance in the circuit model and produced increases in the calculated implosion times. Thus, the first test of the flux-tube model was how well did the calculated implosion times agree with the measured times. Figure 6 shows the results of this comparison for the Table I shots.

The red lines in Figure 6 connect the experimental times of the shots listed in Table I. The greatest disagreement between measured and calculated times (which were determined in both cases as the time to peak K-shell emission) occurs for the load mass (616  $\mu\text{g}/\text{cm}$ ) against which the flux-tube model was benchmarked! However, the benchmarking was done primarily using shot 2693 and only nominally shot 2636. The four red implosion-time data points at 616  $\mu\text{g}/\text{cm}$  illustrate either the degree of experimental noise or irreproducibility or the degree of wire gap spacing dependence, which was fairly large. These times were obtained in a series of shots in which only wire number was varied. The four shots from which the implosion times in Figure 6 were taken are listed in Table II.

**Table I: Variable Mass Experiments** $r = 2\text{cm}, \ell = 2\text{cm}$ 

Shot #	Wire #	Array Mass ( $\mu\text{g}/\text{cm}$ )	Implosion Time (ns)	Total x-ray energy (kJ)	K-shell x-ray energy (kJ)	Total x-ray energy (main pulse) (kJ)	K-shell x-ray energy (main pulse) (kJ)
2640	150	328	134	777	51.2	334	20.1
2636	180	616	175	629	68.8	458	51.9
2637	180	887	183	736	47.3	382	26.6
2641	120	1050	184	845	39.2	546	21.2
2702	180	1576	208	1040	50.9	652	29.3

**Table II: Variable Wire-number Experiments** $r = 2\text{cm}, \ell = 2\text{cm}$ 

Shot #	Wire #	Array Mass ( $\mu\text{g}/\text{cm}$ )	Implosion Time (ns)	Total x-ray energy (kJ)	K-shell x-ray energy (kJ)	Total x-ray energy (main pulse) (kJ)	K-shell x-ray energy (main pulse) (kJ)
2636	180	616	175	629	68.8	458	51.9
2693	180	616	165	1330	62.9	496	23.5
2695	282	617	160	1060	60.4	-	-
2704	282	617	184	367	13	228	6.0

The large variation in Table II implosion times is accompanied by large variations in the amount of x-ray emission observed in these shots. Consequently, while the choice of parameters in the flux-tube model was made to replicate the implosion time and late time behavior of the K-shell x-ray pulse of shot 2693, it could not reproduce the total yield that was measured. It could, however, approximate the yields seen in shot 2636. This same choice of parameters was then found to closely match the observed implosion times of the other four mass-variation shots [Figure 6]. A further benchmark of the model was then carried out. Calculations of implosion times for the five Table I shots that were subsequently carried out in the absence of flux-tube energy generation were found to be in close agreement with the times obtained in Screamer calculations, which are also shown in Figure 6.

Other comparisons between the calculations and the variable-mass experiments were found to be qualitatively and quantitatively favorable. These are shown in Figures 7-10. The time evolution of the calculated K-shell energies for the five Table I shots are shown in Figure 7 and a comparison to the measured yields is made at the end of the time history, i.e., the measured yields are listed at the termination point of each curve. In three of the calculations, the yields continue to rise due to the fact that, in the calculations, the plasmas are stable, continue to be heated by flux-tube energy dissipation, and thus continue to radiate. Late time behavior is the one feature of 1-D calculations least expected to give meaningful comparisons with experiments involving unstable plasmas, especially in light of the large shot-to-shot variations that are possible (see Table II). However, the general yield trends and yield magnitudes seen in the data are replicated by the calculations. Shot 2636 had the greatest yield ( $\sim 70$  kJ) in both the experiment and the calculation, shot 2641, the least yield ( $\sim 40$  kJ), and shots 2640, 2637, and 2702 fell in between ( $\sim 50$  kJ).

The trends in the total x-ray yields that were seen and calculated also agreed well, with one exception (Figure 8). The calculations produced a steady increase in yields as a function of mass rising from  $\sim 180$  kJ for the  $328 \mu\text{g}/\text{cm}$  implosion to  $\sim 780$  kJ for the  $1576 \mu\text{g}/\text{cm}$  implosion. Experimentally, however, the lowest mass shot produced an anomalously high output of 777 kJ, while the yields for the other shots then rose steadily from 629 to 1040 kJ. The shot 2640 anomaly is similar to the anomalously large difference in total yields seen between identical shots (2636 and 2693) in Table II. This behavior may be related to differences in initial conditions that could be and were ostensibly set up in the two otherwise identical experiments. Note, finally, in Figure 8, that the calculations consistently under-calculated the amount of total yield. This may be related to deficiencies in the L-shell model. For lack of a complete level structure, a single multiplier on all L-shell emissions rates was employed. This robbed the calculations of the late-time feet that was seen on the experimental x-ray pulses and that was replicated on the calculated K-shell pulses for which there was a complete level structure.

A comparison between the measured and calculated K-shell x-ray power pulses is made in Figures 9 and 10. Observe that the calculated pulses are narrower, more intensely peaked, and more uniformly shaped and behaved than the experimental pulses. This behavior is expected since the plasmas in the calculations have complete azimuthal symmetry unlike those in the experiments. Moreover, the generation of flux-tube energy, which is postulated to be the end result of surface Rayleigh-Taylor instability growth, does not impair the symmetry in a 1-D calculation as it does in experiments. The late-time foot behavior seen experimentally is also more varied and chaotic than seen in calculations that utilize a fixed set of initial conditions. Nevertheless, there are points of similarity. The feet tend to be more sharply peaked and less extended in both calculations and experiments as the load mass gets smaller. In addition, the green curves in both figures, which correspond to the  $1050 \mu\text{g}/\text{cm}$  shot, show very extended, but not very pronounced feet. Finally, a pronounced foot reappears on the highest mass (black) experimental curve, and there is the hint of such a reappearance on the calculated black curve. This foot behavior, together with the steady increase in peak power seen both experimentally and in the calculations in going from the 887 to the  $1576 \mu\text{g}/\text{cm}$  implosions, both help to explain the fact that the  $1050 \mu\text{g}/\text{cm}$  implosion had the smallest K-shell yield both experimentally and in the calculations.

Because the shape of experimental power pulses is influenced both by wire size and the initial gap spacing between wires, the experimental gap spacings and two of the employed wire sizes are listed below the peaks of the power pulses in Figure 9. There is no theoretical counterpart to these

pulse broadening effects. They cannot be accounted for computationally. Thus, strict comparisons between the shapes of the calculated (either in 1-D or 2-D) and measured power pulses cannot be made. In attempting to interpret trends in experimental data, however, one cannot ignore these influences. Thus, for example, shot 2636 produced the highest peak power in the experiments but not in the calculations, but it also had, correspondingly, the smallest gap spacings and the smallest wire sizes of all the shots.

Comparisons between calculations and measurements in two other series of Saturn shots gave further support to the utility of the flux-tube model. In one series of shots, listed in Table III, the length of a  $616 \mu\text{g}/\text{cm}$ , 2 cm radius array was varied. In the other series, the array length was kept at 2.5 cm and radius variations were made along with concomitant mass changes. These shots are listed in Table IV.

**Table III: Variable Length Experiments**

$r = 2\text{cm}$ ,  $m = 616\mu\text{g}/\text{cm}$ ,  $\text{Wire\#} = 180$

Shot #	Array Length (cm)	Implosion Time (ns)	Total x-ray energy (kJ)	K-shell x-ray energy (kJ)	Total x-ray energy (main pulse) (kJ)	K-shell x-ray energy (main pulse) (kJ)
2636	2.0	175	629	68.8	458	51.9
2706	2.5	163	681	57.0	335	25.9
2701	3.0	175	617	48.1	353	27.3
2703	3.5	167	647	56.9	385	28.7

If the full length of an array can be ionized and imploded, then, as the length of the array is increased, its impedance will increase proportionately. Thus, in the variable length shots, one would expect the measured implosion times to increase as the array length increased. This basic effect was seen in the calculations, but not in the experiments (Figure 11). One must conclude that the full lengths of the arrays were not imploded in the experiments. This interpretation is consistent since, for example, the 2.5 and 3.5 length arrays had both comparable implosion times and comparable K-shell and total yields, whereas the calculations predicted that the K-shell yields would fall monotonically and the total yields would rise monotonically as the array length was increased (Figures 12 and 13). Thus, the experimental data suggests that the 3.5 cm length load imploded as if it were a 2.5 cm length load. Again, the calculated implosion times in Figure 11 are a better match to the data when flux-tube energy is included in the calculation than when it is not.

This interpretation of the variable length experiments carries over to the variable radius and mass shots (Table IV) since these shots were made with arrays of 2.5 cm length that may not have imploded in their entirety. This conclusion is suggested by the small but systematically higher implosion times (therefore higher impedances) that were calculated compared to those measured

(Figure 14). Otherwise, the calculations with flux-tube energy predict a steady rise in implosion times in accord with the data in contrast to a predicted fall when flux-tube energy is excluded from the calculation. These latter calculations also produce implosion times that disagree with the measured times by a larger amount than the calculations carried out with added flux-tube energy impedance.

**Table IV: Variable Radius & Mass Experiments**

$\ell = 2.5\text{cm}$

Shot #	Wire #	Wire Diam ( $\mu\text{m}$ )	Array Radius (cm)	Array Mass ( $\mu\text{g}/\text{cm}$ )	Implosion Time (ns)	Total x-ray energy (kJ)	K-shell x-ray energy (kJ)
2706	180	12.7	2.0	616	163	681	57.0
2699	164	12.7	2.2	561	167	765	59.3
2700	144	12.7	2.5	493	168	799	57.1
2705	144	20.3	2.5	1261	217	875	51.0

Under the ideal plasma conditions assumed in the calculations, K-shell yields in the Table IV experiments are predicted to increase as the array radius is increased (Figure 15). However, experimentally, by and large, this behavior was not seen. The K-shell yield did go up, as predicted, when the wire size and the array mass were reduced as in the 2.5 cm radius shots, however, not by the amount predicted. The reason is suggested by the three shots in which 12.7  $\mu\text{m}$  diameter wires were used. In these experiments, the initial interwire gap spacing was increased (as noted in Figure 14) as the radius was increased and simultaneously the array mass was decreased. As the gap spacing went from 0.7 mm to 0.8 mm, there was only a small increase in K-shell yield followed by a small decrease as the gap increased from 0.8 to 1.1 mm. The predicted yield increases from gains in  $\eta$  values were largely offset by the increases in gap spacings.

#### IV. Flux Tube Model Predictions

The overall agreement between flux-tube model calculations and experimental measurements supports the model's use in evaluating prospects for converting a larger fraction of the flux-tube energy into K-shell rather than L-shell x rays. To make this evaluation, the implosion velocities that were achieved in the Table I, III, and IV Saturn shots needed to be calculated, and two kinds of calculations are informative. Both can be carried out using a 0-D model of the long current-risetime Saturn generator. The first calculation is conventional because it ignores the generation of flux-tube energy; the second calculation includes this energy. When no flux-tube energy is generated, the implosions achieve the eta values shown in Figure 16. In this case, all but one implosion has an eta value in excess of three. By comparing these values to ones achieved in similar implosions that were made on the short current-risetime version of Saturn, one would conclude that the Table I-IV shots should have converted a substantial fraction of the input energy into K-shell x rays. However,

a considerable fraction of this input energy is non-kinetic, flux-tube energy. Its generation adds impedance to the circuit and, as seen in Figures 6, 11, and 14, this added circuit impedance acts to impede the implosion and to delay it. The eta values that one calculates when flux-tube energy is generated during implosion are shown in Figure 17. In these calculations, only the lowest mass implosion (shot 2640) makes it (and only barely) to  $\eta = 3$ . The much reduced eta values achieved by the implosions in these calculations correlates with the poor K-shell conversion efficiencies seen in the experiments.

A series of 0-D, flux-tube, calculations were carried out in which both the array mass and radius were varied over larger intervals than in the experiments in order to map out a larger region in (mass-implosion velocity) space into which long current-risetime Saturn shots would be expected to fall. Load masses were varied between  $60 \mu\text{g}/\text{cm}$  and  $1800 \mu\text{g}/\text{cm}$  and array radii were varied between 2 and 3.5 cm. This region (defined by black squares) is displayed in Figure 18, relative to  $\eta = 4$  and  $\eta = 8$  lines. The red dots in this figure are the Figure 17 experimental shots; the hard and soft breakpoint curves that are drawn for reference were calculated for implosions that did not include any flux tube energy generation. Figure 18 suggests that higher eta values can be achieved in long current-risetime Saturn experiments, but only if larger radii arrays are employed.

The results of the 0-D flux-tube model calculations, together with the results of the Tables I-IV Saturn shots, support the possibility that significantly higher aluminum K-shell yields can be produced on Saturn than have ever been achieved before. Towards this end, consider the Table V shot plan. In these proposed experiments, the array radius would be varied between 2 and 3.25 cm for each of three or four different array masses, one of which (the  $\sim 600 \mu\text{g}/\text{cm}$  shot) produced the highest K-shell yield in the Table I-IV shots. In order to minimize interwire gap spacings as the arrays move out in radius, the smallest diameter aluminum wires should be used. The (benchmarked) 1-D flux-tube model predicts the K-shell yields shown in the last column of Table V. These calculations suggest that experimental K-shell yields well in excess of 100 kJ may be possible.

The shots of Table V are located in (mass-implosion velocity) space as seen in Figure 19. The K-shell yields that were calculated for these shots have been listed next to these locations. The  $\eta = 4$  line is drawn in Figure 19 along with a small portion of the soft mass-breakpoint curve. The trends displayed by the yield numbers suggest that the soft breakpoint curve is shifted significantly to the right and changed in shape when large amounts of flux-tube energy are generated. The predicted trends also suggest the importance of carrying out these experiments to confirm or adjust them. While wire shots have not been tried from such large radii in the past, gas puff experiments have been, and when these experiments were done as gas fills rather than as poorly approximated gas shells, they were relatively successful. Thus, if the wires form a prefill plasma during their vaporization and ionization, this prefill could prove to be an advantage. Another advantage these large radii wire experiments could have over past experiments is with the large mass of the arrays (600 versus  $300 \mu\text{g}/\text{cm}$ ) that can now be employed.

**Table V: Proposed Saturn Shot Plan**

*WireDiam = 10.2 $\mu$ m,  $\ell = 2.0$ cm*

Wire #	Array Mass ( $\mu$ g/cm)	Array Radius (cm)	$\eta$	Interwire Gap Spacing (mm)	Predicted K-shell Yield (kJ)
151	330	2.0	2.96	0.83	60
151	330	2.5	3.76	1.04	76
151	330	2.75	4.07	1.14	56
151	330	3.0	4.44	1.25	42
151	330	3.25	4.79	1.35	36
183	400	2.0	2.69	0.69	68
183	400	2.5	3.34	0.86	98
183	400	2.75	3.66	0.94	100
183	400	3.0	3.97	1.03	80
183	400	3.25	4.26	1.12	64
228	500	2.0	2.33	0.55	76
228	500	2.5	2.92	0.69	96
228	500	2.75	3.16	0.76	114
228	500	3.0	3.44	0.83	124
228	500	3.25	3.69	0.9	130
274	600	2.0	2.09	0.46	76
274	600	2.5	2.61	0.57	90
274	600	2.75	2.84	0.63	106
274	600	3.0	3.04	0.69	126
274	600	3.25	3.20	0.75	180

# Energetics of the 180 Wire-number shot

2693

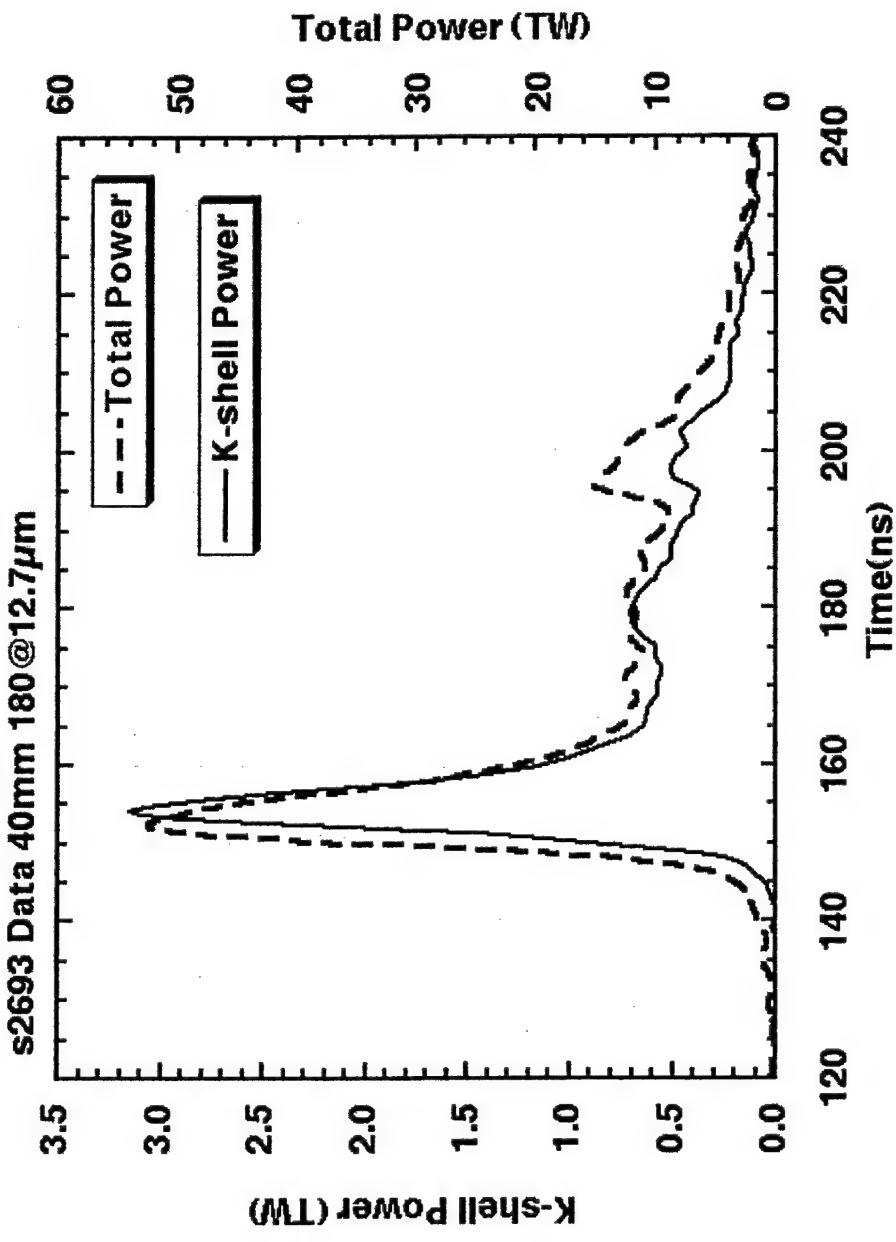


Figure 1

# Energetics of 180 Wire-number Shot 2706

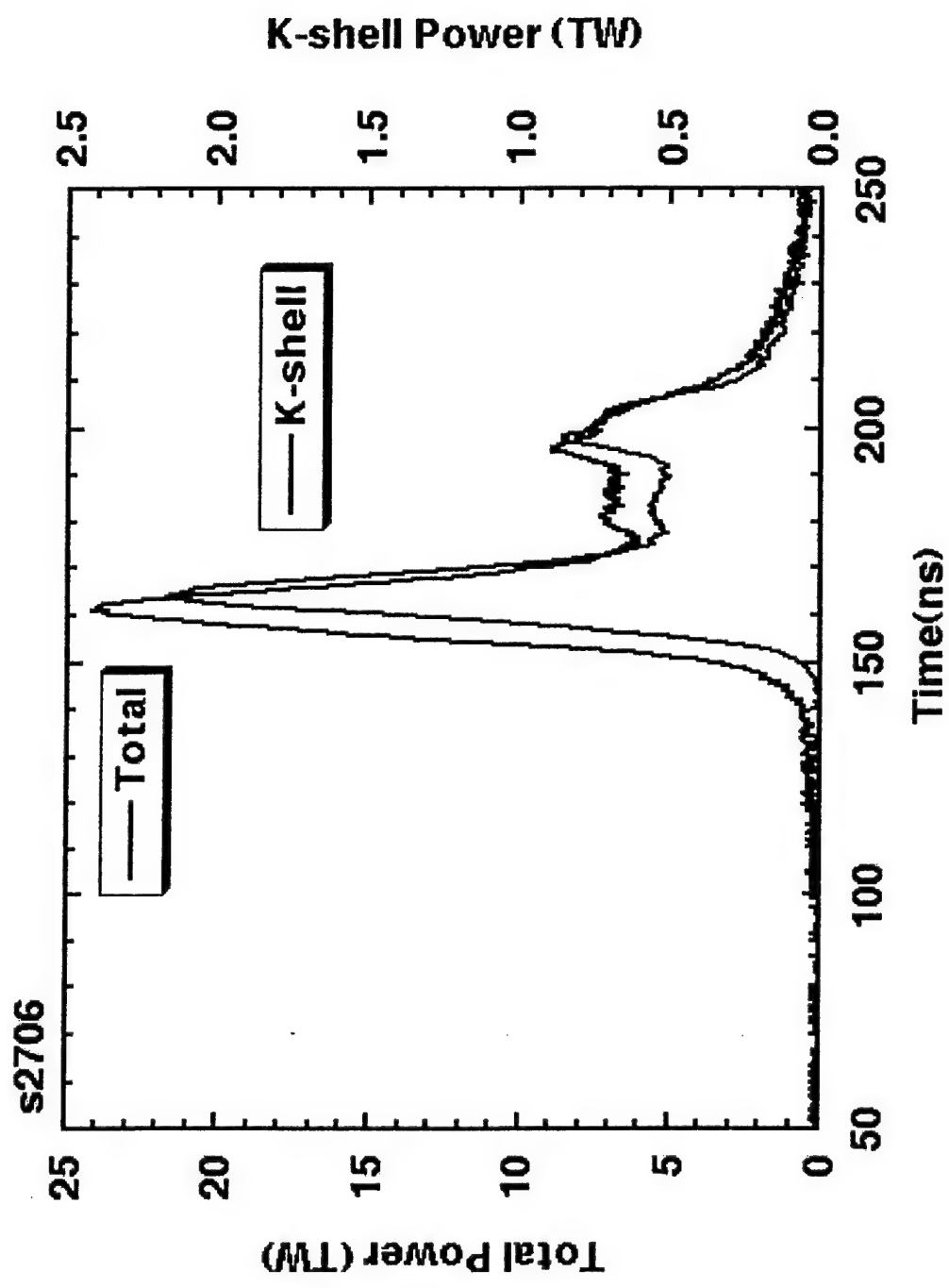


Figure 2

Undelayed generation and deposition

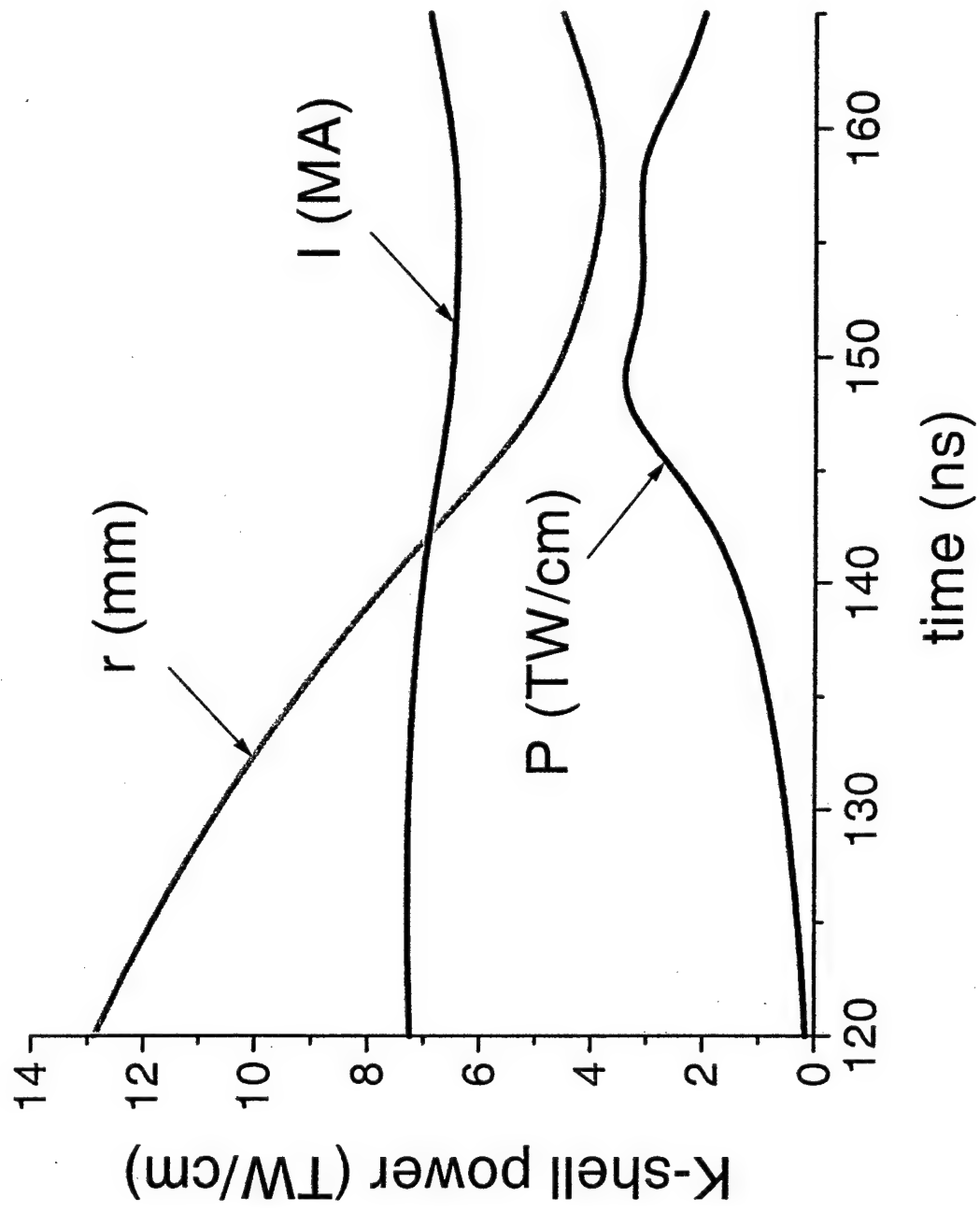


Figure 3

Delayed generation and deposition

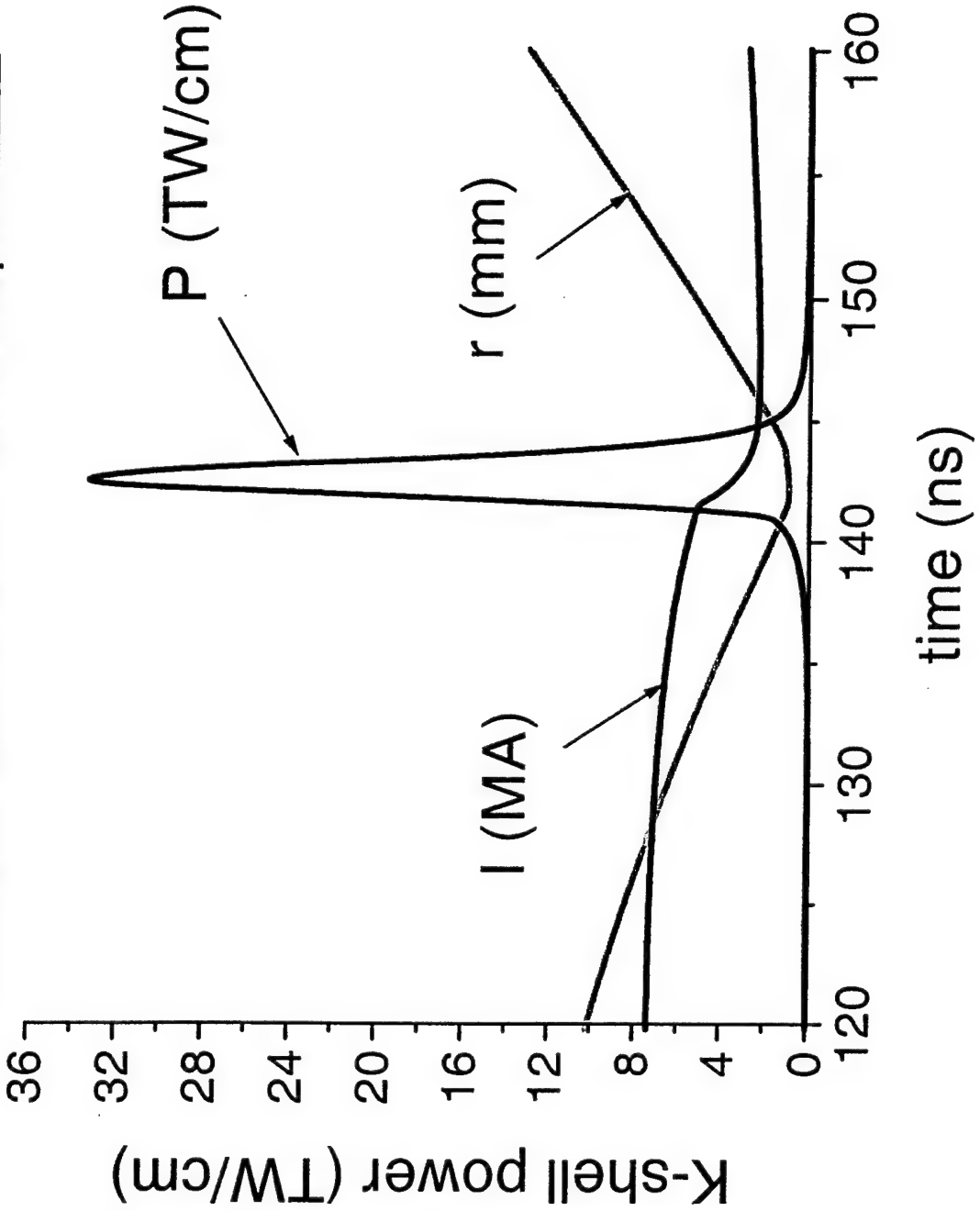


Figure 4

Undelayed generation, Delayed deposition

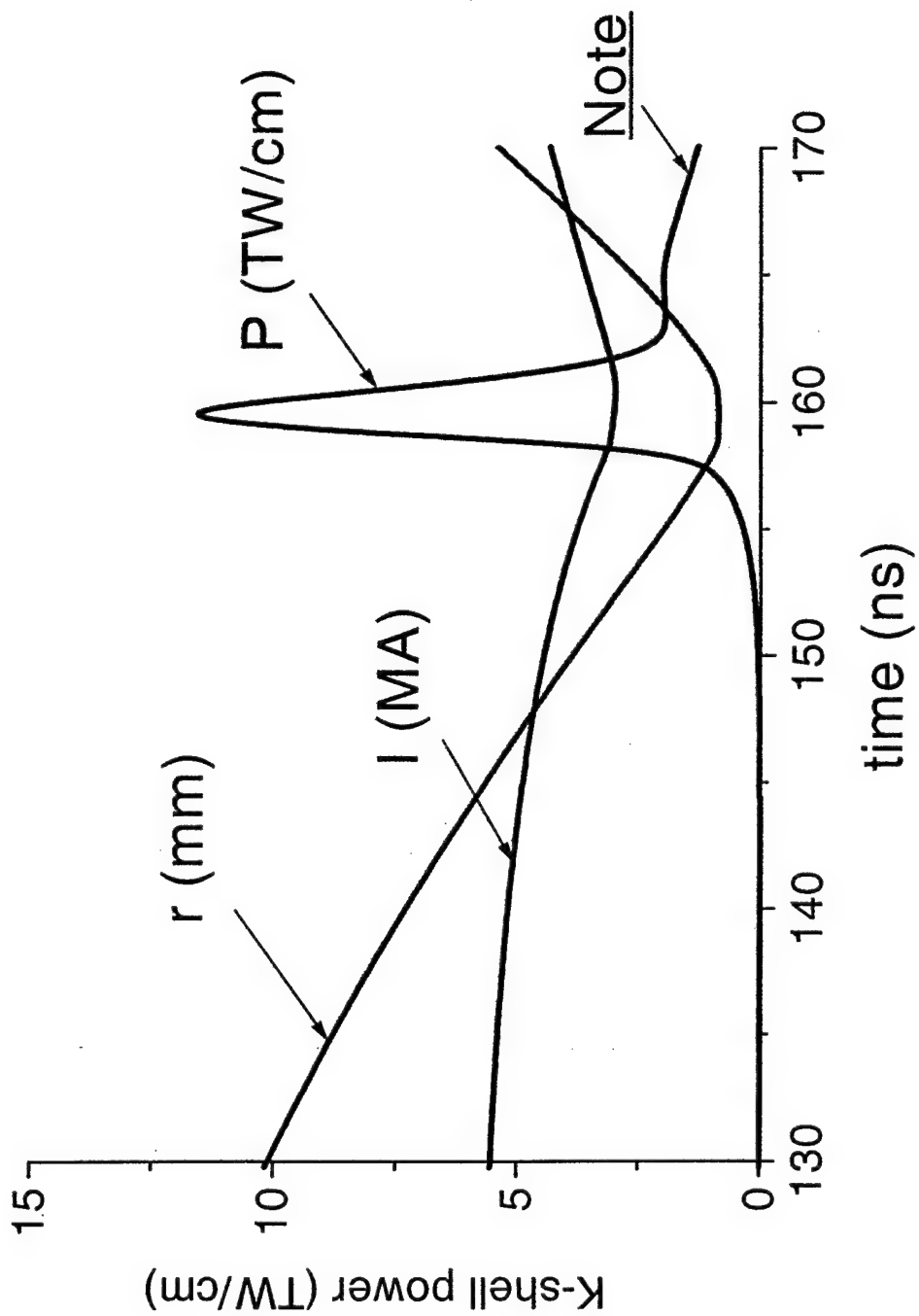


Figure 5

## Variable Mass Shots Implosion Times

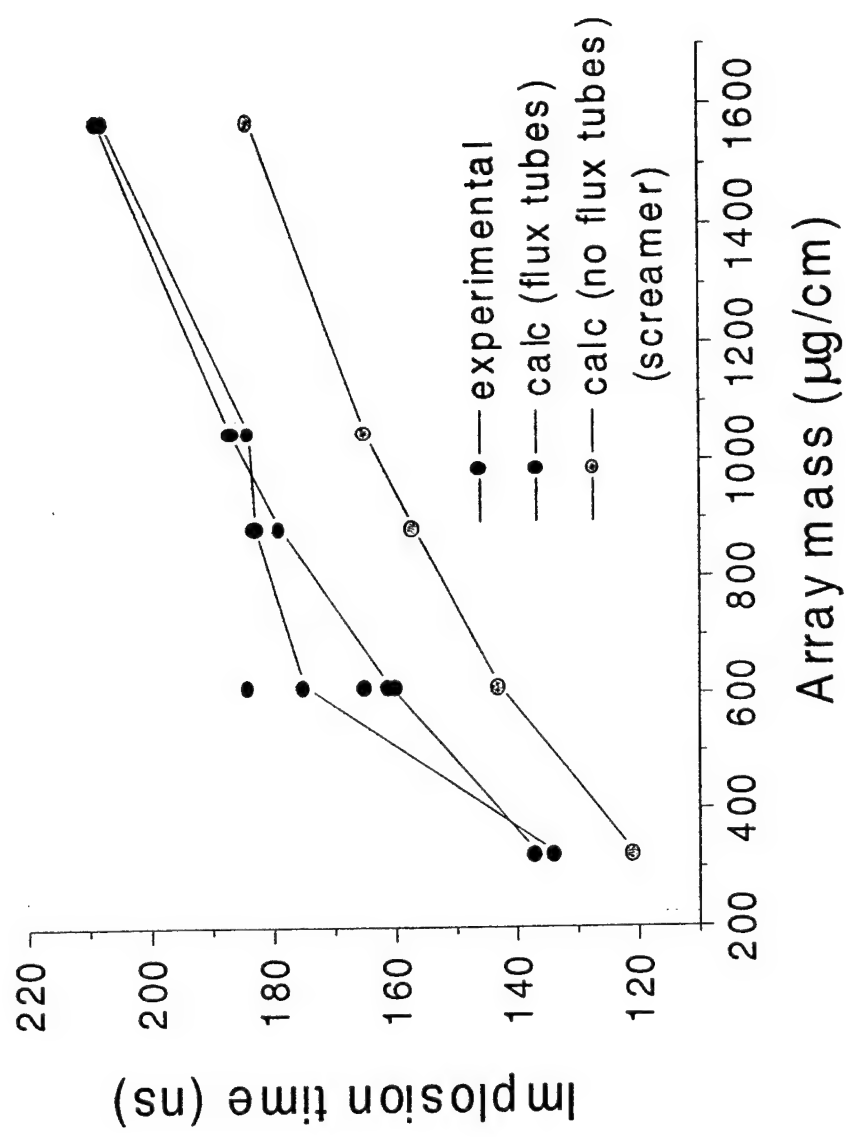


Figure 6

## Variable Mass Shots

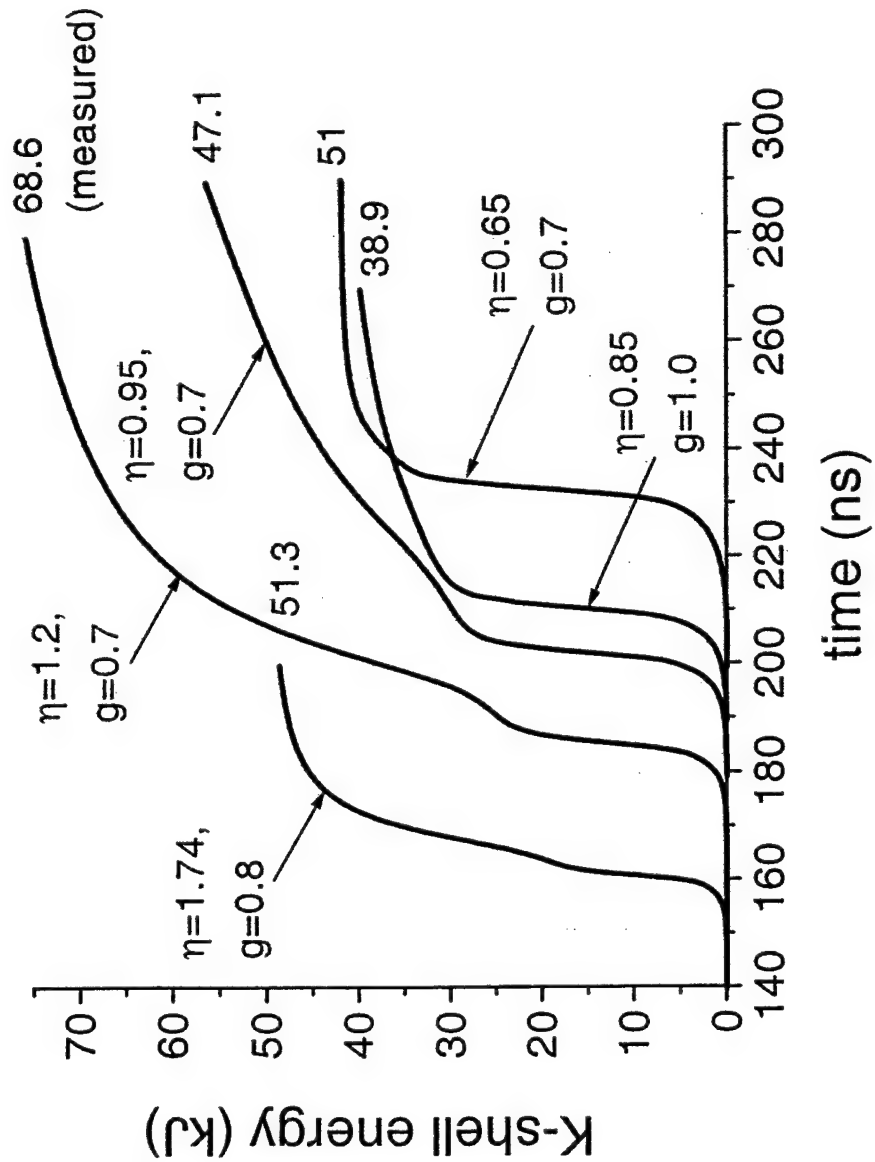


Figure 7

## Variable Mass Shots

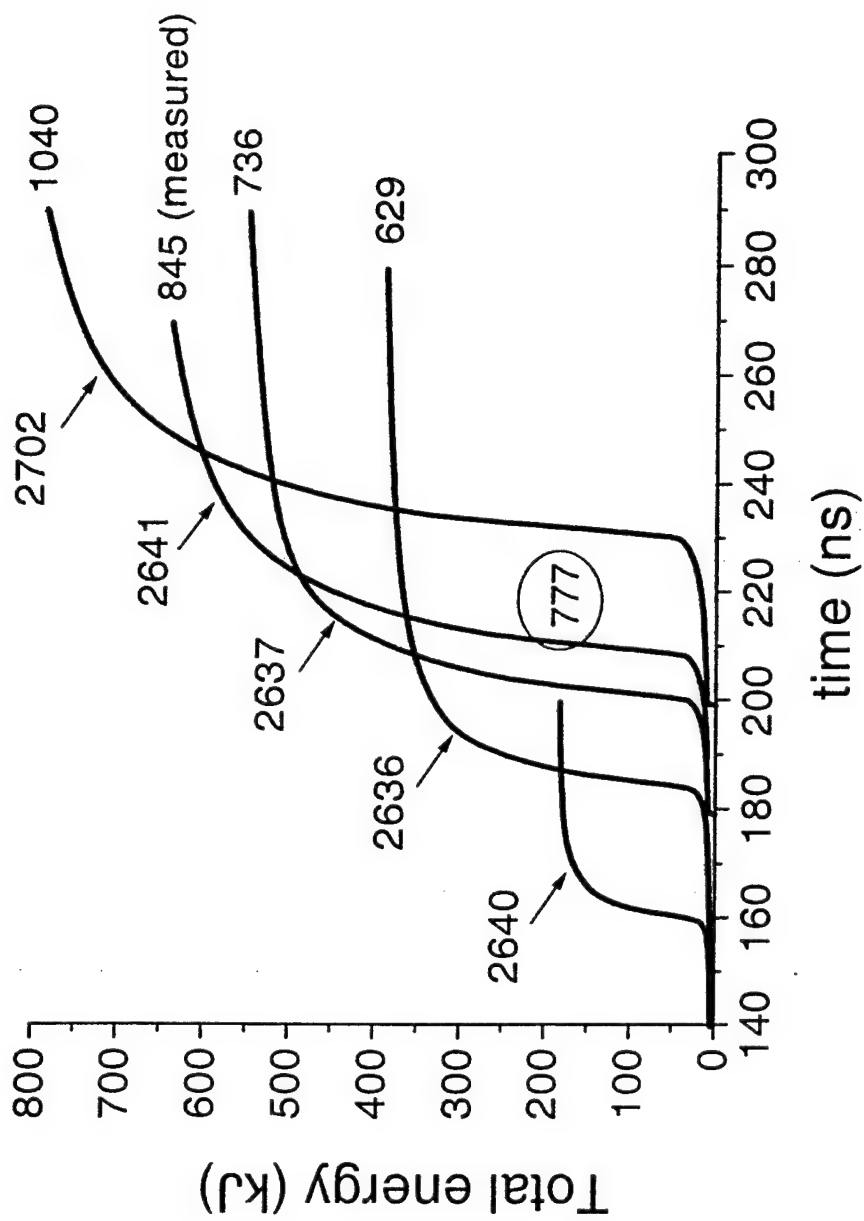


Figure 8

# Measured K-Shell Powers

## Mass Variation Shots

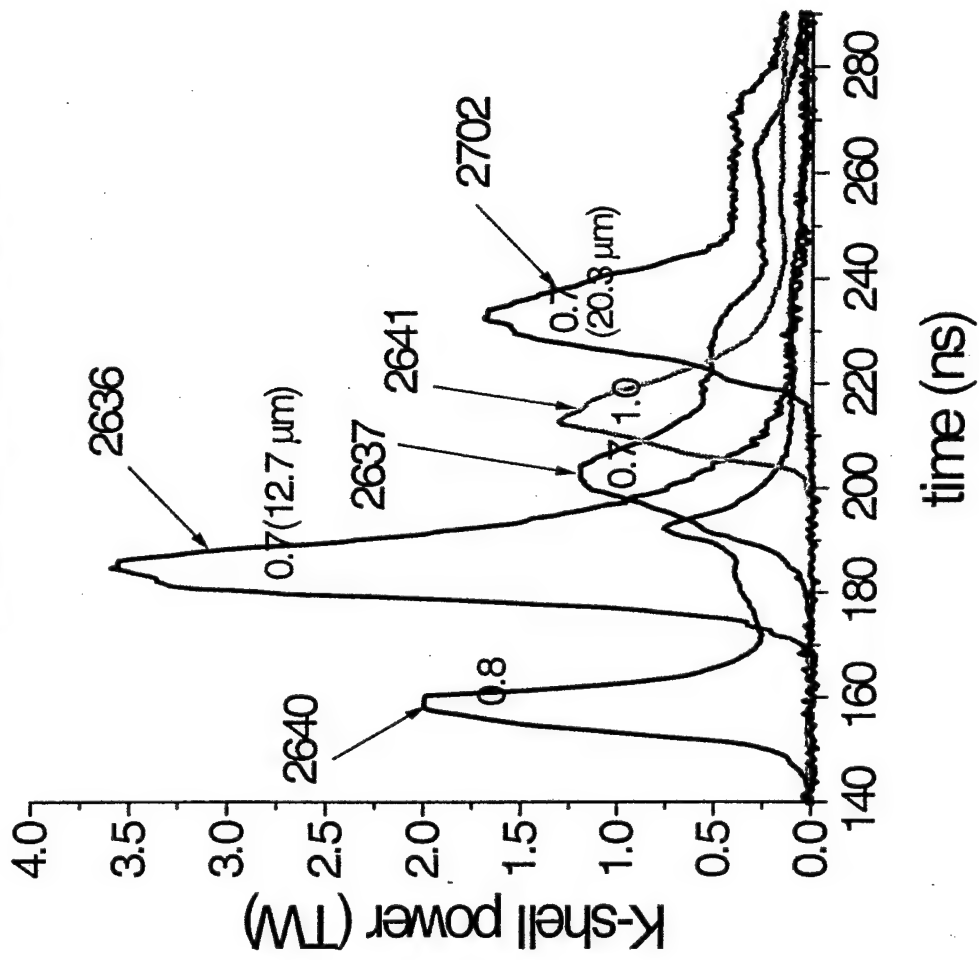


Figure 9

## Calculated K-shell Powers

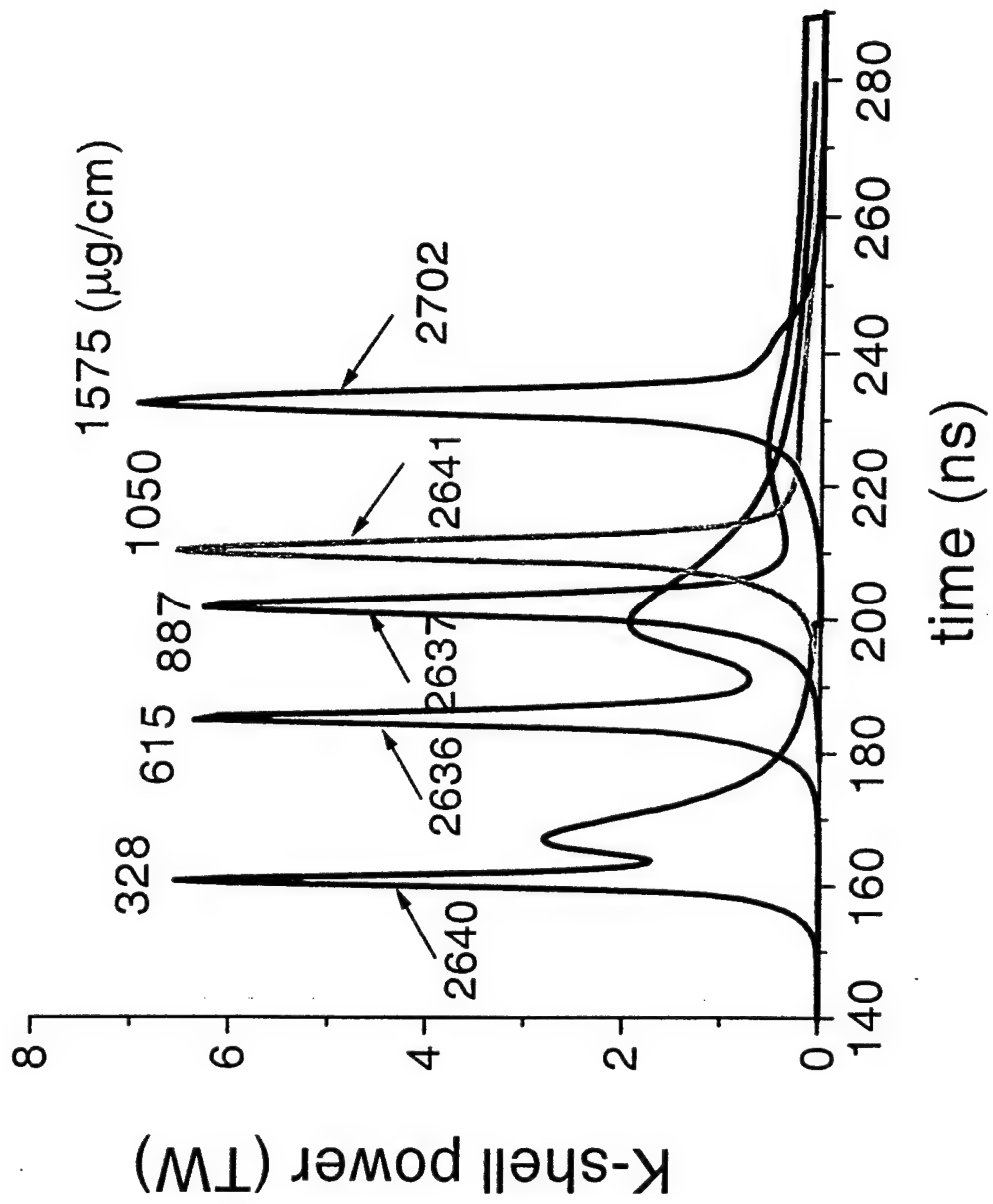


Figure 10

## Variable Length Shots Implosion Times

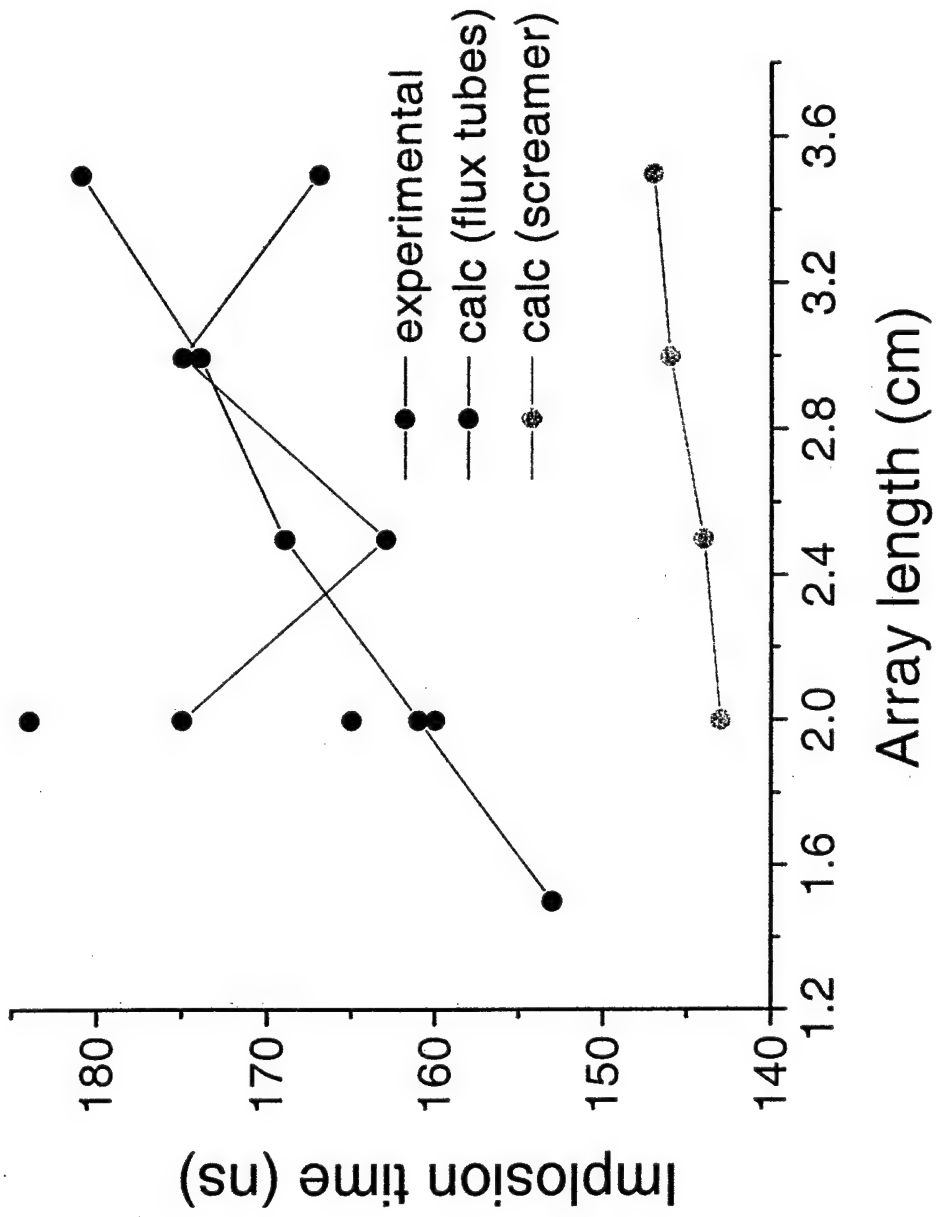


Figure 11

## Variable Length Shots

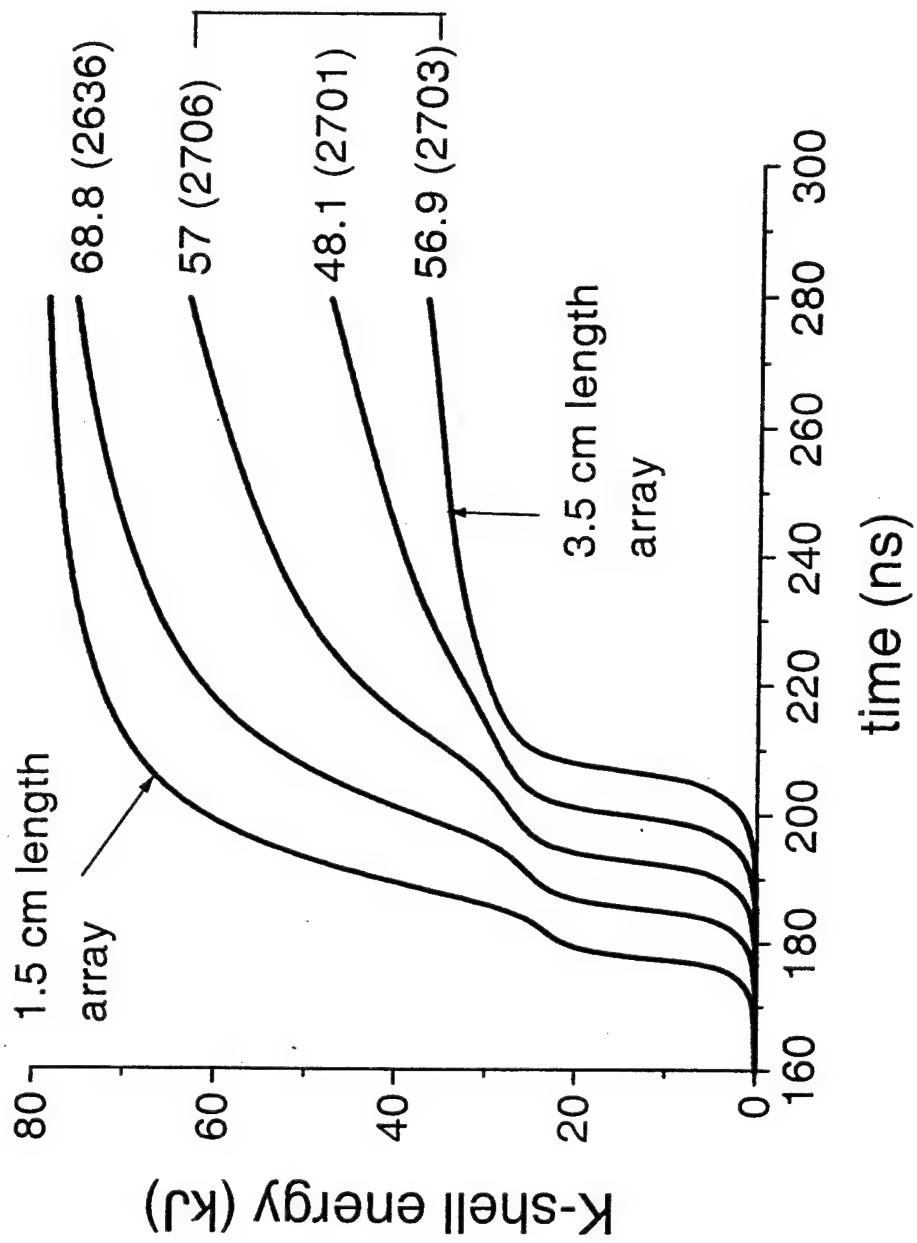


Figure 12

## Variable Length Shots

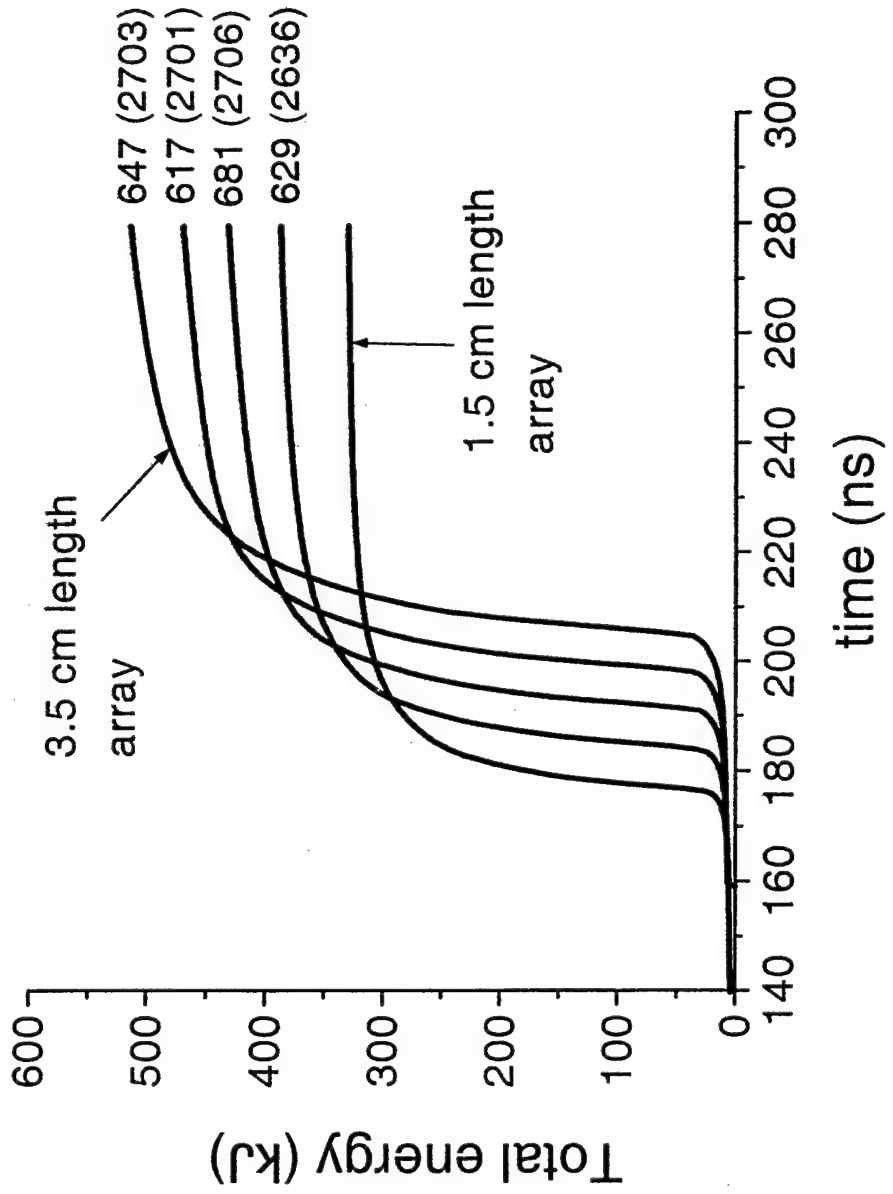


Figure 13

## Variable Radius & Mass Experiments

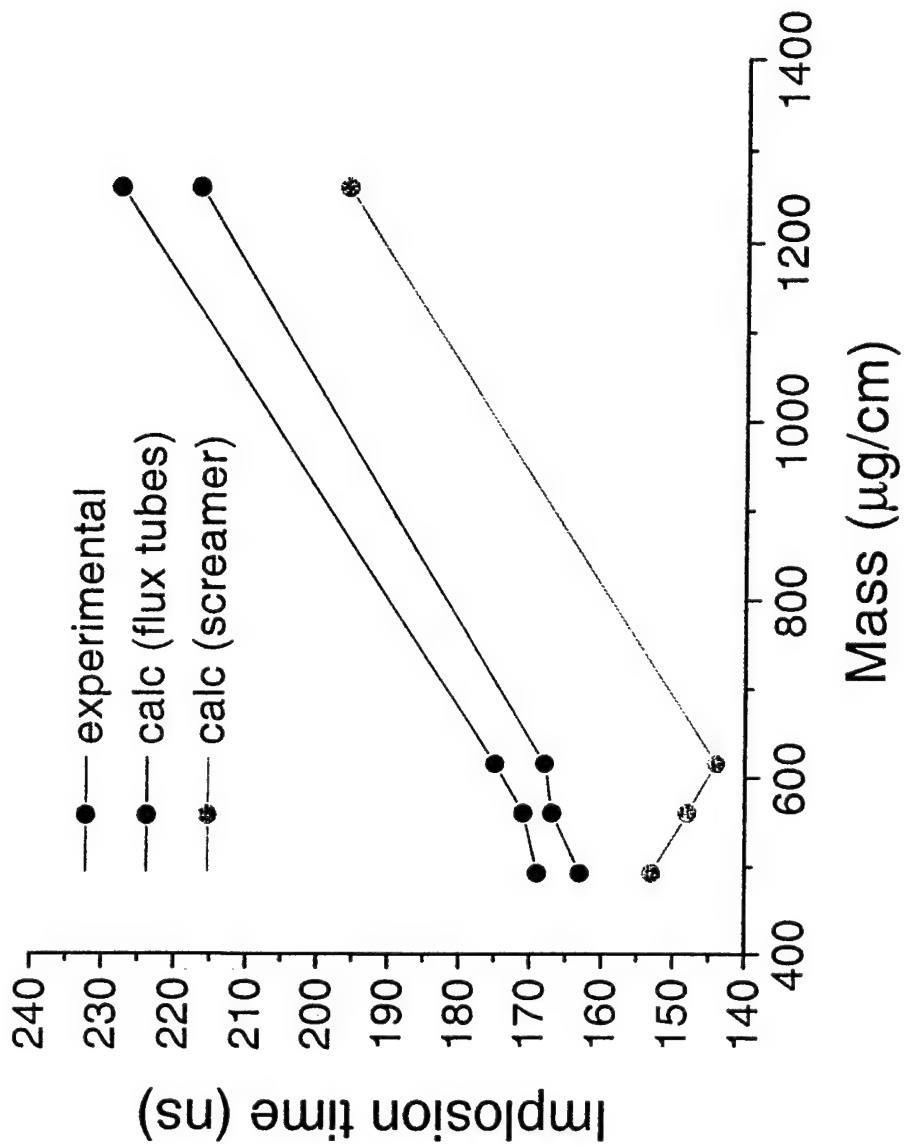


Figure 14

## Variable Radius & Mass Shots

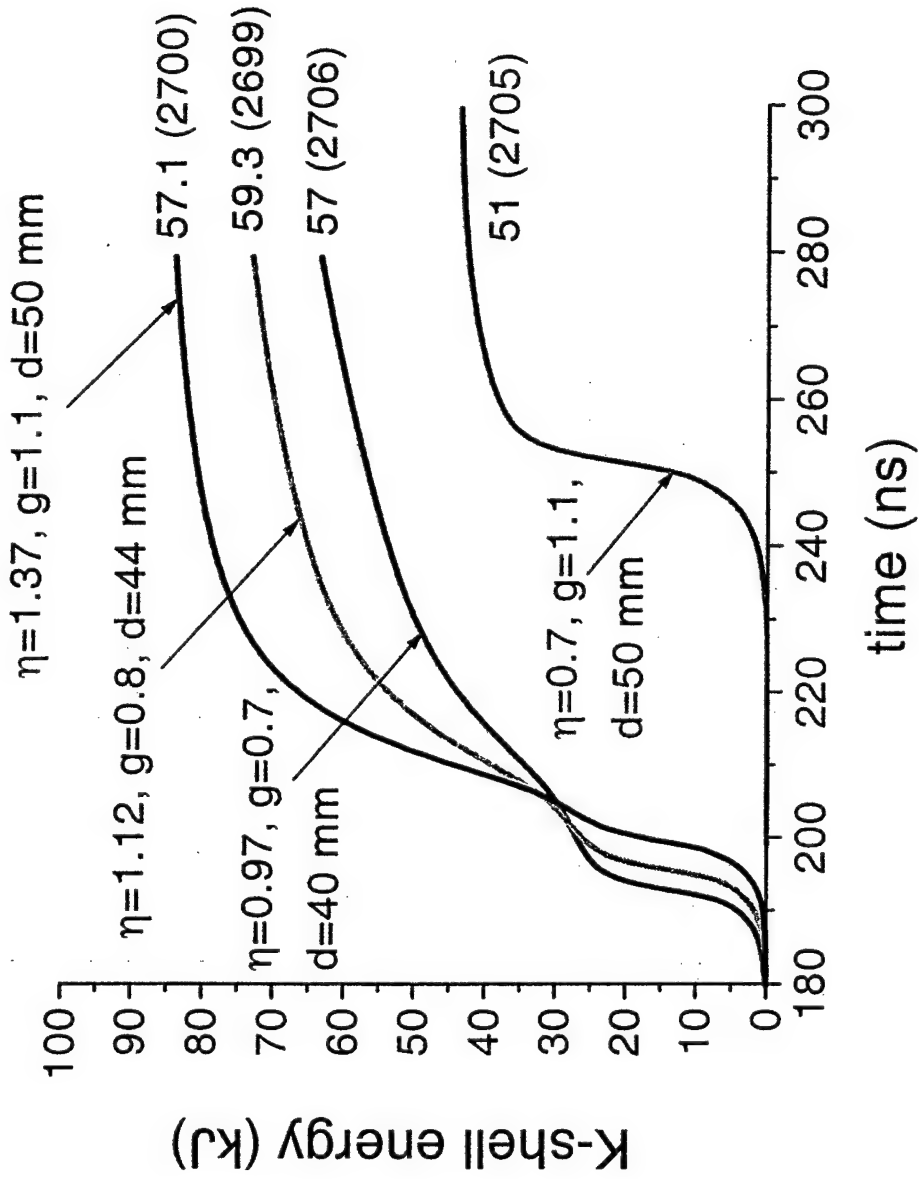


Figure 15

# Calculated $\eta$ Values (no flux tube energy generation)

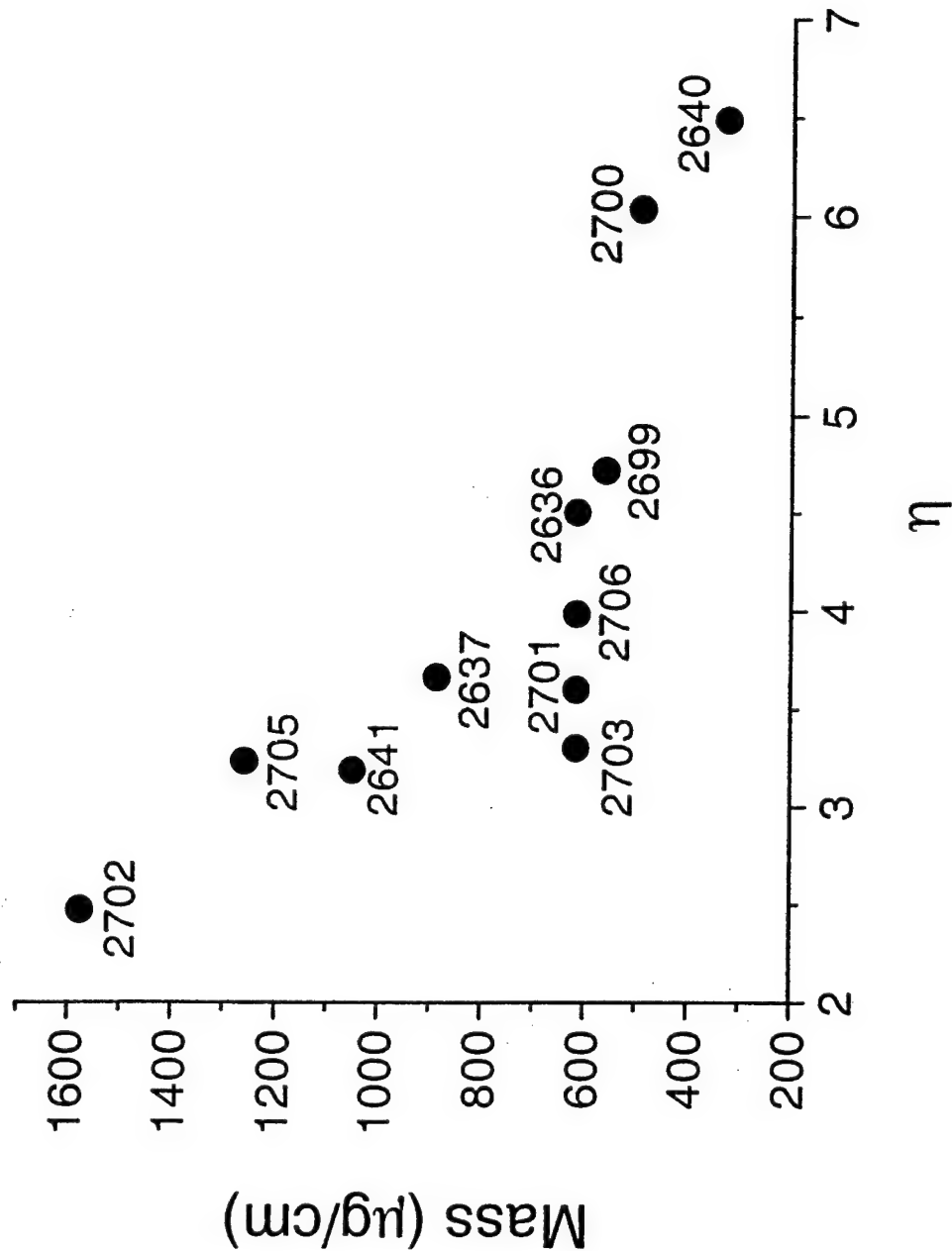


Figure 16

Calculated  $\eta$  Values  
(with flux tube energy generation)

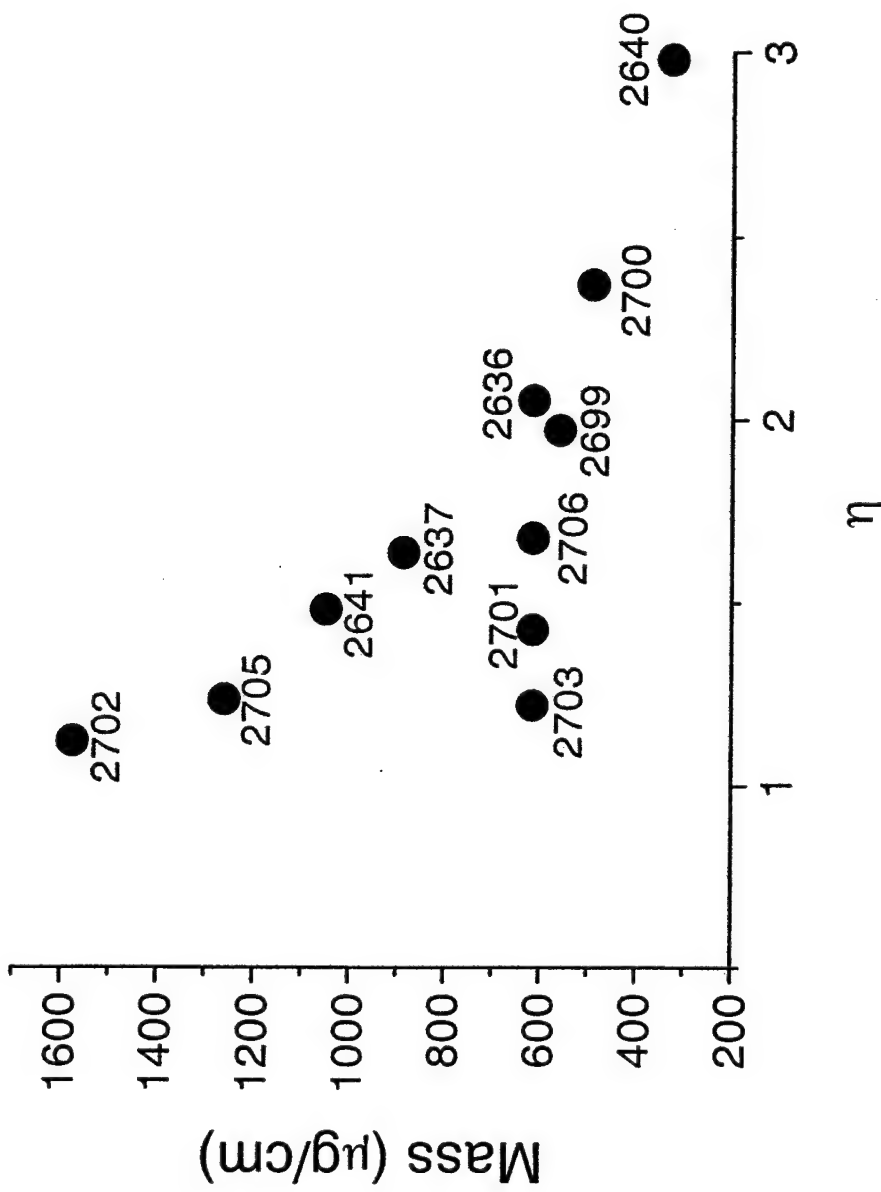


Figure 17

# Long Current-risetime Saturn Implosions with Flux Tube Energy Generation

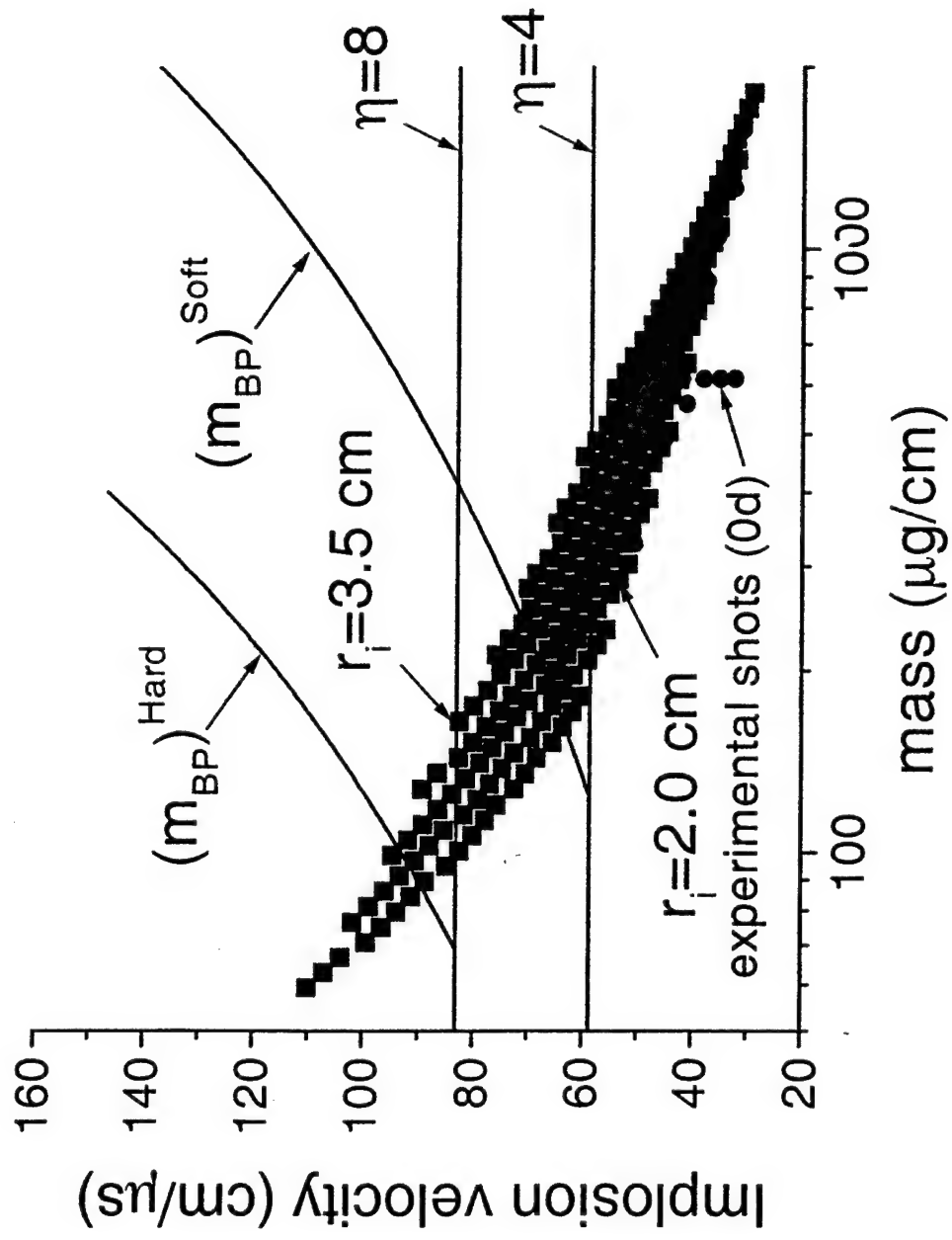


Figure 18

## Proposed Shot Plan (0.4 mil wires)

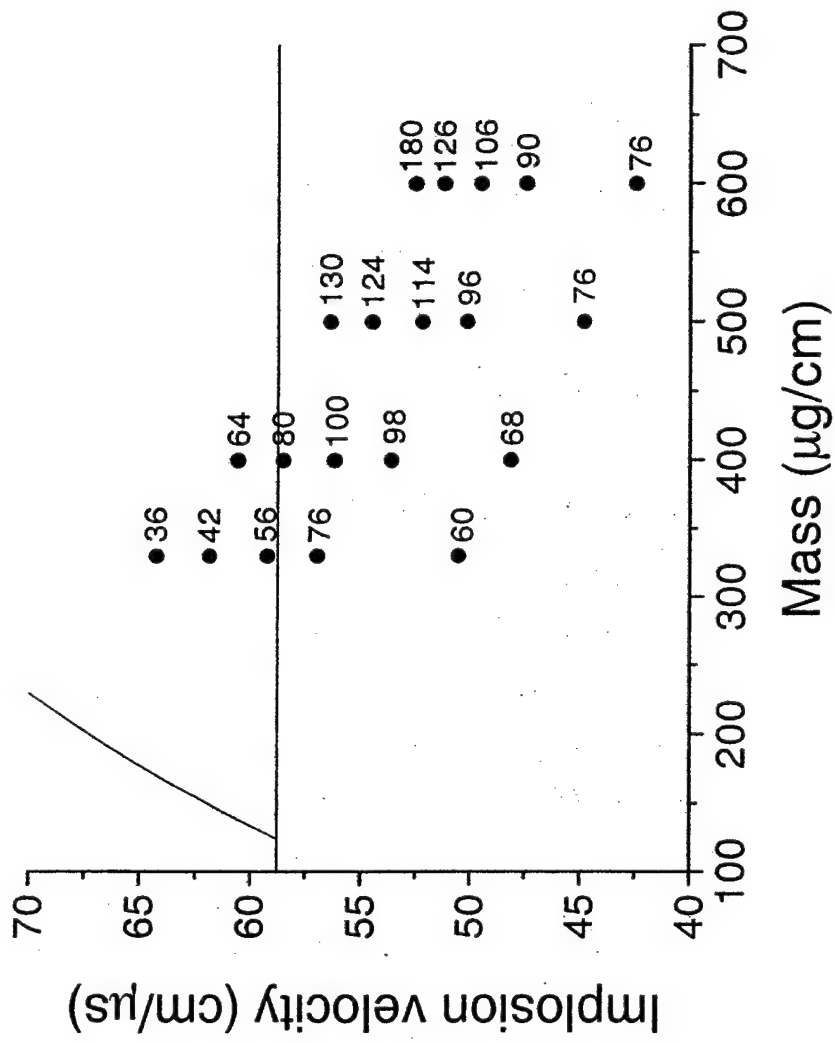


Figure 19

## VI. K-shell Yield Scaling Review for Argon Loads on Decade Quad

### A. Introduction

The work described in this section is an extension of the Decade Quad (DQ) performance assessments that were made in the 1998 and 1999 DTRA Final Reports. Here we examine the performance of Titan 4-3-2-1 nozzle argon loads on the Z machine and Decade Quad (DQ) relative to the performance of similar Double Eagle loads employing the same nozzle configuration. The K-shell yields obtained on Z and DQ are compared with  $I^2$  and  $I^4$  scaling projections from the Double Eagle yields. As stated in the above reports, this scaling projection analysis automatically factors in [and out] initialization and multidimensional effects as long as the performance of a load is viewed in terms of its  $I^0$ ,  $I^2$ , and  $I^4$  scaling projections from the same nozzle's (same ratio of inner to outer nozzle masses, recession, preionization, pinch length, etc) performance on Double Eagle.

### B. Review of $I^2$ and $I^4$ scaling

Figure 1 displays a typical theoretical result for K-shell yield as a function of increasing mass-per-unit length. The calculations used to obtain these results employed a linearly ramped current profile to drive the loads. This current was terminated when a fixed specific energy-per-ion input to the plasma, which is given in terms of  $\eta^*$ , reached a preset value of 4.<sup>1,2</sup> Here  $\eta^*$  is calculated by dividing the maximum JXB energy coupled to the pinch prior to stagnation by the total number of ions and then normalizing this result by  $E_{min}$ , the minimum energy-per-ion needed to instantly heat and ionize into the K shell upon stagnation.<sup>2</sup> For elements up to krypton  $E_{min} \simeq 1.012Z^{3.662}$  eV/ion. One reason for introducing  $\eta^*$  is to provide a relative sense, independent of the atomic number of the plasma, of whether there is enough energy available to ionize the plasma into the K-shell. For example, if  $\eta^* = 1$ , it is doubtful that much K-shell emission is going to be generated because almost all the pinch energy is going to go into ionizing the plasma. On the other hand, if  $\eta^* = 10$ , there is clearly enough energy available to ionize the plasma into the K-shell with a properly designed load. The purpose of showing this figure is to illustrate the  $I^4$  and  $I^2$  K-shell yield scaling trends that are seen in all of our past K-shell yield scaling calculations. These trends are present in the calculations regardless of atomic number,  $\eta^*$ , or whether the modeled load is a

gas puff or wire array, or whether the implosion is modeled as laminar or turbulent. The  $I^4$  scaling regime is characterized by radiative cooling rates that are too small to substantially influence the dynamics of the pinch. Under these low mass conditions (note, low mass is a relative quantity dependent on load atomic number and design) the K-shell radiation increases at its optically thin rate, which scales as the square of the ion density ( $N_i^2$ ) or as  $mass^2$  or  $I^4$ . However, at sufficiently large mass, the rates will begin to affect the pinch dynamics and the radiative yields will be limited by energy conservation to less than or equal to an  $I^2$  increase with *mass*. Conversion efficiencies of 30 percent of JXB coupled energy into K-shell emission are typically calculated in the  $I^2$  regime for  $\eta^* > 4$ .<sup>1</sup> These efficiencies have been achieved experimentally for plasmas with atomic numbers as high as that of aluminum (Z=13).

In addition to the transition from  $I^4$  to  $I^2$  K-shell yield scaling that occurs with increasing mass at fixed  $\eta^*$ , there is another important consideration to take into account when examining K-shell yield performance. This consideration is the fall off of K-shell emission that occurs at large mass loads. Since lower  $\eta^*$  loads are the first to be affected by this behavior, it is an important consideration for DTRA because most argon implosions on Double Eagle and DQ are in this low specific energy regime. Figure 2, illustrates this fall off for  $\eta^* = 1$  aluminum implosions.<sup>1</sup> This figure compares one power input, the peak rate of kinetic energy thermalization, to two power outputs, the peak total and peak K-shell radiative emission rates. This figure demonstrates expected behavior in that the peak rate of energy input scales linearly with the mass or as  $I^2$  and that the peak total radiative power follows the characteristic  $I^4$  to  $I^2$  transition with increasing mass. However, the peak K-shell power deviates from this trend to the extent that the K-shell yield saturates. The reason for this behavior is that in the low mass scaling region both radiative powers increase with  $mass^2$  or  $I^4$ ; whereas the rate at which kinetic energy thermalizes rises only linearly with mass or  $I^2$ . This more rapid rise in the ability of the plasma to radiatively cool compared with its ability to generate input energy that heats the plasma during the thermalization process produces a fall off of plasma temperature with rising mass, see Figure 3.<sup>1</sup> Eventually, at large enough mass, the plasma is too cool to ionize into the K shell and generate K-shell photons. Figure 4 shows that this yield saturation behavior occurs at smaller mass loads for the lower  $\eta^*$  implosions,<sup>1</sup> which is expected since these lower specific energy loads have less energy available for ionizing and radiating K-shell emission.

The Titan 4-3-2-1 nozzle argon experiments are analyzed in the context of the above physics based considerations, which are summarized here: (1)  $I^4$  scaling is valid in the low mass regime because radiation rates there can increase at their optically thin rate, which is proportional to  $N_i^2$ , (2) energy conservation will eventually, at large enough mass, require that K-shell yields asymptote to at best an  $I^2$  scaling, and (3) total radiation rates increase with mass and cool the plasma to the point where it is difficult to ionize into and radiate from the K shell for low  $\eta^*$  implosions.

Figure 5, gives an example of how a Double Eagle experimental K-shell yield at a fixed value of  $\eta^*$  is projected along  $I^2$  and  $I^4$  scaling curves. The formula shown in this figure for the projected yield of Decade Quad

$$Y^{I^\alpha}(\eta^*) = Y_{DE}(\eta^*) \times \left(\frac{I_{DQ}(\eta^*)}{I_{DE}(\eta^*)}\right)^\alpha \quad (1)$$

gives the essence of  $I^\alpha$  yield projections, where  $\alpha = 0, 2, 4$ ; however, when the projections are calculated, the ratio of currents  $I_{DQ}(\eta^*)/I_{DE}(\eta^*)$  is replaced by the ratio of (JxB energy of DQ) $^{1/2}$  / (JxB energy of DE) $^{1/2}$ . The two ratios are approximately equal, but to be precise, coupled energy is the more important quantity of interest. An  $I^0$  yield projection implies that the K-shell yield is saturated at the Double Eagle K-shell yield from a similar experiment with the same nozzle configuration at the same  $\eta^*$  value. Likewise, an  $I^2$  projection implies that the yield is increasing in proportion to the ratio of the JXB coupled energy from the pinch to that of the JXB coupled energy from a similar experiment on Double Eagle at the same  $\eta^*$  value, and an  $I^4$  projection implies a yield increase in proportion to (JXB coupled energy) $^2$ .

Other than the assumption that a given nozzle is expected to behave similarly on Z and DQ as it did on Double Eagle, the only other major requirement of this scaling analysis is that accurate circuit models are needed to assess the relative energy differences between Double Eagle, Z and DQ. A schematic of the circuit models used for analyzing Double Eagle, Z and DQ experiments is shown in Figure 6. It is important to note the  $L^*$  values shown in this figure for the various machines.  $L^*$  is the value of machine inductance that had to be utilized in the 0-D snowplow model of the 4-3-2-1 nozzle configuration in order to get agreement with the experimental values of implosion time and peak currents into the load. This snowplow model calculation was for uniformly distributed equal masses in each shell of the nozzle. We find, for all machines, that it is necessary to significantly increase their inductance above their short circuit inductance value

(L). It is plausible that there are multidimensional, mass distribution, or anomalous effects that can account for this additional impedance to the pinch in the snowplow calculations; however, it is unreasonable to expect such phenomena to account for the additional 22 nh of inductance that had to be added to the Decade Quad circuit. Clearly, a thorough examination of the DQ circuitry should be performed. Note, added impedance due to multidimensional or anomalous effects is not only plausible, but strong evidence for its existence was provided by aluminum wire array experiments performed on Saturn. In these experiments the plasma radiated more than twice the available JXB energy.<sup>3,4</sup> In the past, accounting for energy discrepancies such as this were presumed to be due to anomalous resistivity.<sup>5</sup> More recently, a magnetic bubble model has been postulated to account for this additional energy.<sup>4,6</sup>

The Double Eagle experimental yields from which scaling projections to DQ and Z are performed are shown in Figure 7. These yields are graphed as a function of experimental implosion time along with measured peak values of current. These results are taken from Reference 7. Note, only the results from loads that had approximately the same mass in the inner and outer shells are plotted because only loads having this configuration were imploded on Z and DQ. The  $I_{peak}$  curve shown in Figure 7 illustrates that the additional 8 nh of inductance included in the circuit model provides a reasonable fit to the measured peak current values as a function of implosion time. The inferred  $\eta^*$  and mass curves of Fig. 7 are based on this circuit model. The inferred masses are close to the inferred values of Reference 7. Since high  $\eta^*$  experiments were not performed on Double Eagle, the Double Eagle results were extended to this regime in the following manner.

If the mass at which the transition between  $I^4$  and  $I^2$  scaling occurs is labeled  $M_{bp}$  then the K-shell yield for masses (m) less than this at the same  $\eta^*$  value is given by

$$Y_k(m < M_{bp}) = f \times Energy_{JXB}(mass = M_{bp}) \times (m/M_{bp})^2,$$

$$\text{which is } \propto f \times \eta^* \times M_{bp} \times (m/M_{bp})^2.$$

Our past work (Refs. 1 and 2) showed that  $f$ , the maximum conversion efficiency of JXB coupled energy to K-shell yield, and  $M_{bp}$  are largely insensitive to the value of  $\eta^*$  in the high  $\eta^*$  regime. Based on this work, the K-shell yield in the high  $\eta^*$  regime is expected to scale as

$$Y_k(m < M_{bp}) \propto \eta^* \times m^2,$$

which is  $\propto Energy_{JXB}(mass = m) \times \eta^*$ .

### C. Analysis of DQ and Z experiments

In this section the Z machine and DQ experimental K-shell yield results are analyzed in terms of  $I^\alpha$  projections from Double Eagle experimental results. Figures 8 and 9 show the results for DQ for the reduced voltage experiments,<sup>8</sup> i.e. the voltage was reduced by the factor 0.7/0.85. Figure 8 demonstrates that adding an additional 22 nh to the DQ circuit enabled us to obtain a reasonable match with the measured peak current values as a function of implosion time. The masses and  $\eta^*$  values that are inferred from this circuit as well as the calculated peak current, without any additional inductance, are also shown in Fig. 8. This figure indicates, for a fixed implosion time, that the measured peak current values are about 1 MA below their expected values. This represents approximately 30 percent less energy coupled to the load than expected. The  $I^\alpha$  for  $\alpha = 0, 1, 2$  K-shell yield scaling projections are shown in Fig. 9. This figure illustrates that the 244 ns implosion was probably in a saturated,  $I^\alpha$ , scaling regime. In other words, at this low level of  $\eta^*$  ( $\eta^* \simeq 1.7$ ), as the mass is increased from  $150 \mu\text{g}/\text{cm}$  on Double Eagle to  $260 \mu\text{g}/\text{cm}$  on DQ, the total radiation rates have increased with mass and cooled the plasma to the extent that it is difficult to ionize and radiate from the K shell. Thus, increasing the mass beyond  $260 \mu\text{g}/\text{cm}$  at this specific energy of  $\eta^* = 1.7$  or lower will not produce any additional K-shell emission. As the mass is reduced further and correspondingly  $\eta^*$  is increased (230 ns shot), we find that the DQ K-shell yield is approaching an  $I^2$  scaling projection in which the K-shell yield is increasing in proportion to the coupled energy. For this shot, the conversion efficiency of coupled energy to K-shell emission is about 12 percent. A 12 percent conversion efficiency is reasonable for what is still a relatively low  $\eta^*$  implosion,  $\eta^* \simeq 2$ . On the one hand, Fig. 9 demonstrates that it is not worthwhile to attempt to optimize K-shell emission in future experiments by operating with this nozzle configuration with mass loads in excess of  $200 \mu\text{g}/\text{cm}$  having  $\eta^*$  values less than 2. On the other hand, an encouraging consequence of the  $I^2$  scaling achieved for the 230 ns experiment (with approximately a  $200 \mu\text{g}/\text{cm}$  load) is that mass loads of less than  $200 \mu\text{g}/\text{cm}$  that are imploded at  $\eta^*$  values greater than 2 can be expected to be in an  $I^{>2}$  scaling regime. This consequence was verified by the DQ shot at full voltage (see Fig. 10). The 28 kJ of K-shell emission achieved by this shot clearly lies between the  $I^2$  and  $I^4$  scaling projections.

The Z machine results are displayed in Figures 11 and 12 for the 2.4 cm length pinches and in Fig. 13 for the 2 cm length pinch. The experimental results shown in these figures are taken from Reference 9. Figures 11 and 13 demonstrate that the 2.4 nh/cm that was added to the circuit model inductance reasonably matches the measured peak currents with their respective implosion times (with the exception of the anomalous 135 ns, 2.4 cm length shot). The inferred masses are also in agreement with those quoted in Reference 9. A comparison of current profiles with and without extra inductance (Fig. 11) shows a substantial 3-4 MA reduction in current, which represents about a 40 percent reduction in JXB coupled energy for a given implosion time. Similar to the experience on DQ, this current reduction is not well understood at this point in time. Figure 12 illustrates how the yield behavior changes from nearly saturated,  $I^0$ , at the higher mass and lower  $\eta^*$  values of the 135 ns shot, to yields that are clearly in excess of  $I^2$  projections from Double Eagle as the mass is reduced and the  $\eta^*$  values correspondingly increased. The K-shell yield for the lowest mass shot (800  $\mu\text{g}/\text{cm}$ ,  $\eta^* = 5.5$ , 112 ns) is so large that it begins to approach typical theoretical values of 30 percent of the JXB coupled energy. Based on the results of the 2.4 cm length experiments, one expects an  $\eta^* = 5$  load to produce a K-shell yield somewhere between 75 kJ/cm and 115 kJ/cm. Thus, it was surprising to find that the 2.0 cm length experiment at  $\eta^* \simeq 5$  produced only 68 kJ/cm. This suggests that there is something inherently different in the implosion dynamics of 2 cm length and 2.4 cm length pinches, such that they behave like substantially different load designs.

## D. Conclusions

The DQ and Z machine K-shell yields that were obtained using the Titan 4-3-2-1 nozzle fit well within our general guidelines for understanding the load physics of Z-pinches. These guidelines are: (1)  $I^4$  scaling is valid in the low mass regime because radiation rates there can increase at their optically thin rate, which is proportional to  $N_i^2$ , (2) energy conservation will eventually, at large enough mass, require that K-shell yields asymptote to at best an  $I^2$  scaling, and (3) total radiation rates increase with mass and cool the plasma to the point where it is difficult to ionize into and radiate from the K shell, especially for low  $\eta^*$  implosions because they barely have enough energy to ionize into the K shell. (It is not discussed here, but opacity can also significantly affect the scaling of K-shell emission) Based on these guidelines, one expects the K-shell yield behavior of Z and DQ to transition from an  $I^4$  scaling projection from Double Eagle to an  $I^0$  scaling projection as

the mass of the load is increased. This behavior was exhibited by both the Z and DQ experiments.

Our analysis shows that for the 4-3-2-1 nozzle configuration with equal masses in the inner and outer shells, and given the present level of energy coupling to the load, that the maximum K-shell yields obtained in these experiments are near optimum. Our best option for substantially improving yields with this nozzle configuration on DQ and Z is to improve the power flow, i.e. energy coupling to the load for a specific implosion time. At present it is not well understood why an additional 22 nh of inductance for DQ, 6 nh for the Z machine, and 8 nh for Double Eagle is required in their respective circuits to obtain a reasonable match between measured peak currents and implosion times. There is strong evidence that extra impedance due to magnetic bubbles and/or other anomalous heating mechanisms is playing a role in reducing expected currents and energy coupled to the load. On the other hand, the additional 22 nh of inductance added to the DQ circuit seems excessive (compared to the extra inductances required for Double Eagle and Z) and therefore suggests that there may also be fundamental power flow problems that need to be understood and solved for DQ.

If improvements to DQ's power flow cannot be made, and its present capabilities are employed, then the optimal path for achieving higher argon K-shell yields is to implode loads from larger radius. This will allow more of DQ's energy to couple to higher specific energy,  $\eta^*$ , loads than is possible with the present 4-3-2-1 configuration. However, this entails a substantially different load design than the 4-3-2-1 nozzle configuration so there is no guarantee of higher yield results.

## References

1. J. W. Thornhill, K. G. Whitney, J. Davis, and J. P. Apruzese, *J. Appl. Phys.* 80, July 15, (1996).
2. K. G. Whitney, J. W. Thornhill, J. P. Apruzese, and J. Davis, *J. Appl. Phys.* 67, 1725 (1990).
3. C. Deeney and C. Coverdale, Sandia National Laboratory, private communication
4. A. L. Velikovich, J. Davis, J. W. Thornhill, J. L. Giuliani, Jr., L. I. Rudakov, and C. Deeney, *Phys. of Plasmas* 7, 3265 (2000).
5. D. G. Colombant, M. Lampe, J. Davis and H. W. Bloomberg, "Dynamics and radiative yields from aluminum multiple wire arrays," *NRL Memorandum Report 3840*, Naval Research Laboratory,

Washington, D.C. 20375 (1978); copies may be ordered from NTIS, Springfield, VA 22161, order no. ADA059883.

6. L. I. Rudakov, A. L. Velikovich, J. Davis, J. W. Thornhill, J. L. Giuliani, Jr., and C. Deeney, *Phys. Rev. Lett.*, 84, 3326 (2000).
7. H. Sze, P. L. Coleman, B. H. Failor, A. Fisher, J. S. Levine, Y. Song, E. M. Waisman, J. P. Apruzese, Y. K. Chong, J. Davis, F. L. Cochran, J. W. Thornhill, A. L. Velikovich, B. V. Weber, C. Deeney, C. A. Coverdale, and R. Schneider, *Phys. of Plasmas*, 7, 1 (2000).
8. J. S. Levine and H. Sze, *Titan*, private communication.
9. H. Sze, P. L. Coleman, J. Banister, B. H. Failor, A. Fisher, J. S. Levine, Y. Song, E. M. Waisman, J.P. Apruzese, R. W. Clark, J. Davis, D. Mosher, J. W. Thornhill, A. L. Velikovich, B. V. Weber, C. A. Coverdale, C. Deeney, T. L. Gilliland, J. McGurn, R. B. Spielman, K. W. Struve, and D. Bell, *Phys. of Plasmas Lett.* 8, 3135 (2001).

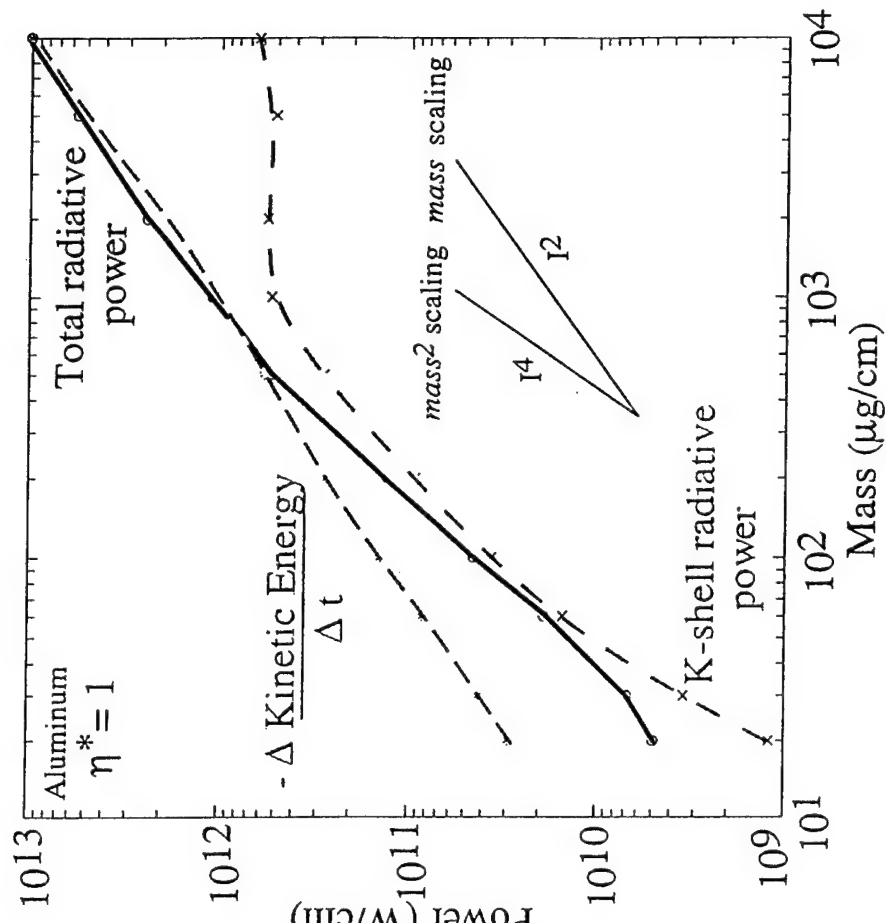
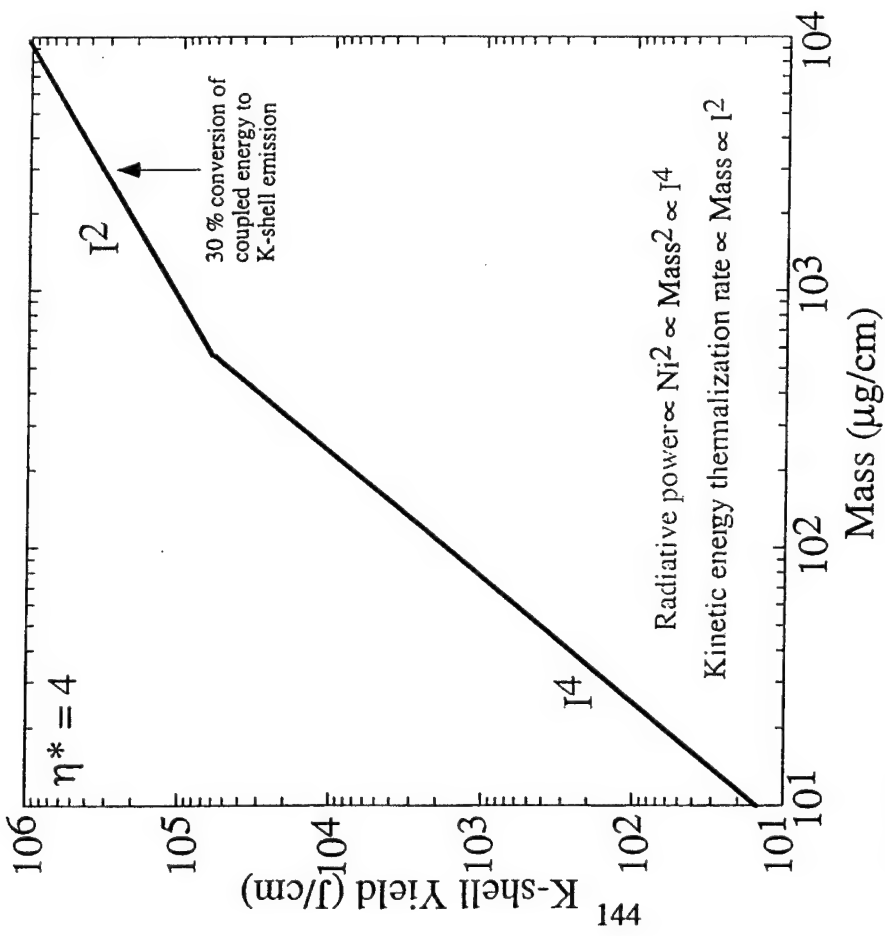


Fig. 1 Example of  $I^4$  to  $I^2$  K-shell yield scaling transition that occurs with increasing mass at fixed  $\eta^*$ , where  $\eta^*$  is the coupled energy-per-ion normalized by the minimum energy-per-ion required to ionize into the K shell.

Fig. 2 Kinetic energy thermalization rate, total radiative power, and K-shell radiative power as a function of load mass for  $\eta^* = 1$  aluminum Z-pinch implosions. Results are shown at time of peak radiative power.

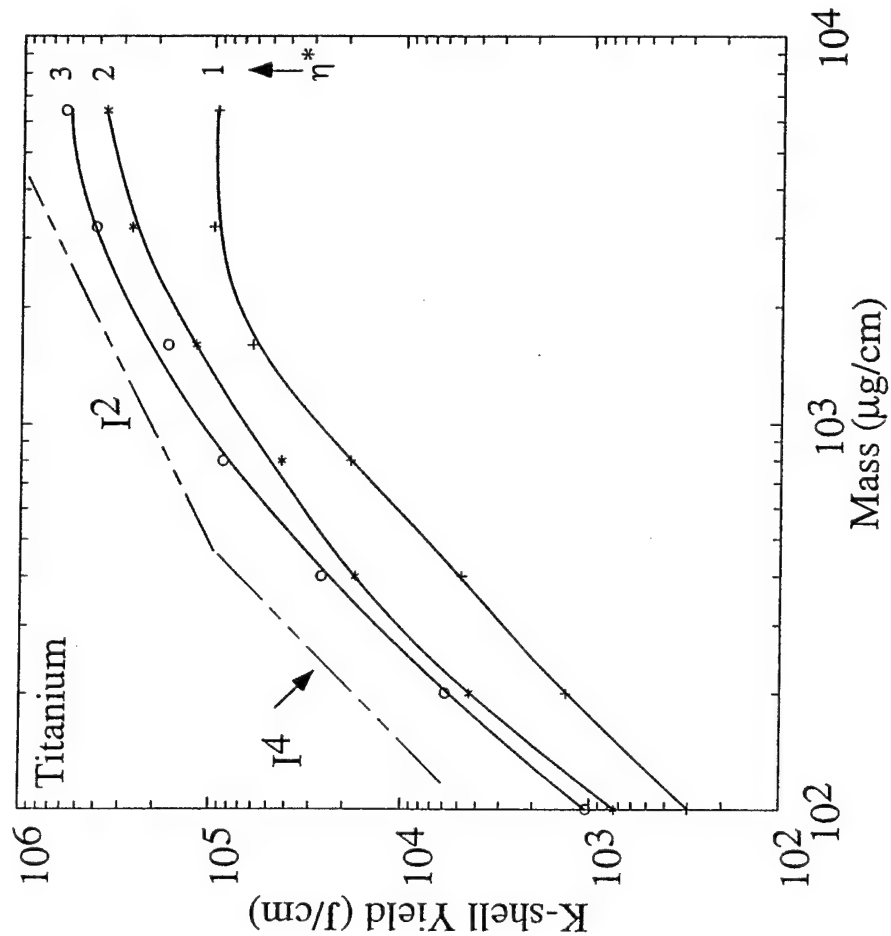


Fig. 4 Titanium K-shell yields as a function of mass load and  $\eta^*$ .

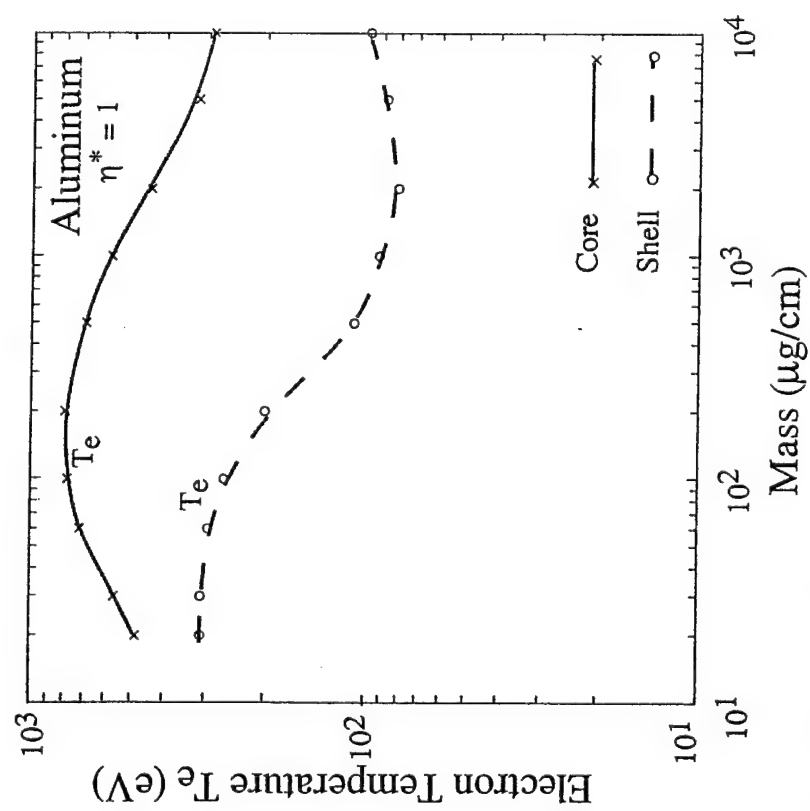


Fig. 3. Mass and time averaged electron temperatures of the core and shell regions of an aluminum plasma as a function of z-pinch mass load. The averaging is over the full-width-half-maximum of the K-shell radiation pulse.

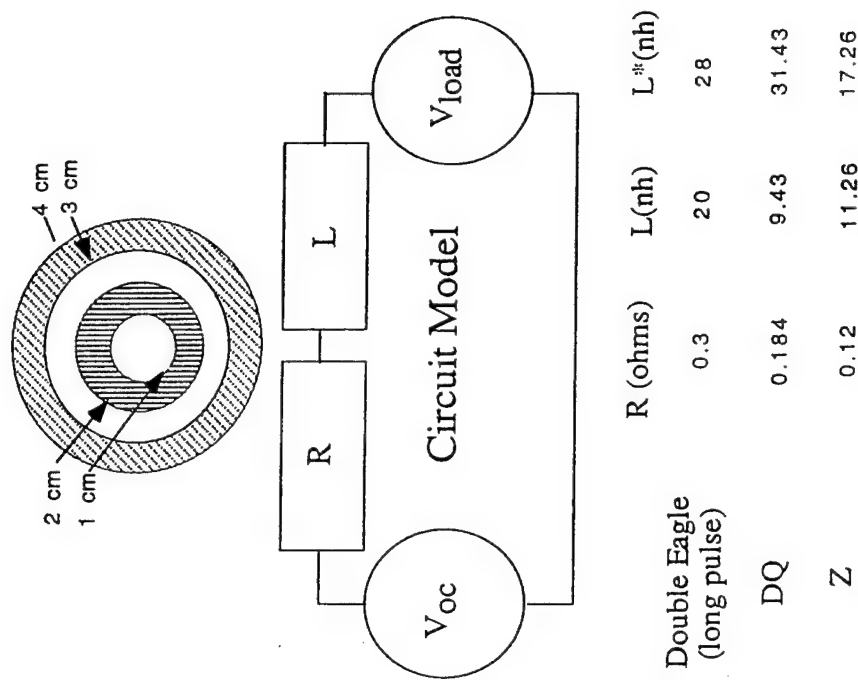


Fig. 6. Schematic diagram of the 4-3-2-1 nozzle configuration (equal masses in inner and outer shells at uniform mass distribution) and equivalent circuit models for Double Eagle, Decade Quad and Zgenerators.

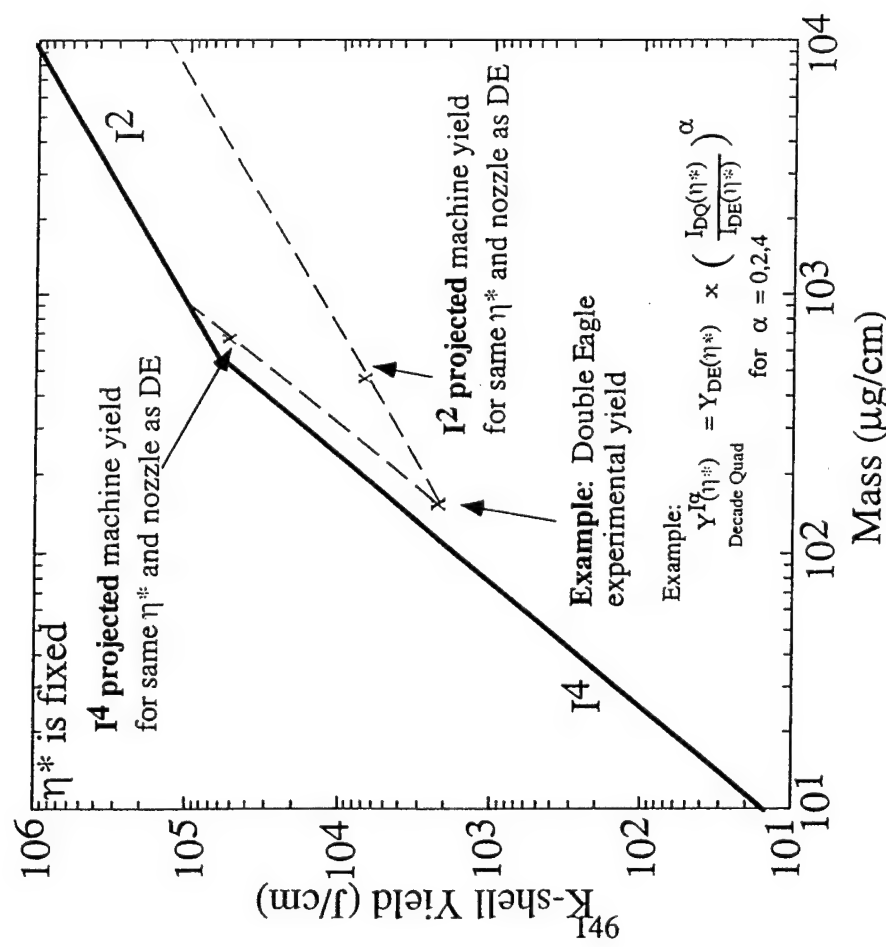


Fig. 5. Example of I2 and I4 K-shell yield scaling projections from Double Eagle experimental yields.

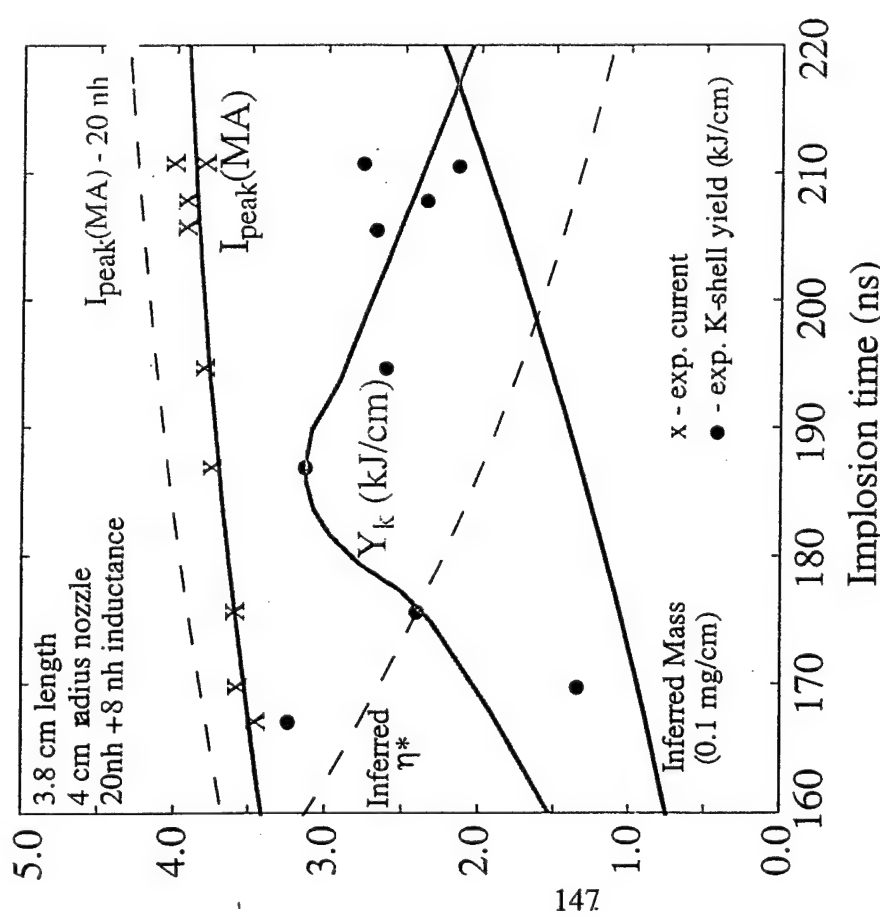
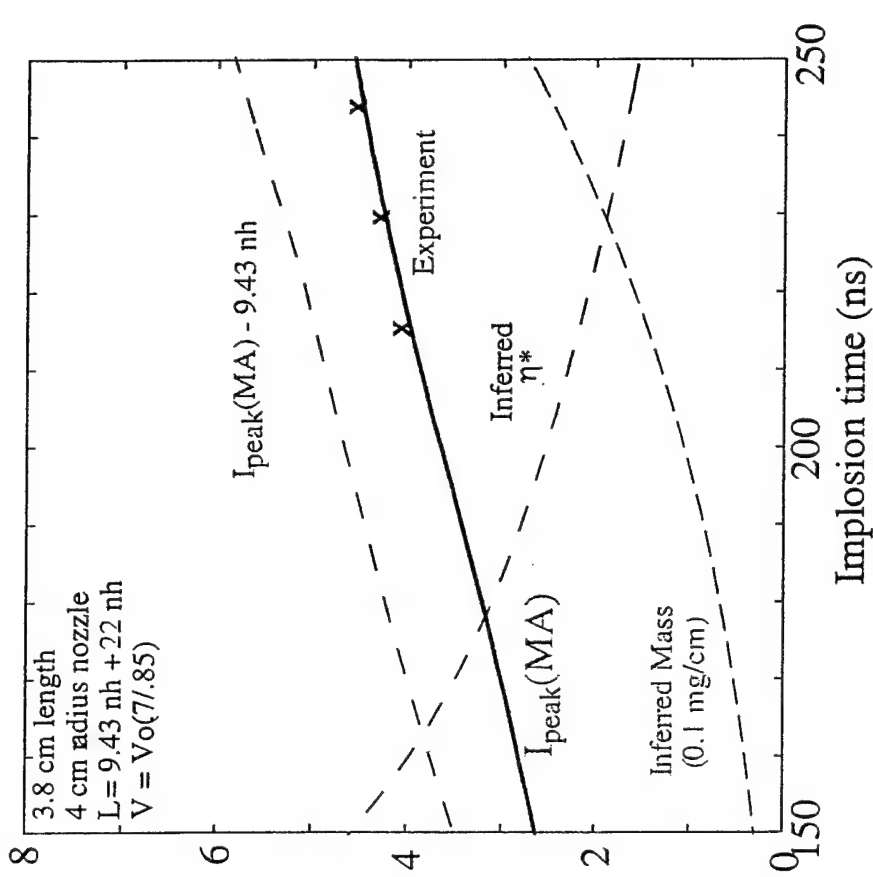


Fig. 7. Double Eagle experimental peak currents and K-shell yields as a function of experimental implosion times. Also shown are inferred mass loads,  $\eta^*$  values, and calculated peak currents.

Fig. 8. Decade Quad (reduced voltage) experimental peak currents as a function of experimental implosion times. Also shown are inferred mass loads,  $\eta^*$  values, and calculated peak currents.

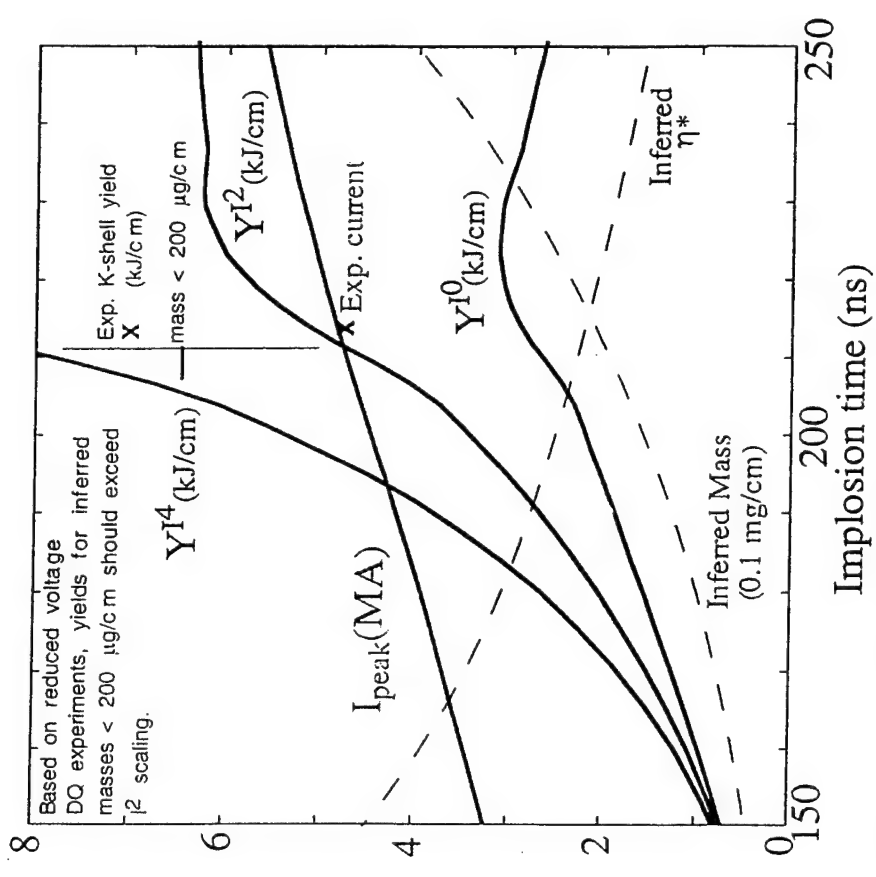
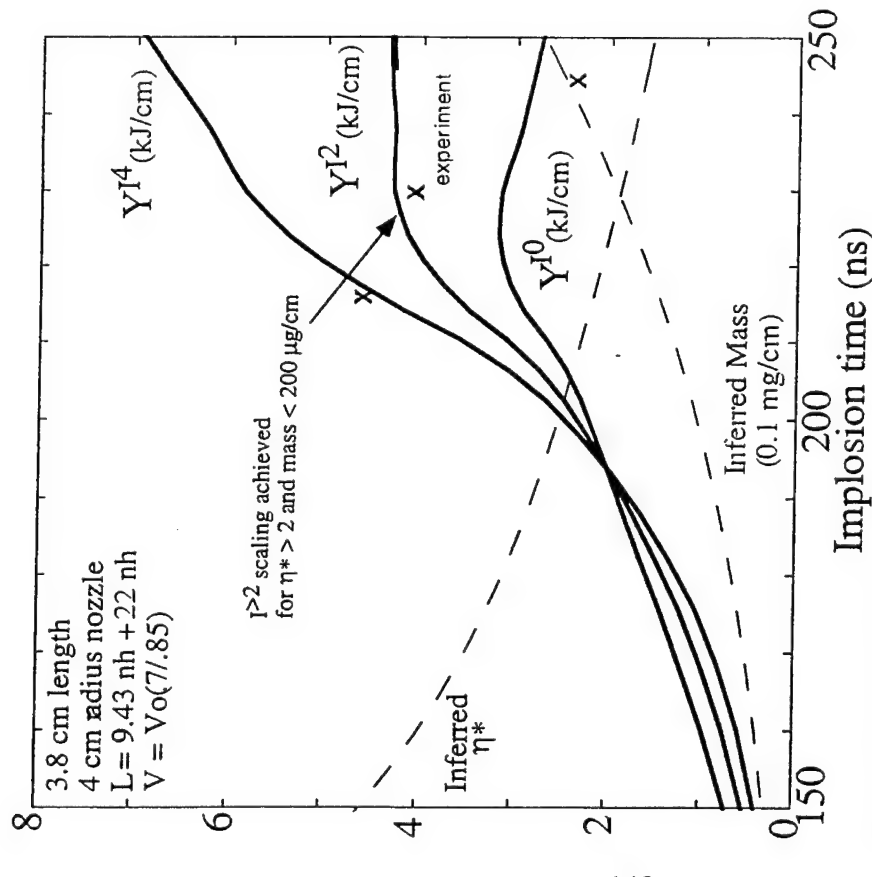


Fig. 9. Comparison of Decade Quad (reduced voltage) experimental K-shell yields with  $I^4$ ,  $I^2$ , and  $I^0$  K-shell yield projections from Double Eagle as a function of experimental implosion time. Also shown are inferred mass loads and  $\eta^*$  values.

Fig. 10. Comparison of Decade Quad (full voltage) experimental K-shell yields with  $I^4$ ,  $I^2$ , and  $I^0$  K-shell yield projections from Double Eagle yields. Also shown are inferred mass loads,  $\eta^*$  values, and experimental and calculated peak currents.

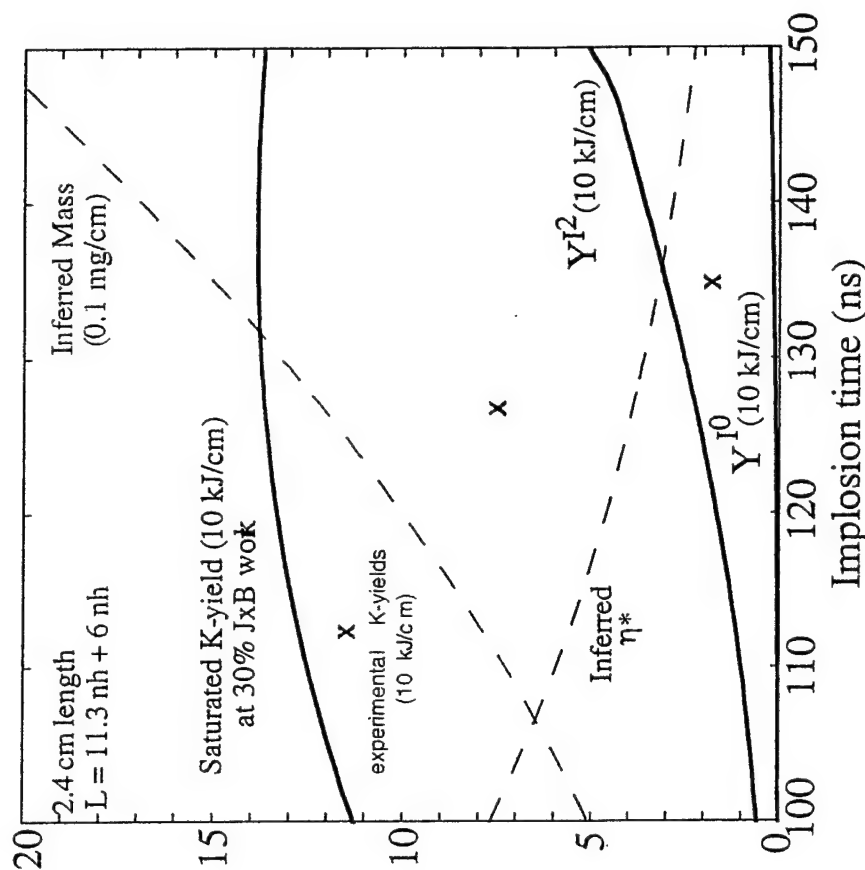
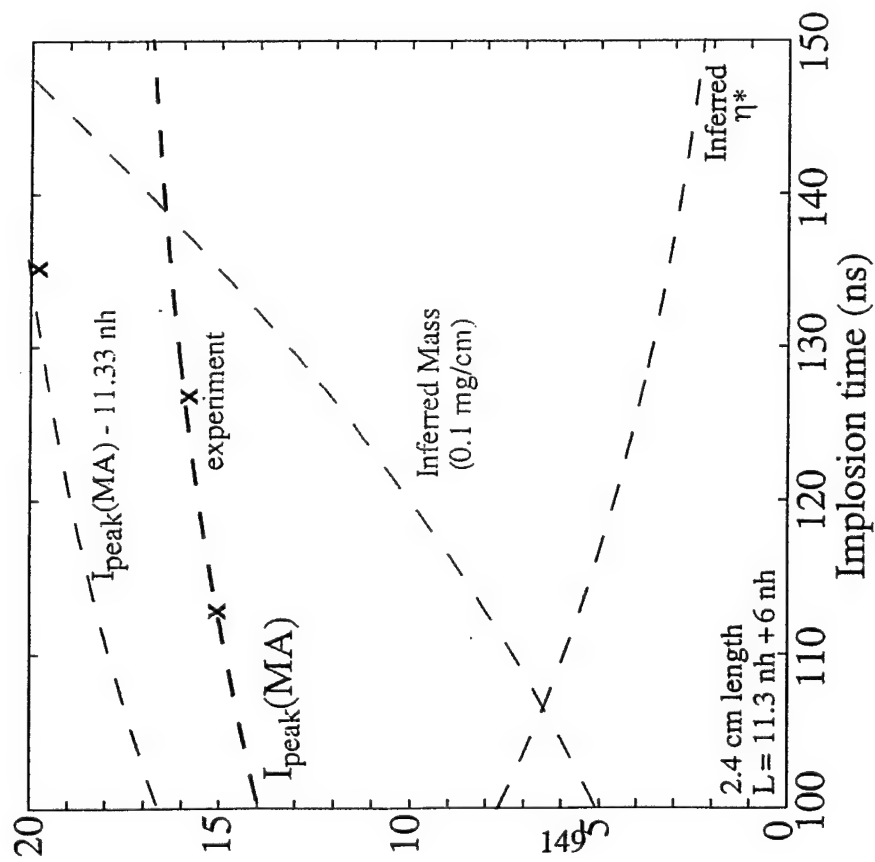


Fig. 11. Z generator experimental peak currents as a function of experimental implosion times. Also shown are inferred mass loads,  $\eta^*$  values, and calculated peak currents with/without added inductance.

Fig. 12. Comparison of Z generator experimental K-shell yields with  $\eta^4$ ,  $\eta^2$ , and  $\eta^0$  K-shell yield projections from Double Eagle as a function of experimental implosion time. Also shown are inferred mass loads and  $\eta^*$  values. (Note,  $\eta^4$  yields are shown as saturated at 30% JxB work.)

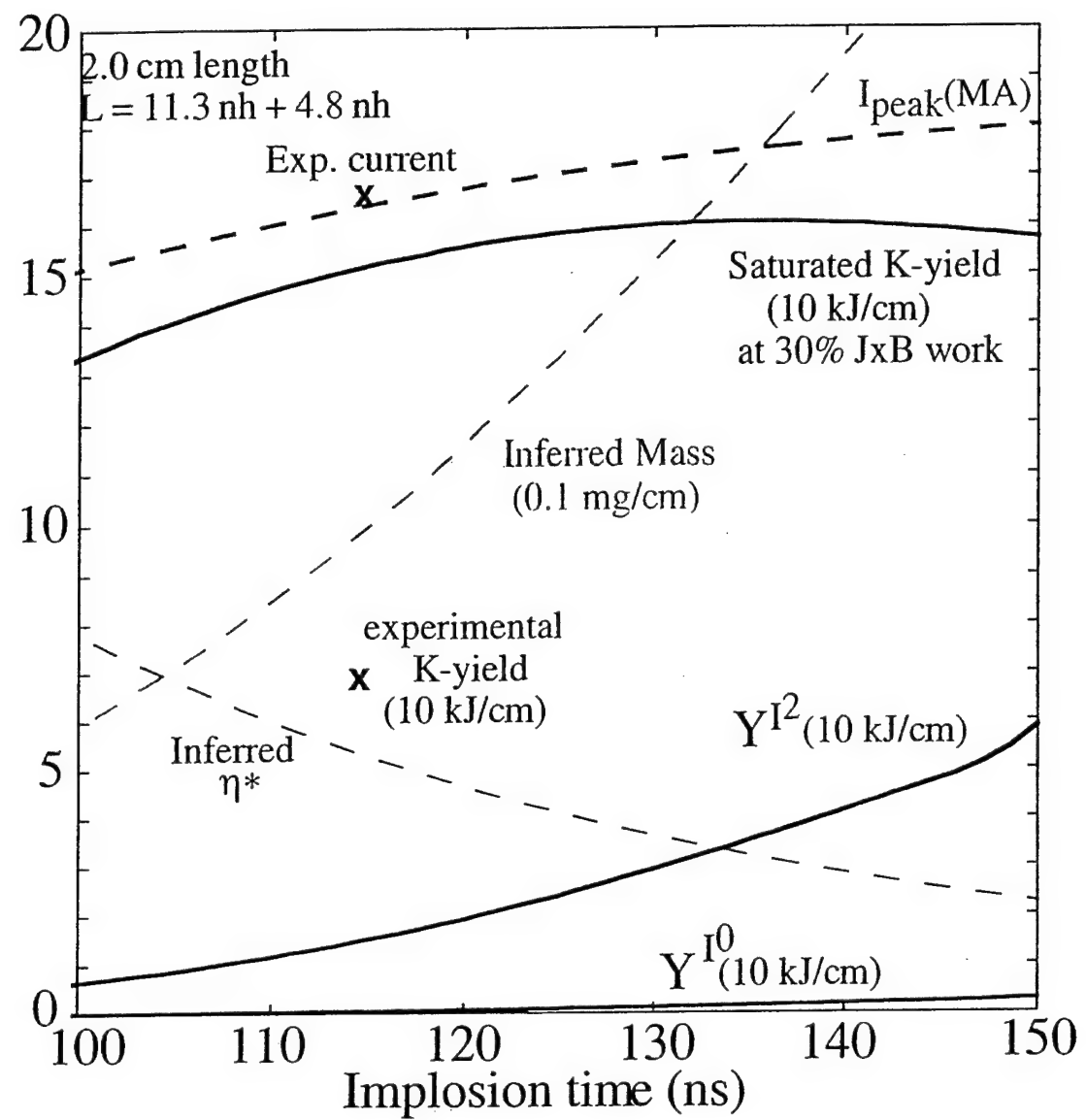


Fig. 13. Comparison of Z-generator (2.0 cm pinch length) experimental K-shell yields with  $I^4$ ,  $I^2$ , and  $I^0$  K-shell yield projections from Double Eagle as a function of experimental implosion time. Also shown are inferred mass loads,  $\eta^*$  values, and experimental and calculated peak currents.

## **Magnetic Flux Compression by Plasma Shells**

### **1. Introduction**

Magnetic flux compression may represent a new opportunity for using low-cost pulsed energy sources to generate currents at tens of MA. These large currents can then be driven through Z-pinch loads to produce x-ray pulses in the >10 keV spectral range. Magnetic flux compression (MFC) as a method for generating high magnetic fields and currents has been developed in the late 1950s, independently in the US<sup>1</sup> and in the Soviet Union,<sup>2</sup> and advanced ever since (see Refs. 3-5 and references therein, as well as the proceedings of the Megagauss conferences). The concept of the method is to compress a closed conducting cavity so rapidly that the magnetic flux trapped inside cannot escape via diffusion through the conducting surface. Then the magnetic field inside the cavity grows in inverse proportion to its shrinking cross-sectional area, due to the conservation of the trapped magnetic flux, and so does the induced diamagnetic current that generates this field. In a cylindrical geometry, we can compress either the axial magnetic field inside an annulus, or the azimuthal magnetic field trapped between the central conductor (stator) and the liner imploding onto it (armature). The former configuration - the MC-1-type generator, using the term originally introduced by A. D. Sakharov<sup>2,6</sup> - produces an ultra-high pulsed axial magnetic field (up to ~28 MG) in the annulus, whereas the latter one, labeled the MC-2-type generator, produces an ultra-high current pulse (up to ~100 MA) in a load connected to it. These generators are explosively driven, which limits the characteristic velocities of imploding solid conductors at the level of ~5 km/s. With initial radii about 5 cm or more, the explosive MFC generators operate in a microsecond range of current and magnetic field rise times. The same time scale is characteristic of other concepts of MFC generators<sup>5</sup>, e. g., compressing magnetic flux with a converging cylindrical shock wave that converts a dielectric medium into a conductor

The MFC concept could be advanced to generate currents and fields with nanosecond-range rise times.<sup>7-9</sup> To make it work the velocity of the conducting liner that compresses the magnetic flux should be of order of 100 km/s. There seems to be no way to accelerate solid conductors to  $\sim$ 100 km/s, explosively or otherwise. The magnetic flux could be compressed fast enough only with a low-mass plasma liner. Then the velocities in the desired range are well within the reach in the multi-MA Z-pinch experiments designed to produce keV x-rays<sup>10</sup> or soft x-rays to heat a hohlraum<sup>11</sup>, imploded annular plasmas are routinely accelerated to hundreds of km/s, e. g., see Refs. 12. Then the liner velocity might not be an issue, but its conductivity can become one, in contrast with the case of a solid conductor. In the latter case, one can ensure the liner thickness exceeds the skin depth, hence the magnetic flux cannot escape. On the contrary, the in-flight thickness of a plasma liner is not known in advance. Rather, it is determined self-consistently in the course of implosion. With the conductivity of the imploding plasma determined by its temperature, which is in most cases is controlled by radiative losses, confinement of the compressed magnetic flux is not ensured in advance: the flux can be lost through the plasma shell or be trapped inside it.

A similar theoretical problem had been studied some time ago in connection with the proposal to generate ultra-high magnetic axial field in a MC-1-like configuration, with a Z-pinch-driven gas-puff plasma shell used as a conducting liner.<sup>13</sup> It was noted<sup>14</sup> that enhanced flux losses characteristic of flux compression could have rendered this concept unworkable. Subsequent theoretical analysis and one-dimensional (1D) simulations<sup>15</sup> had shown that efficient compression of the axial magnetic flux by a plasma shell is possible if the shell velocity is sufficiently high. This conclusion was confirmed in experiments.<sup>16,17</sup> In particular, there were some indications that in the MCF experiment at 7.5 MA on PROTO-II generator at Sandia, a seed field of 100 kG was compressed to about 42 MG.<sup>17</sup>

The possibility of generating multi-MA currents via MC-2-like compression of azimuthal magnetic field by an annular plasma liner remained unexplored until recently.<sup>7-9</sup> It was discussed in

Ref. 18 in the context of the authors' concept of a staged Z pinch, where an outer plasma shell compresses an azimuthal magnetic flux initially created inside it by a small seed current passing through a fiber or wire on axis.

In this paper, the physics of flux compression by a dynamic plasma is studied analytically in planar geometry, and numerically in cylindrical geometry. Our main result is that the diffusive losses of compressed magnetic flux do not constitute a serious problem: the plasma is shown to arrange in such a way that the flux is essentially conserved.

## 2. Analytical theory

Magnetic flux compression (MFC) is considered as an options for increasing of efficiency of the nanosecond x-ray pulses generation in 10 KeV spectra range from Z-pinches at tens of MA. At the moment, several versions of MFC have been suggested.<sup>7-9</sup> The critical physical effects that determine performance of MFC are the loss of magnetic flux and energy in the primary circuit due to the flux diffusion into the plasma shell and the Rayleigh-Taylor instability of the shell implosion.

Here we present a simple one-dimensional (1-D) analytical theory to describe the magnetic flux losses in an imploding primary plasma liner whose thickness is of order of its skin depth.

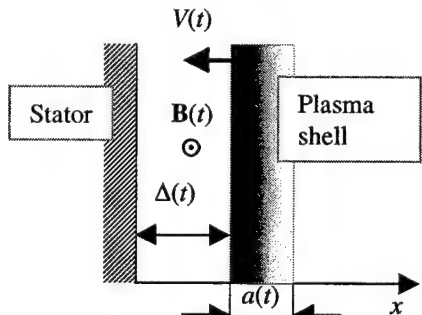


Fig. 1

The problem that we consider here for plane geometry is illustrated by Fig. 1. A plasma shell of finite conductivity whose thickness (or a characteristic length scale) is  $a(t)$

approaches a perfectly conducting stator, compressing the magnetic field  $\mathbf{B}(t)$  in the vacuum gap [whose width is  $\Delta(t)$ ] between the shell and the stator. Amplification of the magnetic field is due to compression of magnetic flux in the gap. The magnetic flux, however, is not fully confined to the

gap spacing. Some of it is trapped in the plasma shell or lost through it to infinity. We assume that the magnetic field is zero behind the plasma shell, and the flux, having been lost through the shell, is instantly distributed in the infinite space behind it without producing a finite magnetic field there.

Initially, the plasma shell velocity is  $-v_0$ , the magnetic field is  $B_0$ , the distance between the shell and the stator is  $\Delta_0$ . Supposing the shell to be thin, we can find the peak field  $B_{\max}$  that could be produced by equating the initial kinetic energy of the shell to the increase in the energy of the compressed field at the instant when the shell is stopped:

$$\frac{B_{\max}}{B_0} = 1 + \frac{4\pi M v_0^2}{B_0^2 \Delta_0}, \quad (1)$$

where  $M$  is the shell mass. Formula (1) says that the lower the initial field  $B_0$  is, the higher peak field  $B_{\max}$  would be produced, which is not surprising, since the compression ratios required for that must be very high:  $\Delta_0 / \Delta_{\min} = B_{\max} / B_0$ . Since the compression ratio itself is limited by the instability of the decelerated plasma interface, we can conclude that magnetic field compression ratio is approximately equal to the initial kinetic-to-magnetic energy ratio, and could be made as high as the stability limitations on the radial compression ratio would permit. The question we seek to answer in this study is: What are the additional limitations on magnetic flux compression due to finite conductivity of the plasma shell? Under what conditions they become critical or turn out to be inessential?

Our physical model is given by the following 1D MHD equations:

$$\frac{\partial \rho}{\partial t} + \frac{\partial}{\partial x} (\rho u) = 0, \quad (2)$$

$$\frac{\partial u}{\partial t} + u \frac{\partial u}{\partial x} + \frac{1}{\rho} \frac{\partial}{\partial x} \frac{B^2}{8\pi} = g(t), \quad (3)$$

$$\frac{\partial B}{\partial t} + \frac{\partial}{\partial x} (Bu) - \frac{\partial}{\partial x} \left( \nu_m \frac{\partial B}{\partial x} \right) = 0. \quad (4)$$

These equations are written in a non-inertial reference frame, in which the inner boundary of the plasma shell, which corresponds to  $x = 0$ , is at rest; the effective gravity acceleration in (3) is, of course,

$$g(t) = -\frac{d^2\Delta}{dt^2}. \quad (5)$$

The plasma is supposed to be cold, with its kinetic pressure much less than the magnetic pressure, so that only the latter is retained in the equation of motion (3). We assume the plasma temperature to be radiation-controlled, and essentially constant during the implosion, so that magnetic diffusivity,

$$\nu_m(t) = \frac{c^2}{4\pi\sigma(t)}. \quad (6)$$

will be taken constant below,  $\sigma$  being the plasma conductivity.

Our boundary conditions are:

$$\begin{cases} B = B(t) \text{ at } x = 0; \\ B = 0 \text{ at } x = a(t). \end{cases} \quad (7)$$

Our initial conditions are:

$$\begin{cases} B(0) = B_0; \\ a(0) = a_0; \\ \Delta(0) = \Delta_0; \\ \left( \frac{d\Delta}{dt} \right)_{t=0} = -\nu_0. \end{cases} \quad (8)$$

We seek a solution of Eqs. (2)-(4) with the initial and boundary conditions (7), (8) within the class of self-similar solutions with homogeneous deformation. Some particular solution of this type was investigated in paper<sup>19</sup>. We introduce a dimensionless self-similar coordinate and compression ratio

$$\eta = \frac{x}{a(t)}, \quad \alpha(t) = \frac{a(t)}{a_0}, \quad (9)$$

and use the self-similarity ansatz

$$u = \frac{a_0}{t_0} \frac{d\alpha}{d\tau} \eta, \quad \rho = \rho_0 \frac{N(\eta)}{\alpha(\tau)}, \quad B = B_0 \beta(\tau) H(\eta). \quad (10)$$

Here, the normalization constant  $\rho_0$  is chosen so that the total areal mass of the plasma shell  $M = \rho_0 a_0$ , so that the dimensionless density function  $N(\eta)$  should satisfy the normalization condition

$$\int_0^{\eta_m} N(\eta) d\eta = 1, \quad (11)$$

where  $\eta = \eta_m$  corresponds to the outer boundary of the plasma shell ( $\eta_m = \infty$  is the shell is diffuse).

We choose the time unit as

$$t_0 = \frac{1}{B_0} (8\pi M \Delta_0)^{1/2} \quad (12)$$

and introduce dimensionless time as

$$\tau = \frac{t}{t_0}. \quad (13)$$

Substituting (9), (10) into (2), we find that the continuity equation is identically satisfied with arbitrary density function  $N(\eta)$ . The equation of motion (3) is reduced to

$$\frac{a_0}{\Delta_0} \ddot{\alpha} \eta + \beta^2 \frac{1}{N} \frac{d}{d\eta} H^2 = -\ddot{\delta}, \quad (14)$$

where

$$\delta(\tau) = \frac{\Delta(t)}{\Delta_0} \quad (15)$$

is the dimensionless gap between the shell and the stator, and the dot denotes differentiation with respect to normalized time,  $\tau$ .

The thin-shell approximation means neglecting the first term in the left-hand side of (14) compared to its right-hand side. It is justified, at least for some time, because of the smallness of the

initial ratio  $a_0 / \Delta_0$ . For our solution to be applicable, we need to verify the smallness of  $(a_0 / \Delta_0)(\ddot{\alpha} / \ddot{\delta})$  in the process of compression.

The thin-shell approximation allows us to separate the variables in Eq. (14) if the  $\eta$ -dependent term is constant. The choice of this constant

$$N = -\frac{d}{d\eta} H^2 \quad (16)$$

satisfies the normalization condition (11), since the initial and boundary conditions (7), (8) for  $B$  imply that

$$\begin{cases} H(0) = 1; \\ H(\eta_m) = 0. \end{cases} \quad (17)$$

The solution is physically meaningful only if  $N(\eta) \geq 0$  for all  $\eta$ , so the derivative of magnetic field (and thus, the current density) cannot change sign.

Substitution of (16) into (14) yields:

$$\ddot{\delta} = \beta^2. \quad (18)$$

The induction equation (4) yields:

$$\alpha^2 \left( \frac{\dot{\beta}}{\beta} + \frac{\dot{\alpha}}{\alpha} \right) = \frac{1}{Rm} \frac{1}{H} \frac{d^2 H}{d\eta^2}, \quad (19)$$

where the magnetic Reynolds number is defined as

$$Rm = \frac{a_0^2}{v_m t_0}. \quad (20)$$

The left-hand side of (19) depends only on  $\tau$ , the right-hand side – on  $\eta$ . The variables in Eq. (19) could only be separated if both the left- and right- hand sides of this equation are equal to some separation constant. We denote this constant  $\pm s^2$ , depending on its sign. Three options are immediately seen.

1. Separation constant is positive,  $s^2$ . Then the profile shape is exponential:

$$H(\eta) = \exp(-\eta s \sqrt{Rm}) - \frac{2}{\exp(2\eta_m s \sqrt{Rm}) - 1} \sinh(\eta s \sqrt{Rm}). \quad (21)$$

This choice of constants satisfies the boundary conditions (17) If the shell is diffuse and extends to infinity ( $\eta_m = \infty$ ), then only the decaying exponential remains. We see that this solution exists and is physically meaningful [corresponds to a positive  $N(\eta)$  in Eq. (16)] for any  $\eta_m$ . In this case the magnetic flux contained in the plasma

$$\Phi_{pl}(\tau) = \int_0^{\Delta_m} B dx = a_0 B_0 \alpha(\tau) \beta(\tau) \int_0^{\eta_m} H(\eta) d\eta \quad (22)$$

grows with time.

2. Separation constant is zero. The magnetic field profile is linear,

$$H(\eta) = 1 - \eta / \eta_m. \quad (23)$$

The shell thickness is finite. Again, the solution is physically meaningful for arbitrary  $\eta_m$ .

The magnetic flux contained in the shell is constant in time: as much flux diffuses from the inside as is lost through the outside surface.

3. Separation constant is negative,  $-s^2$ . The profile shape is trigonometric

$$H(\eta) = \cos(\eta s \sqrt{Rm}) - \cot(\eta_m s \sqrt{Rm}) \sin(\eta s \sqrt{Rm}). \quad (24)$$

The solution is only physically meaningful for

$$\eta_m s \sqrt{Rm} < \frac{\pi}{2}. \quad (25)$$

The magnetic flux contained in the shell decreases with time, since more flux is lost through the outside surface than added via diffusion from the inside.

Let us start with the first option, which obviously is the most interesting physically. We derived two equations, (18) and

$$\frac{\dot{\beta}}{\beta} + \frac{\dot{\alpha}}{\alpha} = \frac{s^2}{\alpha^2}. \quad (26)$$

To close the system, we need one more equation.

It could be derived, say, from conservation of magnetic flux. If, for instance, we assume that no flux losses take place through the outer surface [which means a diffuse shell,  $\eta_m = \infty$ ] then we can state:

$$\Phi_{pl} + \Phi_{vac} = a_0 B_0 s \sqrt{Rm} \alpha(\tau) \beta(\tau) + \Delta_0 B_0 \delta(\tau) \beta(\tau) = \Phi_0 = const \quad (27)$$

or

$$\delta = \frac{\Phi_0}{B_0 \Delta_0} \times \frac{1}{\beta} - \frac{a_0 s \sqrt{Rm}}{\Delta_0} \times \alpha = \frac{1}{\beta} + \frac{\Phi_{0,pl}}{\Phi_{0,vac}} \left( \frac{1}{\beta} - \alpha \right). \quad (28)$$

Here,  $\Phi_{0,pl} / \Phi_{0,vac} = a_0 s \sqrt{Rm} / \Delta_0$  denotes the ratio of magnetic fluxes initially contained in the shell plasma and in vacuum between the shell and the stator, respectively.

For the particular case of the exponential solution with  $\eta_m = \infty$ , we can reduce the number of dimensionless parameters of the system using its symmetry. Indeed, definition of the length scale  $a(t)$  characteristic of the exponential profile allows multiplying it by any number  $a(t) \rightarrow \lambda a(t)$ . Consequently, we have some arbitrariness in the choice of  $a_0$  and  $Rm$ : our exponential solution depends on  $xs \sqrt{Rm} / a_0 \alpha(t) = xs / \alpha(t) \sqrt{v_m t_0}$ , a combination, which does not include  $a_0$  at all. Since  $\Delta_0$  is well-defined, we can get rid of this arbitrariness by requiring that the initial ratio of magnetic fluxes contained in the gap and in the shell was equal to the ratio of their length scales:

$$\frac{\Phi_{0,pl}}{\Phi_{0,vac}} = \frac{a_0}{\Delta_0}, \quad (29)$$

implying that

$$s = \frac{1}{\sqrt{Rm}}. \quad (30)$$

Thus we have fixed all the dimensionless parameters on which the solution should depend. They are: the small ratio of initial magnetic energy in the gap to the initial kinetic energy of the shell,

$$\varepsilon = \frac{\frac{B_0^2}{8\pi} \Delta_0}{\frac{1}{2} M v_0^2} \ll 1; \quad (31)$$

the small ratio of initial shell thickness to the initial gap spacing,

$$\phi = \frac{a_0}{\Delta_0} = \frac{\Phi_{0,pl}}{\Phi_{0,vac}} \ll 1, \quad (32)$$

and the magnetic Reynolds number defined by (20) with the length scale  $a_0$  consistent with (32), which, in principle, could be either large or small. Equations (26) and (28) are re-written as

$$\frac{\dot{\beta}}{\beta} + \frac{\dot{\alpha}}{\alpha} = \frac{1}{\alpha^2 Rm}, \quad (33)$$

$$\delta = \frac{1+\phi}{\beta} - \phi \alpha. \quad (34)$$

The initial conditions for variables  $\alpha$ ,  $\beta$ ,  $\delta$  are:

$$\alpha(0) = \beta(0) = \delta(0) = 1. \quad (35)$$

The initial velocity of the shell is  $-v_0$ , the corresponding normalized combination being

$$v_0 t_0 / \Delta_0 = (8\pi M v_0^2 / B_0^2 \Delta_0)^{1/2} = (2/\varepsilon)^{1/2}, \text{ see (12) and (31). Therefore,}$$

$$\dot{\delta}(0) = -(2/\varepsilon)^{1/2}. \quad (36)$$

With the aid of (33), (34), we find the initial conditions for derivatives of  $\alpha$  and  $\beta$ :

$$\dot{\alpha}(0) = \frac{1+\phi}{Rm} - (2/\varepsilon)^{1/2}, \quad (37)$$

$$\dot{\beta}(0) = (2/\varepsilon)^{1/2} - \frac{\phi}{Rm}. \quad (38)$$

To make our equations convenient for numerical integration, we re-write them in the form

$$\dot{\alpha} = v, \quad (39)$$

$$\dot{\beta} = \frac{\beta(1 - \alpha v Rm)}{\alpha^2 Rm}, \quad (40)$$

$$\dot{v} = \frac{1 + \phi - \alpha^4 \beta^3 Rm^2}{(1 + \phi + \alpha \beta \phi) \alpha^3 Rm^2}. \quad (41)$$

Now our problem is well defined. A full study of its solution is beyond the scope of the present paper. Here we describe some of them, presenting the self-similar solution in a dimensional form:

$$B(x, t) = (8\pi m |g|)^{1/2} H(\pm \xi) = \left| B_1^2(t) - B_2^2(t) \right|^{1/2} \exp \left[ \pm \frac{x - x_0(t)}{a(t)} \right]; \quad (42)$$

$$a^2(t) = \frac{8\pi m g_0 a_0^2 + 2\nu_m \int_0^t g dt}{g(t)} = \frac{\left[ B_1^2(0) - B_2^2(0) \right] a_0^2 + 2\nu_m \int_0^t \left[ B_1^2(t') - B_2^2(t') \right] dt'}{B_1^2(t) - B_2^2(t)}, \quad (43)$$

where the subscripts 1 and 2 correspond to the outer and the inner boundaries of the plasma shell, respectively. Note the important feature of the solution (21), (42): the profile of magnetic field is exponential rather than Gaussian, which is characteristic for diffusion!

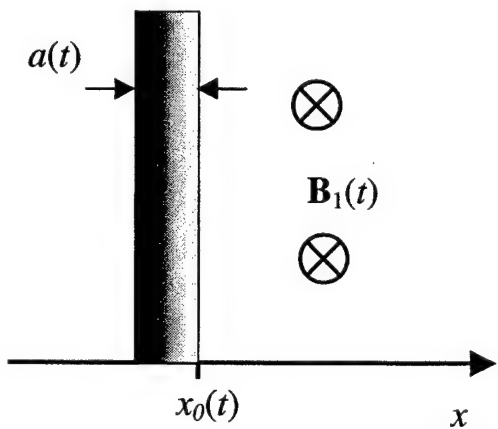


Fig. 2

Let us consider the early-time acceleration of a plasma shell neglecting the counter-pressure of compressed flux [that is,  $\mathbf{B}_2(t) \equiv 0$ ,  $x_1(t) \equiv x_0(t)$ ], varying the time dependence of the driving magnetic field: 1) linear growth,  $\mathbf{B}_1(t) \propto t$ ; 2) constant drive  $\mathbf{B}_1(t) \propto \theta(t)$ ; 3) decreasing  $\mathbf{B}_1(t) \propto 1/(t + t_0)$ . For these three cases, we find, respectively:

$$\begin{cases} a(t) = (v_m t / 3)^{1/2} \text{ for linear growth;} \\ a(t) = (v_m t)^{1/2} \text{ for constant drive;} \\ a(t) = [v_m t(t_0 + t) / t_0]^{1/2} \text{ for decrease.} \end{cases} \quad (44)$$

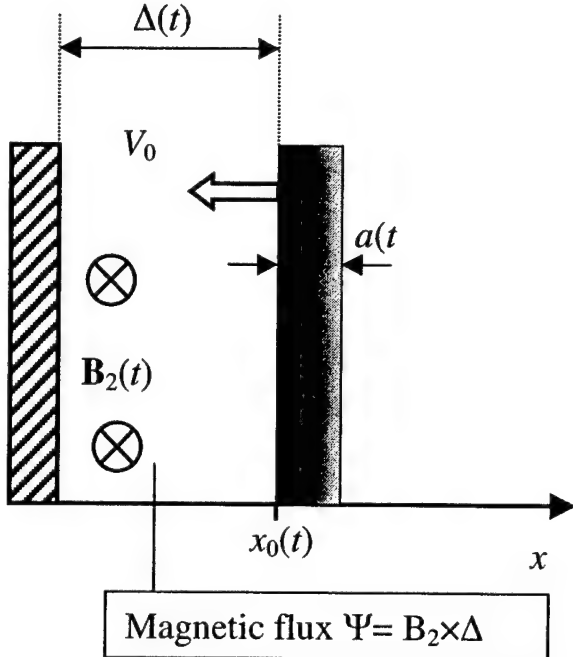


Fig. 3

At the instant  $t = t_0$  the relative values of the shell thickness are 0.58, 1, and 1.4, respectively, for the three case described by (44). This theoretical prediction is favorably tested in a simulation, see below.

Another particular solution refers to the late time, when the plasma shell is decelerated by the compressed magnetic field, and the driving magnetic pressure is negligible. In this case,

$\mathbf{B}_1(t) \equiv 0$ ,  $x_2(t) \equiv x_0(t)$ , and we again obtain

exponential profiles decaying in a different direction:

$$B(x, t) = B_2(t) \exp\left[-\frac{x - x_0(t)}{a(t)}\right], \quad \rho(x, t) = \frac{2m}{a(t)} \exp\left[-2\frac{x - x_0(t)}{a(t)}\right]. \quad (45)$$

From the approximate condition of energy conservation

$$m \frac{V_0^2 - V^2(\Delta)}{2} = \frac{\Psi^2}{8\pi} \left( \frac{1}{\Delta} - \frac{1}{\Delta_0} \right), \quad (46)$$

we obtain the expression for the thickness of the compressed shell:

$$a^2(\Delta) = 2v_m \Delta^2 \int_{\Delta_0}^{\Delta} \frac{d\Delta}{V(\Delta) \Delta^2}. \quad (47)$$

It says that as long as the plasma shell has not decelerated substantially, its thickness scales roughly as a square root of the gap between the shell and the stator.

### 3. Numerical modeling

We started the numerical studies with testing our self-similar solution of the problem of acceleration of a thin plasma shell by a magnetic field and of the magnetic field compression by the shell. The objective of the one-dimensional (1D) numerical modeling was verification of the fact that the self-similar solution found theoretically indeed describes the dynamics of the actual plasma shell. In particular, it was necessary to clarify the following questions: 1) the self-similar solution is established; 2) this self-similar solution is always stable in 1D. The simulations were performed by Dr. A. S. Chuvatin of Ecole Polytechnique (France) using a fully radiative MHD code ZETA and reported in Ref. 20.

In our 1D Lagrangian numerical simulations of the plasma shell formation, both the initial

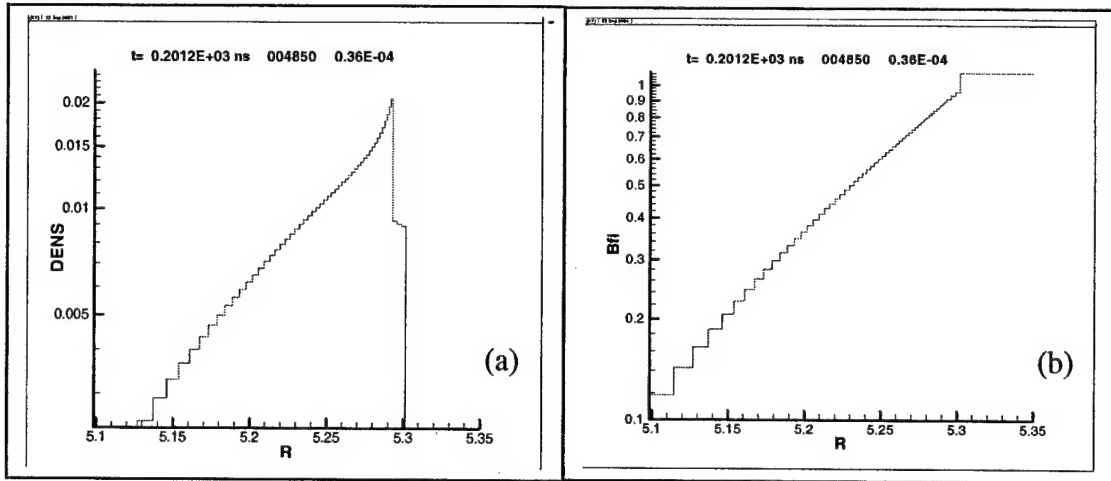


Fig. 4

thickness of the plasma shell and the waveform of the driving current pulse have been varied. The plasma conductivity was taken constant,  $\sigma = 10^{15} \text{ s}^{-1}$ , which for a microsecond current rise time would correspond to the skin depth of 2.7 mm. We took the initial thickness of the plasma shell slightly larger and much smaller than the skin depth, 3 mm and 0.3 mm, respectively. We found that at the distance of few skin depths the theoretical exponential distribution is established with a good accuracy, see Fig. 4. The profiles of density [Fig. 4(a)] and magnetic field [Fig. 4(b)] are linear in

linear-log scale, which means exponential. The self-similar exponential profiles are established as the plasma shell travels the distance of a few skin depths.

We have verified the scaling of the shell thickness with the conductivity value, as well as with the rise time of the driving current in the primary circuit and, especially, time shape (sine, constant, decreasing). It was found that with a good precision the thickness of the exponential

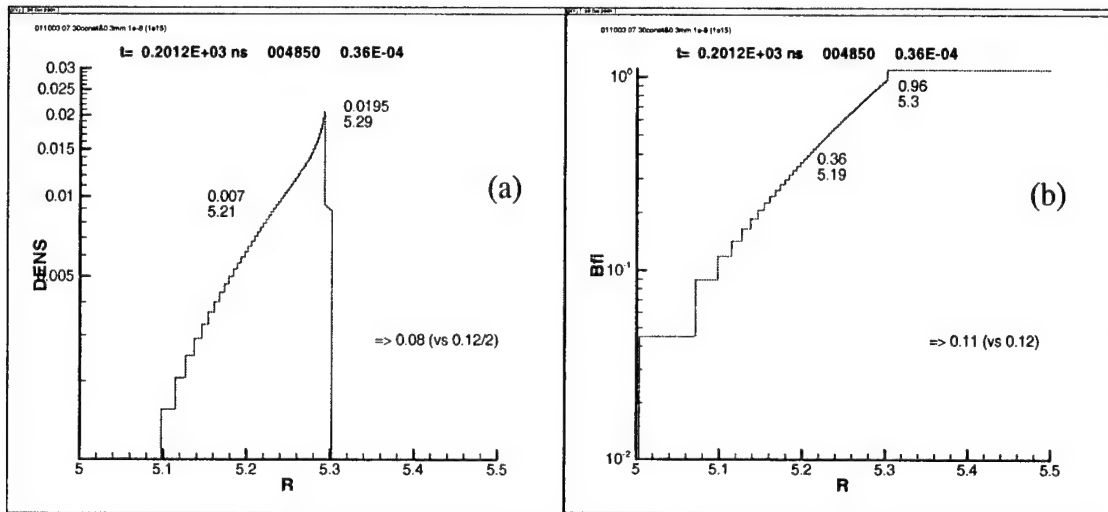


Fig. 5

distribution of the magnetic field and plasma shell density corresponds to the prediction of the self-similar solution (44). In particular, when the driving current waveform from a sine wave to slowly

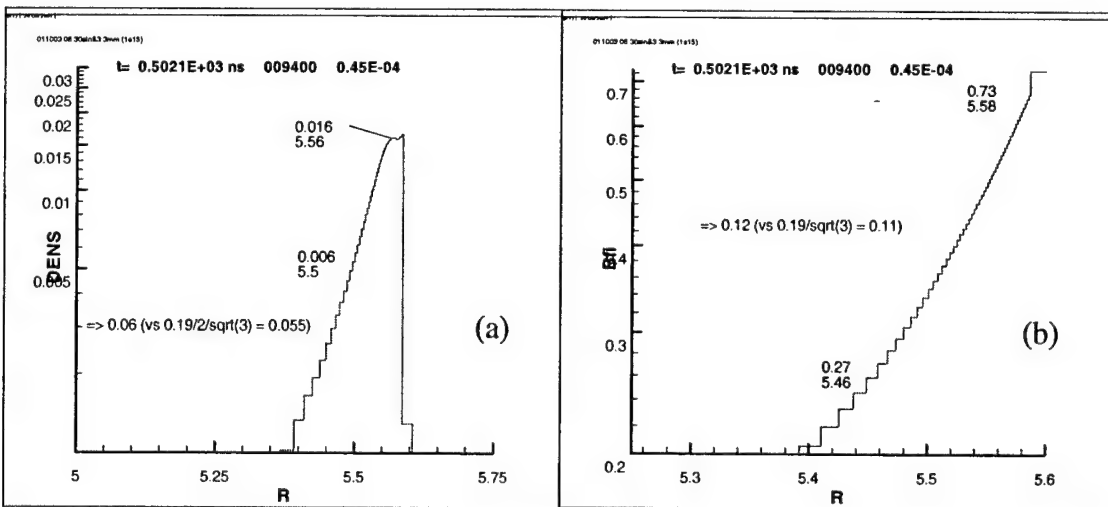


Fig. 6

decreasing with time, the shell thickness increases by a factor of  $\sim \sqrt{6}$ . This is illustrated by Figures 5, 6, showing the profiles of density (a) and magnetic field (b) for a plasma shell initially located at 6 cm, which is compressed by the magnetic field, which is either constant (Fig. 5) or varies as

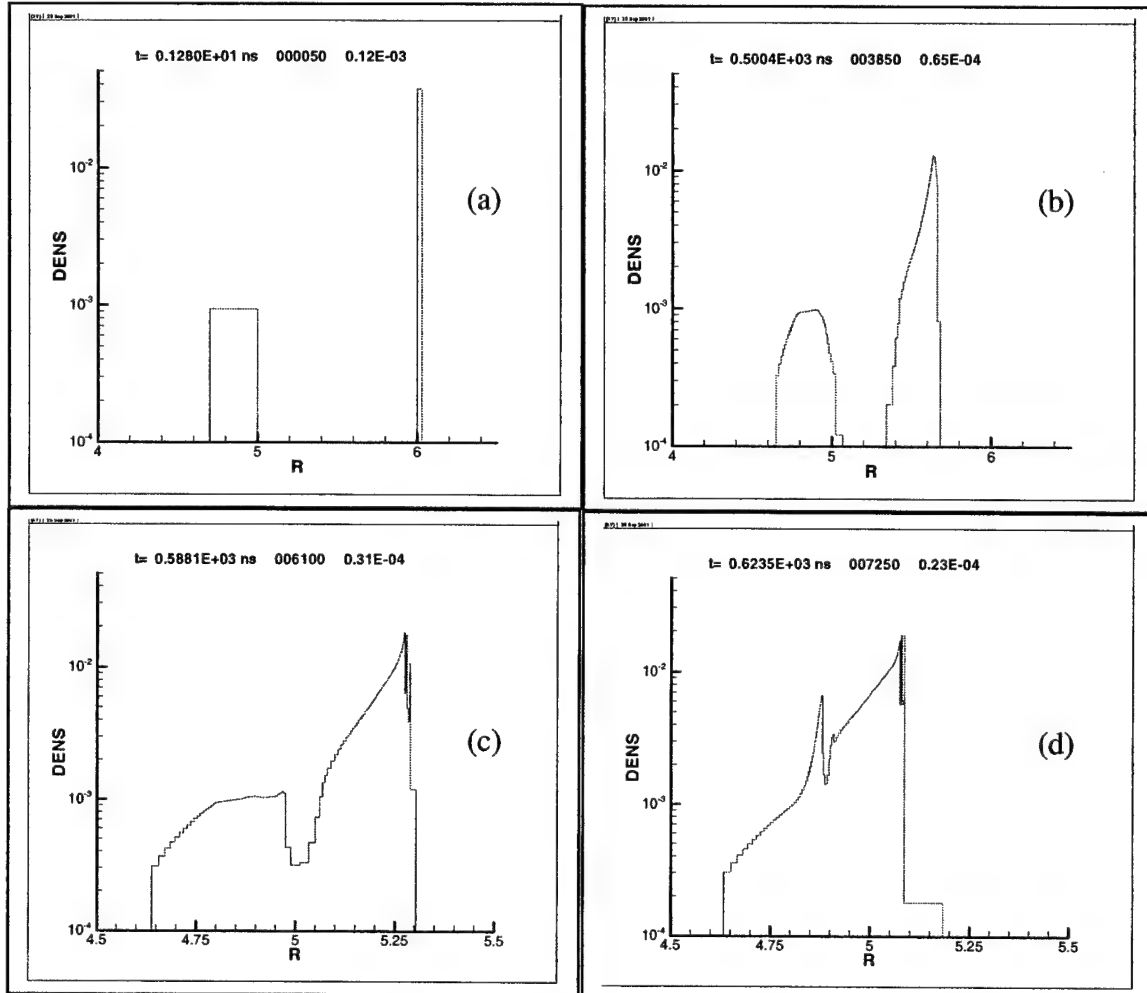


Fig. 7

$B_0 \sin \omega t$  (Fig. 6). The shell is seen to be thinner by a factor of  $\sqrt{3}$  in Fig. 6, in agreement with Eq. (44).

Another important issue is the 1D stability of the plasma shell. Of course, no Rayleigh-Taylor bubble and spikes can form within a 1D model of an imploding plasma shell. However, this does not guarantee that the shell does not break down into pieces. For instance, the worst-case scenario can be visualized as follows. Let the mass of the annular plasma shell be concentrated in a shell whose thickness is less than the skin depth, with some low-density plasma present in the

annulus. The current is thus free to diffuse through the plasma shell into the low-density plasma inside, which then can be rapidly imploded by the current flowing in it, leaving the main plasma mass behind, as it happens with precursor flows in wire-array Z-pinchers.<sup>21</sup> We have investigated this

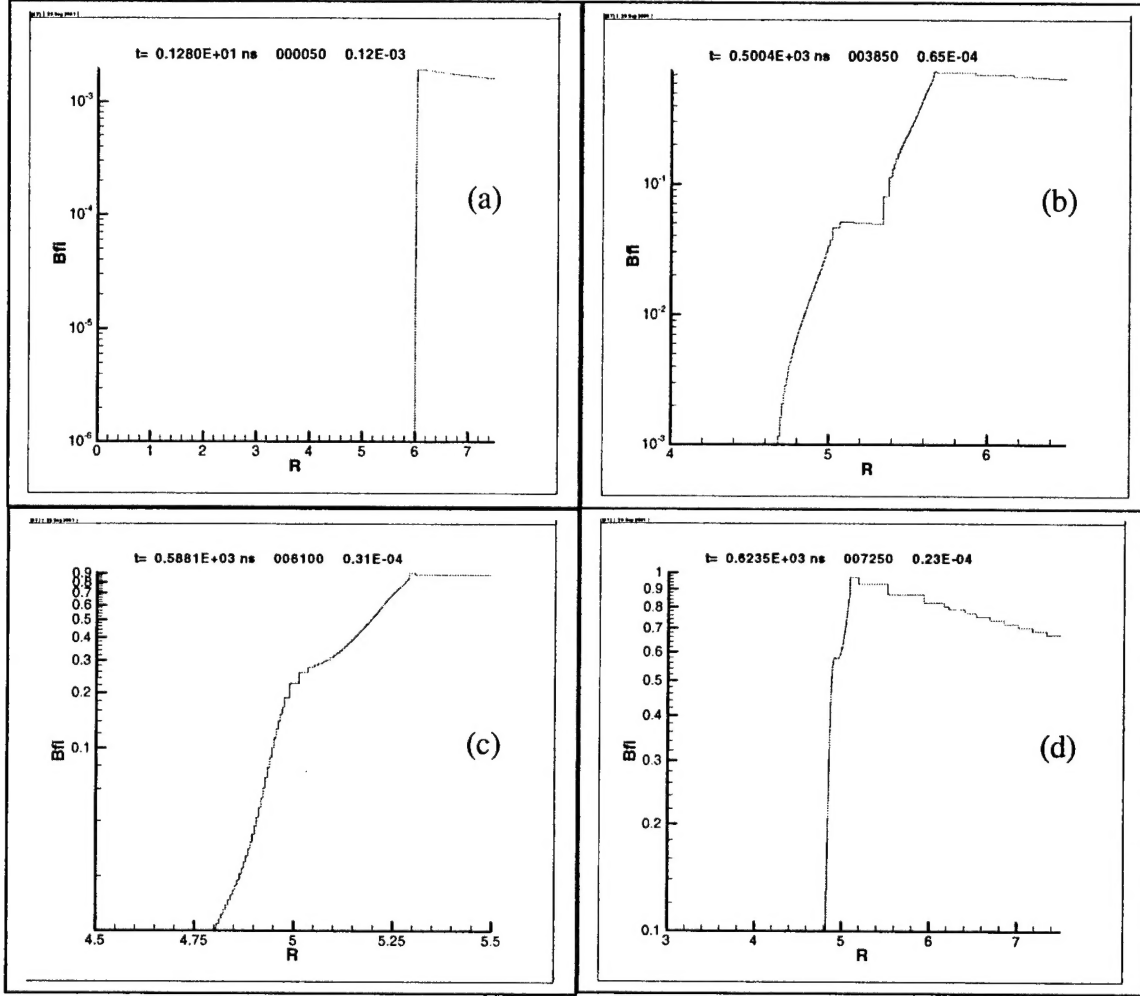


Fig. 8

possibility numerically and found that the breakdown of a plasma shell due to a 1D diffusion of the current inside it does not happen. The magnetic field is first seen to penetrate through the thin shell and reach the lighter inner shell, whose thickness is greater than the skin depth. However, the outer shell starts to expand with the velocity comparable to the radial velocity of the inner light shell. When the outer shell thickness reaches the skin depth, it starts intercepting most of the current. Eventually, the light inner and the heavy outer shell coalesce, forming a single shell with the self-

similar exponential profiles discussed above. This is illustrated by Figs. 7 and 8, showing the profiles of density and magnetic field, respectively, for the run where an initially thick light shell (1/5 total mass, 3 mm thickness) and an initially thin heavy shell (4/5 total mass, 0.3 mm thickness) are driven by the magnetic field of a constant 30 MA current. Initially (a) the current flows through the heavy outer shell and the magnetic field is nonzero only in this shell and outside it. Then the magnetic field penetrates to the inner shell, which starts accelerating inward and expanding (b). Expansion of the outer shell tends to close the gap between the shells (c), after which the two shells coalesce into a single thick shell (d).

We conclude that the 1D dynamics of the plasma shell compressing azimuthal magnetic flux is reasonably well approximated by analytical self-similar solutions. The cylindrical plasma shell behaves as a self-regulating structure, adjusting its thickness in such a way that it always remains of the order of the skin depth and is therefore capable of confining the enclosed magnetic flux. When perturbed (we tried a strong perturbation, breaking the shell into two parts), the shell eventually recovers its thickness and the profiles predicted by the theory. We have established therefore that the diffusive losses of magnetic flux do not constitute a major problem for the approach to high-energy photon radiation in Z-pinch plasma radiation sources based on the use of the azimuthal magnetic flux compression with a plasma shell used as an armature.

## References

<sup>1</sup> C. M. Fowler, W. B. Garn, and R. S. Caird, *J. Appl. Phys.* **31**, 588 (1960).

<sup>2</sup> A. D. Sakharov, R. Z. Lyudaev, E. N. Smirnov, Y. I. Plyushch, A. I. Pavlovskii, V. K. Chernyshev, E. A. Feoktistov, E. I. Zharinov, Y. A. Zysin, *Sov. Phys. Doklady AN SSSR* **165**, 65 (1965); A. D. Sakharov, *Physics, Uspekhi* **161**, 51 (1991) [reprinted from *Sov. Phys. Uspekhi* **88**, 725 (1966)].

<sup>3</sup> C. M. Fowler, *Physica B* **246**, 158 (1998).

<sup>4</sup> A. I. Bykov, M. I. Dolotenko, N. P. Kolokolchikov, V. D. Selemir, O. M. Tatsenko, *Physica B* **294**, 574 (2001).

<sup>5</sup> H. Knoepfel, *Pulsed High Magnetic Fields: Physical Effects and Generation Methods Concerning Pulsed Fields up to the Megaoersted Level* (North-Holland, London, 1970).

<sup>6</sup> E. I. Bichenkov, S. D. Gilev, and A. M. Trubachev, *J. Appl. Mech. Tech. Phys.*, no. 5, 125 (1980); K. Nagayama, *Appl. Phys. Lett.* **38**, 109 (1981).

<sup>7</sup> G. Avrillaud *et al.*, *Proc. 11<sup>th</sup> IEEE International Pulsed Power Conference*, v. 1, p. 47 (1997).

<sup>8</sup> J. F. Leon *et al.*, *Proc. 12<sup>th</sup> IEEE International Pulsed Power Conference*, v. 1, p. 275 (1999).

<sup>9</sup> L. I. Rudakov and E. M. Waisman, *Proc. 13<sup>th</sup> IEEE International Pulsed Power Conference*, (2001).

<sup>10</sup> N. R. Pereira and J. Davis, *J. Appl. Phys.* **64**, R1 (1988).

<sup>11</sup> M. K. Matzen, *Phys. Plasmas* **4**, 1519 (1997).

<sup>12</sup> C. Deeney, M. R. Douglas, R. B. Spielman, T. J. Nash, D. L. Peterson, P. L'Eplattenier, G. A. Chandler, J. F. Seaman, and K. W. Struve, *Phys. Rev. Lett.* **81**, 4883 (1998); C. Deeney, C. A. Coverdale, M. R. Douglas, T. J. Nash, R. B. Spielman, K. W. Struve, K. G. Whitney, J. W. Thornhill, J. P. Apruzese, R. W. Clark, J. Davis, F. N. Beg and J. Ruiz-Camacho, *Phys. Plasmas* **61**, 2081 (1999); H. Sze, J. Banister, P. L. Coleman, B. H. Failor, A. Fisher, J. S. Levine, Y. Song, E. M. Waisman, J. P. Apruzese, R. W. Clark, J. Davis, D. Mosher, J. W. Thornhill, A. L. Velikovich, B. V.

Weber, C. A. Coverdale, C. Deeney, T. Gilliland, J. McGurn, R. Spielman, K. Struve, W. Stygar, and D. Bell, *Phys. Plasmas* **8**, 3135 (2001).

<sup>13</sup> F. S. Felber, M. A. Liberman and A. L. Velikovich, *Appl. Phys. Lett.* **46**, 1042 (1985).

<sup>14</sup> G. E. Vekshtein, *Sov. Tech. Phys. Lett.* **10**, 319 (1984).

<sup>15</sup> A. L. Velikovich, S. M. Gol'berg, M. A. Liberman, and F. S. Felber, *Sov. Phys. JETP* **61**, 261 (1985); F. S. Felber, M. A. Liberman, and A. L. Velikovich, *Phys. Fluids* **31**, 3675 (1988).

<sup>16</sup> R. B. Baksh, A. L. Velikovich, B. A. Kablambaev, M. A. Liberman, A. V. Luchinskii, and N. A. Ratakhin, *Sov. Phys. Tech. Phys.* **32**, 145 (1987); F. S. Felber, F. J. Wessel, N. C. Wild, H. U. Rahman, A. Fisher, C. M. Fowler, M. A. Liberman, and A. L. Velikovich, *J. Appl. Phys.* **64**, 3831 (1988).

<sup>17</sup> F. S. Felber, M. M. Malley, F. J. Wessel, M. K. Matzen, M. A. Palmer, R. B. Spielman, M. A. Liberman, and A. L. Velikovich, *Phys. Fluids* **31**, 2053 (1988).

<sup>18</sup> H. U. Rahman, F. J. Wessel, and N. Rostoker, *Phys. Rev. Lett.* **74**, 714 (1995).

<sup>19</sup> S. F. Grigor'ev and S. V. Zakharov, *Sov. Tech. Phys. Lett.* **13**, 254 (1987).

<sup>20</sup> A. S. Chuvatin, L. I. Rudakov, and A. L. Velikovich, "Magnetic Flux Compression by Plasma Shells," presented at the APS-DPP Annual Meeting 2001, Long Beach, CA; *Bull. Am. Phys. Soc.* **46**, 316 (2001).

<sup>21</sup> S. V. Lebedev, F. N. Beg, S. N. Bland, J. P. Chittenden, A. F. Dangor, M. G. Haines, K. H. Kwek, S. A. Pikuz, and T. A. Shelkovenko, *Phys. Rev. Lett.* **85**, 98 (2000).